UNIVERSITE DE LIEGE

Faculté des sciences appliquées

Diffractive straylight rejection system for wide field imagers

Design, performance and application to the STEREO solar space mission

Année académique 2012-2013

Thèse présentée en vue de l'obtention du grade de Docteur en Sciences Appliquées par Jean-Philippe Halain, sous la direction du Pr. Pierre Rochus

Décembre 2012

A Camille et Guillaume.

Acknowledgements

My sincere thanks go to my advisor, Pierre Rochus, who provided me the opportunity of carrying out this work within the University of Liège.

I am grateful to the Belgian Science Policy Office (BELSPO) that funded the Belgian contribution to the development of the STEREO – HI instrument, in which frame the present work was conducted.

I also thanks the Centre Spatial of Liège, in which most of the work was performed. I would like to especially thank Emmanuel Mazy for his support, help and advices all along this work, but also Jean-Marc Defise who led me during the major part of this work

At the University of Birmingham and Rutherford Appleton Laboratory, I would like to thank Chris Eyles for his regular advices and support, but also Chris Davis, Danielle Bewsher, Steve Crothers and Jackie Davies for their help in the STEREO-HI image processing.

At the Naval Research Laboratory, I would like to thank Clarence Korendyke, Dennis Socker, Dan Moses and Jeff Newmark for their support to this work.

I also thanks my father, Michel Renard, Nicolas Grevesse and Yvan Stockman, but also the member of the Jury for their help in improving the present manuscript.

Last but not least, I want to thank all my family and friends, and in particular Laurence, Camille and Guillaume, for their support and patience all along this work.

Table of Contents

Executive Summary

Diffractive straylight rejection system for wide field imagers: design, performance and application to the STEREO solar space mission

Space-born wide field imagers have become a new tool used in the frame of Solar Physics and in particular in the field of Space Weather. One particular application is the tracking of coronal mass ejection (CME), generated by violent eruptions on the sun's surface, that propagates in the heliosphere. The CME brightness however rapidly decreases with the distance from the Sun.

To reach a sufficient signal to noise ratio and follow CME away from the Sun, a high sensitivity is therefore required and the unwanted parasitic light (so called straylight) must be minimized. In particular, the Sun disk brightness must be occulted by a highly rejecting baffle system.

A multi-edge diffractive baffle can provide a very high level of straylight attenuation for nearly collimated light source. A model of the multi-edge diffractive rejection has been implemented on the basis of the Fresnel diffraction theory. It allows the design and optimisation of such diffractive baffle as function of the instrument and observing geometries. The model was validated on a diffractive baffle mock-up, providing rejection down to an un-precedent level of 10^{-10} of the input flux.

The model of multi-edge diffractive baffle has been applied to the specific configuration of the Heliospheric Imager (HI), on-board the NASA scientific Solar Terrestrial Relations Observatory (STEREO) mission, as part of its overall straylight reduction. The STEREO-HI baffle performance has been validated on a prototype and during the final end-to-end calibration of the flight instrument.

After launch, the in-flight straylight level has been quantified, showing a very good correspondence with the on-ground measurements. The straylight evolution has also been shown to be stable during the mission, showing the baffle efficiency does not degrade with the space environment.

The STEREO-HI instrument achieves a 10^{-13} rejection level, or greater, of the solar brightness at the detector pixel level. This instrument is the first wide field space imager viewing from outside the Sun-Earth line, and therefore able to directly follow the propagation of CME from the Sun to the Earth with a high accuracy and sensitivity. Since its launch, it provides unprecedented images and information on solar wind and CME propagation and evolution in the heliosphere.

The next generation of wide-field solar imagers are under development for the ESA Solar Orbiter and NASA Solar Probe Plus missions. Their concept benefits from of the STEREO-HI front diffractive baffle system and is based on a multi-edge diffractive baffle to protect their cameras from solar disk brightness.

The straylight calibration of these two instruments is in preparation and will be performed at the Centre Spatial de Liège with the tools and methods developed in the frame of the present work.

Acronyms

AIT	Assembly, Integration and Tests
ASAP	Advanced Systems Analysis Program
AR	Anti-Reflective
arcdeg	degree of an arc
arcmin	minute of an arc
arcsec	second of an arc
AU	Astronomical Unit
AZP	Azimuthal/Zenithal Perspective
BRDF	Bidirectional Reflectance Distribution Function
CAD	Computer Assisted Design
CCD	Charged Coupled Device
CEB	Camera Electronics Box
CFRP	Carbon Fibre Reinforced Plastic
CME	Coronal Mass Ejection
COR	Coronograph
CSL	Centre Spatial de Liège
DC	Dark Current
DN	Digital Number
EIT	Extreme ultraviolet Imaging Telescope
EQM	Engineering Qualification Model
ESA	European Space Agency
EUV	Extreme UltraViolet
EUVI	Extreme UltraViolet Imager
FFT	Fast Fourier Transform
FM	Flight Model
ft	foot
FOV	Field of View
FPA	Focal Plane Assembly
HEW	Half Energy Width
HI	Heliospheric Imager
IMPACT	In situ Measurements of Particles and CME Transients
LASCO	Large Angle and Spectrometric Coronagraph
LGA	Low Gain Antenna
LOS	Line Of Sight
MSB	Mean Surface Brightness
mv	Visual magnitude
NASA	National Aeronautics and Space Administration
NaN	Not a Number
NRL	Naval Research Laboratory
OA	Optical Axis
ph	photon
px	pixel
PLASTIC	PLAsma and SupraThermal Ion and Composition
ppm	parts per million

PSF	Point Spread Function
RMS	Root Mean Square
S/C	Spacecraft
SEB	SECCHI Electronic Box
SECCHI	Sun Earth Connection Coronal and Heliospheric Investigation
SMEI	Solar Mass Ejection Imager
SO	Solar Orbiter
SOHO	SOlar and heliospheric Observatory
SOLOHI	Solar Orbiter Heliospheric Imager
SPP	Solar Probe Plus
sr	steradian
STEREO	Solar Terrestrial Relations Observatory
SNR	Signal to Noise Ratio
SWAVES	STEREO WAVES Instrumentation
TIS	Total Integrated Scatter
TQCM	Thermally Controlled Quartz Crystal Microbalance
UFOV	Unobstructed Field Of View
VIS	Visible
WISPR	Wide Angle Imager on-board Solar PRobe Plus
w.r.t.	with respect to

Chapter 1. Introduction

1. Introduction

1.1. Context

Solar physics is a branch of astrophysics that is specialized in the observation and analysis of our Sun to better understand its structure, dynamics and behaviour. As part of Solar Physics, Space Weather aims to study, determine and monitor the influence of the Sun on the performance and reliability of space-borne and earth ground-based technological systems and on human life. Figure 1-1 provides a schematic overview of the space weather context, with the Sun impact on the Earth magnetosphere [60][61].

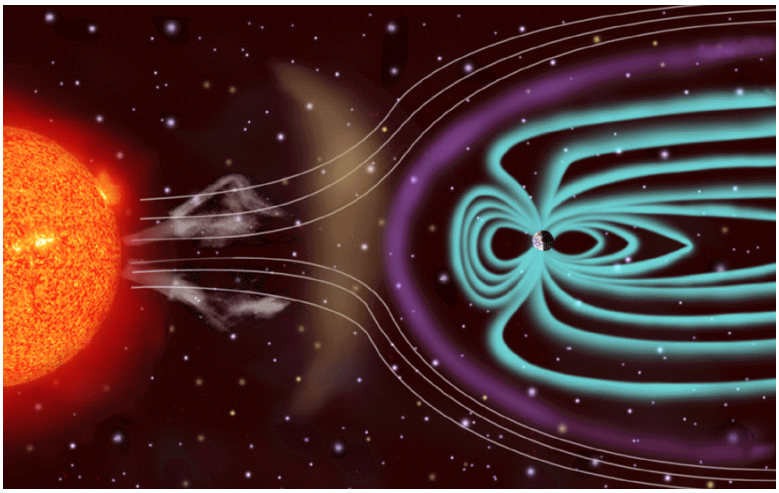

Figure 1-1 : Space weather program is based on Sun and Earth observations. The solar activity results in events that can propagate up to the Earth magnetosphere and interact with our atmosphere. [Courtesy of SOHO consortium. SOHO is a project of international cooperation between ESA and NASA].

Our Sun is an active star where eruptions take place with an intensity and frequency varying with an approximately 11-year cycle. Its corona is composed of electron and dust (so called K corona and F corona) [38], and is extremely modulated by the solar activity. A solar wind constantly propagates into the heliosphere, and regular ejection of material from the solar limb occurs. The ejection of material from the solar limb can be of very large scale, as shown on Figure 1-2 [41].

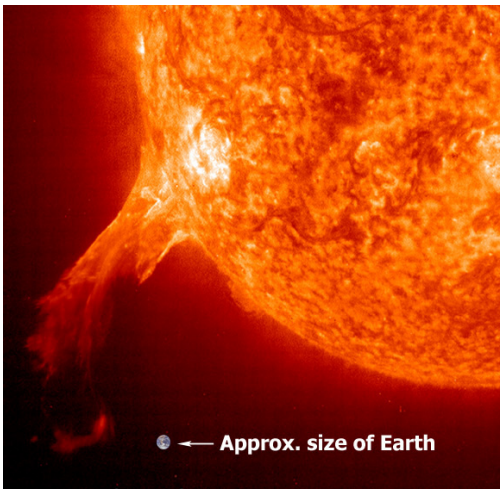

Figure 1-2 : Ejection of material from the solar limb captured by the EIT instrument on-board the SOHO mission, with Earth approximate size for comparison [Courtesy of SOHO consortium. SOHO is a project of international cooperation between ESA and NASA].

One particularly violent ejection is the so-called Coronal Mass Ejection (CME). A CME is a large-scale transient phenomenon where the sun magnetic field lines open, resulting in an intense explosion where billions of tons of energetic and ionised particles are ejected into the heliosphere with velocities ranging from 300 to 2000 km/s [37].

1.2. Solar corona wide-field imager

1.2.1. Coronal imaging

Coronal material ejections were discovered in 1973 [37] and have since been observed from ground and from space instruments. The three-dimensional structure of the CMEs, their motion and their interaction with the heliosphere are mostly investigated with white light time-series observations but also through the solar wind, charged particles measured in space.

White-light emission of the corona originates by Thomson scattering of the photospheric light by coronal electrons [35]. The observation of Coronal mass ejection (CMEs) is a spectacular example of this process. The CME enhances the density of the coronal plasma propagating away from the Sun and solar photons are Thompson scattered by free electrons in the corona into visible-light towards the line of sight.

The scattered emission is maximum when the line of sight (LOS) is the closest of the Sun centre (Figure 1-3), but also when it is normal to the radius through the scattering electron (so-called "impact radius"). The loci of maximum scattering as a function of elongation[1] ε lie on the surface of a sphere, which is called the Thomson surface [31][47].

Visible images of the solar corona and of the heliosphere thus provide a map of the heliosphere electron density and allow tracking in particular CMEs along their path in the heliosphere. To detect CME at very large elongations, it is however necessary to attenuate the solar disk brightness with a residual straylight level < 10^{-13} x the Sun Brightness per pixel of the camera detector [10].

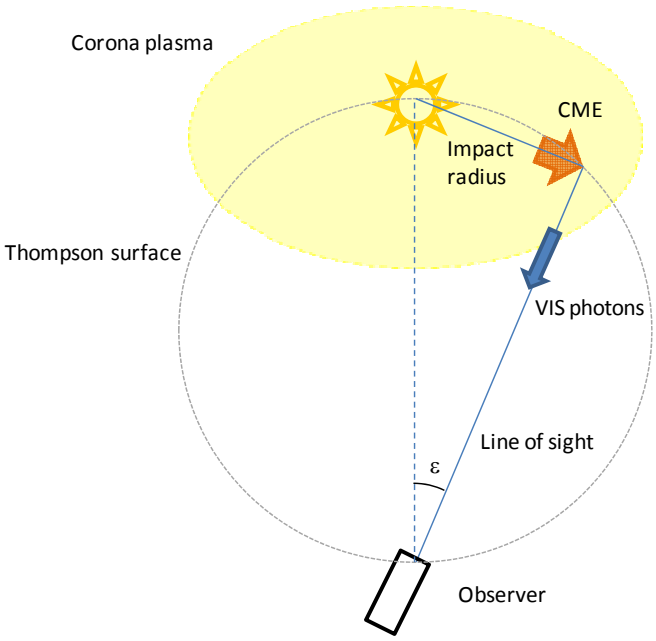

Figure 1-3 : Thomson scattering geometry. The electrons in coronal plasma, and in CME, interact with photospheric light resulting in scattered white-light emission that is maximum on the Thomson surface [47].

The observation of the solar corona has been improved in the 90's with in-space visible-light imagers providing observation of the CME behaviour from their source away from the Sun [39].

The evolution of the CME structure during their travel through the heliosphere, the forecasting of CME arrival on Earth, and the correlation with ground-based observation of CME arriving on Earth had however never been observed with high accuracy and sensitivity. Instruments providing large field of view (FOV) with sufficient signal to noise ratio (SNR) are therefore needed to make the link between solar disk imagers and solar activity analyses at Earth level.

[1] The elongation is defined as the angular distance between the Sun centre and the line of sight.

1.2.2. Straylight rejection

Straylight is the unwanted part of a measured signal, coming from a light source or an illuminated surface located either outside or within a camera FOV, which reduces the SNR. In many optical systems and instruments, straylight reduction is therefore one of the most important aspects of the design to improve the performance of imaging and in particular for a wide field imager.

Straylight reduction, or "rejection", is obtained with a so-called "baffle", providing shadow for the optical system. The baffles are usually combined with additional elements in the camera (field stop, light trap….).

Imaging instruments traditionally use baffle where the straylight is trapped by multi-reflections, taking advantage of an adequate absorbing black surface coating. These reflective and diffusive baffles are well suited for non-collimated straylight source but usually suffer from their edges that produce an additional diffracted straylight.

For a nearly collimated straylight source, i.e. coming from one particular direction with a limited divergence, the diffraction property of the baffle edge can however be efficiently used. A knife-edge can indeed provide an efficient light attenuation.

The combination of multiple edges, so that each edge intercepts the diffracted light from the previous edge, allows to achieve an even much higher rejection level and is the only method to guarantee a sufficient straylight rejection for wide-field imagers looking close to the a bright source (like the Sun for example).

The use of diffraction for straylight reduction has already been used in the past as for example in the coronographs [3].

1.2.3. Coronographs

In 1930 B. Lyot invented the coronagraph [36]. This instrument is essentially an on-axis telescope with an occulting disk to eclipse the Sun and observe the solar corona in visible wavelengths. The occulter reduces the straylight, from the Sun to a level where the corona surrounding the occulting disk can be observed.

The straylight level of a coronograph thus mainly depends on the occulter diffraction performance, usually combined with other features within the light path in the instrument.

In the original Lyot design, shown in Figure 1-4 [40], the occulter (O2) is internally mounted in the optical path and so-called "Lyot occulter". This occulter eliminates the straylight from the aperture (AO) diffraction and from multiple reflections in the objective lens O1.

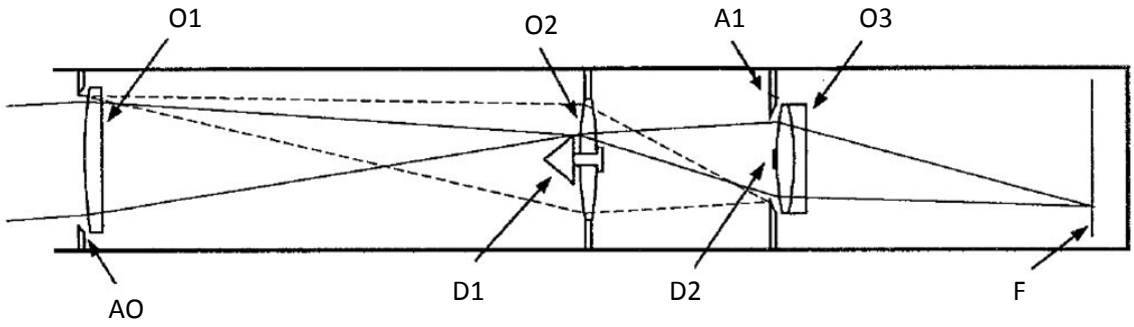

Figure 1-4 : Optical components of an internally occulted Lyot coronograph: entrance aperture A0; objective lens O1; internal occulter D1; field lens 02; Lyot stop A1; Lyot spot D2; objective lens O3; and focal plane F [40].

An externally mounted occulter can also be used, as shown in Figure 1-5 [40], where the occulter is composed of multiple circular disks (D1) so that each disk intercepts the diffracted sunlight from the edge of the previous one in order to achieve a higher rejection level on the entrance aperture (A1).

Such occulter thus takes advantage of multi-edge diffraction to achieve the required SNR. The rejection level reached is however limited by the presence of the Sun as part of the image and the field of view of the coronograph is limited to a few arc-degrees (arcdeg).

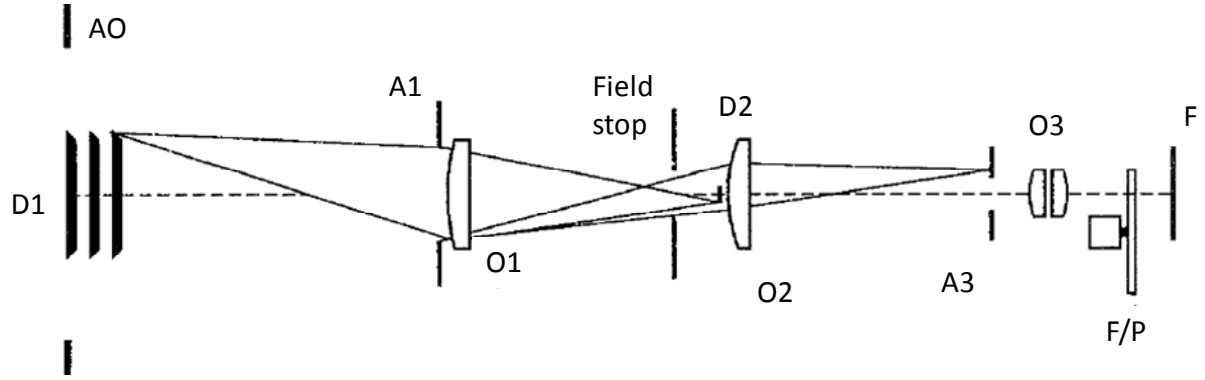

Figure 1-5 : Optical components of an externally occulted Lyot coronograph: front aperture A0, external occulter D1, entrance aperture A1, objective lens O1, internal occulter D2, field lens 02, Lyot stop A3, relay lens with Lyot spot 03, filter/polarizer wheels F/P, and focal plane F [40].

One of the most sensitive wide-field coronograph is the Large Angle and Spectrometric Coronagraph (LASCO) instrument, on-board the SOlar and Heliospheric Observatory (SOHO) mission launched in December 1995 [40][43].

LASCO is composed of three coronographs, LASCO C1, C2 and C3. The LASCO C2 and C3 uses both an external occulter to shadow the instrument and an internal occulter to block diffraction around the external occulter. An internal baffle is also used to eliminate straylight scattering from the internal surfaces.

LASCO C3 provides coronal observation up to 32 solar radii (R_{sun} = 0.27 arcdeg), i.e. 8.5 arcdeg, as shown on Figure 1-6.

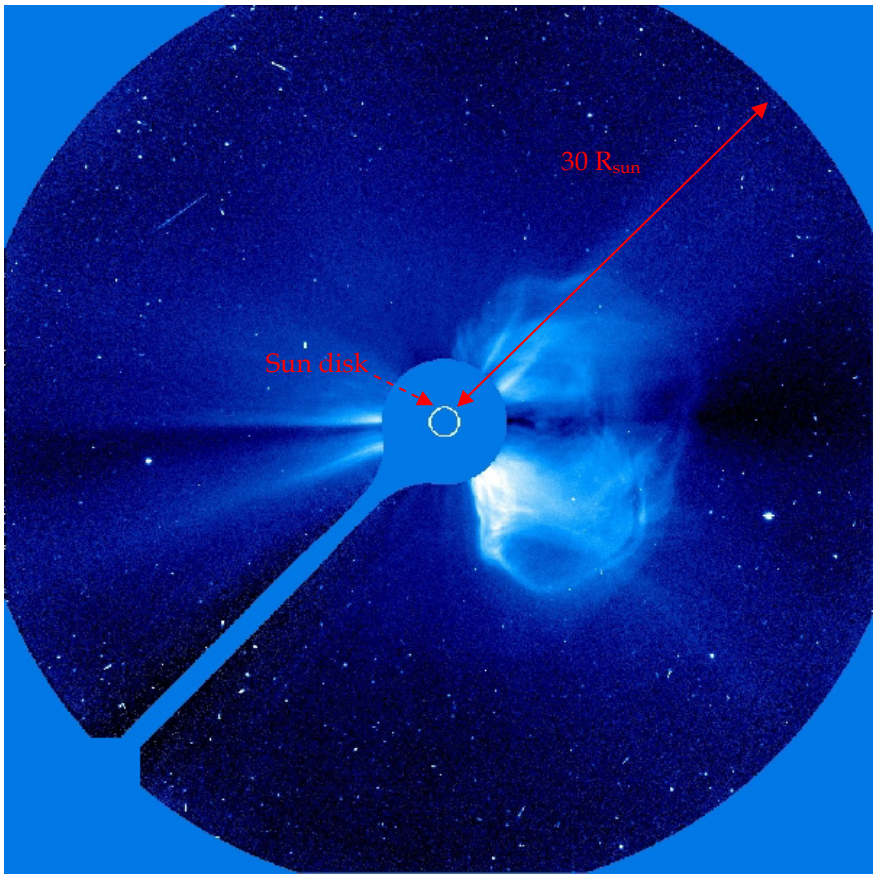

Figure 1-6 : CME observed up to 32 solar radii (R_{Sun}) with the space-born LASCO C3 instrument on-board SOHO mission. The Sun is located at the center of the image. [Courtesy of SOHO/LASCO C-3 consortium. SOHO is a project of international cooperation between ESA and NASA].

Another very-wide field coronograph is the Solar Mass Ejection Imager (SMEI) instrument on-board the Coriolis spacecraft launched in January 2003 [45] [46].

SMEI was the first space instrument to observe CME propagation up to the Earth, from an Earth orbiting viewpoint [48].

It provided an overview of the heliosphere by recombination of 3 x 60 arcdeg (~ 12 x 225 R_{Sun}) strips of the sky captured sequentially and allowed to follow the propagation of a CME away from the Sun. The combination of the images provides a view of the corona similar to an externally occulted coronograph but over a wider field of view (Figure 1-7).

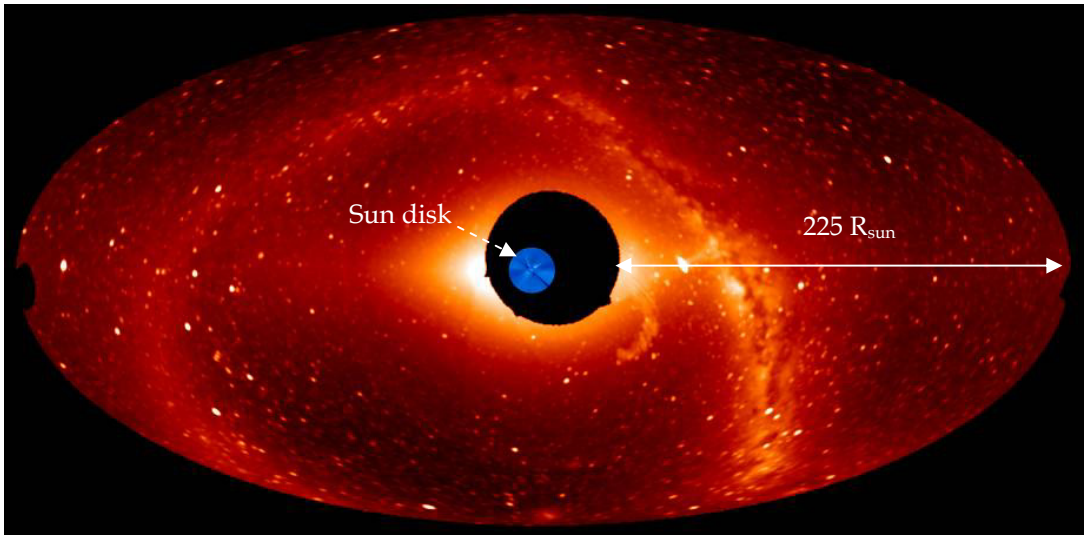

Figure 1-7 : Image of the solar heliosphere obtained with the SMEI Coriolis spacecraft, launched in 2003, composed of combined 3 x 60 arcdeg strips. The Sun is located at the center of the image. [Courtesy of University of Birmingham].

The straylight of the SMEI instrument is controlled by three multi-reflection absorbing external baffles with black coated edges to trap solar disk light reaching the interior of the baffle aperture, as shown on Figure 1-8 [45].

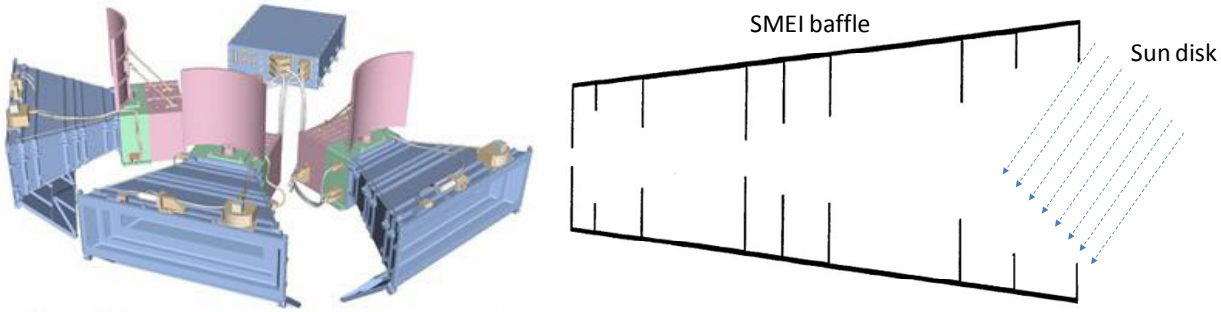

Figure 1-8 : Left: The three SMEI camera baffles. Right: The SMEI baffle takes advantage of multi-reflections in a black coated multi-edges system [45].

1.2.4. State of the art

Internally occulted coronographs, as LASCO C2, have a rejection level ~10^{-6} x the Sun brightness [40]. Externally occulted coronographs, as LASCO C3 and other coronograph-like instrument, as SMEI, have a residual straylight level < 10^{-9} x the Sun brightness [40] [45].

Because of the Sun location as part of the image, the residual straylight reduction in a coronograph is however intrinsically limited and the corona can only be observed with enough resolution and sensitivity up to a few tens of R_{sun} from the Sun limb.

A new type of solar corona wide field imagers was therefore proposed in the frame of the STEREO mission, with a multi-edge linear diffractive baffle providing the solar disk rejection [5][6][10], as shown

in Figure 1-9. In that concept, the instrument's camera is located in the shadow of the diffractive baffle and covers a much larger field of view.

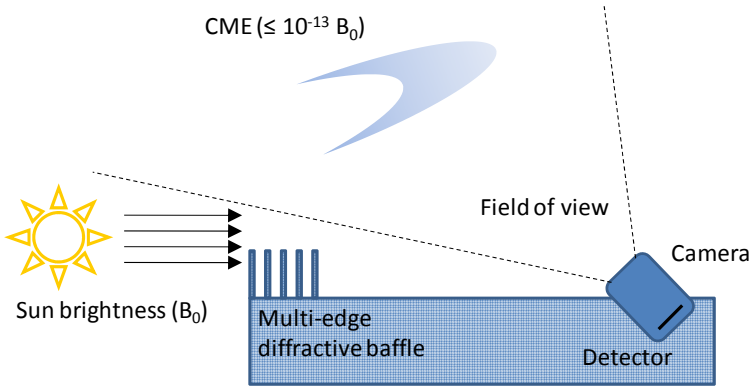

Figure 1-9 : Concept of a wide field heliospheric imager, where the camera is in the shadow of a multi-edge linear diffractive baffle.

The main advantage of this new baffle concept is to keep the Sun out of the image, on the contrary of traditional coronographs, allowing a fine and very sensitive observation of the heliosphere.

Preliminary laboratory measurements were conducted to determine the scattering rejection as function of the number of edges [5] showing that a 3 diffracting edge baffle provides a rejection of ~10^{-10}. Computation also showed that a five edge baffle should provide a sufficient solar baffle rejection [5] but it has never been proved or measured.

The front diffractive baffle being the key element of the STEREO-HI instrument, it was therefore necessary to design it, but also to measure its effective performance and validate the model predicting a rejection down to 10^{-13} of the Sun mean brightness.

1.3. The STEREO Heliospheric imager

1.3.1. The STEREO mission

The Solar Terrestrial Relations Observatory (STEREO) mission is a NASA program composed of two identical satellites launched in October 2006 into Earth-like orbits [17]. One spacecraft is leading (named "A" for ahead) and the other one is lagging ("B" for behind) the Earth, with a 22.5 arcdeg angle increase per year, providing two observation points of view of the Sun and its environment (Figure 1-10) [17].

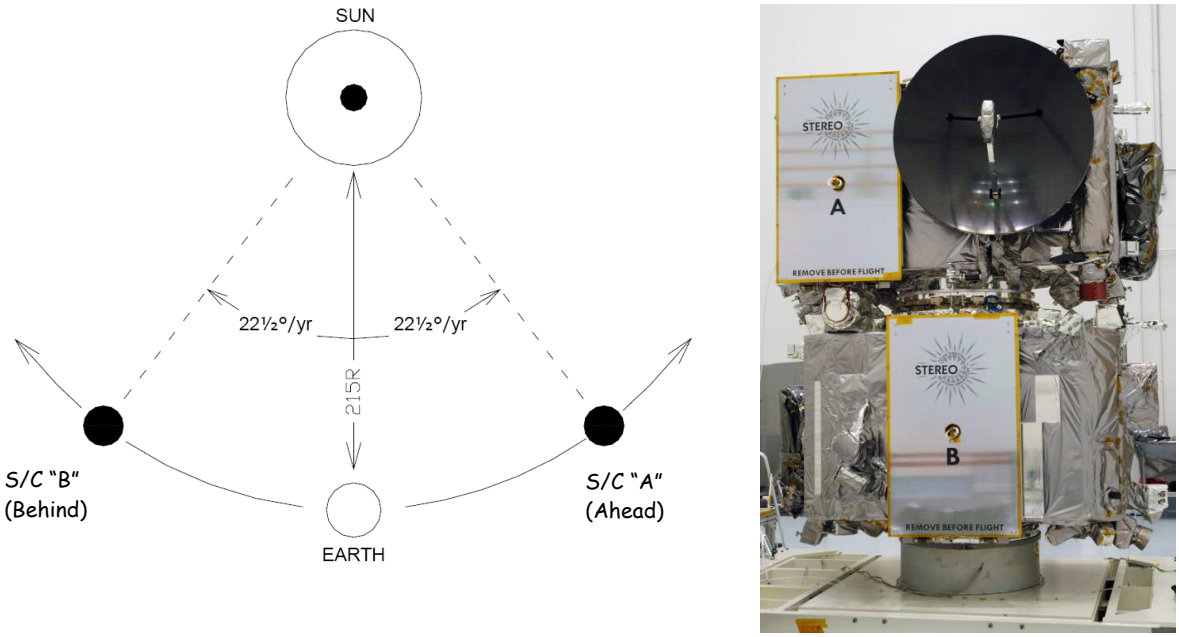

Figure 1-10 : Left: STEREO spacecraft A and B orbit as viewed from north ecliptic pole. STEREO A is ahead (leading) and B is behind (lagging) the Earth on Earth-like orbits, with a 22.5 arcdeg increase per year [18]. Right: the two STEREO spacecrafts are mounted on top of each other before being integrated in the launcher fair.

The science objectives of the STEREO mission are to [17]:

- Discover mechanisms of solar energetic particle acceleration
- Understand origins and consequences of CMEs
- Determine processes that control CME evolution in heliosphere
- Determine 3-D structure and dynamics of corona, interplanetary plasmas and magnetic fields
- Characterize CMEs from their initiation to 1 AU

On-board STEREO, two groups of instruments are implemented [17].

- The remote sensing instruments:
    - The Sun-Earth Connection Coronal and Heliospheric Investigation (SECCHI) is composed of four imaging instruments to study the 3-D evolution of CME's from the surface of the Sun through corona and interplanetary medium to eventual impact at Earth.
    - The STEREO/WAVES (SWAVES) is an interplanetary radio burst tracker to study the generation and evolution of travelling radio disturbances from Sun to Earth orbit.
- The in situ instruments:
    - The In situ Measurements of Particles and CME Transients (IMPACT) samples the 3-D distribution and provides plasma characteristics of solar energetic particles (SEP) and the local vector magnetic field.
    - The PLAsma and SupraThermal Ion and Composition (PLASTIC) provides plasma characteristics of protons, alpha particles and heavy ions, to characterize CME plasma from ambient coronal plasma.

The SECCHI is a suite of imaging instruments observing the entire region from the disk of the Sun to the Earth, allowing in particular to track CME in the heliosphere [19]. The main characteristics of these instruments are summarised in Table 1-1:

- an Extreme Ultraviolet Imager (EUVI) instrument, that provides EUV observation of the Sun disk;
- two coronographs (COR1 and COR2) instruments, that provide visible light coronographic images of the solar limb up to 15 solar radii;
- an Heliospheric Imager (HI) instrument, that provides visible light images out to the Earth orbit and beyond of the heliosphere up to the Earth orbit, and is composed of two cameras (HI-1 and HI-2) to cover this extended field of view.

Instrument	Wavelength	Pixel angular size	FOV	Nominal cadence
EUVI	171, 195, 284, 304 Å	1.4 arcsec	1.7 R_{Sun}	2.5 minutes
COR1	650 – 660 nm	7.6 arcsec	1.4 - 4 R_{Sun}	8 minutes
COR2	650 – 750 nm	14 arcsec	2.5 - 15 R_{Sun}	20 minutes
HI-1	630 – 730 nm	35 arcsec	15 - 90 R_{Sun}	60 minutes
HI-2	400 – 1000 nm	120 arcsec	70 - 330 R_{Sun}	120 minutes

Table 1-1 : The main characteristics of the SECCHI instruments showing how the solar disk, corona and heliosphere are imaged by the STEREO mission [19].

The SECCHI fields of view are shown on Figure 1-11, with in particular the HI FOV borders. A CME propagating from the Sun towards the Earth is therefore detected first by EUVI, then successively by COR1 and COR2, and finally by the HI instrument.

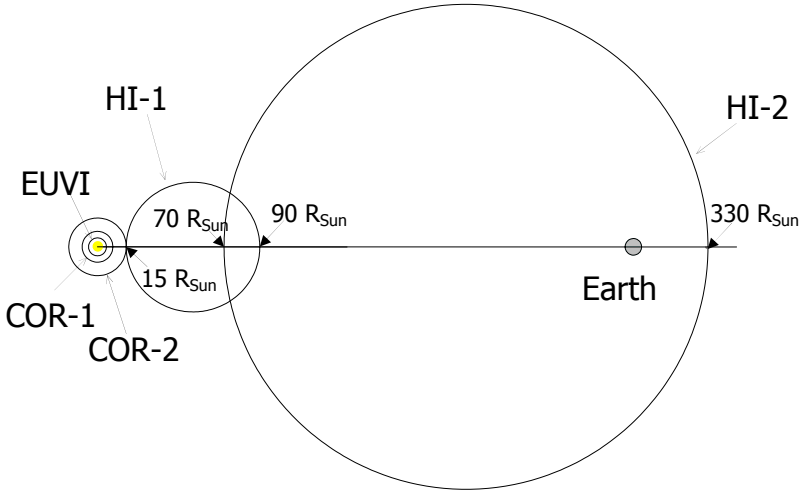

Figure 1-11 : Fields of view of the SECCHI suite of instruments: EUVI imaging the Sun disk, COR1 and COR2 provide visible coronographic views of the Sun close heliosphere (up to 15 R_{Sun}) and HI provides visible images of the heliosphere up to the Earth and beyond (from 15 R_{Sun} up to 330 R_{Sun}) and is composed over two cameras fields of view (HI-1 and HI-2) [19].

1.3.2. The STEREO-HI instrument

Unlike the coronographs that have circular field of view, the STEREO-HI instrument is composed of two optical systems with rectangular fields of view, the Sun being located outside and not at the centre of the images. To achieve the required imager performance, the two cameras are in the shadow of a multi-edge diffractive baffle that protects the optics from the brightness of the Sun [10].

A typical STEREO-HI image of a CME propagating through the heliosphere is shown on Figure 1-12. The unprecedented high sensitivity of this instrument allows the observation of the fine structure of the solar wind and of CME's.

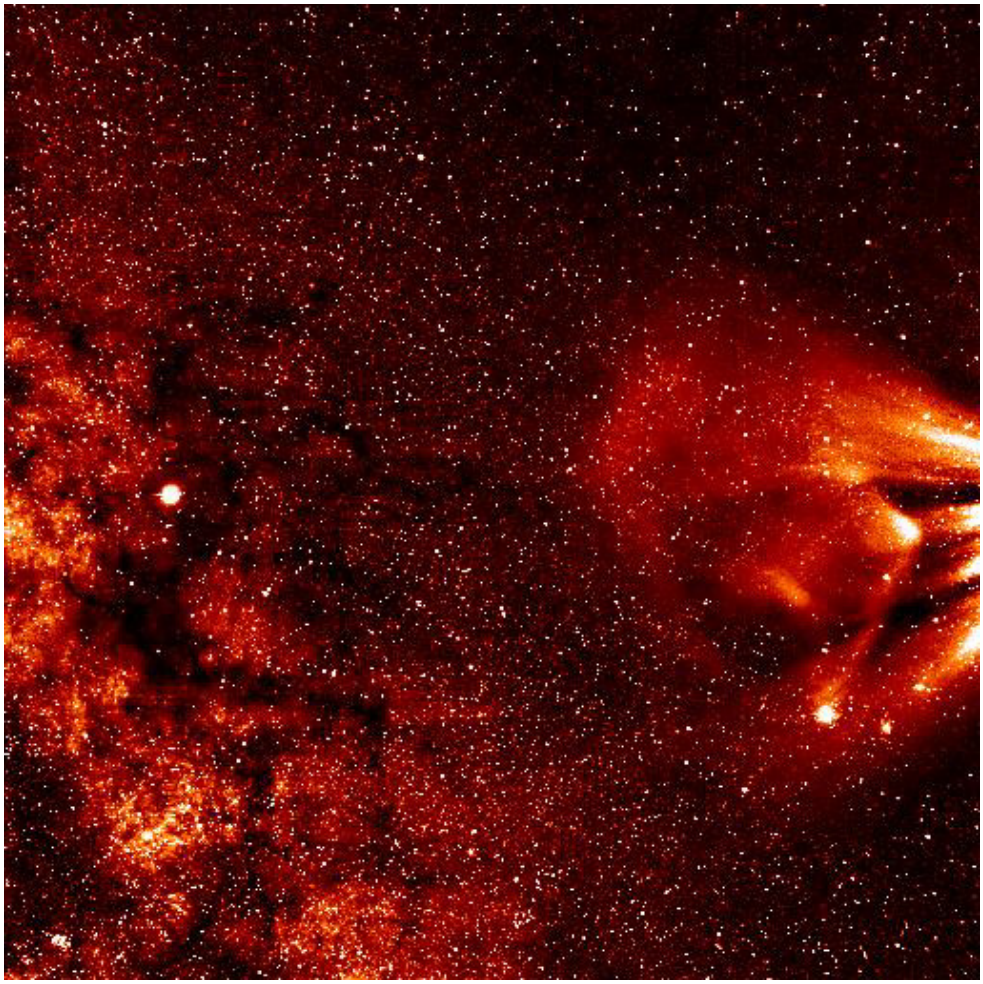

Figure 1-12 : Typical STEREO-HI image shows CME propagation through the heliosphere. The image is 20 x 20 arcdeg wide, and the Sun is located at 3.98 arcdeg on the right out of the image. The Milky Way is visible in the background together with Jupiter (bright object on middle left side of the image). The image is colored with red tone, which corresponds to the instrument wavelength bandpass. [Courtesy of Rutherford Appleton Laboratory]

1.4. Scope of the work

The flow and logic of the present work is summarized in Figure 1-13.

- Taking heritage of previous laboratory measurement [4][5], the present work has been initiated with the design and test of a multi-edge linear diffractive baffle mock-up.
- Based on encouraging results obtained with this mock-up and on a conceptual instrument design [11][13], the multi-edge baffle model was applied to the particular configuration of the STEREO-HI instrument providing an efficient front diffractive baffle needed to attenuate the direct solar light located out of the instrument field of view [12]. A prototype of this baffle has then been tested, proving its theoretical rejection performance [13].
- In addition to the front diffractive baffle protecting from the Sun disk brightness, a lateral diffractive baffle and an internal diffusive baffle have also been designed to protect the STEREO-HI cameras from other potential straylight sources [12].
- The two STEREO-HI cameras, designed at the Centre Spatial de Liège, were modeled by ray-tracing to derive their contribution in the overall instrument straylight performance [14].
- As part of the assembly and test process of the STEREO-HI flight model, the optical systems were characterized before a final optical calibration and an end-to-end straylight validation of the two flight instruments [14].
- After launch, the work has been continued with the analysis of the STEREO-HI in-flight straylight performance allowing a comparison with theoretical and on-ground measured performances [16].

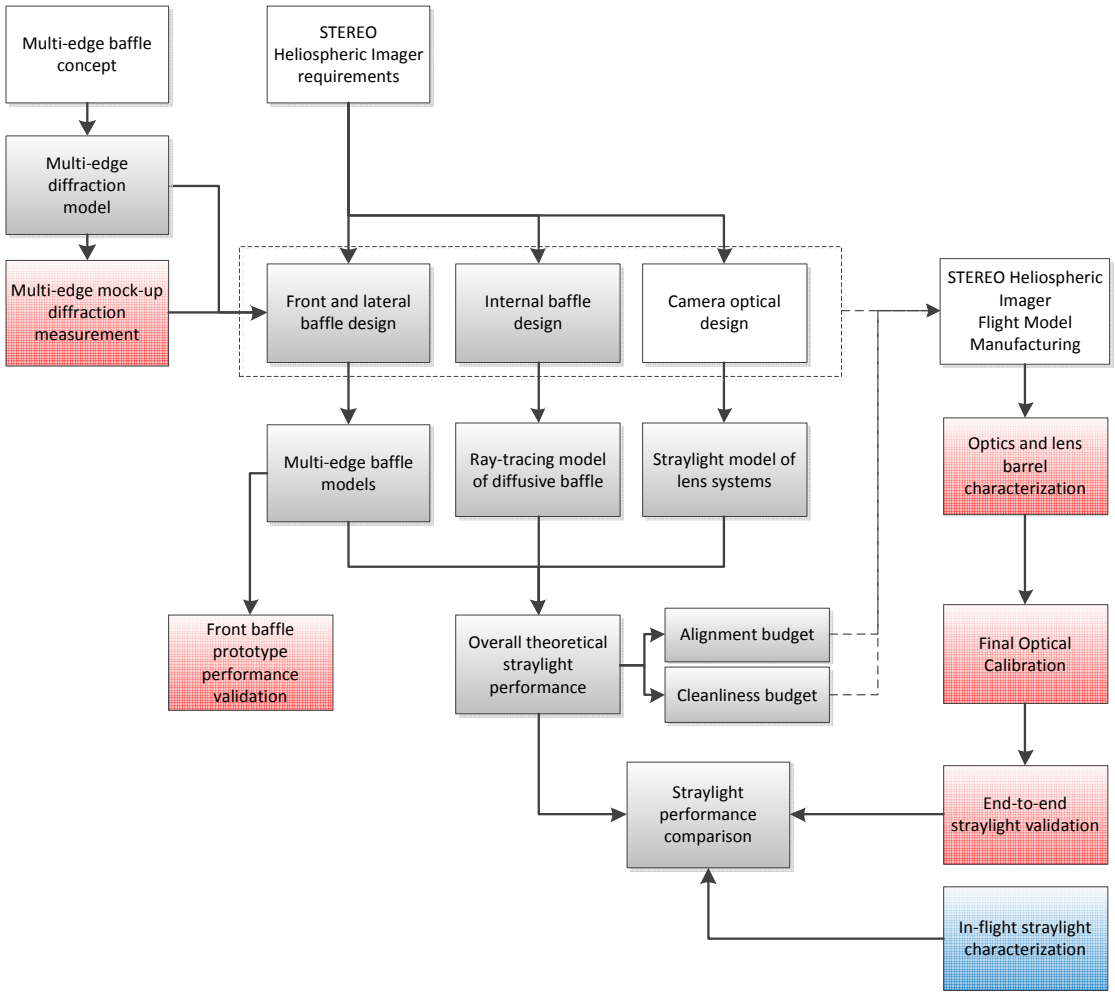

Figure 1-13: The flow of the present work was organized around three activities: modeling (grey boxes), testing (red boxes) and in-flight images analysis (blue box). The white boxes were input for the present work.

1.5. Manuscript overview

The following chapters of the manuscript are organized as follow (Figure 1-14):

- The Chapter 1 is an introduction with the context of the present work and the state of the art.
- The Chapter 2 provides a description of straylight rejection, and in particular of single and multi-edge linear diffractive baffles, with the associated measurements that were performed to validate and characterize their efficiency.
- The Chapter 3 gives an overview of STEREO-HI instrument design. In particular it details how the multi-edge diffractive model has been applied to the particular case of the STEREO-HI configuration. The theoretical instrument global straylight performance is derived, including the performance of the diffractive and multi-reflective baffles and of the camera straylight rejection.
- The Chapter 4 summarizes the on-ground calibrations performed in the frame of the STEREO-HI development and in particular the end-to-end instrument straylight performance.
- The Chapter 5 describes the STEREO-HI in-flight measurements, which demonstrate that the instrument straylight level is effectively achieved and that its evolution over the first years of the mission is stable.
- The Chapter 6 provides conclusions and lessons learned, but also perspectives of future similar instruments. It also gives some examples of the STEREO-HI observations.
- The Bibliography lists all the papers published in the frame of this work and the references cited in the present manuscript. The bibliography is organized by topic (Diffraction and Straylight, STEREO-HI instrument, STEREO science, Solar Observation, Image processing…) for an easier reading.
- The appendix contains the computation sheet of the STEREO-HI diffractive baffle, as example for future similar design. It has been written in Mathcad© but can be easily converted in another programming language.

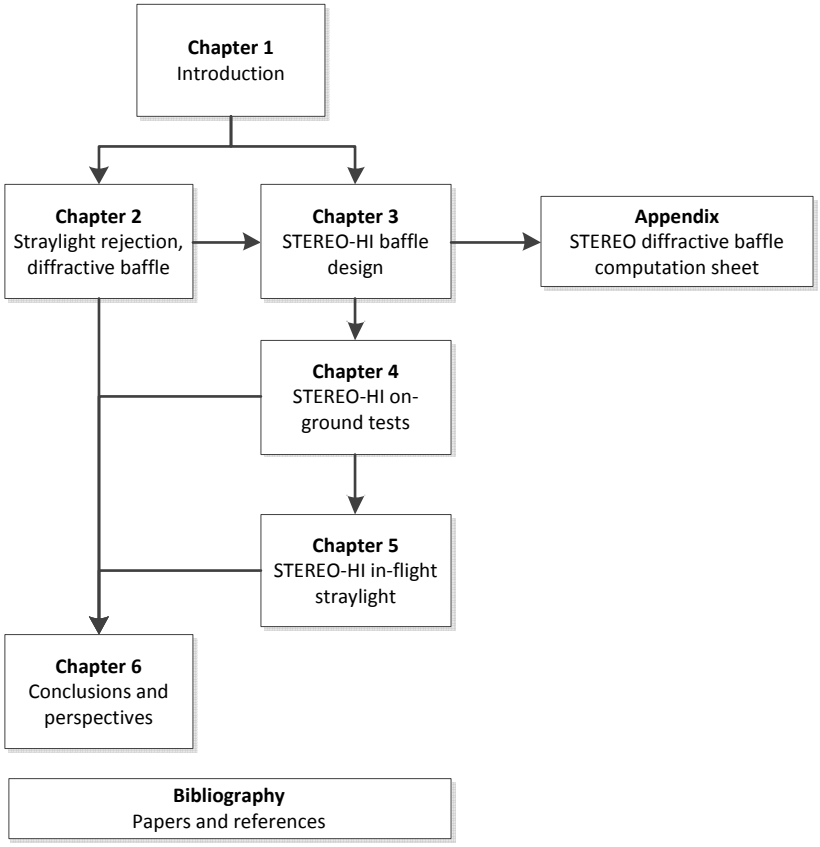

Figure 1-14: Organization of this manuscript.

Chapter 2. Straylight rejection

2. Straylight rejection

Straylight is the unwanted part of a measured signal, coming from a light source or an illuminated surface located either outside or within a camera FOV, which reduces the SNR. The rejection of straylight is obtained with a baffle combined with elements in the optical system (field stop, light trap, adequate coatings….).

The baffles can either use absorption or diffraction to attenuate the straylight.

- Absorptive baffles takes advantage of an appropriate absorbing black surface coating to trap straylight by multi-reflections. These baffles are well suited from non-collimated straylight source but usually suffer from diffraction by their edges.
- Diffractive baffles are efficient for nearly-collimated straylight source. A knife-edge or a combination of edges can then provide a very efficient light rejection.

2.1. Absorptive baffle

2.1.1. Ray-tracing modelling

One of the most efficient tools to design an optical system is the ray tracing method. It simulates the propagation of incoherent light by a set of rays that are geometrically traced through the system. Each ray is a vector representation of light normal to a wavefront. Ray-tracing allows taking into account material refraction but also scattering by the various surfaces in the light path.

Some common ray-tracing software used in space applications are ASAP© [67], FRED© [68] and Zemax © [69]. In the present work, ray-tracing computations were made in ASAP© which is part of the development tools at the Centre Spatial de Liège.

Figure 2-1 shows an example of ray-tracing model. It corresponds to the geometry of the STEREO-HI instrument internal baffle system that was built to verify the baffle efficiency for various incident angles, as further described in § 3.3. Only the scattered and reflected rays toward the optical system are traced, to limit computation time.

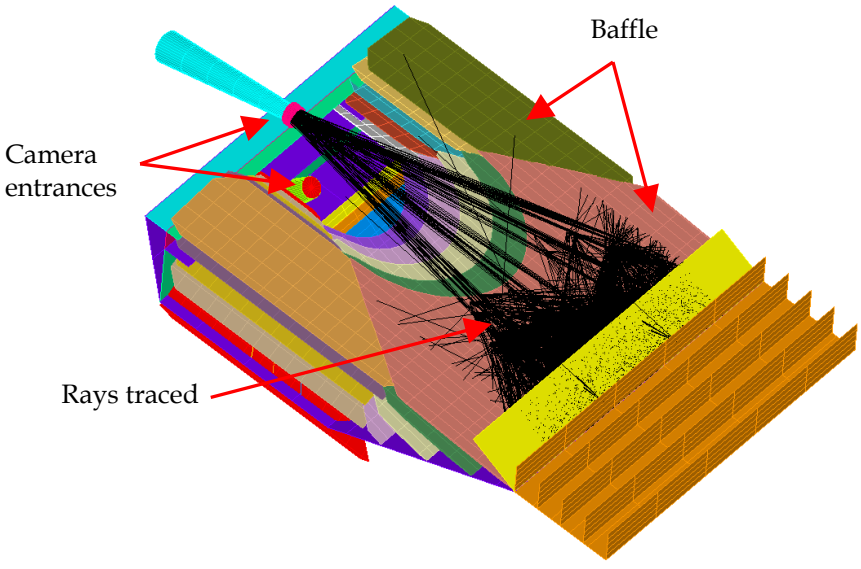

Figure 2-1 : Ray-tracing model (in the ASAP© ray-tracing software) of the STEREO-HI instrument internal baffle. It is used to verify the baffle efficiency for various incident angles.

2.1.2. Scattering properties

Scattered light is all deviating light that is not explained by optical aberrations.

The accuracy of ray-tracing simulation thus strongly depends on the knowledge of the scattering properties of the diffusing surfaces.

BRDF

The scatter behaviour of a surface is characterized by its Bidirectional Reflectance Distribution Function (BRDF). It gives the reflectance of a surface as a function of illumination and viewing geometries. The BRDF depends on the wavelength and on the structural and optical properties of the surface. The BRDF is a four-dimensional function that defines how an incident light is reflected by a surface. It is the ratio of reflected radiance L_r on the incident irradiance E_i on the surface, for a pair of incident and observation angles defined with respect to the surface normal by their azimuth and zenith angles (θ, φ), as shown in Figure 2-2. The BRDF is obtained by equation (2-1), where $d\Omega_i$ is the small solid angles associated with the incident beam, and is expressed in steradian^{-1} (sr^{-1}) solid angle unit.

$$BRDF(\theta_i,\phi_i,\theta_o,\phi_o,\lambda) = \frac{dL_o(\theta_o,\phi_o,\lambda)}{dE_i(\theta_i,\phi_i,\lambda)} = \frac{dL_o(\theta_o,\phi_o,\lambda)}{L_i(\theta_i,\phi_i,\lambda)\cdot\cos(\theta_i)\cdot d\Omega_i} \qquad \textbf{(2-1)}$$

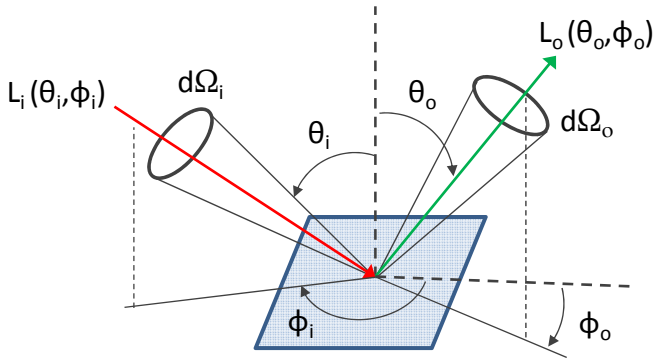

Figure 2-2 : BRDF is defined for a set of incident (θ_i, φ_i) and observation (θ_o, φ_o) angles.

For an isotropic surface, reflection is symmetric with respect to the plane of incidence and surface normal and consequently the reflectivity does not change when the surface is rotated about its normal.

The BRDF of an isotropic surface can thus be measured according to the in-plane formula (2-2), for a set of θ_i and θ_r incident and reflection angles (Figure 2-3), using a calibrated light source (P_{input}) and a detector power signal ($P_{measured}$). The power measured by the detector ($P_{measured}$) is divided by the detector area (S) and multiplied by the square of the distance (D) from surface to detector. A cosine factor is considered for the projected area of the detector because it is not necessarily perpendicular to the sample surface.

$$BRDF(\theta_o,\theta_i) = \frac{\frac{P_{measured}}{S}\cdot D^2}{P_{input}\cos(\theta_o+\theta_i)} \qquad \textbf{(2-2)}$$

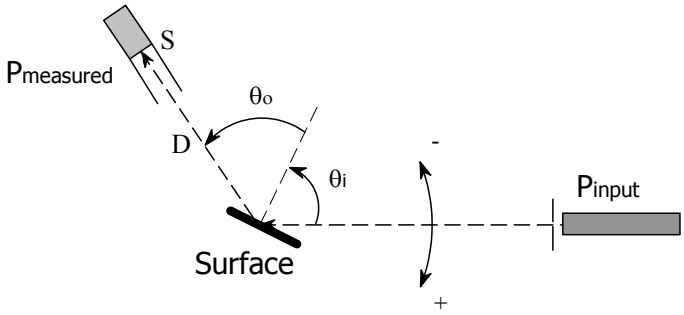

Figure 2-3 : BRDF around one axis measurement principle, where S is the collecting area of the detector located at distance D of the measured sample, the BRDF being measured for various pairs of θi and θ_o angles.

The relative error of an isotropic surface BRDF measurement is computed according to formula (2-3) where the error on BRDF is computed with formula (2-4), using known uncertainties of the measurement parameters of Figure 2-3.

$$Err_{Rel}(\theta_o,\theta_i) = \frac{Err_{BRDF}(\theta_o,\theta_i)}{BRDF(\theta_o,\theta_i)} \qquad \textbf{(2-3)}$$

$$Err_{BRDF}(\theta_o,\theta_i) = \sqrt{\left(\left|\frac{d}{dP_{input}}BRDF\right|\cdot Err\_P_{input}\right)^2 + \left(\left|\frac{d}{d\theta_o}BRDF\right|\cdot Err\_\theta_o\right)^2 + \left(\left|\frac{d}{d\theta_i}BRDF\right|\cdot Err\_\theta_i\right)^2 \ldots + \left(\left|\frac{d}{dP_{mesured}}BRDF\right|\cdot Err\_P_{mesured}\right)^2 + \left(\left|\frac{d}{dD}BRDF\right|\cdot Err\_D\right)^2 + \left(\left|\frac{d}{dS}BRDF\right|\cdot Err\_S\right)^2} \qquad \textbf{(2-4)}$$

Once an in-plane BRDF has been measured for a set of incident and observation angles, it is introduced in the ray-tracing software. In case of specular surface, a Harvey law [56] is used to model it, with a minimum of two parameters. In case of lambertian surface, a one-parameter model is used, with the hemispherical reflectivity. For other isotropic surfaces, a linear polynomial model is used with coefficients computed by fitted measured BRDF.

TIS

The other important scattering property for ray-tracing model is the Total Integrated Scatter (TIS). It is the ratio of power scattered into a hemisphere from a surface divided by the power incident on the surface, and is a function of the incident polar and azimuth angles (for isotropic surfaces it is only a function of the polar angle). The TIS is the integral of the BRDF over all angles and is computed with equation (2-5).

$$TIS(\theta_o,\phi_o,\lambda) = \frac{Scattered\_Power}{Incident\_Power} = \int_0^{2\pi}\int_0^{\frac{\pi}{2}} BRDF(\theta_i,\phi_i,\theta_o,\phi_o,\lambda)\cdot\cos(\theta_i)\cdot\sin(\theta_i)\,d\theta_i\,d\phi_i \qquad \textbf{(2-5)}$$

For a lambertian surface, the BRDF is constant and the TIS = π x BRDF.

2.1.3. BRDF measurement

In the frame of this work, the BRDF of various black paint coatings, usually applied on baffle systems, was measured with a simple test setup (Figure 2-4) based on the in-plane BRDF formula (2-2) and measurement principle of Figure 2-3.

A 633 nm laser source and a photodiode detector were used, within a black shroud to limit noise (~ 2.10^{-8} x P_{input}). The measured sample and the detector were located on independent rotation tables, of a few arcsec accuracy, to measure BRDF for various couples of incident/observation angles (except for observation angle 0° where the detector is in front of the light source).

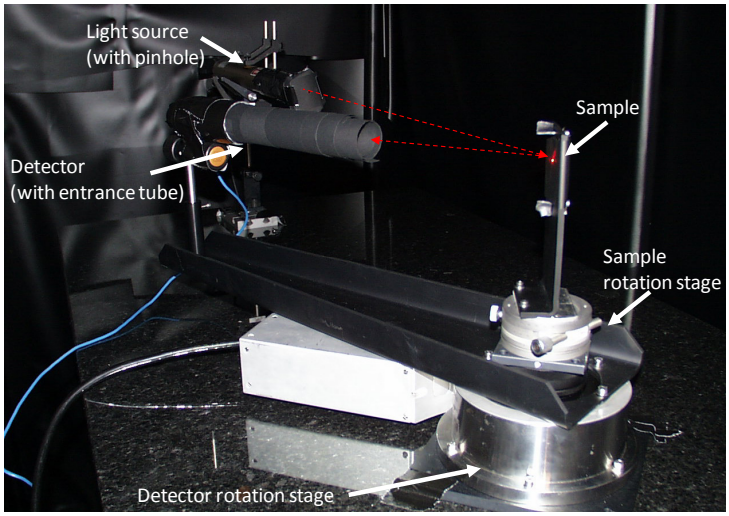

Figure 2-4 : Test setup used to measure BRDF around one axis. The system is located in a black shroud to avoid perturbation of BRDF measurement by external light source.

Figure 2-5 shows some typical BRDF measured with this setup and computed with relation (2-2): white lambertian, black diffusive and black specular coatings. The error bars of Figure 2-5 were computed with relations (2-3) and (2-4).

- The lambertian property of the white sample results in a flat BRDF over the range of observation and incident angles. A white PTFE sample has been here measured.
- The diffusive black coating is close to a lambertian one, with much lower TIS. It only differs from lambertian at grazing angles where its BRDF increases with the observation angle, mainly for incident angles larger than 30 arcdeg. The Chemglaze Z307 has been here measured (intended to be used for the STEREO-HI baffles).
- The specular coating results in a BRDF with peak of reflectivity at observation angle equal to the incident angle. A black aluminium anodised sample has been here measured.

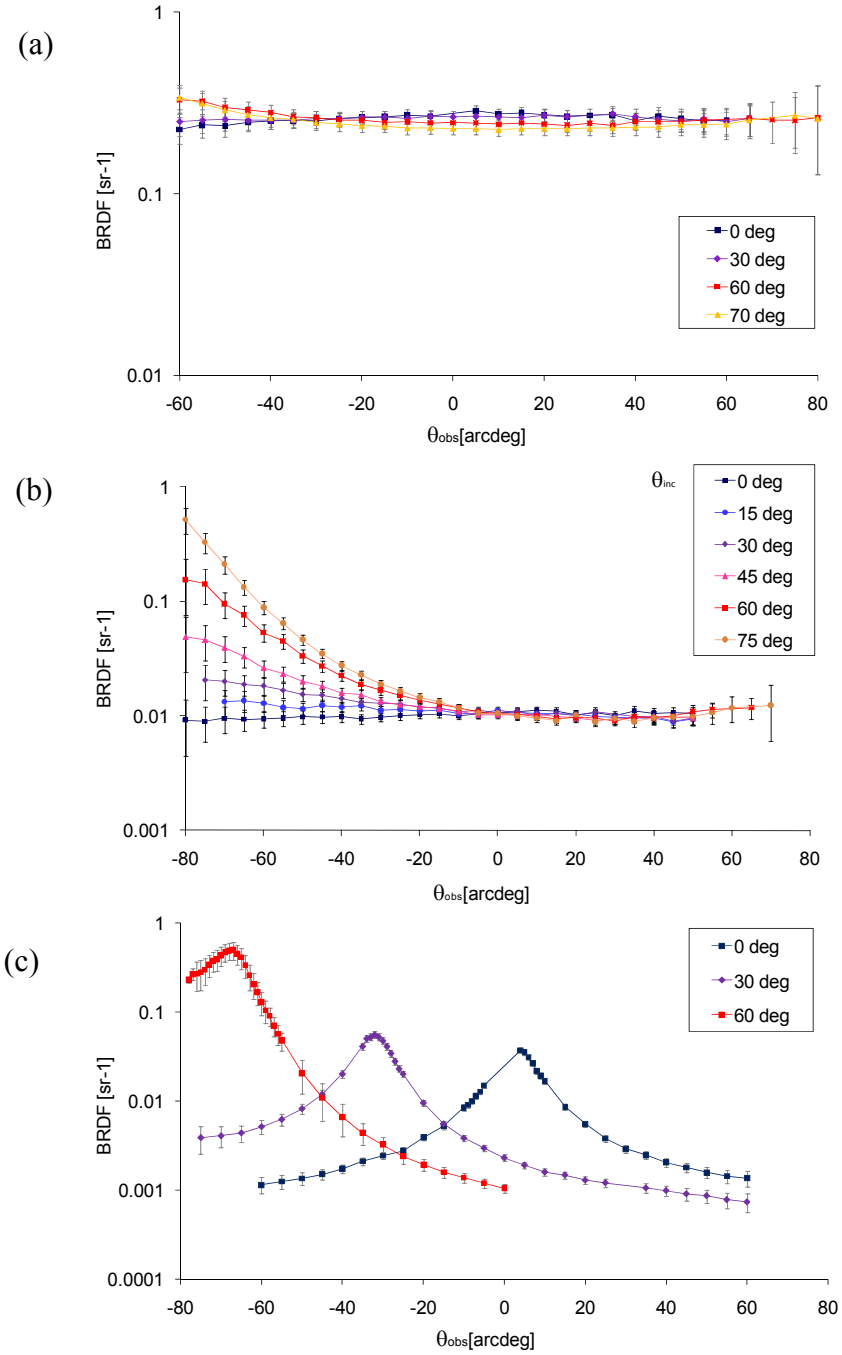

Figure 2-5 : Measured in-plane BRDF for various incident and observation angles counted relatively to the sample normal of (a) white lambertian PTFE sample, (b) black diffusive coating (Chemglaze Z307) on CFRP sample, (c) black anodisation on aluminium sample. Negative angles are towards the direct beam.

2.2. Diffractive baffle

2.2.1. History

Diffraction refers to the phenomenon resulting from a wave interaction with the edges of an object.

This wave property of light has been first observed by F. M. Grimaldi in the 17th century [1] . In a black room, he let the Sun going through pinholes in a back curtain and observed on a screen the effect of an edge or a slice in the beam. He noticed that the shadow on the screen is not sharp but forms a serie of alternative dark and colored fringes. He rejected the idea that this phenomenon was the direct beam or its reflection by the object in the path and understood it was related to an interaction of the beam with the object edge. He named it "diffraction".

In the 18th Century, Newton did the same type of experiments with lights of different colors, and found that the distance between the fringes is reduced when using blue instead of red light, and is increased with the distance from the diffracting object and the screen. He proposed a theoretical explanation for this phenomenon based on its corpuscular theory of light by assuming it was due to attractive or repulsive forces applied by the edge on the moving particles.

On his side, Young (also on the 18th Century) proposed a first explanation of the diffraction in a wave theory of light. He considered that the fringes resulted from the interference of rays passing close of the edge and of the rays reflected in grazing incidence by the edge. This explanation was however not sufficient to explain the fringes located in the shadow and would result in a constant value between min and max values of the fringes located out of the shadow. He thus assumed that the fringes in the shadow were due to interference between curved rays, without explanation of this curvature.

At the same time, Fresnel studied diffraction in a similar wave theory than Young. Based on many experimental results, he introduced a model of the observed phenomena. With a magnifying glass, he observed the fringes and used a micrometer to accurately measure their step, and changed the Sun beam input size by using lenses of different focal lengths. This helped him to understand the importance of light beam coherence in the diffraction. By using black or polished surfaces he also observed that the fringes do not depend on the edge material. He also noticed equidistant fringes in the geometrical shadow of a wire, in addition to the non-equidistant fringes out of the shadow. Fresnel mathematically modeled what he observed on the basis of sine wave for a monochromatic light, with frequency characterizing the color. The mathematical result of diffraction is then solved by using the Huygens principle that each point of the edge is a secondary source and by applying the Young interference principle. The measured value in each point of the screen is then the result of interference of all secondary vibrations.

2.2.2. Fresnel regime

The Fresnel number is defined by equation (2-6) where d is the characteristic size of the aperture, λ is the wavelength of the wave and z is the distance of the observation plane from the aperture.

$$F = \frac{d^2}{z \cdot \lambda} \qquad \textbf{(2-6)}$$

In the so-called Fresnel regime, the Fresnel number is around or greater than 1. The diffracted wave is considered to be in the near field[2], and the Fresnel approximation of propagation equation can be used to calculate diffraction. In this regime, the aperture creates a beam whose edges will have the same shape and size as the aperture itself, and will be reasonably sharp (with an oscillation near the geometrical shadow) and the field behaves approximately as one would predict using geometric optics. The direction of the diffracted light is thus the same than the incoming light, i.e. that each point on the edge diffracts without diffusion to other directions.

[2] In the optical domain, "near field" is commonly used when dimensions are in the order of magnitude of the wavelength. In the present case, the dimension z is in the order of several cm up to a few meters. It is not far field, in the sense of the Fraunhofer diffraction regime and we are thus in an intermediate size domain.

By contrast, in the more distant Fraunhofer regime, wave-front spreading will cause the transverse size of the entire beam to grow linearly with distance; and, as the intensity pattern typically will not resemble the aperture at all.

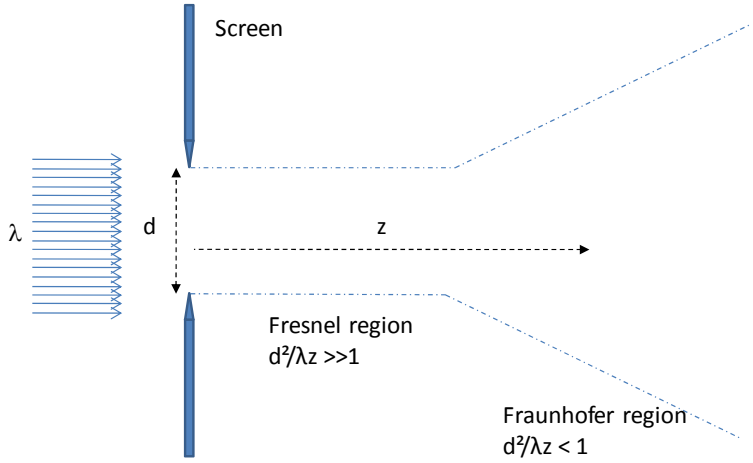

Figure 2-6 : Fresnel region corresponds to the near-field where beam edges will have the same shape and size as the aperture itself. In the Fraunhofer regime, transverse size of the entire beam grows linearly with distance z from the screen.

2.2.3. Linear edge diffraction

In case of a one–dimension linear edge, the Fresnel regime applies as the dimension d is infinite and the diffracted intensity can then be modelled by the approximation (2-7) of the Kirchhoff-Fresnel diffraction [2] where B_0 is the collimated incident intensity on the edge and λ is the wavelength of the diffracted light. It is a function of the distance x in the shadow of the edge (x < 0 in the shadow and x > 0 above the edge) and of the square root of the distance z between the edge and an observation plane (Figure 2-7).

$$B(x,z,\lambda) = \frac{1}{2}\cdot B_0\cdot\left[\left(\frac{1}{2}+C\left(\sqrt{\frac{2}{\lambda\cdot z}}\cdot x\right)\right)^2+\left(\frac{1}{2}+S\left(\sqrt{\frac{2}{\lambda\cdot z}}\cdot x\right)\right)^2\right] \qquad \textbf{(2-7)}$$

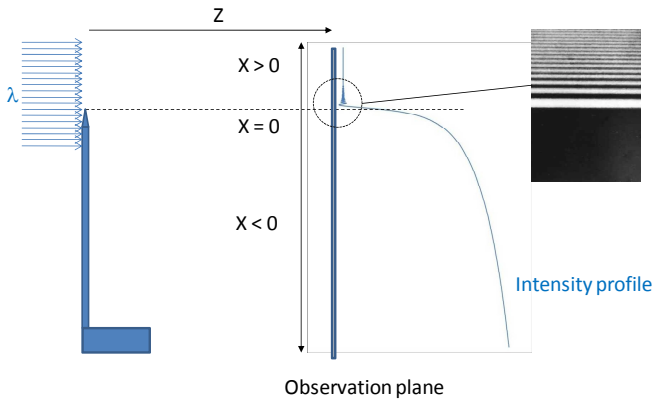

Figure 2-7 : The one-edge diffraction intensity profile in an observation plane located at distance z from the edge is function of the distance x along this observation plane. The intensity oscillates above the edge and asymptotically approaches the unity value, and monotonically decreases in the shadow.

The C and S functions are the Fresnel's integrals defined in (2-8). They are usually represented in the parametric plot of Figure 2-8, known as the Cornu Spiral, which shows their convergence for increasing parameter α (i.e. C(∞) = S(∞) = - C(-∞) = - S(-∞) = ½).

$$C(\alpha) = \int_0^{\alpha}\cos\left(\frac{\pi}{2}\right)\cdot x^2\,dx \qquad S(\alpha) = \int_0^{\alpha}\sin\left(\frac{\pi}{2}\right)\cdot x^2\,dx \qquad \textbf{(2-8)}$$

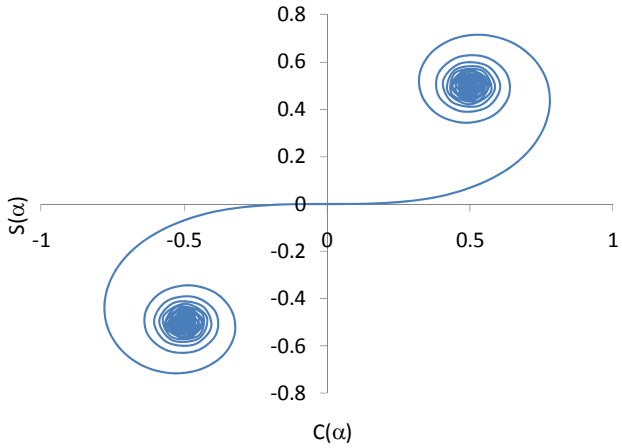

Figure 2-8 : The Fresnel integrals are graphically represented using the *Cornu Spiral* parametric plot. It shows that their value converge for increasing parameter α. The integrals are here computed for α in the [-115, 115] range by steps of 0.1.

As shown on the resulting plot of Figure 2-9 (left), obtained in the particular case of a 0.5 m distance between edge and observation plane and a 500 nm wavelength, the relative intensity profile B/B_0 of the diffracted beam (B) over the direct beam (B_0) intensity value oscillates above the edge level with diminishing amplitude and decreasing fringe separation as the distance above the edge increases, and asymptotically approaches the unity value.

The maximum value is thus not at the edge of the geometrical shadow, where it is ¼, and then exponentially decreases in the shadow. Below the edge, the diffracted value monotonically decreases and some orders of direct light attenuation are reached in the edge shadow.

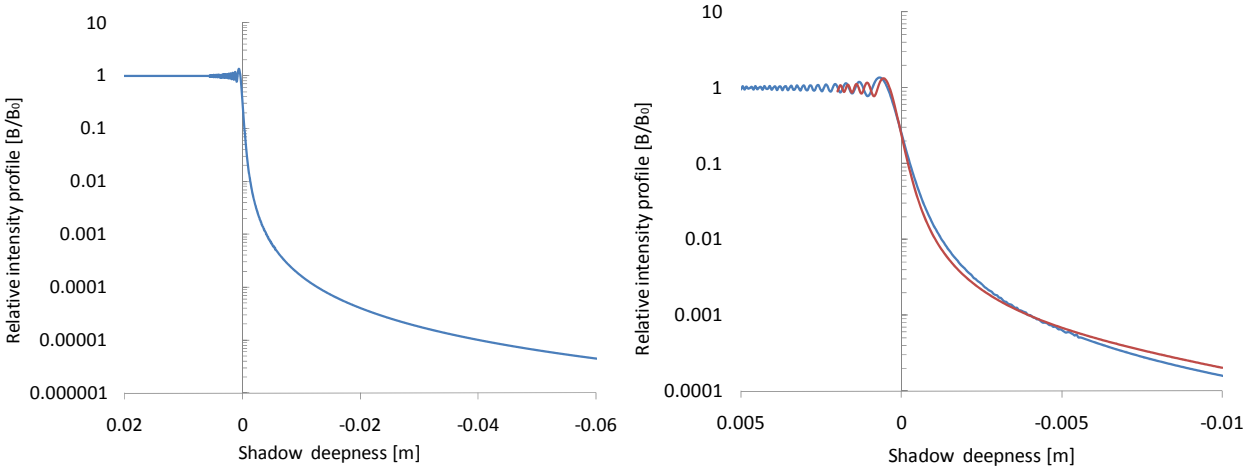

Figure 2-9 : Left: Relative intensity profile B/B_0 of one-edge diffraction (in log scale), where B_0 is the direct beam intensity, computed using Fresnel's integrals (left). The plot is computed for a 0.5 m distance between edge and observation plane, and a 500 nm wavelength. Right: Comparison of Fresnel diffraction computed in ray-tracing software (red curve) with Fresnel's integral (blue curve).

The one-edge diffraction can also be modelled by ray-tracing. The obtained relative intensity profile for a one-edge configuration (Figure 2-9 right) is very close to the numerical method result.

The ray-tracing software computes coherent diffraction by summing Gaussian beams that are geometrically propagated through the system. The Gaussian beam is represented by a base ray with additional parabasal rays (i.e. paraxial propagation relative to the base ray) [55]. The ray-tracing parameters to compute edge diffraction are thus the Gaussian size and the number of parabasal rays (500 rays and 8 parabasal rays were used).

2.2.4. Multi-edge diffraction

A knife-edge baffle system can provide an efficient light attenuation system for a collimated (or near collimated) straylight source (like the Sun for example), resulting in a rejection of many orders of magnitude. A one edge baffle however requires a large distance between the baffle and the camera to achieve a very deep shadow needed to observe faint objects. Such large distance is usually not possible for a space instrument, and to improve diffractive baffle efficiency it is necessary to combine the diffraction of more than one edge. The optical system that shall be protected by the multi-edge baffle is located in the shadow of the last edge where the combined diffraction from the multi-edges is maximum, as shown on Figure 2-10 for a 5 equidistant edges baffle.

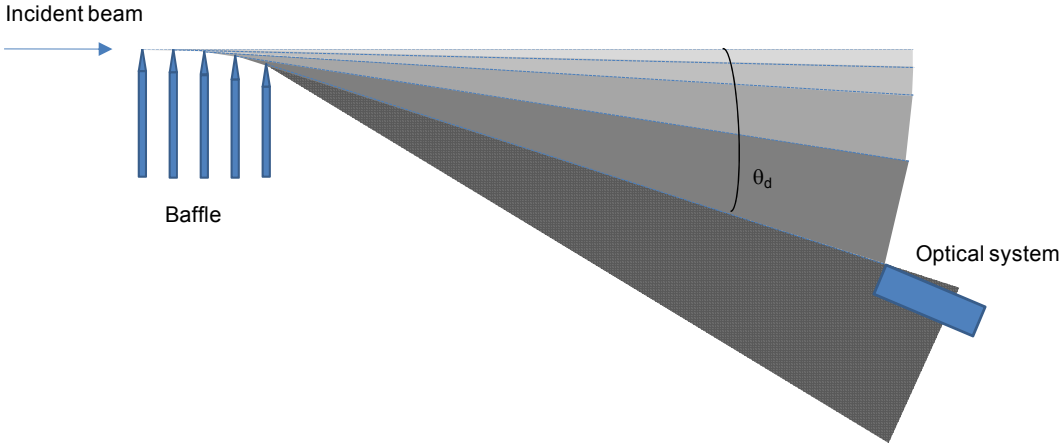

Figure 2-10 : Multi-edge cascading diffractive baffle: the edges are arranged in an arc such that the n^{th} intermediate edge blocks the diffracting light of the $n\text{-}1^{th}$ edge from the view of the $n+1^{th}$ edge. The diffraction angle, θ_d, is defined as the angle between the incident beam direction and the line connecting the last edge to the optics entrance aperture.

In a multi-edge system, the best efficiency is obtained when the edges are arranged in an arc such that the n^{th} intermediate edge blocks the bright linear diffracting edge of the $n\text{-}1^{th}$ edge from the view of the $n+1^{th}$ edge [3][5].

This arc is defined by the diffraction angle, θ_d, between the direction of the light source and the line connecting the last edge to the optical system entrances which is protected by the baffle, shown on Figure 2-10 and Figure 2-11. The diffraction angle is then shared between consecutive edges in order to optimise the rejection of the system.

The diffraction angle θ_d is obtained with relation (2-9), as shown on Figure 2-11, where:

- OA is the angle between the optical system axis and the light source direction
- Ap is the diameter of the optical system entrance aperture
- D is the distance between the last edge and entrance aperture
- FOV_{border} is the angle between the border of the optical system FOV and the light source direction

$$\theta_d = \operatorname{atan}\left[\frac{(D - Ap\cdot\sin(OA))\cdot\tan\left(FOV_{border}\right) - 2\cdot Ap\cdot\cos(OA)}{D + Ap\cdot\sin(OA)}\right] \qquad \textbf{(2-9)}$$

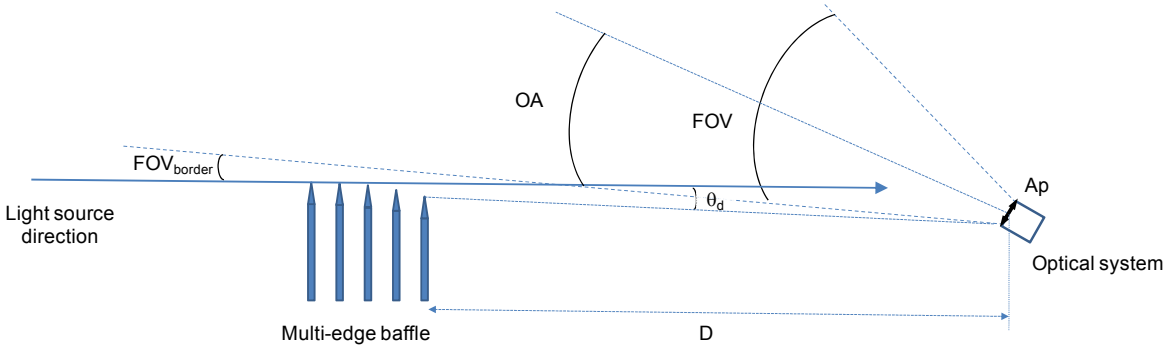

Figure 2-11 : Diffraction angle definition in the STEREO-HI instrument configuration.

Ray-tracing modelling of a multi-edge system is not practical as it required a huge number of rays, and traditional software does not allow diffraction of diffracted rays.

Fresnel's approximation can however be applied in a cascading way to obtain the multi-edge diffraction performance. The equation (2-7) is used to obtain the first edge diffracted intensity, and the generalised relation (2-10) is used for the following edges, where Z_{N-1} and Z_N are the distance between consecutive edges, and between last edge and observation plane [2].

$$B\left(x, z_{N-1}, z_N, \gamma_N, \lambda\right) = \frac{1}{2}\cdot B_0 \cdot \left[\left[\frac{1}{2} + C\left[\sqrt{\frac{2}{\lambda}\cdot\left(\frac{1}{z_{N-1}} + \frac{1}{z_N}\right)}\cos\left(\gamma_N\right)\cdot x\right]\right]^2 + \left[\frac{1}{2} + S\left[\sqrt{\frac{2}{\lambda}\cdot\left(\frac{1}{z_{N-1}} + \frac{1}{z_N}\right)}\cdot\cos\left(\gamma_N\right)\cdot x\right]\right]^2\right] \quad \textbf{(2-10)}$$

The θ_N angles between consecutive edge tips and the light source direction are used to obtain the relative edge height h_N w.r.t. the incident beam direction according to relation (2-11) as shown on Figure 2-12. The angle γ_N of Figure 2-12 is computed with equation (2-12).

$$h_N = Z_N \cdot \tan\left(\theta_N\right) \quad \textbf{(2-11)}$$

$$\gamma_N = \operatorname{atan}\left(\frac{z_N\cdot\tan\left(\theta_N\right) + z_{N-1}\cdot\tan\left(\theta_{N-1}\right)}{z_N + z_{N-1}}\right) \quad \textbf{(2-12)}$$

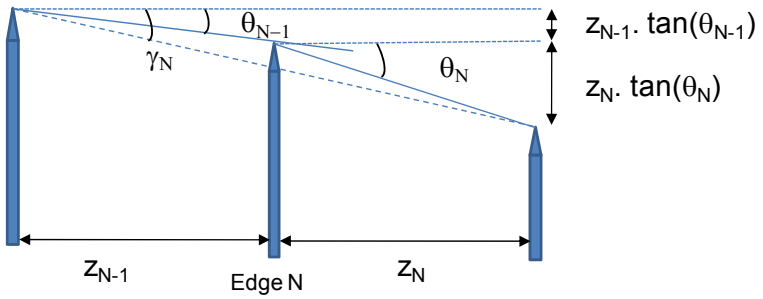

Figure 2-12 : The height between two consecutive edges is used to compute the effect of each edge as part of the cascading diffraction.

The cascading equation (2-13) is then used to obtain rejection at the level of a observator located at shadow distance x. The rejection from the first edge is computed with equation (2-7) for z = d. The following multiplicative factor B_j are the diffraction value of edge N-1 at the depth of edge N computed with equation (2-10), as shown in Figure 2-13, and B(x) is the rejection of last edge obtained with (2-10) on the observation plane located at distance Z from the last edge and at distance x in the shadow.

$$B_{N_d} = \left(B_1 \cdot B_2 \cdot \ldots \cdot B_{N_d-1}\right)B(x) \quad \textbf{(2-13)}$$

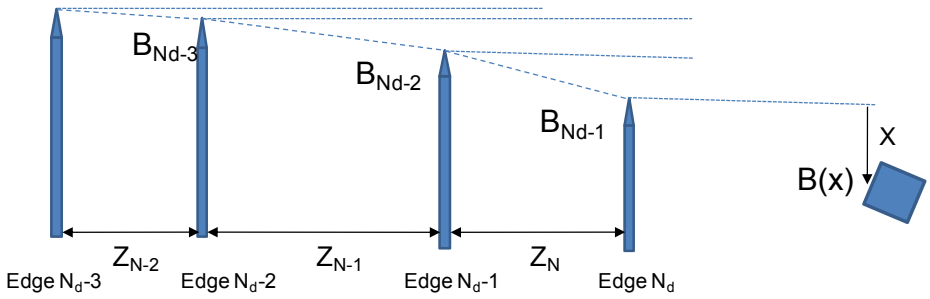

Figure 2-13 : Cascading diffraction geometry, where edges are not equidistant and respective heights are obtained with equation (2-11).

As shown on Figure 2-14, the zone of influence of the successive edges in an observation plane can be expressed as a function of the distance from the first edge tip or as a function of the shadow angle from the incident direction.

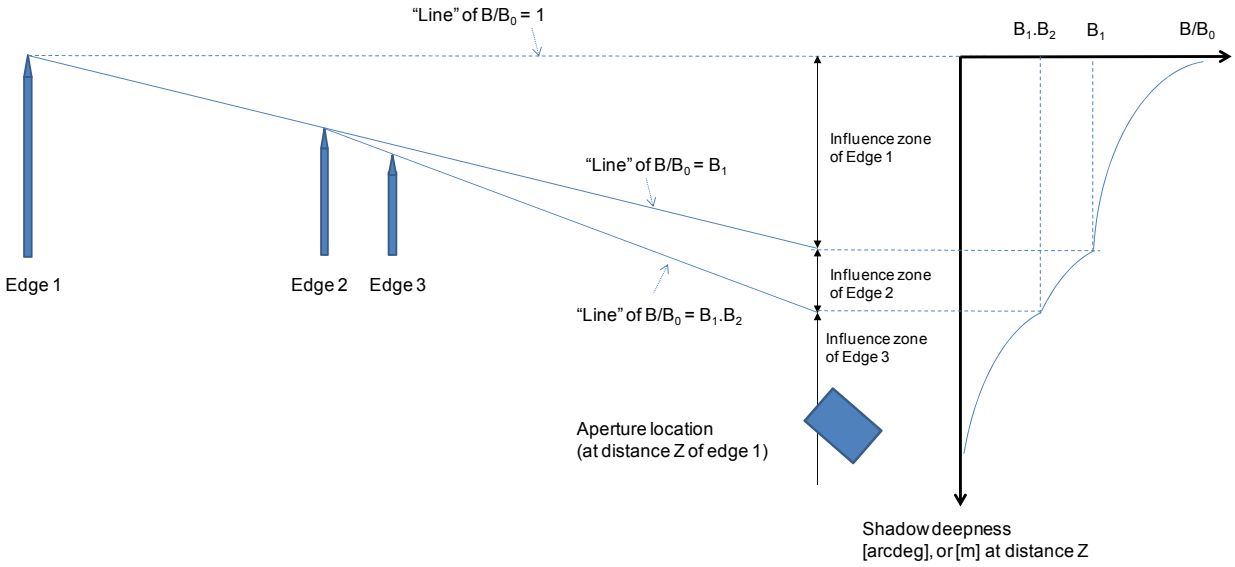

Figure 2-14 : Influence zone of non-equidistant multi-edge diffractive baffle (here for 3 edges) as function of the shadow deepness (expressed versus the angle from the direct line or versus the distance from the first edge at the observation plane).

2.2.5. Equidistant edges

The baffle geometry (i.e. edge heights and distance between edges) is optimum when the diffraction of the N^{th} edge starts at the maximum diffraction slope of the $N\text{-}1^{th}$ edge. This is the case when edges are equidistant, i.e. when the distance between the edges is the same ($Z_N = Z_{N-1} = d$) and the diffraction angle θ_d is equally shared between consecutive edges. The relation (2-14) is then used to obtain the angle between edge N and edge N-1 (as shown on Figure 2-12), where N_d is the number of equidistant edges.

$$\theta_N = N \cdot \frac{\theta_d}{N_d} \qquad \textbf{(2-14)}$$

In case of equidistane edges, the cascading equation (2-13) can be simplified with equation (2-15).

$$B_{N_d} = B_1 \left(B_2\right)^{N_d-2} B(x) \qquad \textbf{(2-15)}$$

The rejection B_1 is the diffraction value from the first at the second edge tip level, computed with equation (2-7) where z = d. The rejection B_2 is the second edge diffraction value at the third edge depth computed with equation (2-10) for $z_{N-1} = z_N = d$. The following edges provide the same rejection at the next edge depth than the second one, i.e. the same rejection level B_2 is achieved between next edges, and B_2 is powered by N_d-2 in the equation to take into account edges 2 to N_d-1. The rejection B(x) is from the last edge (N_d^{th} edge) and is obtained with (2-10) for $z_{N-1} = d$ and $z_{Nd} = D$ is distance from last edge to the optical system located at distance x in the shadow, as shown in the Figure 2-15.

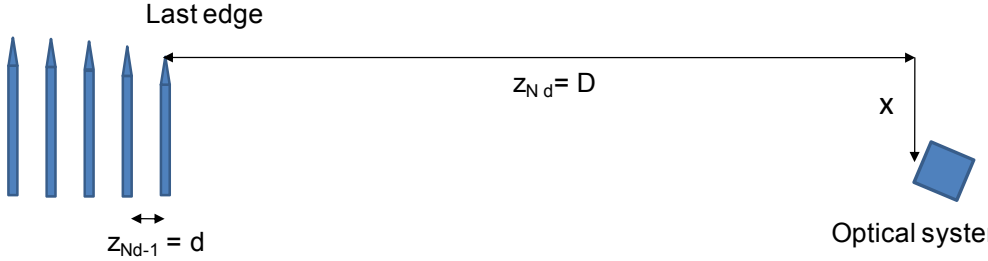

Figure 2-15 : Distance between last edge and optical system entrance is used to compute rejection of this last edge.

The angle γ_N between tip of N-1th edge and N+1th edge of Figure 2-12 can be computed with relations (2-16), where D is the distance between last edge and entrance aperture of the optical system.

$$\gamma_1 = 0 \qquad \gamma_N = \operatorname{atan}\left(\frac{\tan(\theta_N) + \tan(\theta_{N-1})}{2}\right) \qquad \gamma_{N_d} = \operatorname{atan}\left(\frac{D\cdot\tan(\theta_{N_d}) + d\cdot\tan(\theta_{N_d-1})}{D + d}\right) \qquad \textbf{(2-16)}$$

Figure 2-16 shows a typical relative rejection curve for a 5 equidistant edges systems. The cascading effect is clearly visible, where each edge provides an additional rejection. A relative intensity of 10^{-12} B/B_0 can easily be achieved with such multi-edge diffractive baffle.

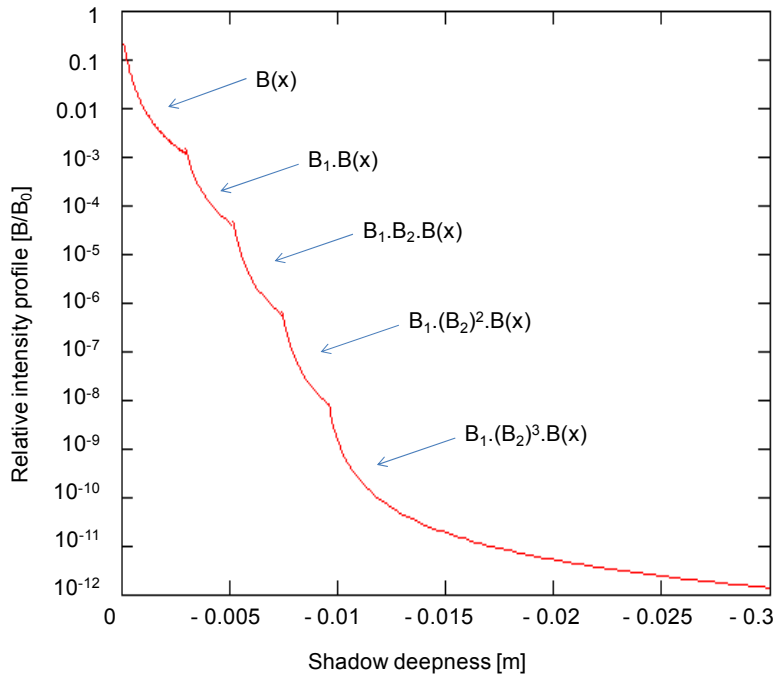

Figure 2-16 : Cascading relative diffraction rejection curve (log scale) for a 5 equidistant edges as function of the shadow deepness, where B_0 is the direct beam intensity. Each edge provides an additional multiplicative rejection factor. The computation is here performed for a 700 nm monochromatic wavelgenth.

As for non-equidistant edges, the zone of influence of the successive edges in an observation plane can be expressed as a function of the shadow angle from the incident direction or a function of the distance from the first edge, as shown on Figure 2-17.

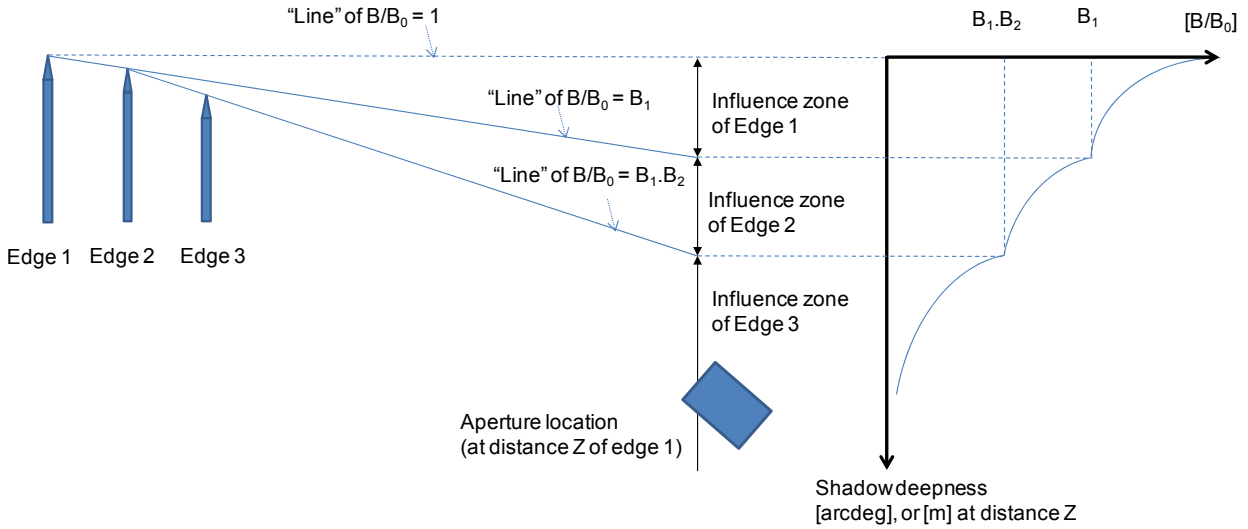

Figure 2-17 : Influence zone of multi-edge diffractive baffle (here for 3 equidistant edges) as function of the shadow deepness (expressed versus the angle from the incident direction or versus the distance from the first edge).

The rejection in the observation plane of an equidistant multi-edge diffractive baffle thus only depends on the distance d between edges, on the distance D between last edge and entrance aperture of the optical system, and on the number of edges N_d. The diffraction angle θ_d is indeed obtained with relation (2-9) that depends on distances d and D, and on the optical system location and dimensions in the observation plane.

The design of a multi-edge baffle thus depends on the instrument overall dimension constraints that drives the total distance $D_{tot,}$ linked to d and D by relation (2-17), between first edge and entrance aperture.

$$D_{tot} = D + \left(N_d - 1\right)d \qquad \textbf{(2-17)}$$

The rejection of a multi-edge diffractive baffle logically increases with this distance D_{tot}, as shown on Figure 2-18 for the particular case of a 5 equidistant edges[3]. It also shows that there is an optimum distance d for each D_{tot} that increases with it.

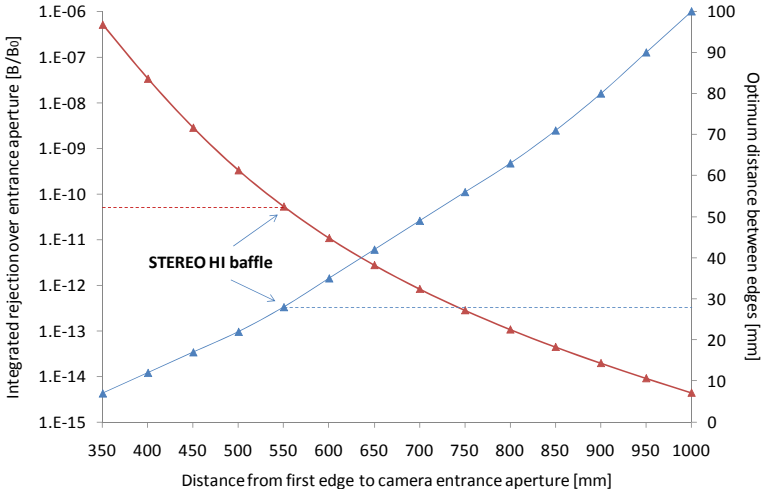

Figure 2-18: Integrated rejection over an entrance aperture (left axis) from a 5 equidistant edges and a 700 nm wavelength, with corresponding optimum distance between these 5 edges (right axis) versus total distance between the 1st edge and the entrance aperture. The particular case of the STEREO-HI instrument is shown.

As shown in Figure 2-19, the effect of D_{tot} increases with the number of edges. For one edge, it (logically) has no impact. Similarly, Figure 2-20 shows that the rejection logically increases w.r.t. the number of edges but that the larger is the distance D_{tot}, the faster the rejection improves for increasing number of edges.

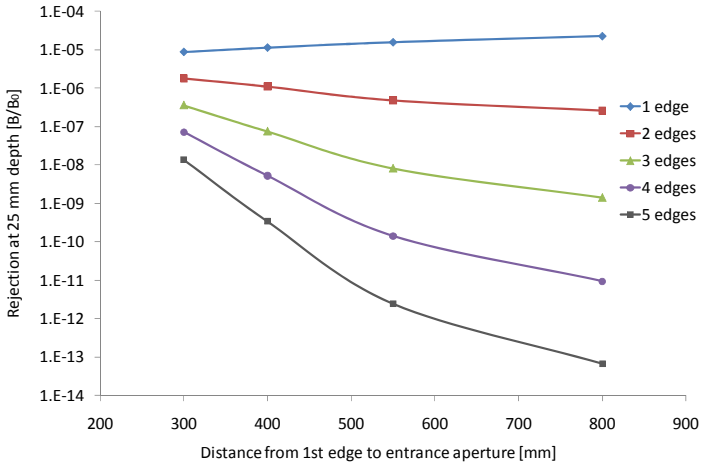

Figure 2-19: Effect of distance D_{tot} on a multi-edge diffractive baffle rejection, for increasing number of edges, computed for a 16 mm entrance aperture located at 25 mm in the shadow of the baffle.

[3] The rejection is here integrated over a 16 mm entrance aperture at 22 mm in the shadow of the first edge, corresponding to the STEREO HI-1 optical system entrance aperture.

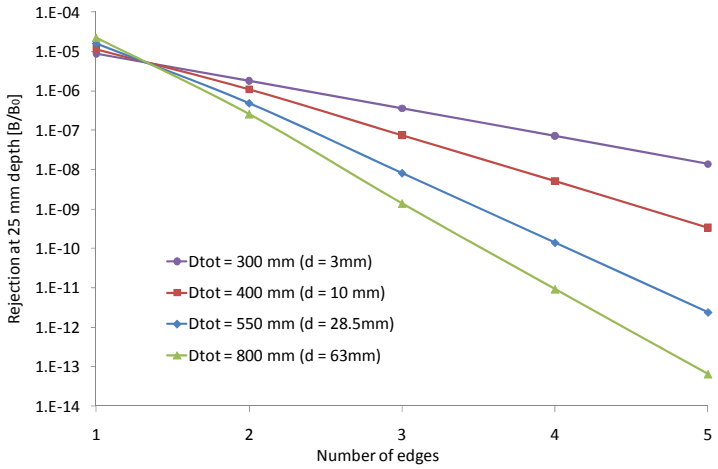

Figure 2-20: Effect of number of edge on a multi-edge diffractive baffle rejection, for increasing distance D_{tot}, computed for a 16 mm entrance aperture located at 25 mm in the shadow of the baffle.

2.3. Diffraction measurement

2.3.1. Knife-edge baffle

One edge diffraction

The ratio of the diffracted intensity (B) by a one-edge over the direct beam intensity (B_0) can be measured versus the shadow deepness and compared with theoretical values (Figure 2-21).

First measurements were obtained with a 633-nm laser beam collimated onto a knife edge by a simple lens, and a photodiode located at 500 mm from the edge measuring the diffracted light from the edge. The photodiode aperture is limited by a 1 mm pinhole and is mounted on a vertical translation to be moved down in the shadow deepness.

The error bar on such measurement (computed as the standard deviation over multiple measurements) is however large. It is dominated by the ambient background and the detector sensitivity, in particular for the largest values in the shadow deepness where it is close to 100%.

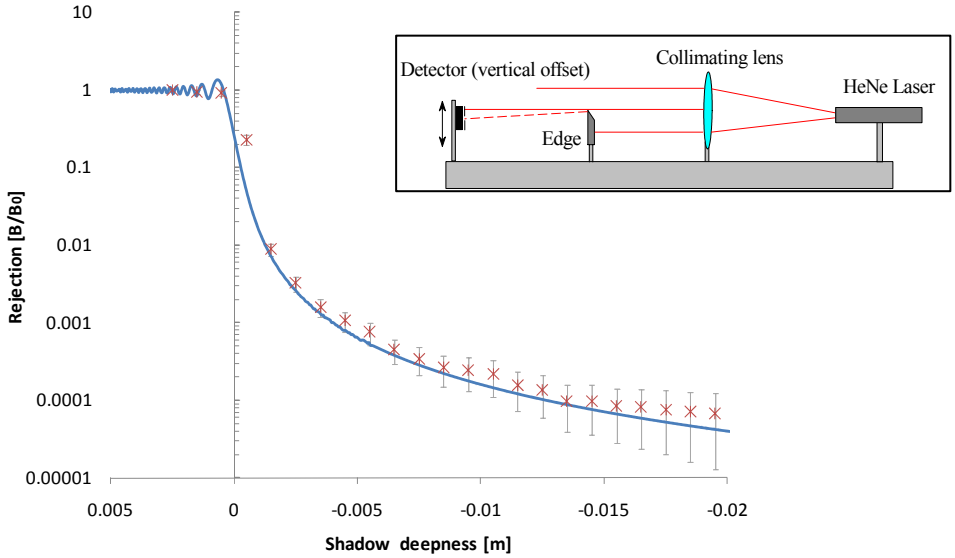

Figure 2-21 : Simple setup used to measure a one-edge relative diffraction profile B/B_0 (log scale), where B_0 is the direct beam intensity. A 633-nm laser beam is collimated on a knife edge, and the diffracted light is measured by a photodiode, of aperture limited by a 1 mm pinhole, mounted on a 20-mm translation stage. The measured rejection is plotted (red crosses) and compared with Fresnel one-edge diffraction model (blue line).

Improved test setup

To improve the accuracy at low level of diffracted light, a Thomson-CFS continuous laser diode emitting at 805 nm has been used with a dedicated electronic to vary the output power from 5 W to 23 W (Figure 2-22). The laser diode is directly connector to a 600 µm core optical fibre, whose transmission is 90%.

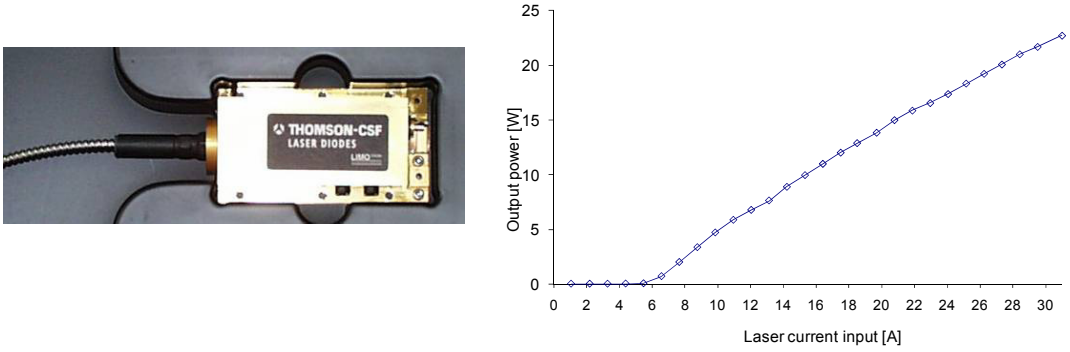

Figure 2-22 : Left: A Thomson-CFS continuous laser diode has been used to increase the dynamic range of diffraction measurement. The diode is current driven, and its temperature is monitored. Right: The laser diode power was measured versus the input current. It is quasi-linear over a range from 5 W to 23 W allowing an increase of the measurement dynamic range.

The powerful laser diode has been used in combination with an F/3 collimator (Figure 2-23) specially designed for this application, providing a divergence of 27.5 arcmin. The resulting collimated beam is a 20 x 10 mm² rectangular cross section that is centred on the baffle edge tip. The drawback of this collimator is the absorbed beam power reducing the maximum output power. It also results in a heating of its structure, requiring to be cooled down to limit the variation of collimation.

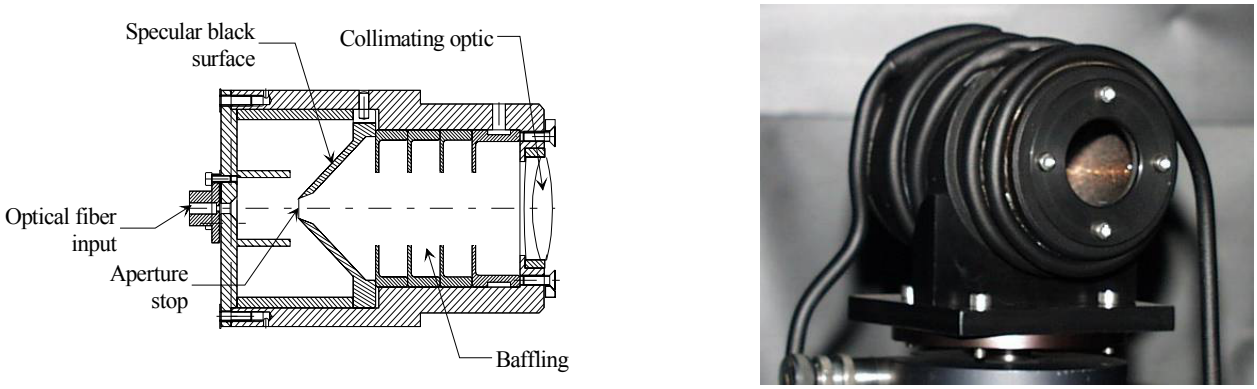

Figure 2-23 : Sketch and picture of the F/3 collimator used for the mock-up diffraction test. The collimator is cooled down with water circulating in a closed piping system to limit the temperature effect on the divergence when used with the laser diode source.

Any deviation of the collimator divergence can become an important source of noise in the straylight measurement. The divergence was thus measured by rotating the collimator around its vertical and horizontal axes and recording the output flux versus the angle with a photodiode. The collimation verification shows a 10^4 rejection level for output angles larger than ± 5 arcdeg divergence angle (Figure 2-24). A 9.66% absolute transmission was also measured as compared to the beam injected in the collimator.

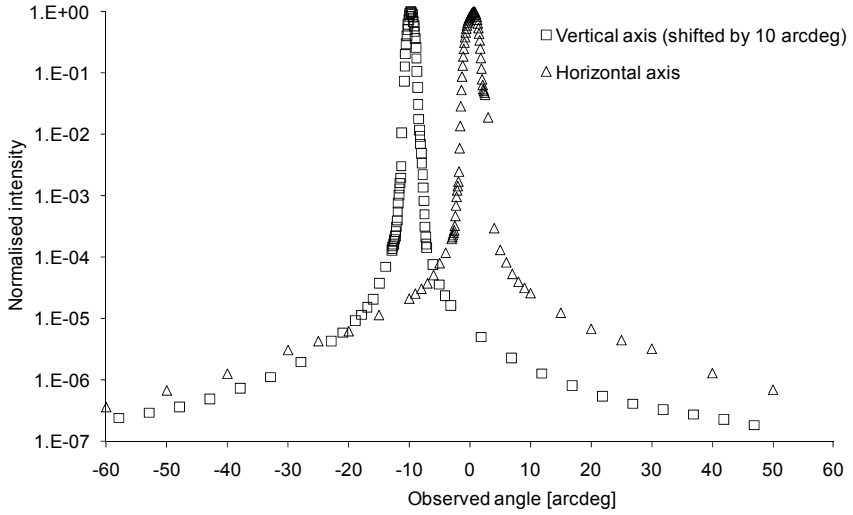

Figure 2-24 : The collimation verification has been measured from -60 to +50 arcdeg w.r.t. direct output beam along both horizontal and vertical axis. For clarity of the figure, the measured values along vertical axis were artificially shifted by 10 arcdeg on the plot.

The diffraction measurement sensitivity and accuracy of the simple setup being also limited by the dynamic range and noise of the detector, it has been improved with the use of a photomultiplier tube (GaAs photocathode) operated in photon counting mode, with maximum response at 800 nm (i.e. close to the laser diode emitting wavelength).

The direct beam and diffracted beam are thus measured in counts. The conversion of number of counts C into ph/s is given by formula (2-18), where P is the value in ph/s, G is the gain of the photomultiplier (2.10^6) and R is the photomultiplier cathode quantum efficiency (10%).

$$P = \frac{C}{R.G} \qquad \textbf{(2-18)}$$

The photomultiplier has an intrinsic non-linearity (due to time resolution error within the signal processing circuit), as shown on Figure 2-25 - left. A linearity factor (i.e. number of counts/s versus input beam flux) has thus been computed and used to correct the measured number of counts (Figure 2-25 - right). The linearity has been measured by use of a set of calibrated densities inserted in the beam, and the corrective factor computed as the deviation from a perfectly linear system. The dynamic range of the photomultiplier is then given by the ratio of minimum number of counts and the maximum number of counts before saturation, that were respectively measured at 2 10^4 ph/s and 8.5 10^5 ph/s providing a dynamic range of more than 40.

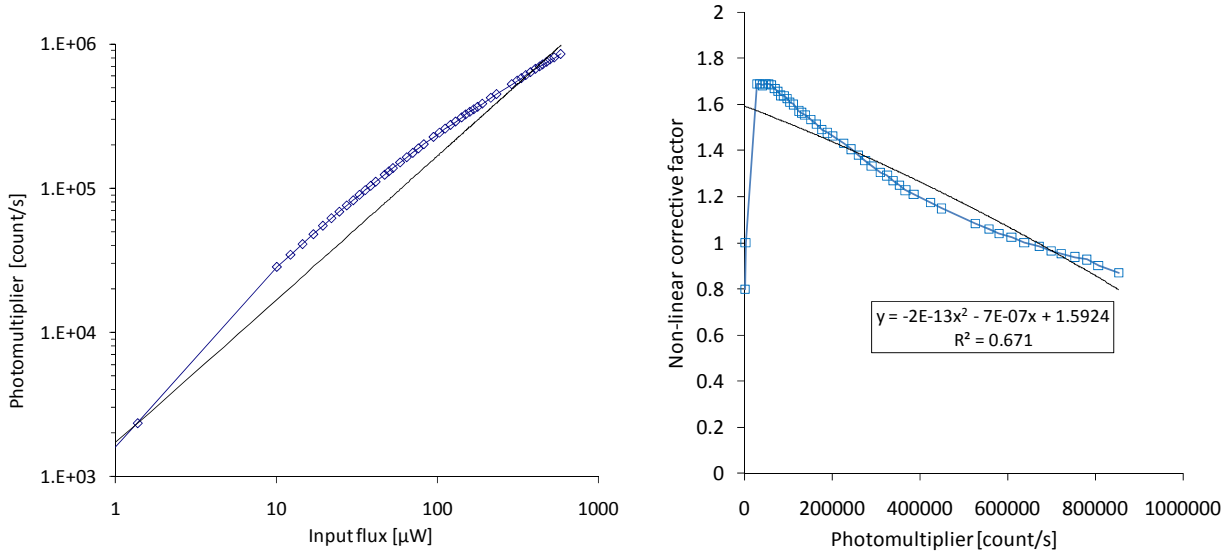

Figure 2-25 : Photomultiplier measured non-linearity factor (left) and corresponding corrective factor to be used in the diffraction measurements (right).

To reduce the photomultiplier Dark Current (DC), that was measured versus temperature (Figure 2-26), it was also cooled down below -30 °C.

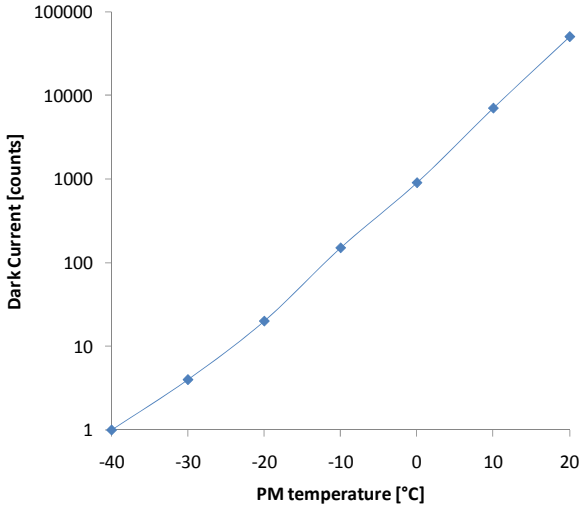

Figure 2-26 : Photomultiplier dark current dependence with temperature.

The photomultiplier is combined with an optical system to minimise the part of the system illuminated by the direct beam, as shown on Figure 2-27. The optical system is composed of a single lens with appropriate focal length to focus on the photomultiplier entrance window, providing a 1.9 arcdeg FOV. A flat mirror is inserted between the lens and the photomultiplier to limit the direct beam obstruction.

The direct beam is measured by inserting calibrated densities to reduce the flux incident on the photomultiplier.

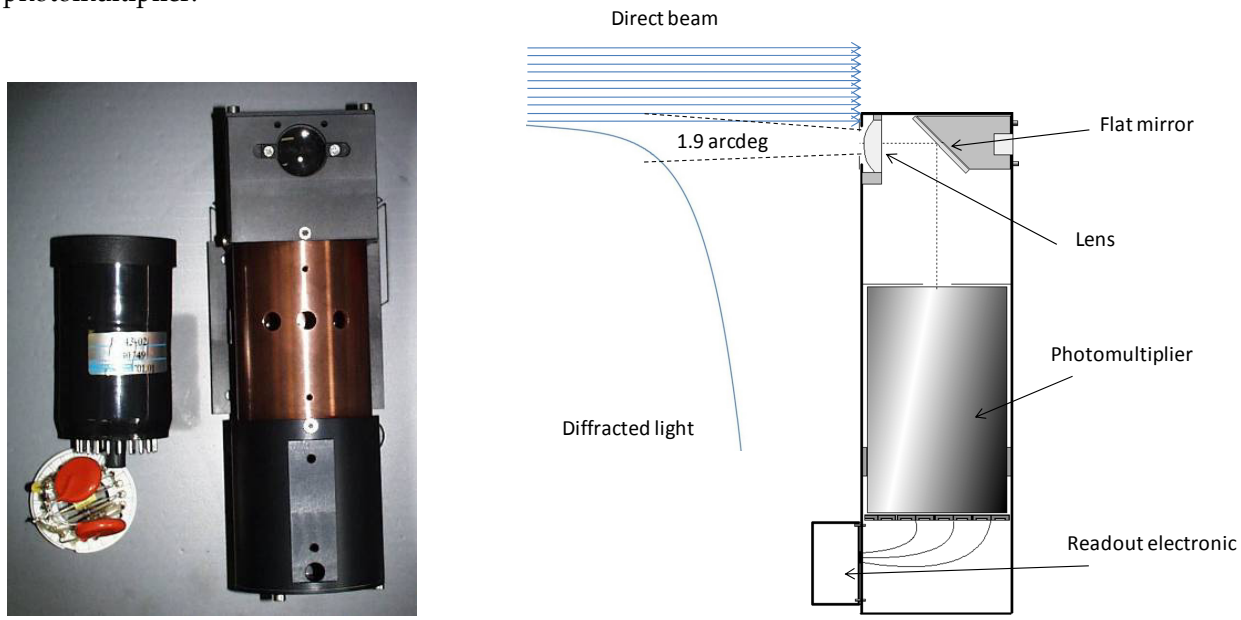

Figure 2-27 : A photomultiplier (Hamamatsu), left item on picture, is used to improve the diffraction measurement sensitivity. The area directly illuminated by the direct beam has been minimised by use of a focusing lens combined with a flat mirror, as shown on sketch (right). The photomultiplier and its associated optical system are mounted on a common structure (right item on picture).

The photomultiplier and its lens system are mounted on a combined rotation and translation movement system that allows recording the rejection curve in the edge shadow with limited reflection of the direct beam onto the photomultiplier assembly.

- The rotation is performed around the tip of the edge (Figure 2-28 left), located at 650 mm from the lens, to keep the optical system field of view centred on the edge, and translation compensate for small horizontal distance change between the edge and the entrance aperture consecutive to the rotation (Figure 2-28 right).
- To measure the direct beam, the detector is translated vertically to move the optical system entrance aperture in it (Figure 2-29).

The shadow deepness is expressed in arcdeg, and can be converted in vertical distance using the distance between the edge and the detector (1 arcdeg ⇔ 11.35 mm in the shadow for a 650 mm separation between edge and detector).

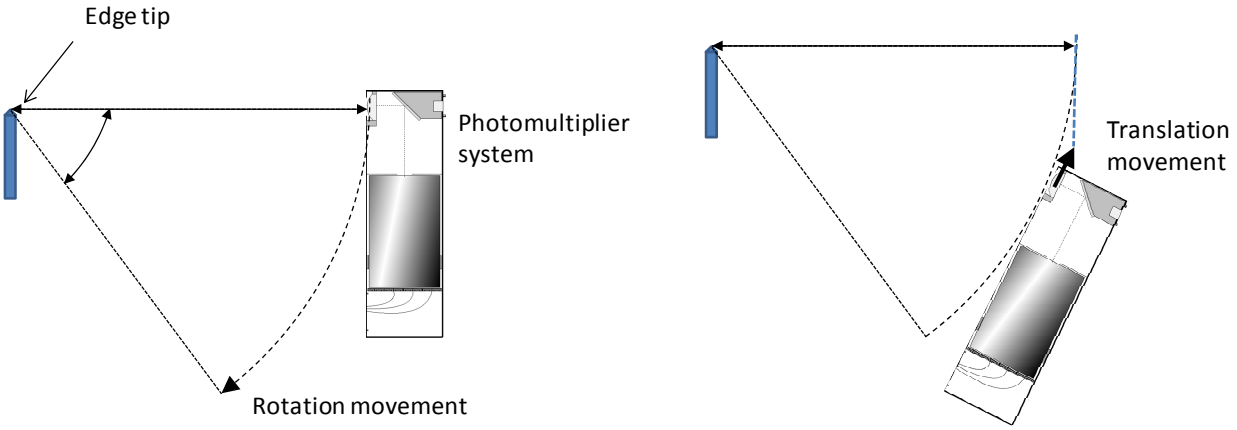

Figure 2-28 : The diffraction shadow is measured by a combination of rotation around the edge tip (left) and translation (right).

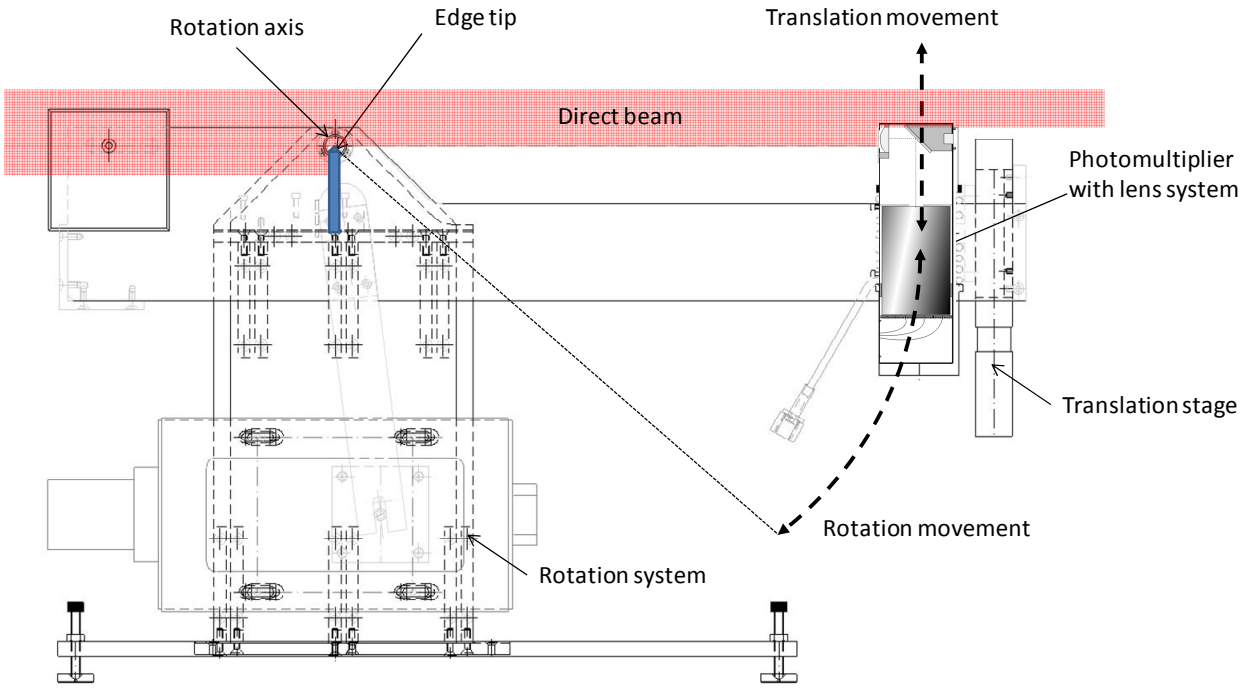

Figure 2-29 : A combined rotation and translation movement allows using the photomultiplier with limited reflection of the direct beam on it. The translation stage is also used for direct beam measurement.

Improved results

The test setup combining adjustable laser output power, detector dynamic range and integration time, provides a more sensitive straylight measurement, down to 10^{-5} B/B_0 (i.e. one order below first measurements of Figure 2-21) with smaller error bars.

Figure 2-30 gives the average of three measurements performed on a one-edge as a function of the rotation angle in the shadow, with error bar computed as the standard deviation. At 2.5 arcdeg, corresponding to a shadow deepness of 20 mm, the standard deviation is ~55%. It is a factor 1.7 lower than what was obtained with the simple test setup of Figure 2-21.

On counterpart, the edge diffraction differs from the theory at small angles because of the optical system aperture that results in a rounded shape at the beginning of the measured curves as shown on Figure 2-30. A more powerful source being not available at the time of the work, it was not possible to reduce the aperture without loss of sensitivity.

A convolution (floating average) of the theoretical curve by the lens system angular aperture of 1.9 arcdeg, using formula (2-19), however allows to match the measurements with the theory. For each angle α, the theoretical rejection R is integrated over a range of angles equal to the FOV (here 1.9 arcdeg) centered on the angle α.

$$R_{convolved}(\alpha) = \frac{1}{FOV} \cdot \int_{\alpha - \frac{FOV}{2}}^{\alpha + \frac{FOV}{2}} R(\alpha)\, d\alpha \qquad \textbf{(2-19)}$$

At the largest angles in the shadow, theory is however slightly above the measured values, but within the error bar, showing the limitation of the measurements at large angles in the shadow.

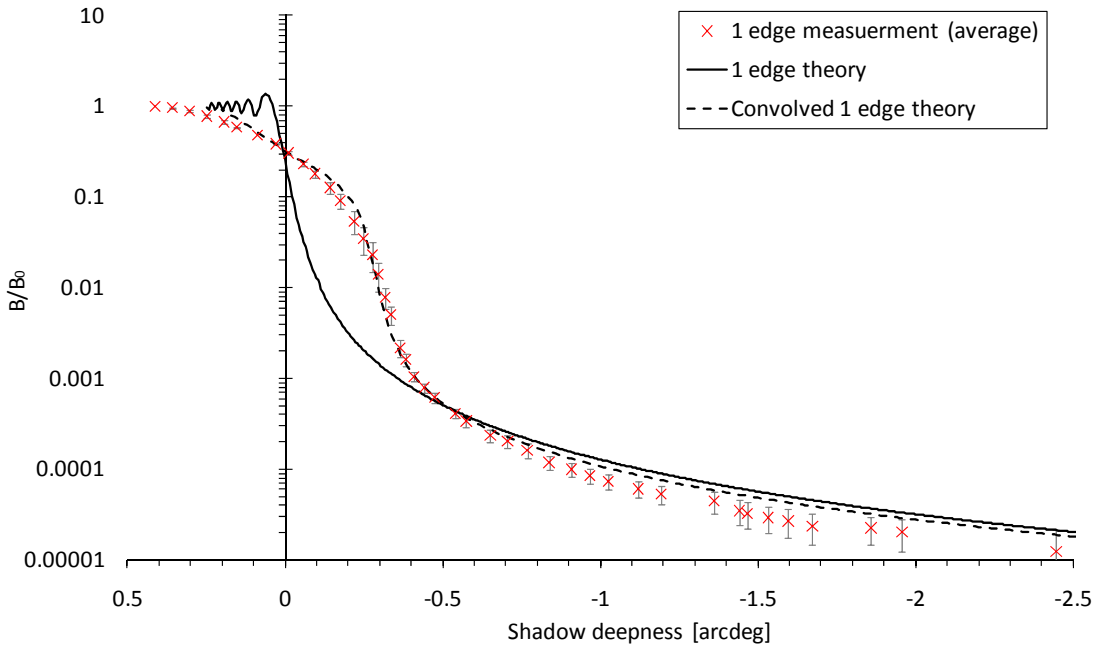

Figure 2-30 : One-edge relative B/B_0 diffraction profile (log scale), where B_0 is the direct beam intensity, measured with the photomultiplier and its lens system, and for a 805 nm wavelength. The shadow deepness is expressed in arcdeg. The measured rejection curve (red crosses) is compared with the 1-edge diffraction theory (black solid line) and its convolved curve (black dashed line) by the aperture size.

Error budget

In order to understand the error bars of Figure 2-30 and later try to improve it, an error budget has been built.

It is composed of noise and offsets that contribute to the uncertainty in the measured values.

- **The photomultiplier noise**.

  The photomultiplier noise is less than 10 counts/s when cooled down below -20 °C (with 0.5 °C stability), and thus results in a very small 0.001% error on the measured values.

- **The photomultiplier measurement accuracy**.

  The counting accuracy is ~ 1000 counts/s in the lowest part of the dynamic range (i.e. around 20000 count/s) and 2000 counts/s in the highest part (i.e. 80000 counts/s). It thus corresponds to a maximum 5% error noise.

- **The collimator divergence**.

  As a potential large source of error (the absorbed heat corresponds to 90% of the incoming beam power), it was stabilized by cooling down the collimator ensuring its temperature is constant whatever the input beam and the offset contribution of the collimator divergence to the measured signal is limited to a 5% offset.

- **The laser stability**.

  As a potential large contributor to the error budget, it was maintained by a dedicated cooling of the diode. The noise contribution of the laser stability into the error budget can therefore be assumed below 1%.

- **The environment background straylight**.

  It is produced by reflections of the input beam onto surfaces located around the detector and the edge, but also by scattering on dust particles in the air and on the edge. These reflections enter the optical system and perturb the measured diffracted signal. The resulting background value is not negligible at large angles in the shadow. It was minimized by using black surfaces on and around the test setup but remains the main contributor to the obtained error bar. This offset cannot be easily measured and cannot be simply removed from the measured values. It has thus been assumed to be ~50% of the measured signal, in order to be close of the 55% standard deviation of Figure 2-30 obtained with three measurements.

The error budget of Figure 2-31 is obtained by summing the noise contributors (root mean square (RMS) sum) with the offset (arithmetic sum), according to formula (2-20).

$$\text{Error} = \sqrt{\left(\text{Noise}_{\text{PM}}\right)^2 + \left(\text{Accuracy}_{\text{PM}}\right)^2 + \left(\text{Divergence}_{\text{Collimator}}\right)^2 + \left(\text{Stability}_{\text{Laser}}\right)^2} + \text{Offset}_{\text{Environment}} \qquad \textbf{(2-20)}$$

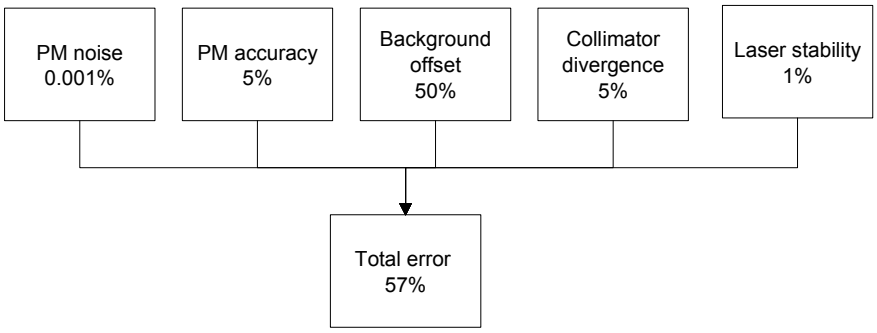

Figure 2-31 : One-edge diffraction measurement error budget

There is no horizontal error bars on Figure 2-32, because the translation and rotation stage accuracy is ~ 100 steps (each step is a few µm for translation stage and few arcsec for rotation stage), i.e. < 0.1% of the movement range and is therefore negligible.

Edge shape effect

The test setup was also used to compare the straylight rejection of various edge tip shapes (Figure 2-32) showing that it has very little impact on the diffraction performance. The reason is that only the diffraction on the edge tip is observed, and not the effect from other parts of the edge.

The orientation of an edge can thus be selected depending on other considerations, as for example the need to avoid back reflection from the edge towards the detector.

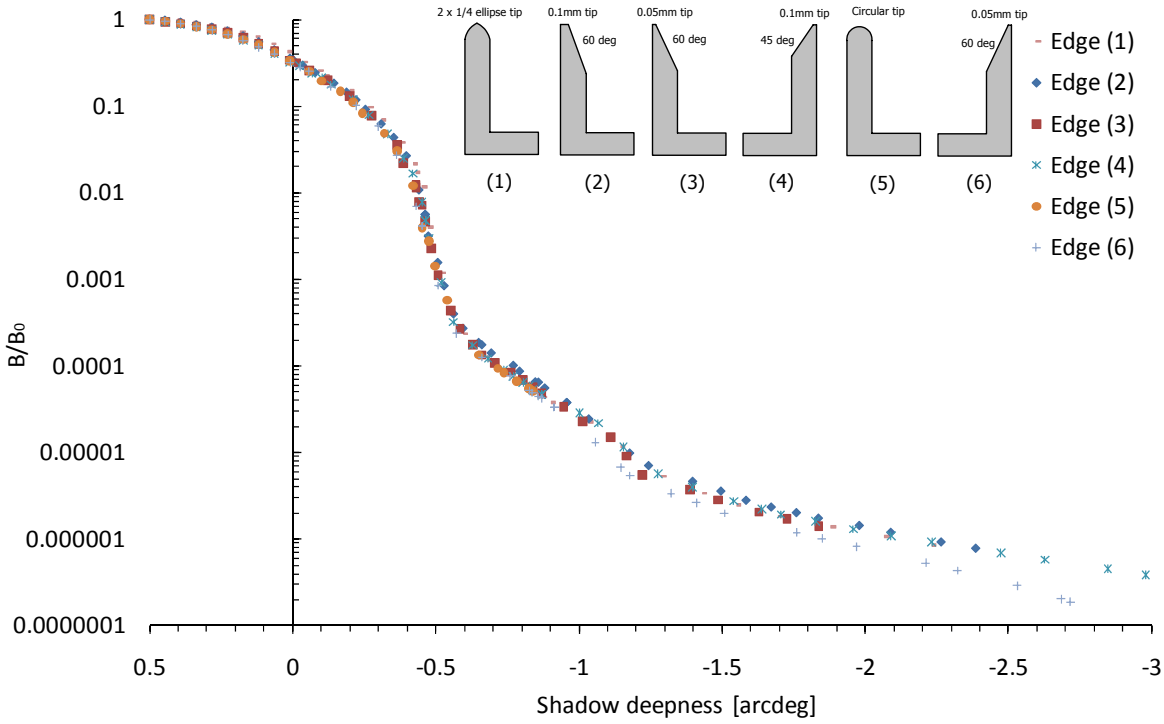

Figure 2-32 : One-edge relative B/B_0 diffraction measurement (log scale), where B_0 is the direct beam intensity, for six types of tip shape shows that it has little impact on the diffraction profile. Measurements were performed using a photomultiplier tube operated in photon counting mode, combined with a 1.9 arcdeg optical system.

2.3.2. Multi-edge baffle

In order to validate the theoretical computation of a multi-edge diffractive baffle, a 5-edges mock-up, whose heights have been optimized for a 10 mm distance between the edges, has been manufactured (Figure 2-33) and its rejection measured [13].

The edges of the mock-up were measured using a 3-D machine to confirm their heights. The edges alignment was materialised by a reference mirror located at the back-side of the assembly. This mirror was used to align the collimated beam with the mock-up direct axis. The mock-up was also positioned such that the detector system of Figure 2-29 is rotated around the last edge tip of the baffle as shown on Figure 2-34. To remove the part of this beam that is not reflected back by the baffle, the first edge was tilted to redirect it straight to a high-absorbing surface (Figure 2-33).

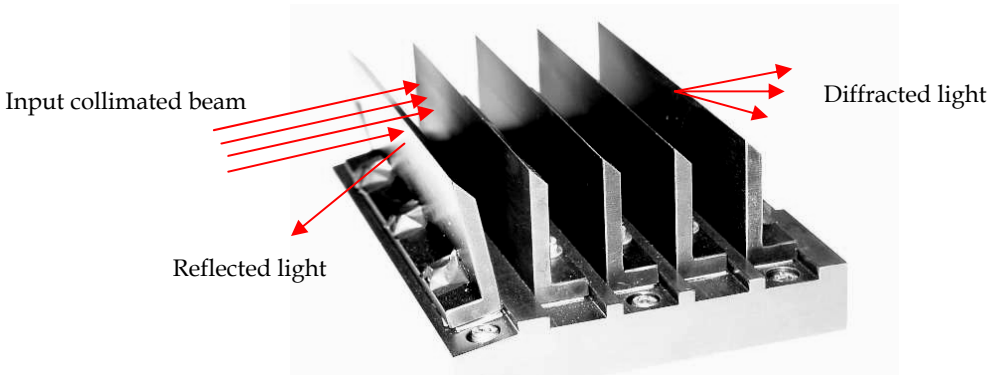

Figure 2-33 : Mock-up of a 5-edges cascading diffraction baffle, optimised for a 10 mm distance between the edges. The baffle is made of aluminium, which is black anodised. Edge #1 is tilted to redirect the reflected flux toward a black cavity.

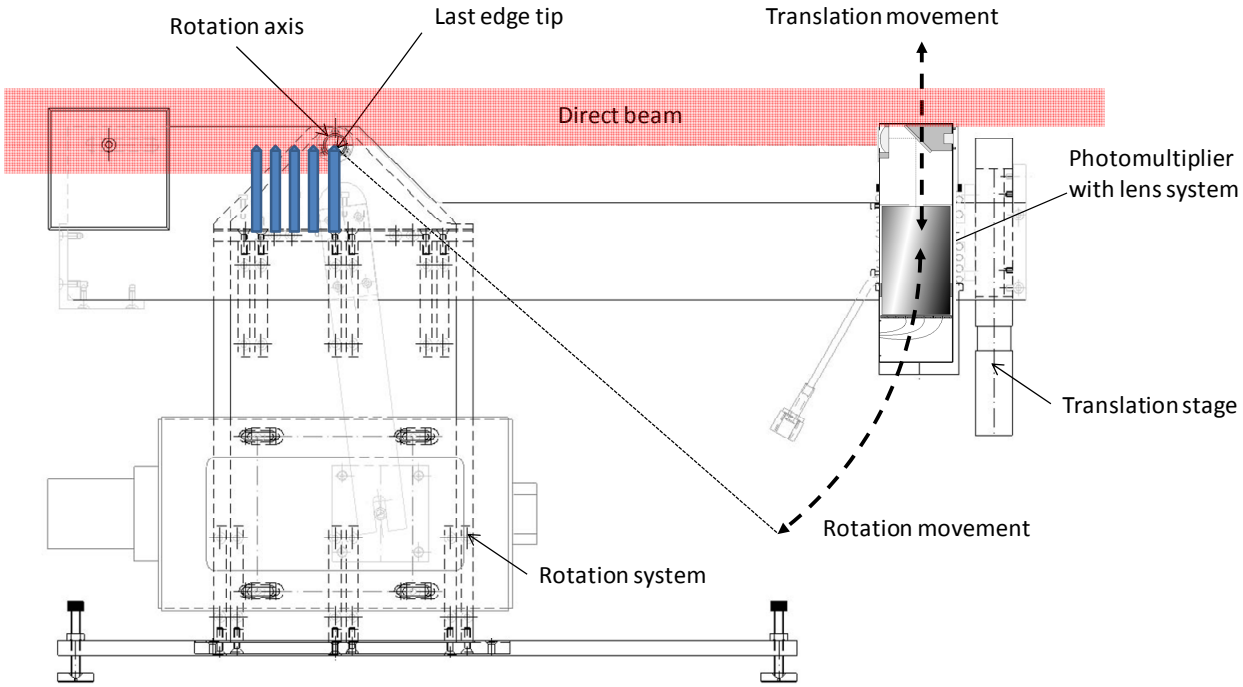

Figure 2-34 : The rotation is performed around the last edge of the measured 5-edges baffle.

Test setup

To limit straylight contamination by parasitic reflections and diffusion of the air (Rayleigh scattering by particles smaller than the wavelength of the light beam, or Mie scattering by particles similar to or larger than the wavelength as the water vapour), the mock-up was integrated in a black enclosure installed in a vacuum chamber (2 meters diameter in the Centre Spatial de Liège (CSL) cleanroom facilities), as shown on Figure 2-35 and Figure 2-36.

The vacuum chamber also allowed cooling down the collimator and the detector, and provided a stable temperature for the light trap absorbing elements.

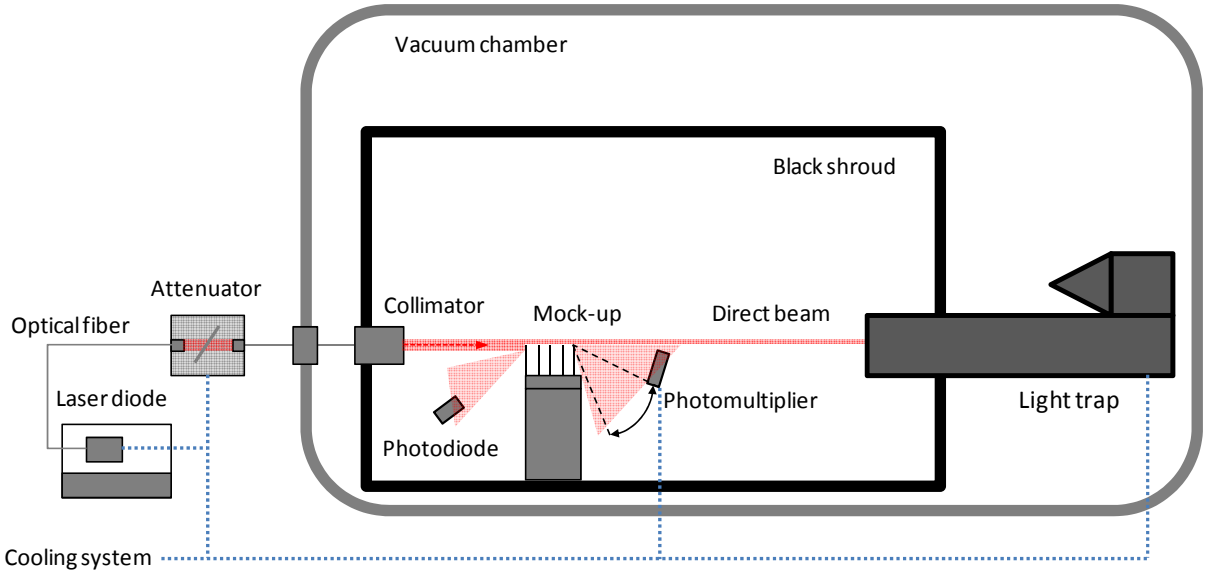

Figure 2-35 : A dedicated test setup has been implemented to measure the 5-edges diffraction baffle efficiency. It is based on the previously used detector assembly mounted a rotation stage, and combined with a specific collimator and a direct-beam light trap. The setup, except the laser source, was implemented in vacuum chamber to allow cooling down these two elements.

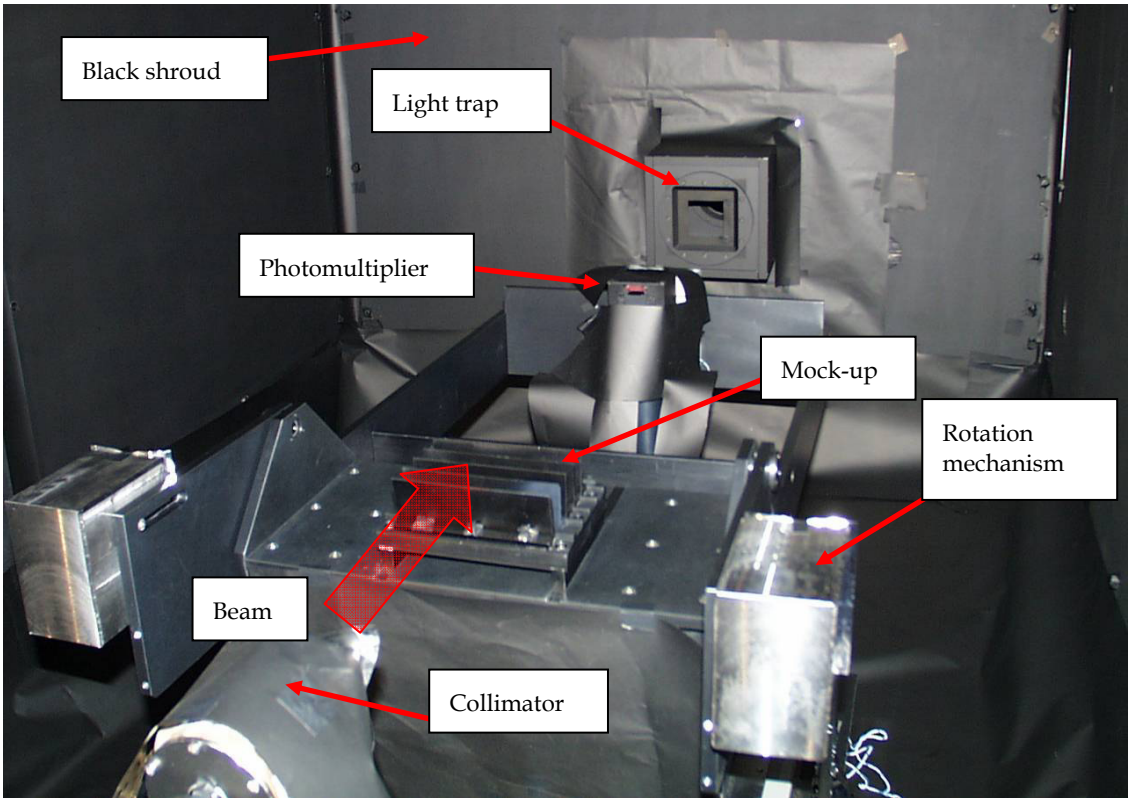

Figure 2-36 : The 5-edges mock-up is integrated in the test setup with the collimator providing the beam input (visible on the first edge and on the top of the photomultiplier) and a light trap catching the non-diffracted direct beam. Black Kapton was used to warp as much as possible all parts that were potential reflection source.

In addition to the very sensitive detector (photomultiplier) and the powerful collimated laser diode used for the one-edge diffraction measurement, the test setup has been improved to measure the expected very high rejection level with the following elements.

- A linear photodiode has been used to monitor the collimator output flux variation during the measurements.

  The photodiode was located in front of the first edge (Figure 2-35) and measured the light reflected by this edge, where it is attenuated by a factor ~ 20 as compared to the direct flux.

- An attenuator has been used on the path between the laser diode and the collimator to increase the dynamic range. This attenuator is a small black box where a transmission density is inserted in the light path to reduce its intensity (Figure 2-37).

  The attenuator also contains a small light trap, which consists in a simple black "U-shape" to limit the light reflected by the density filter entering the output coupler.

  The junction between the input and output optical fibres is realised by two small optical fibre couplers (66% transmission), one collimating the laser output toward the density filter and the other one collecting the beam toward the second fibre (Figure 2-37).

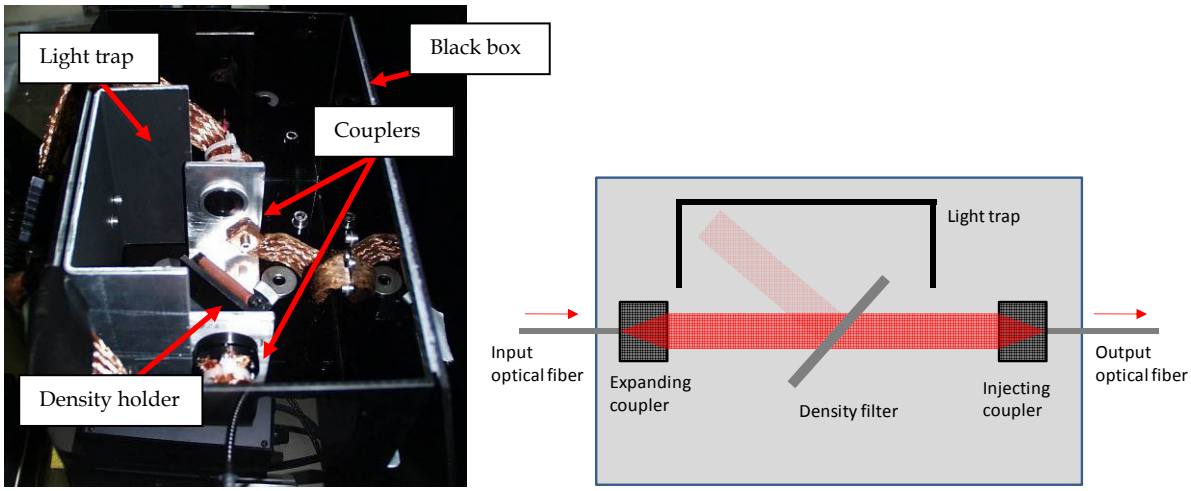

Figure 2-37 : The attenuator is composed of two small collimators used to interrupt the optical fibre path and to allow inserting transmission densities within the beam. The density holder is connected to a small radiator in order to reduce the effect of temperature on density transmission.

A set of densities with various thickness has been calibrated (Figure 2-38) by measuring their transmission for a known input flux. To reduce the temperature dependence of the density transmission, the density holder was connected to a small radiator to evacuate most of the absorbed heat.

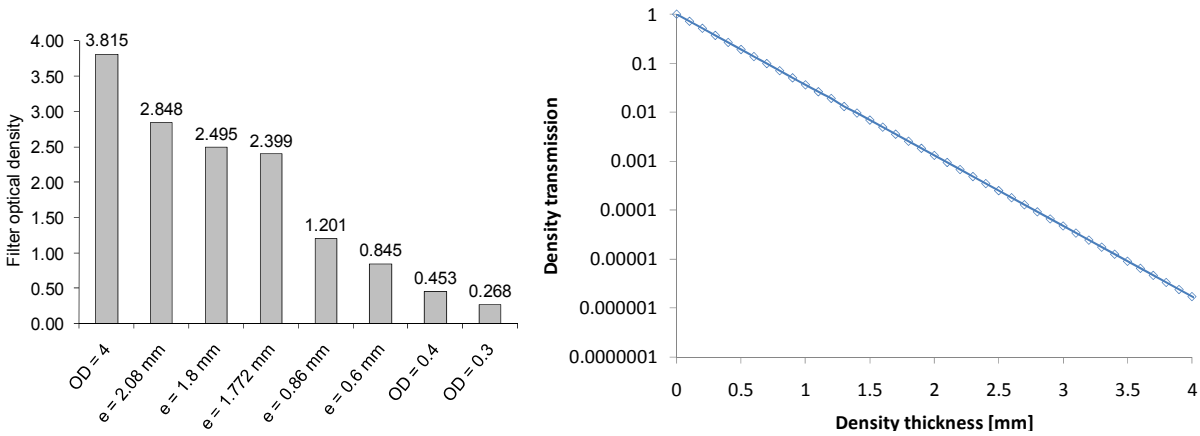

Figure 2-38 : Left: optical densities have been calibrated to accurately know their transmission based. Right: the density transmission is directly linked to its thickness.

- A "direct beam" light trap has been designed and implemented to catch the light that is passing over the baffle (Figure 2-39). This light trap is designed to absorb the nearly collimated beam from

the collimator and is a key element of the test setup as it guarantees the required low straylight environment to measure the multi-edge diffraction.

The light trap optical design is based on the known characteristics of the light to attenuate. As the entrance beam is nearly collimated, the light trap performance is obtained by keeping this beam characteristic as far as possible into the light trap. The first interaction of the beam with a surface occurs as deep as possible into the light trap to limit the first order backscattered light. Moreover, the micro-roughness of this first surface is as best as possible for, once more, limit the backscattered light.

The input collimated beam interacts with a first Schott NG1 neutral density (filter #1), which absorbs 86% of the incoming light flux and reflects the rest specularly toward a second Schott NG1 density (filter #2). The second density also absorbs 86% of the remaining light flux and reflects the rest specularly toward a conical light trap coated with a black specular paint.

The backscattered light, coming from the conical light trap and from the filter (mainly due to the micro-roughness scattering) is further limited by the tube and its four vanes. The main attenuation occurs into the filter #1 while the major contribution of the backscattered light comes from the micro-roughness scattering of the filter #1 and filter #2.

The light trap is thus designed to absorb a collimated beam from one particular direction defined by the tube axis and the filters size and location. From other directions, the light trap rejection is not optimized and depends mainly on the black coating applied on the tube and vanes. All parts of the light trap, including the vanes are thus coated with a quasi-lambertian black paint (Chemglaze Z306) with TIS lower than a few % (as measured in Figure 2-5) in the considered spectral range for incidence angle lower than 70 arcdeg. The inner surface of the conical light trap is however coated with a glossy black paint (Chemglaze Z302) to avoid back reflections and direct trapped light toward the end of the cone.

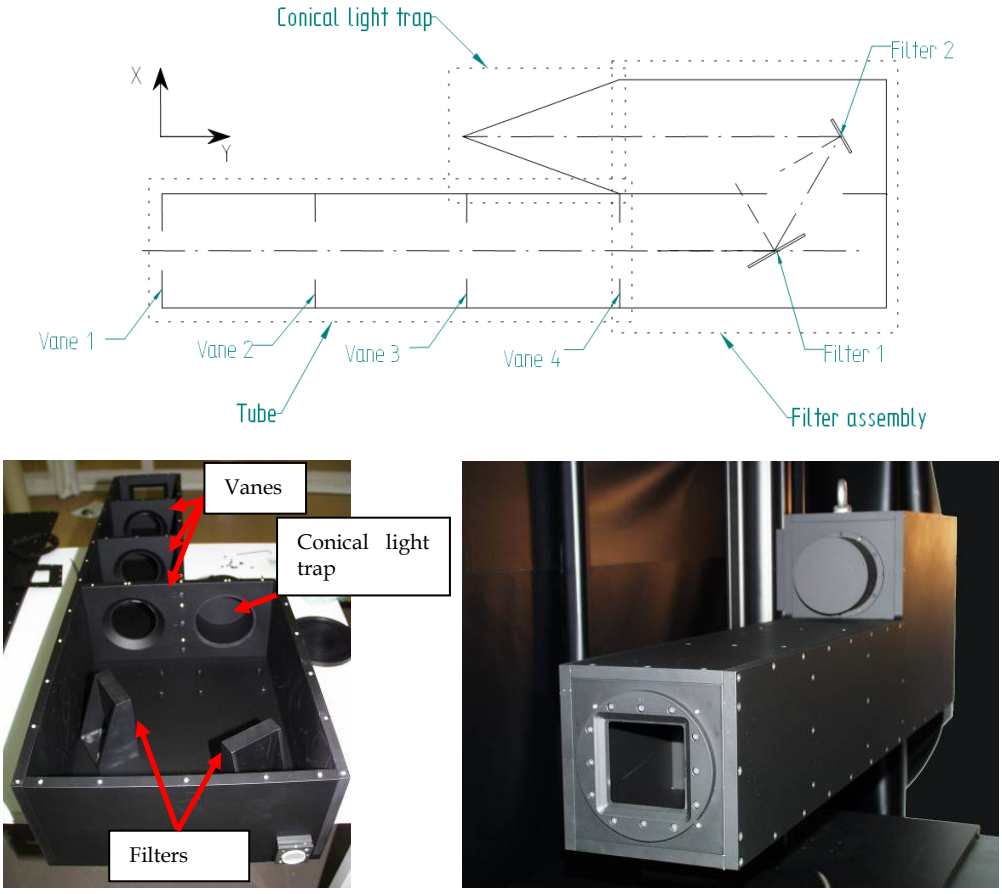

Figure 2-39 : The light trap is composed of three parts: a tube with 4 annular vanes, a set of two reflective filters and a conical light trap. It provides the attenuation of the direct beam passing over the edges, allowing a reduction of the cavity straylight level at a level lower than measured edges diffraction.

The rejection of the light trap for one particular angle is defined by the ratio (2-21) of the measured light coming out of the light trap on the total incident light entering it.

$$R(\theta) = \frac{\text{Total light flux coming from the light trap}_{\,along\ direction\ \theta}}{\text{Total incident light flux}_{\,in\ all\ direction}} \qquad \textbf{(2-21)}$$

The light trap computed rejection for the input collimated beam in the axial incidence ($\theta = 0 \pm 0.7$ arcdeg) is better than 10^9. This direction is defined by an alignment cube, used to co-align the light trap with the incident beam. The light trap rejection for light flux coming from any other direction is better than 10^7.

The effective rejection of the light trap has been measured as a function of the observation angle. The light trap rejection is < 10^{-8} (Figure 2-40) except close to the direct path where it is ~ 1.2 10^{-8}. The rejection cannot be measured in the direct path but can be expected to be better than 10^{-9} on the basis of its rejection out of the direct path.

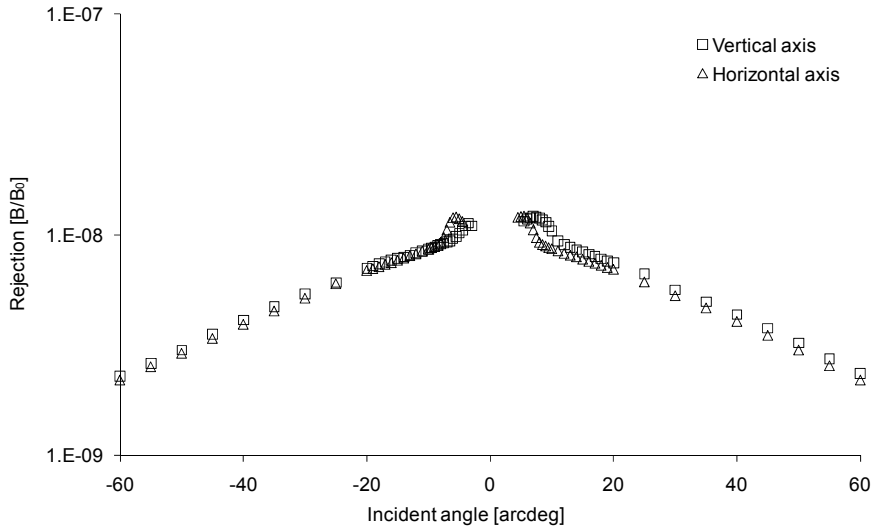

Figure 2-40 : The light trap performance measured from -60 to +60 arcdeg w.r.t. input beam direction along both horizontal and vertical axis.

Results

When combined with the black enclosure and the view factors to the detector, the measured mock-up diffraction is higher than the setup straylight level.

The baffle mock-up diffraction measurement was first performed at ambient pressure with the following sequence:

- Direct beam is measured with a total neutral density of 8.6 and lowest laser output within its linear range
- When diffraction reached 10^{-1}, 10^{-3}, 10^{-5} and 10^{-9}, the laser power and density value are adjusted as per values given in (2-22).

$$\text{Diffraction} = \begin{pmatrix} 1 \\ 0.1 \\ 0.001 \\ 0.00001 \\ 0.0000001 \\ 0.000000001 \end{pmatrix} \quad \text{Density} = \begin{pmatrix} 8.64 \\ 8.99 \\ 6.99 \\ 4.99 \\ 2.99 \\ 2 \end{pmatrix} \quad \text{LaserOutput} = \begin{pmatrix} 0.015 \\ 2.357 \\ 2.357 \\ 2.357 \\ 2.357 \\ 21.434 \end{pmatrix} \text{W} \qquad \textbf{(2-22)}$$

- The number of edges was then progressively removed to test with 4, 3, 2, 1 edge(s) for comparison of the experimental curves with the theory.

As shown on Figure 2-41, the matching between theory and measured slope is very good. For 5 edges, the measured diffraction is close of $B/B_0 = 10^{-11}$ for angles larger than 5 arcdeg in the shadow.

- The final plateau for large offset angles and the value at null offset confirms the diffractive model is correct.
- Each additional edge provides an additional amount of shadow, as predicted by the Fresnel theory and cascading equation used to define and optimize the multi-edge configuration.
- The measurement with 5 edges is slightly above prediction for the largest angles, most probably because of the air particular diffusion that adds a contribution to the very faint diffracted measured light.

As previously notice for the 1-edge measurement (Figure 2-30), the measured values in the first 0.5 arcdeg do not match with the theory because of the photomultiplier lens system field of view. The theoretical plot has however not been adapted to keep track of the initial theoretical multi-edge curve.

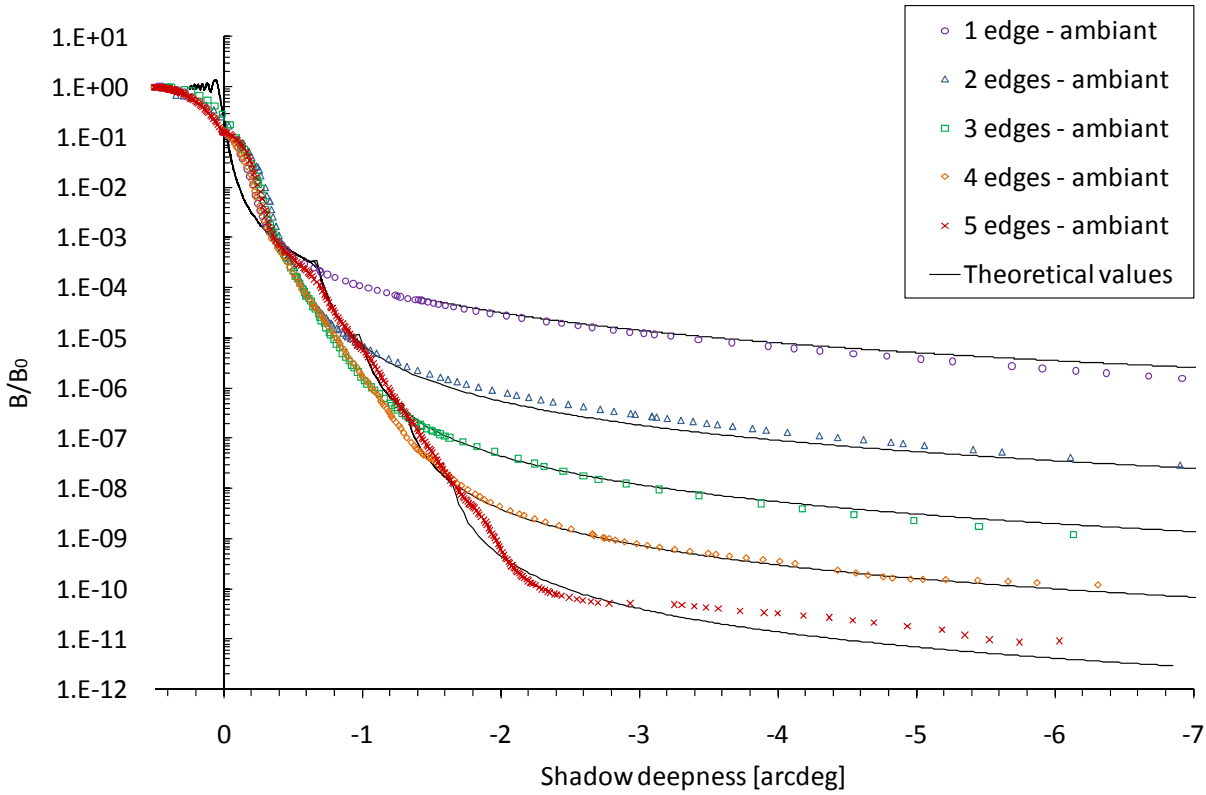

Figure 2-41 : Mock-up relative diffraction profile B/B_0 (in log scale) measured for 1, 2, 3, 4 and 5 edges (in air) at 805 nm, where B_0 is the direct beam intensity, compared with corresponding theoretical predictions.

The baffle mock-up was then re-assembled and the 5-edges diffraction was measured under vacuum. Figure 2-42 shows the comparison of the 5-edges diffraction measurement under vacuum and in the chamber at ambient (after repressurization).

The level of measured straylight reached an unprecedented value of $B/B_0 = 2.10^{-12}$. As already measured at ambient, the vacuum measurement is some order of magnitude lower than what was previously measured on similar multi-edge diffractive baffle [3][5].

There is however a difference between the vacuum and the ambient data, which progressively increases with the angle in the shadow. The difference is due to the following two factors:

- A very small difference in the edge heights between the ambient and vacuum tests, which were progressively removed to obtain Figure 2-41 and mounted back for vacuum measurement without metrology control of their heights.
- The effect of air diffusion which adds a contribution to the measured signal at ambient pressure and dominates for the large angles where straylight is very faint.

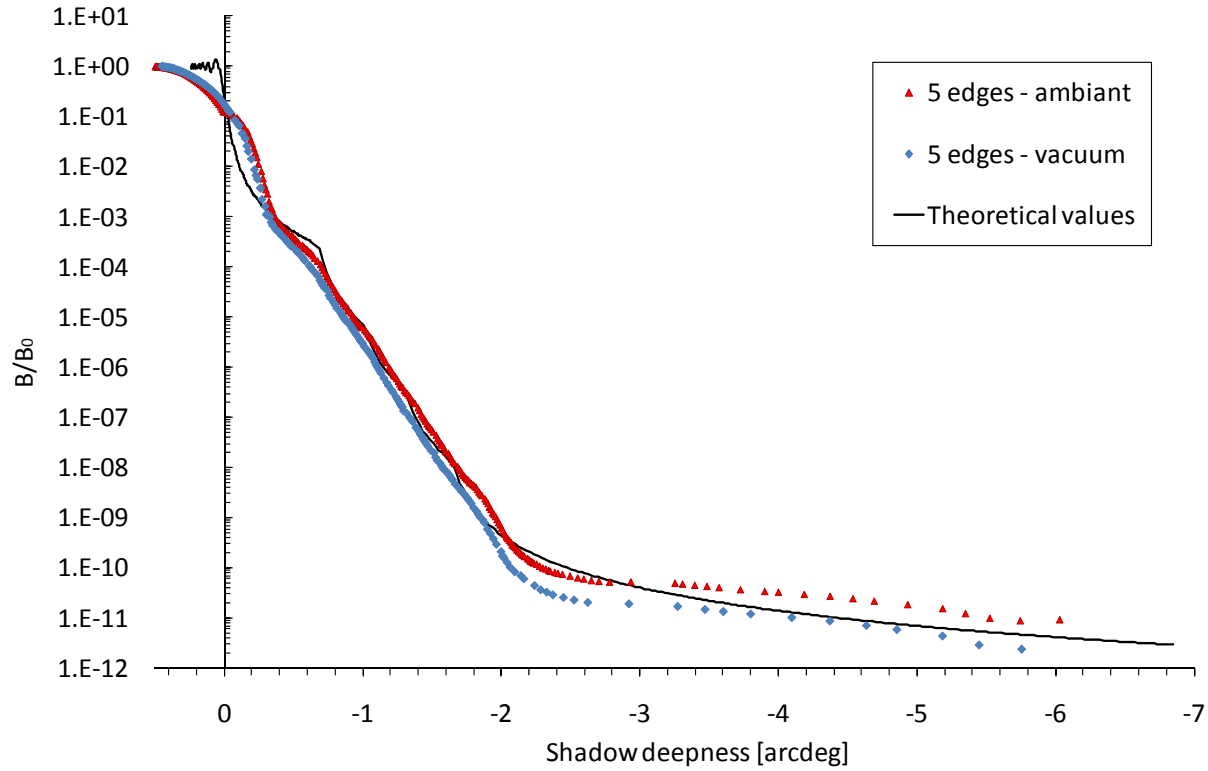

Figure 2-42 : Mock-up relative diffraction intensity profile B/B_0 (log scale) measured for 5 edges (in air and under vacuum) at 805 nm, where B_0 is the direct beam intensity, compared with the 5-edges theoretical prediction.

Error budget

No error bar is shown on Figure 2-41 and Figure 2-42 because measurements were performed only once and no standard deviation over a set of values could be computed.

An error budget similar to the one of the knife edge measurement (Figure 2-31) can however be built. The error contributions of the photomultiplier noise and measurement accuracy, the collimator divergence are the same. The only differences are the potential source of error from the density filters used in the attenuator, and the background that is reduced with the light trap.

- **The density filters transmission variation**.

  The filters were also cooled down to limit their transmission variation during the measurements, and the offset contribution of the filter variation into the error budget is limited to a few % (5% is considered).

- **The background straylight**

  Assuming the background offset is reduced to 30% (rough estimate) with the light trap, the error budget of Figure 2-43 is obtained.

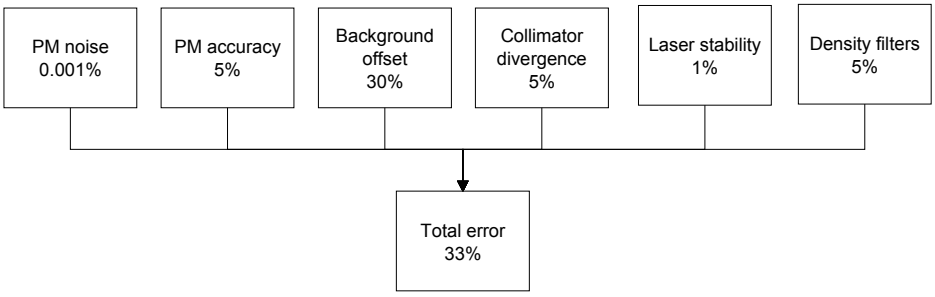

Figure 2-43 : Multi-edge diffraction measurement error budget

As for the one edge measurement, there is no horizontal error bars, because of the high accuracy of translation and rotation movements.

2.4. Chapter summary

This chapter is focused on the straylight rejection by an edge or a combination of edges, providing an efficient diffractive protection from straylight.

A diffractive baffle is however only efficient for nearly collimated light source, on the contrary of absorptive baffle where light is trapped by multiple reflections. The absorptive baffle performance depends on the scattering properties of the black coating applied on the edges, and on their configuration to trap light. The diffractive baffle performance however only depends on the distance between the edges (along light path) and on the distance to the observation area.

Ray-tracing is a powerful tool to model absorptive baffle. It can also be used to model edge diffraction but is limited in the case of a combination of diffractive edges.

For a multiple-edge diffractive baffle, a numerical computation method has thus been implemented providing a simple way to derive its rejection by considering a cascading of their diffraction effect. This method is theoretically valid for a semi-infinite plane. The Fresnel approximation can however be applied for finite edge size when the measurement plane is far enough to neglect the effect of the lateral side of the edges.

The multi-edge diffraction model has been validated on a 5-edges mock-up, with a finite size laser beam, proving the multi-edge diffraction concept.

No verification of the lateral effect of the edge was performed. It is however similar to the diffraction in the nominal direction, i.e. by the edge perpendicular to the direct beam, as every point on the edge diffracts in a similar way, except that the distance to the detector is increased. The diffraction at the detector plane shall therefore be the sum of diffraction by every point of the edge and considering the diffraction level obtained from the central part of the edge is therefore a conservative approach.

The multi-edge diffraction has been tested at one wavelength (805 nm) using the most powerful laser source available at the time of test. In the case of a non-temporally coherent source, composed of a complete wavelength spectrum, the principle can however be extended as the cascading diffraction is valid for every wavelength (with lower or higher rejection depending on the wavelength).

The multi-edge diffraction theory has been developed for a spatially coherent light source, but has been tested for a 27.5 arcmin divergent light source, providing confidence it is valid for non-spatially coherent source like the Sun (32 arcmin divergence).

Chapter 3. Straylight design of the STEREO-HI instrument

3. Straylight design of the STEREO-HI instrument

While observation of the heliosphere out to about 32 solar radii (R_{Sun}) has been accomplished in the past with conventional coronagraphs [40] and 225 R_{sun} with coronograph-like telescope [46] [47], optical remote sensing observation of CMEs in the region of the heliosphere up to Earth orbit has only been achieved with non-imaging instruments such as the scanning helio-zodiacal light photometers [39] and with the imaging cameras of the Solar Mass Ejection Imager [45] from a viewpoint close to the Earth, with consequent limitations for observing Earth-directed CMEs.

The HI instrument on board STEREO has been designed to detect and follow the faint emission of CME at large distances from the Sun up to Earth distance and beyond, for the first time from a viewpoint distant from the Sun-Earth line..

3.1. The STEREO-HI instrument

3.1.1. Straylight design

The straylight design of an instrument is organised as shown on Figure 3-1.

The instrument requirements are first established with the required sensitivity, the potential straylight sources facing the instrument, and the instrument constraints (envelope…). The critical objects as seen by the detector are then obtained by ray-tracing simulation. The protection is then derived (baffle(s), lens barrel and detector cavity improvement) to ensure the scientific requirements are achieved.

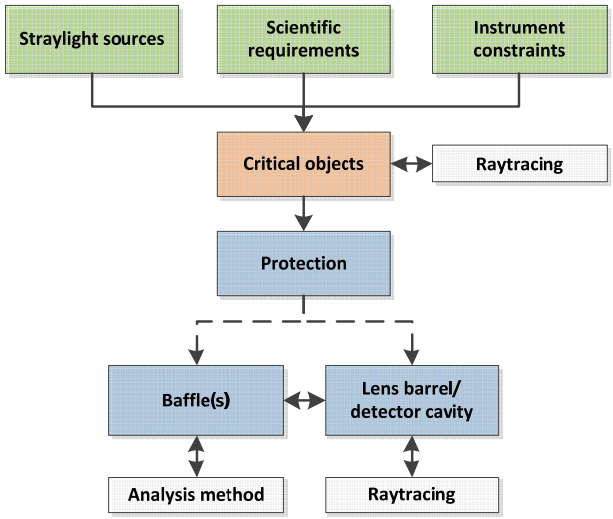

Figure 3-1 : The flow to follow for straylight design is composed of three levels: inputs, critical objects and protection.

3.1.2. Mean Surface Brightness

The Mean Surface Brightness (MSB) of the solar disk is generally considered as the most appropriate unit of radiance in terms of the phenomena of interest in Solar Physics and is used as the input source (B_0) of the relative brightness measurements (B/B_0).

It is obtained with equation (3-1) [44] and is independent on the distance, where L_0 is the solar luminosity (i.e. the power emitted by the Sun = $3.9\ 10^{26}$ W), $\Omega_{sun} = 6.8\ 10^{-5}$ sr is the solid angle subtended by the Sun at the distance[4] R = 1 Astronomical Unit (AU) = $1.5\ 10^{11}$ m, and the solar constant B_{Sun} is 1365 W/m² at 1 AU.

$$MSB = \frac{L_0}{4\cdot\pi\cdot R^2\cdot\Omega_{sun}} = \frac{B_{Sun}}{\Omega_{sun}} = 2\cdot 10^7 \frac{W}{m^2\cdot sr} \qquad \textbf{(3-1)}$$

[4] The two STEREO spacecrafts are on an orbit close to 1 AU.

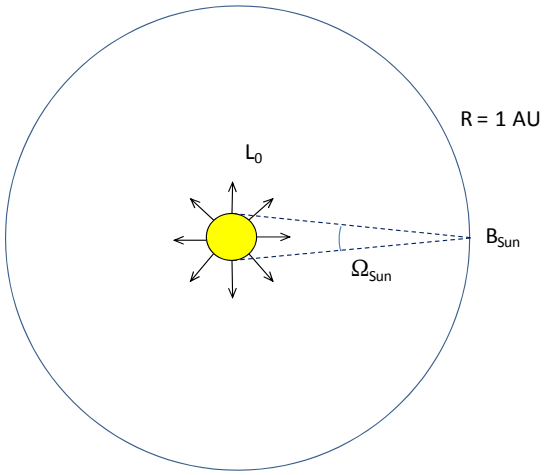

Figure 3-2 : The Mean Surface Brightness of the solar disk is the ratio of the solar luminosity L_0 by the surface of a sphere of 1 AU radius and the angle Ω_{Sun} subtended by the Sun at a distance of 1AU.

Remark:

The MSB can also be expressed as the average surface brightness of the solar disk if the Sun was imaged on the detector by equation (3-2) [52].

It is thus derived from equation (3-1) by replacing the angular size of the Sun by the number of pixels Npx_{Sun} of the Sun if it was imaged on the detector multiplied by the instrument pixel angular size $\Omega_{px.}$

$$MSB = \frac{B_{Sun}}{\Omega_{px} \cdot Npx_{Sun}} \qquad \textbf{(3-2)}$$

The number of pixels[5] is obtained by equation (3-3) where α_{Sun} is the Sun angular diameter (as seen from at 1 AU, i.e. 32 arcmin) and α_{px} is the camera pixel resolution (in arcsec[6]).

$$Npx_{Sun} = \pi \cdot \left(\frac{\alpha_{Sun}}{2 \cdot \alpha_{px}} \right)^2 \qquad \textbf{(3-3)}$$

The angular size of a pixel7 is obtained with equation (3-4) where FOV is the instrument field of view and $(n_{px})^2$ is the number of pixel of the detector.

$$\Omega_{px} = \frac{\Omega_{FOV}}{(n_{px})^2} = \frac{4 \cdot \pi \cdot \left(\sin\left(\frac{FOV}{4} \right) \right)^2}{(2048)^2} \qquad \textbf{(3-4)}$$

3.1.3. Straylight requirement

The challenge of the STEREO-HI instrument is to image CME over a wide field of view with a very faint visible light detection capability.

For that purpose its field of view has been split in two cameras. The two HI fields of view are centred on the Sun-Earth line (ecliptic plane). They are of 20 and 70 arcdeg, offset from the Sun centre by 13.65 and 53.35 arcdeg (Figure 3-3).

[5] The size of the Sun is respectively 2363 and 202 pixels in the STEREO HI-1 and HI-2 cameras.

[6] The pixel size in arcsec of the STEREO HI-1 and HI-2 is given in Table 1-1.

[7] The pixel angular size of the STEREO HI-1 and HI-2 is respectively 2.3 10^{-8} and 2.8 10^{-7} sr.

The STEREO-HI instrument required sensitivity is driven by the CME signal level. It is ~ 1% of the solar corona background, which is ~10^{-12} to 10^{-15} of the MSB over the two HI-1 and HI-2 FOV, as shown on Figure 3-3 where the HI fields of view are shown versus the elongation from the Sun centre [10].

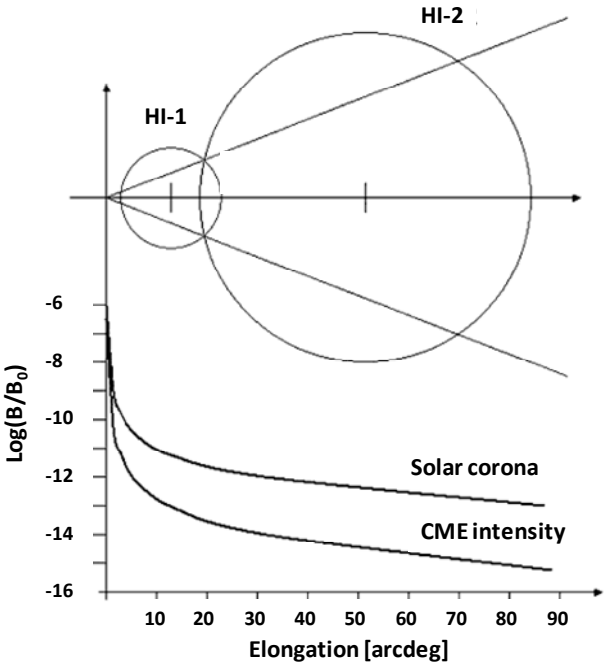

Figure 3-3 : CME and solar corona level relative B/B_0 brightness (B_0 is here the Mean Surface Brightness of the solar disk), in log scale, as a function of the elongation over the HI FOV (split in two cameras, HI-1 and HI-2) [10].

It resulted in the straylight requirement at the HI-1 and HI-2 detector level of Table 3-1 [20]. With such levels of straylight, one order of magnitude below the solar corona brightness, the background added to the solar corona has a negligible effect on the measurement accuracy of the corona signal. The CME can indeed be obtained by subtracting[8] images of long enough periods to ensure that the noise on the F-corona is less than the CME signal [20].

	Straylight requirement at detector level
HI-1	≤ 3 10^{-13}
HI-2	≤ 10^{-14}

Table 3-1 : HI-1 and HI-2 straylight requirement at detector level [20], expressed in relative brightness B/B_0 where B_0 is the MSB of the solar disk.

3.1.4. Design overview

The HI instrument is essentially a box shape, of major dimensions about 840 x 550 x 260 mm (Figure 3-4), containing the two HI-1 and HI-2 cameras, a front and an internal straylight protection baffles [20]. The two HI-1 and HI-2 cameras have respectively 20 arcdeg and 70 arcdeg fields of view.

The two camera detectors are passively cooled down by radiators located at the back of the instrument and viewing the cold space. A Camera Electronic Box (CEB) provides the interface between the two HI cameras and the SECCHI Electronic Box (SEB), itself connected to the STEREO on-board computer. A one-shot door mechanism also provides protection of the camera and baffles from on-ground S/C AIT and launch.

[8] This principle applies when the background straylight is stable over the orbit. Otherwise, the straylight requirements shall be below the order of magnitude of what is observed (i.e. here the CME).

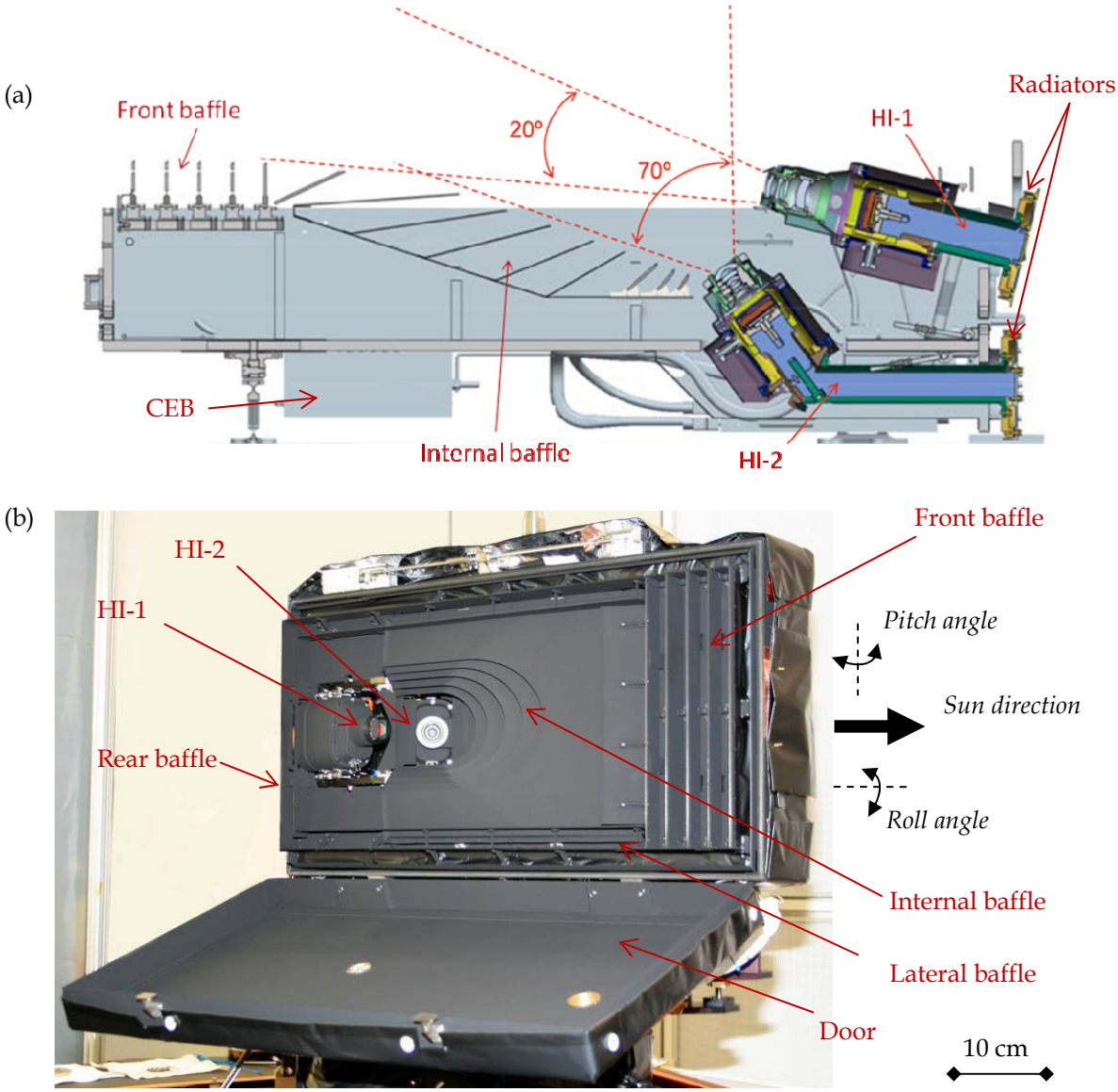

Figure 3-4: (a) Side view of the STEREO-HI instrument, with its HI-1 and HI-2 cameras and associated detector cooling radiators, the front and internal baffles, and the CEB [20]. (b) One of the two HI instruments (HI-B) during environmental and calibration tests (at CSL).

The STEREO-HI instrument was developed in collaboration between four institutes:

- the University of Birmingham (UB - UK) that was responsible for the instrument mechanical and thermal design, together with the instrument manufacturing and assembly
- the Rutherford Appleton Laboratory (RAL - UK) responsible for the CCD and the camera design
- the Centre Spatial de Liège (CSL - Belgium) responsible for the optical and baffle design, together with for the on-ground testing
- and the Naval Research Laboratory (NRL - US) responsible for the imager suite of instruments on STEREO, including the on-board command and data processing by a common electronics box

3.1.5. HI-A and HI-B

The STEREO mission is composed of two spacecrafts [17]. One HI instrument is mounted on the side panel of each STEREO spacecraft with their field of view (FOV) oriented toward the Sun-Earth line (Figure 3-5).

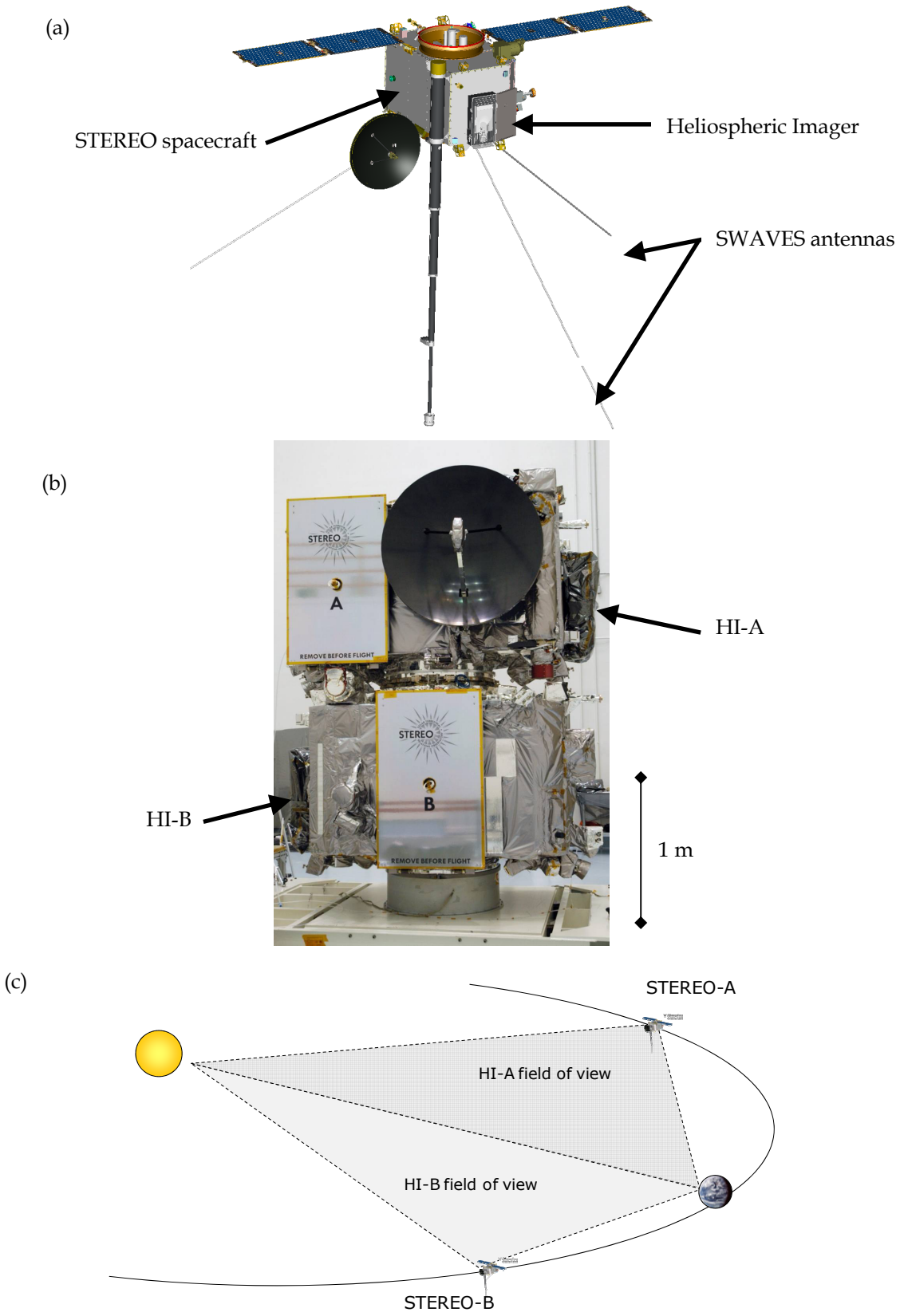

Figure 3-5 : (a) The Heliospheric Imager instrument is mounted on the side of the STEREO spacecraft [17]. The SWAVES antenna is marked, as potential straylight source. (b) The STEREO mission twin spacecrafts [courtesy NASA], each with its HI instrument. (c) The Heliospheric Imager HI-A and HI-B fields of view.

3.2. The HI-1 and HI-2 cameras

The STEREO-HI instrument has two optical systems.

- **The HI-1 camera**. It is positioned with its field of view border at 3.98 arcdeg[9] (~15 R_{Sun}) from the Sun centre (Figure 3-6) and is protected by a front baffle from the solar disk light grazing to the instrument top side, taking advantage of the quasi-collimation of the solar flux.
- **The HI-2 camera**. It is positioned in the instrument with its field of view border at 18.66 arcdeg (~70 R_{Sun}) from the Sun centre (Figure 3-6) and is surrounded by a multi-edge absorptive internal baffle (Figure 3-6) that attenuates reflected light from the bright sources reaching the instrument.

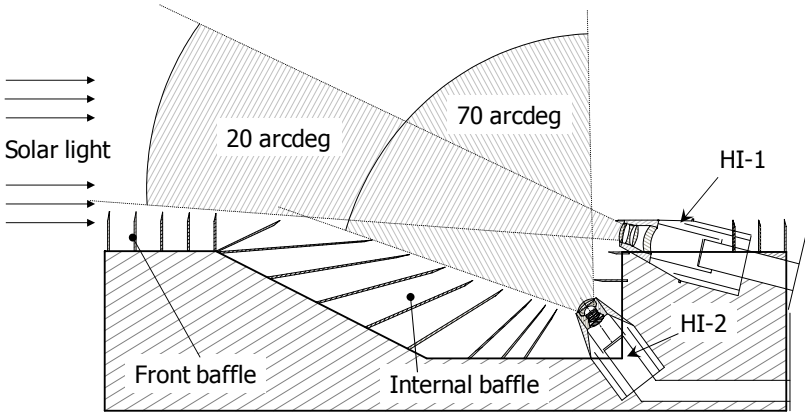

Figure 3-6 : Conceptual design of the STEREO-HI instrument. The two HI-1 and HI-2 camera have respectively 20 and 70 arcdeg FOV, and are protected by a front baffle and an internal baffle. The sun is on the left hand side.

3.2.1. Optical design

The HI-1 camera is a 20 arcdeg refractive optical system with an F number of 4.93 and a 15.9 mm entrance pupil diameter defined by an aperture stop located at the back of the first lens (Figure 3-7 - a). The first lens physical aperture has been limited to 16 mm to minimise its height in the shadow of the front baffle. The detector plane is located at 88.4 mm from the first lens with a 35 arcsec pixel resolution [12].

The HI-2 camera is a 70 arcdeg refractive optical system with an F number of 3.08 and a 7 mm entrance pupil diameter defined by an aperture stop located between the third and fourth lens (Figure 3-7 - b). The first lens physical aperture is 20 mm and its detector plane is located at 46.4 mm from the first lens [12].

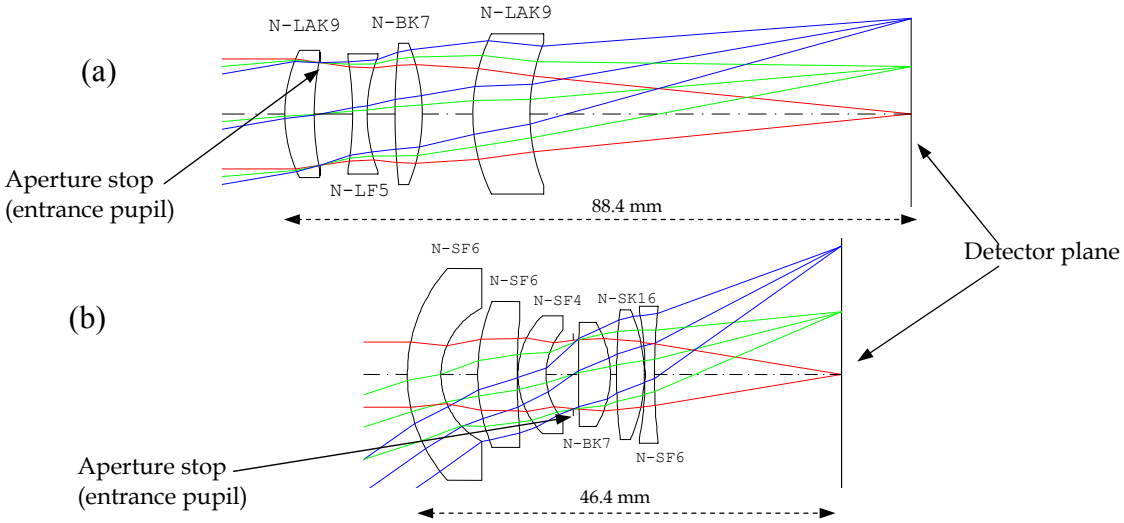

Figure 3-7 : Optical layout of (a) HI-1 and (b) HI-2 lens systems, shown with glass types selected for the various elements [12].

[9] The instrument was design for a 3.65 arcdeg inner angle but an additional 0.33 arcdeg off-point angle was added on the spacecrafts to increase the margin on solar straylight rejection.

Both optical designs are not diffraction limited and optimised to minimise the RMS spot diameter over an assumed operational temperature range of – 20 °C to + 30 °C. Both telescopes are designed to image visible light.

- In HI-1, the 630 – 730 nm spectral selection is achieved with a SiO2 / ZrO2 multilayer bandpass coating applied on first internal optical surfaces [12][20].
- In HI-2, no bandpass coating has been used to have the widest spectral response as possible, i.e. 400 – 1000 nm limited by the CCD detector spectral response together with the absorption by the optical components below 400 nm [12][20].

Table 3-2 summarises the optical design parameters of the two HI-1 and HI-2 optics.

	HI-1	**HI-2**
FOV diameter[10]	20 arcdeg	70 arcdeg
Focal length	78.46 mm	21.67 mm
Optical axis length	88.4 mm	46.4 mm
F number	F/4.93	F/3.08
Entrance pupil diameter	15.9 mm	7.0 mm
Spectral range	630 – 730 nm	400 – 1000 nm
RMS spot size (against off-axis angle)	14.9 µm at 0 arcdeg 16.5 µm at 5 arcdeg 20.2 µm at 10 arcdeg	40.6 µm at 0 arcdeg 46 µm at 5 arcdeg 50 µm at 10 arcdeg
Distortion[11]	< 2%	< 8%

Table 3-2 : HI-1 and HI-2 optical design parameters [20].

3.2.2. Mechanical design

The HI-1 and HI-2 optics are maintained within their respective cameras by a lens barrel made of titanium to limit thermo-elastic deformation (Figure 3-8). The lens barrels are of primary importance for the reduction of the out of field straylight.

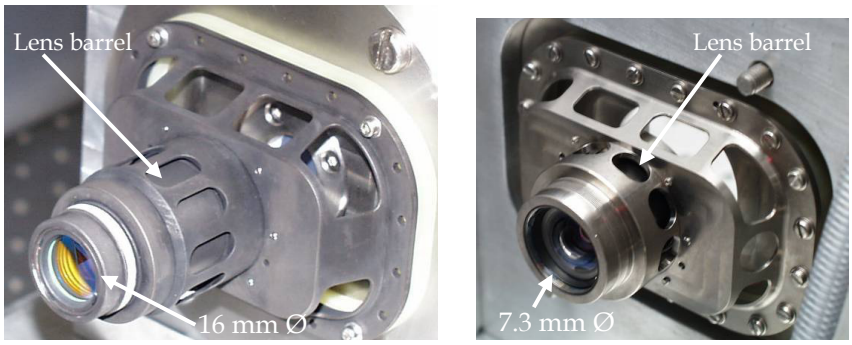

Figure 3-8 : The HI-1 (left) and HI-2 (right) lens barrel are mounted in a housing that provides the mechanical interface with the rest of the camera structure (here mounted on a test interface used for the optical characterization).

The HI detectors are 2048 x 2048 CCD arrays of 13.5 µm pixels [20] located in a Focal Plane Assembly (FPA) that ensure their mechanical stability and thermal link to a passive cooling radiator, via a cold finger (Figure 3-9).

The two lens barrel housings are mechanically connected to their respective FPA (Figure 3-10), which are attached to the instrument structure. The detector cavity also takes part of the overall straylight performance.

[10] The HI-1 and HI-2 optical systems have been optimized for 20 and 70 circular fields of view, and not for the square detector corners (the effective FOV being square).

[11] Defined as the deviation from a linear projection at the edge of the (circular) field of view.

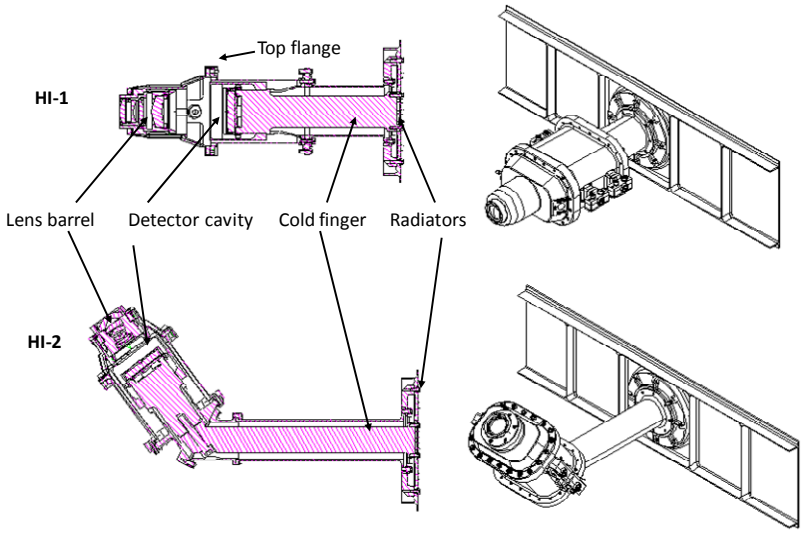

Figure 3-9 : The two HI-1 and HI-2 cameras are composed of a lens barrel, a detector cavity and a passive cooling system (cold finger and radiator). [Courtesy of Naval Research Laboratory]

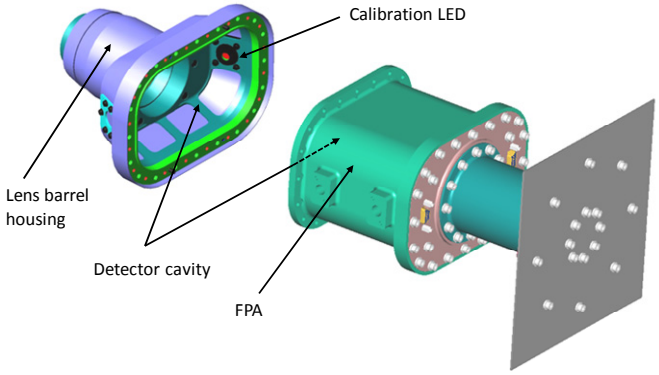

Figure 3-10 : The HI-1 and HI-2 camera lens barrel are mechanically maintained by the FPA that is attached the instrument structure (here the HI-1 camera). A set of calibration LED is also part of the lens barrel housing, within the detector cavity. [Courtesy of University of Birmingham]

3.2.3. Straylight analysis

Located in the shadow of the straylight protective baffles, the optical systems play a significant role in the overall instrument straylight performance. The lens design and the mechanical housing design indeed contribute to the straylight rejection.

A ray-tracing model of the two HI-1 and HI-2 cameras (Figure 3-11) was therefore built to analyse their straylight performance. The models include the lenses, their lens barrel and the detector cavity.

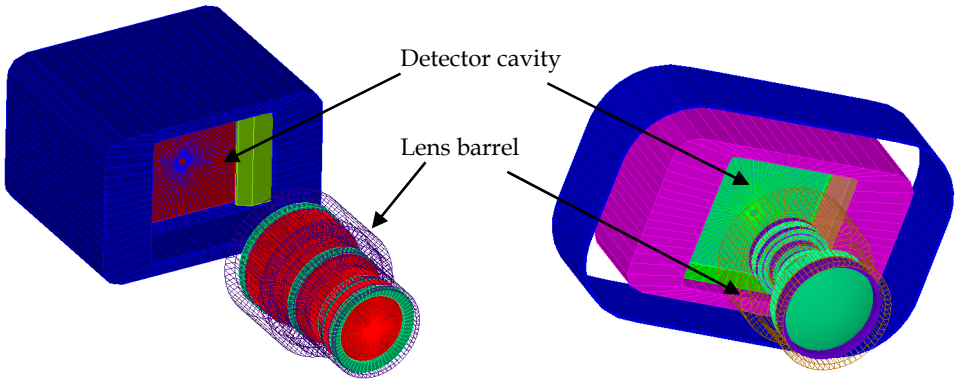

Figure 3-11 : Ray-tracing model of the HI-1 (left) and HI-2 (right) camera (external camera housing is hidden, but use in the ray-tracing model). For both cameras, it comprises the lenses, the lens barrel and detector cavity and the detector surface, with their respective transmission and scattering properties.

The following straylight contributors were considered (Figure 3-12):

- The out-of-field light sources. These sources are not focused on the detector and must be attenuated by the lens barrel to limit the corresponding additional straylight background.
- The in-field light sources. These sources are focused on the detector. When too bright, they can however produce straylight resulting from reflection on detector and consequent multiple reflections onto the optical surfaces and in the detector cavity.

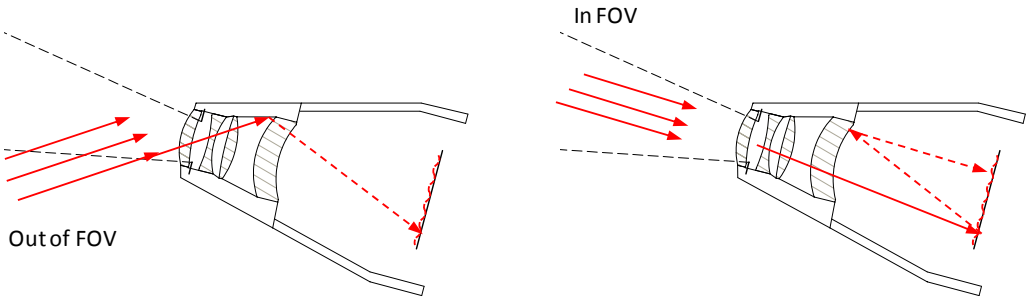

Figure 3-12 : Out-of-field and in-field straylight entering the optical system (shown here on HI-1 layout)

In addition, the diffusion by micro-roughness of optical surfaces and bubbles/inclusions into the optical glass were analysed as potential straylight source for both in-field and out-of-field sources.

Lens barrel rejection (out-of-field straylight)

A first attenuation of the out-of-field light is provided by the aperture stop of the optical system.

- In HI-1, the aperture stop is located on the back of the first lens, as shown in Figure 3-7, to minimize the first lens dimension.
- In HI-2, the aperture stop is located after the third lens, as shown in Figure 3-7 and provides a better attenuation of the out-of FOV straylight sources.

To further reduce reflections and scattering from out-of-field straylight, the inner geometry of the lens barrels was optimised based on the ray-tracing model taking into account envelope constraints due to the camera locations within the instrument. Cavities within the lens barrel (Figure 3-13) were added to act as light traps and internal surfaces of the lens barrels were treated with black coatings to provide additional absorption.

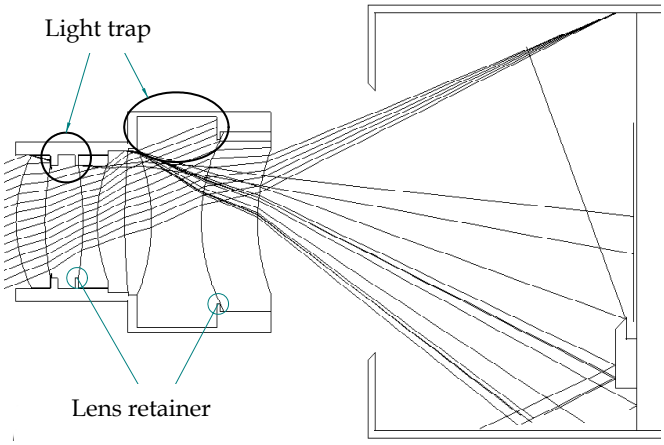

Figure 3-13 : Lens barrels were optimised to trap out-of-field light. Here is an example of ray tracing from a 2 arcdeg direction out of the nominal 20 arcdeg HI-1 FOV, showing the rays that are trapped by the lens barrel light trap located next to the lenses.

The following scattering properties have been considered in the ray-tracing model:

- Diffuse black coating (TIS ~ 8 %) on lens barrel and detector cavity
- Lambertian scattering model for the CCD support and the wire mask (TIS ~ 50 %)

The ray-tracing analysis of the HI-1 and HI-2 lens barrel provides, for each incident angle, the out-of-field light rejection per mm² on the detector plane. The rejection per pixel (Figure 3-14) is then derived using the pixel size (13.5 µm).

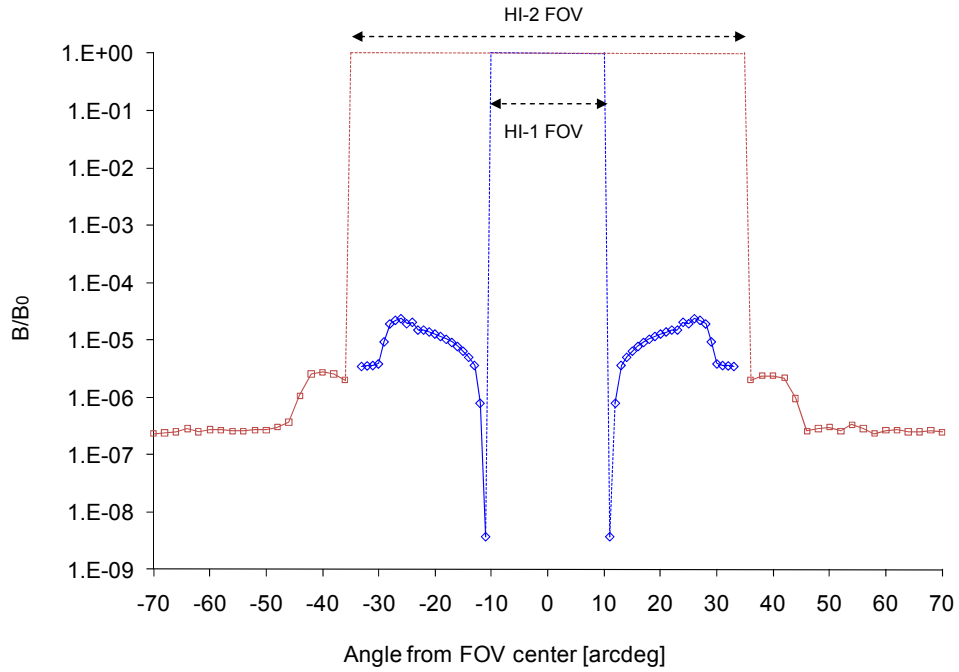

Figure 3-14 : HI-1 (blue) and HI-2 (red) out-of-field B/B_0 rejection at detector pixel level, where B_0 is an input flux entering the optic. The value in the FOV is set to 1 assuming no other effect.

The ray-tracing model also provides the corresponding straylight pattern on the detector. Figure 3-15 shows the pattern on HI-1 detector from out-of-field light source, produced by reflection on the lens barrel retainers (Figure 3-13).

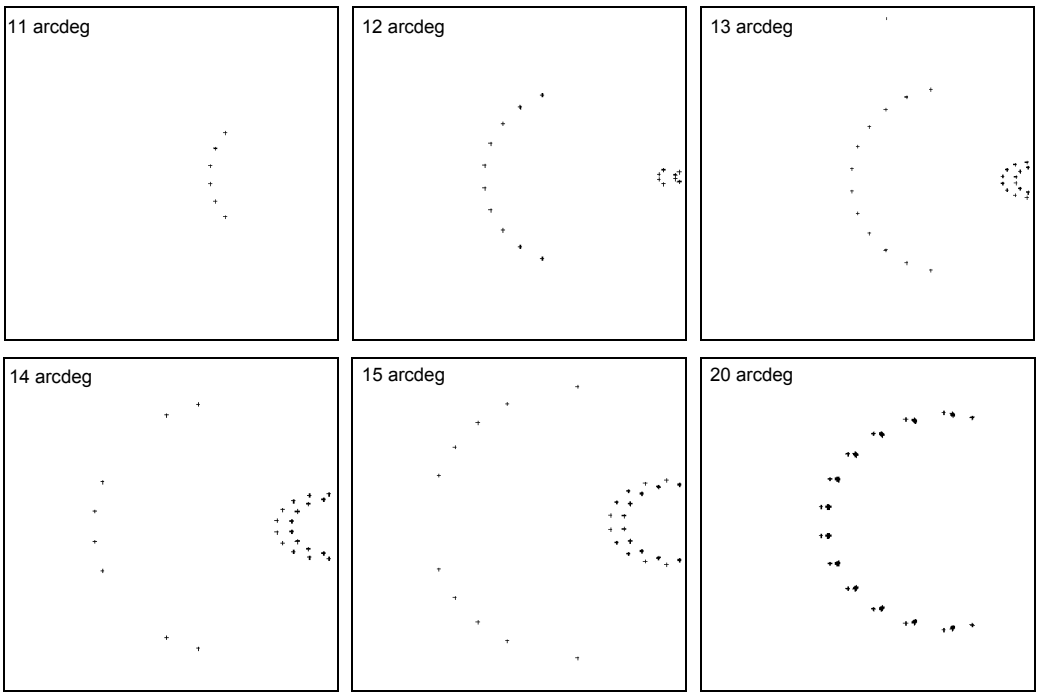

Figure 3-15 : The out of field straylight pattern on the HI-1 detector (here shown for a 11, 12, 13, 14, 15 and 20 arcdeg from the field of view centre) has ring shape that increases with the angle. For 1 arcdeg, a single ring is present on the detector. For angles from 2 to 10 arcdeg, two rings are present. For larger angles the two rings superpose and straylight level per pixel increases.

Ghosts (in-field straylight)

The straylight produced by reflections on the lens surfaces is an out-of-focus pattern (called "ghost") on the detector. One objective of the optical design is to enlarge the ghosts as much as possible on the detector to reduce their impact on the straylight level [14].

- To limit reflection of focused light from the detector surface towards the lenses, and consequently limit the ghosts, the STEREO-HI CCD was thus coated with an anti-reflective (AR) coating optimised for the 450 – 750 nm spectral range.
- As part of ghost reduction, an MgF2 anti-reflective coating was also applied on all the lens surfaces, except the first ones which are exposed to the outer space. The first lenses are SiO2-coated to limit ageing due to solar light and radiation. In the case of HI-2, the effectiveness of the AR coatings is however limited by the large spectral range and the wide range of incidence angles.
- An occulter has also been implemented on the HI-2 detector to limit back reflection of the Earth spot during first months of the orbit, when the Earth is in the HI-2 FOV and the two spacecraft close of the Earth.

One particular ghost in HI-1, is ring pattern similar to Figure 3-15. It is present when a bright source lies within the field of view close of one corner (Figure 3-16), which is unexpected as it should only be imaged on the detector. This is due to the HI optical design, which has been optimized for a 10 arcdeg circular field of view and not for the square detector corners. As shown in Figure 3-17, the size of the ring pattern logically reduces when the light source moves from the corner toward the centre of the field of view.

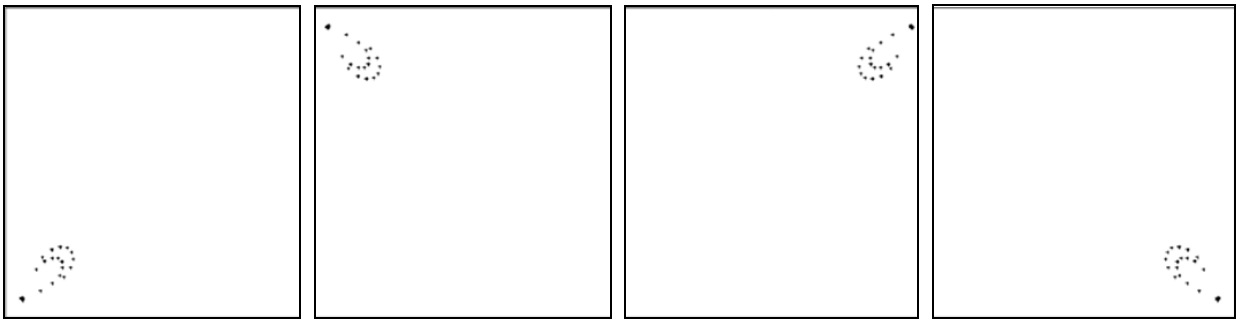

Figure 3-16 : Ray-tracing results for a bright source located in each of the four corners of the HI-1 field of view at 12.7 arcdeg from the field of view centre.

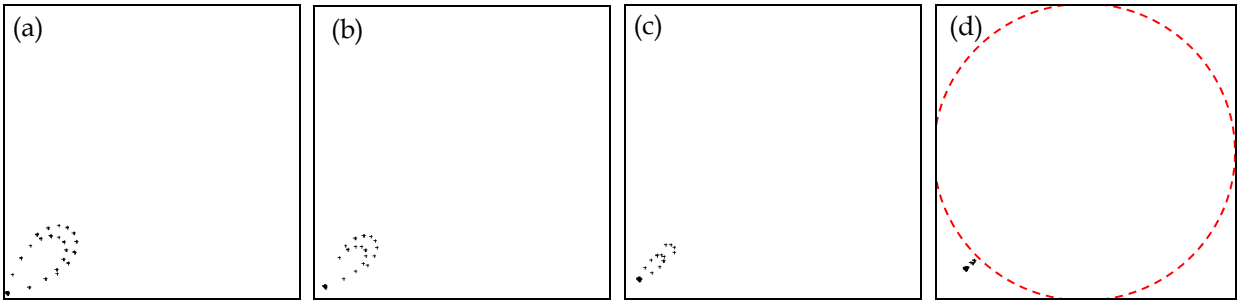

Figure 3-17 : Ray-tracing results for a bright source located in the lower left corner of the HI-1 field of view at 13.4 arcdeg (panel a), 12.7 arcdeg (b), 12 arcdeg (c) and 11.3 arcdeg (d) from the field of view centre. The nominal 10 arcdeg field of view is shown on (d).

Ghosts were computed with the HI-1 and HI-2 ray-tracing model with a 1% AR coating on the CCD and 2% AR coating on all optical surfaces [14]. Figure 3-18 shows the maximum ghosts contribution on HI-1 and HI-2 detectors (i.e. from the brightest ghosts) versus the in-field but also from out-of-field incident angle.

Micro-roughness and bubble diffusion

Incident light onto the HI-1 and HI-2 lens surfaces produces near-field diffusion that produces straylight, similar to wings added to the nominal Point Spread Function (PSF). All optical surfaces were specified

with a 10 Å RMS micro-roughness to attenuate and enlarge these wings, resulting in the maximum straylight level of Figure 3-18 computed with the ray-tracing model of the two cameras for an input beam within the FOV, and is much lower than the ghost contribution to the in-field straylight.

The optical glasses also contain little quantities of bubbles or inclusions. The required level of bubbles/inclusions has been specified to class B1 (according the Schott glass provider nomenclature), corresponding to a total projected surface (with diameter larger than 0.25 mm) between 0.03 and 0.1 mm² per 100 cm³ of glass.

The maximum contribution of bubbles/inclusions onto the CCD was computed with the ray-tracing model of the two cameras (Figure 3-18), and is also much lower than the ghost and lens barrel contributions.

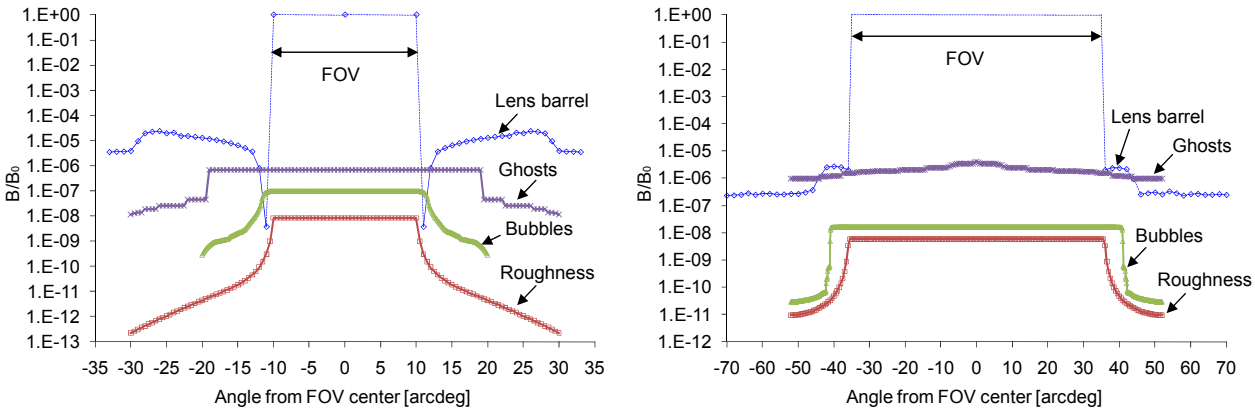

Figure 3-18 : Maximum ghost, micro-roughness and bubbles/inclusions straylight contribution in HI-1 (left) and HI-2 (right), as compared with out-of field rejection by the lens barrel (B/B_0 where B_0 is the input flux entering the optic).

It resulted from that analysis, summarised in Table 3-3, that:

- For out-field light source, the lens barrel diffusion is the major straylight contributor on the detector.
- For in-field light source, the ghost effect is the major straylight contributor on the detector.

	HI-1	**HI-2**
Lens barrel rejection	$2.4\ 10^{-5}$	$2.7\ 10^{-6}$
Ghost level	$7\ 10^{-7}$	$3.4\ 10^{-6}$
Bubbles	$9.7\ 10^{-8}$	$1.6\ 10^{-8}$
Micro-roughness	$8.4\ 10^{-9}$	$5.8\ 10^{-9}$

Table 3-3 : Maximum values of optical system straylight contributors per pixel on the detector (B/B_0 where B_0 is an input flux entering the optic).

3.3. The baffle system

The baffles of the STEREO-HI instrument were designed to attenuate potential out-of-field straylight sources before they enter the optical systems.

To meet the requirement of Table 3-1, the baffles were specified taking into account the HI-1 and HI-2 lens barrel rejection (Table 3-3) and the brightness of the potential sources of straylight in each optical system.

The HI instrument baffle system is composed of:

- A front diffractive baffle, located at front of the instrument. It provides straylight protection from the direct Sun illumination.
- A lateral diffractive baffle, located around the instrument cavity. It provides straylight protection from the solar light scattering by objects located around the instrument.
- An absorptive internal baffle, located in the instrument cavity. It damps the reflections of the sky brightness but also attenuate the light reflected by a boom located behind the instrument.

3.3.1. Straylight sources

The instrument is indeed exposed to a set of straylight sources which affects differently the two HI-1 and HI-2 cameras.

- **Solar flux**

  The major straylight source is the solar brightness (B_0 = MSB). It illuminates the front of the instrument and mostly affects HI-1 due to the vicinity of the Sun direction with its FOV, but also HI-2 that requires an even lower background level.

- **HI-1 flange**

  As shown on Figure 3-6, a diffractive front baffle protects the HI instrument from the direct sunshine. The HI-1 camera flange (Figure 3-9) is however located a few mm above this front baffle top edge. It can thus reflect Sun light towards the instrument baffles, and in particular to the last edge of the front baffle, as shown on Figure 3-19.

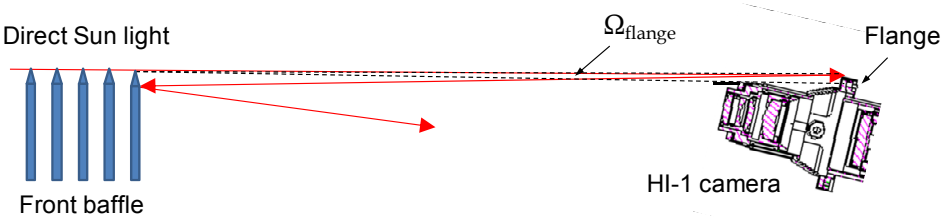

Figure 3-19 : Direct Sun light can be reflected by the HI-1 camera flange, located a few mm above the front baffle edges. It is a potential straylight source, in particular for the last edge of the front baffle. The drawing is not at scale.

From the final instrument design [20], the HI-1 camera housing top flange surface (S_{flange}) effectively directly illuminated by the Sun is ~ 2 mm x 10 mm. The solid angle Ω_{flange} of the flange is computed with equation (3-5) where d_{flange} is the distance from the flange to the baffle.

$$\Omega_{flange} = \frac{S_{flange}}{(d_{flange})^2} = \frac{0.2 \cdot cm^2}{(0.6 \cdot m)^2} = 5.5 \cdot 10^{-5} \qquad \textbf{(3-5)}$$

The resulting brightness on the front baffle last edge (B_{flange}) from the HI-1 flange is obtained by equation (3-6) assuming a 2% TIS black coating on top flange [20].

$$B_{flange} = \Omega_{flange} \cdot BRDF \cdot B_0 = 5.5 \cdot 10^{-5} \cdot 0.02 \cdot B_0 = 1.1 \cdot 10^{-6} \cdot B_0 \qquad \textbf{(3-6)}$$

- **SWAVES antenna**

  One of the three SWAVES antennae, part of the STEREO payload (Figure 3-5 - a), is in the direct solar flux and back-scatter light towards the HI instrument. It is thus a potential important straylight contributor, even if located far (in the anti-Sunward direction), because of its brightness.

The incident brightness from this boom on the HI instrument cavity is computed with equation (3-7) as assuming that the boom re-emits with a 5% TIS [10] and with the solid angle Ω_{boom} (3-8) of the boom as seen from the HI instrument (Figure 3-20).

$$B_{boom} = \Omega_{boom} \cdot BRDF \cdot B_0 = 4.5 \cdot 10^{-4} \cdot 5 \cdot 10^{-2} \cdot B_0 = 2 \cdot 10^{-5} \cdot B_0 \quad \textbf{(3-7)}$$

$$\Omega_{boom} = \frac{S_{boom}}{(d_{boom})^2} = \frac{2m \cdot 5mm}{(4.7 \cdot m)^2} = 9.4 \cdot 10^{-4} \quad \textbf{(3-8)}$$

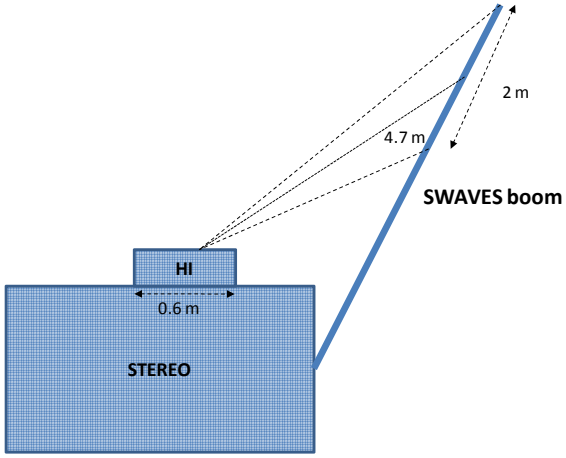

Figure 3-20 : SWAVES boom geometry w.r.t. the HI instrument on STEREO spacecraft

- **Planets**

The Earth (with the moon) illuminates the HI instrument cavity and is also regularly within the HI-1 and HI-2 FOV. It is one of the brightest objects in the scene at the beginning of the mission.

The Earth to Sun relative brightness is computed from their apparent visual magnitude (mv) at 1 AU (mv_{Earth} = -3.87 and mv_{Sun} = -26.7) with equation (3-9).

$$B_{Earth(1AU)} = 2.512^{mv_{Sun} - mv_{Earth}} \cdot B_0 \quad \textbf{(3-9)}$$

The Earth brightness however varies (Figure 3-21) with the S/C angular location (i.e. with the S/C - Sun – Earth angle α) according to the equation (3-10) as an inverse square law of the distance between the Earth and the S/C (3-12), and with the phase coefficient (3-11).

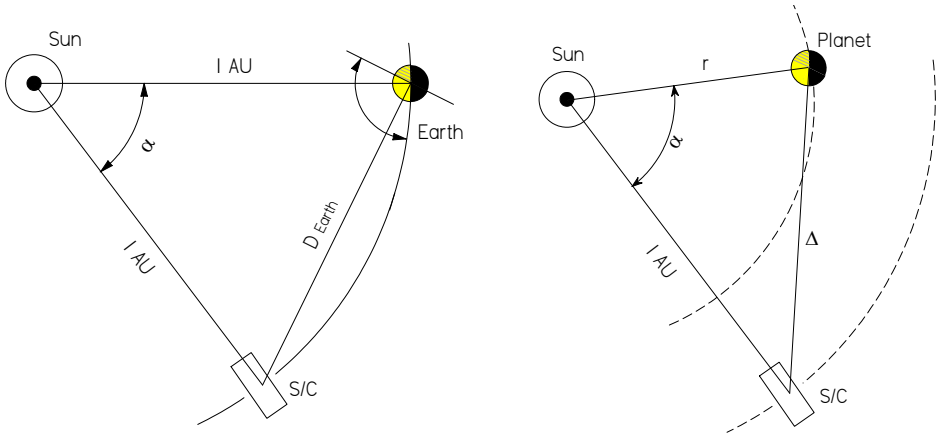

Figure 3-21 : Left: The Earth – Sun – S/C angle is used to define the Earth phase brightness function, assuming the S/C is at 1 AU. Right: The Planet – Sun – S/C angle and the distance between the planet and the Sun are used to obtain the distance between the planet and the S/C

$$B_{Earth} = \frac{1}{\left(D_{Earth}\right)^2} \cdot P_{Earth} \cdot B_{Earth(1AU)} \quad \textbf{(3-10)}$$

$$P_{Earth} = 0.5 \cdot \left(1 + \cos\left(\frac{\pi - \alpha}{2}\right)\right) \quad \textbf{(3-11)}$$

$$D_{Earth} = 2 \cdot \sin\left(\frac{\alpha}{2}\right) \quad \textbf{(3-12)}$$

Other bright planets (Venus, Mercury, and Jupiter) also periodically illuminate the instrument, resulting in both in and out of FOV straylight in the HI-1 and HI-2 cameras. As for the Earth, the planet to Sun relative brightness is computed with equation (3-13) with their visual magnitude at 1 AU, a phase coefficient (assumed to be same than the Earth) and the S/C-planet distance Δ (computed with equation (3-14) according to Figure 3-21) [54].

$$B_{planet} = \frac{1}{\left(\Delta_{planet}\right)^2} \cdot P_{planet} \cdot B_{planet(1 \cdot AU)} = \frac{1}{\left(\Delta_{planet}\right)^2} \cdot P_{planet} \cdot 2.512^{mv_{Sun} - mv_{planet}} \cdot B_0 \quad \textbf{(3-13)}$$

$$\Delta = \sqrt{\left(r \cdot \sin\alpha\right)^2 + \left[(1 - r) + r \cdot \left(1 - \cos(\alpha)\right)\right]^2} = \sqrt{r^2 - 2r \cdot \cos(\alpha) + 1} \quad \textbf{(3-14)}$$

The resulting brightness variation with the S/C – Sun – Planet angle is shown on Figure 3-22, for the Earth and Venus (mv_{Venus} = -4.89). The maximum brightness of the Earth is ~ 10^{-6} B_0 and of Venus ~5 10^{-9} B_0, where B_0 is the MSB.

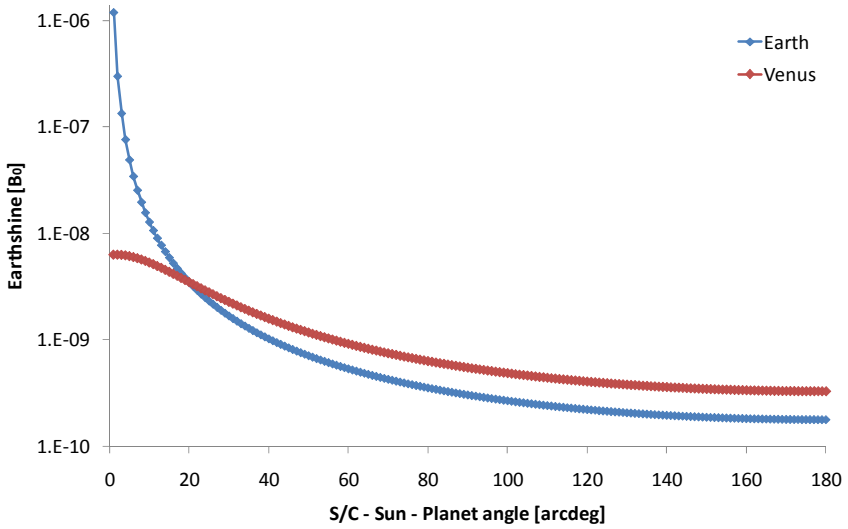

Figure 3-22 : Earth and Venus brightness (in B_0 unit) as a function of the S/C – Sun – Planet angle.

- **Stars**

Bright stars also regularly illuminate the instrument, resulting in both in and out of FOV straylight in the HI-1 and HI-2 cameras. Assuming solar type stars, their corresponding brightness can be computed from their apparent visual magnitude according to equation (3-15).

$$B_{Star} = 2.512^{mv_{Sun} - mv_{Star}} \cdot B_0 \quad \textbf{(3-15)}$$

For the brightest stars (i.e. mv_{Sirius}=-1.47) [70], it corresponds to a brightness ~ 8 10^{-11} B_0.

- **Low Gain Antenna and HI door**

A Low Gain Antenna (LGA) [17] and the HI instrument door mechanism [20] are located close of the HI instrument cavity and can potentially scatter the Sun brightness (Figure 3-23).

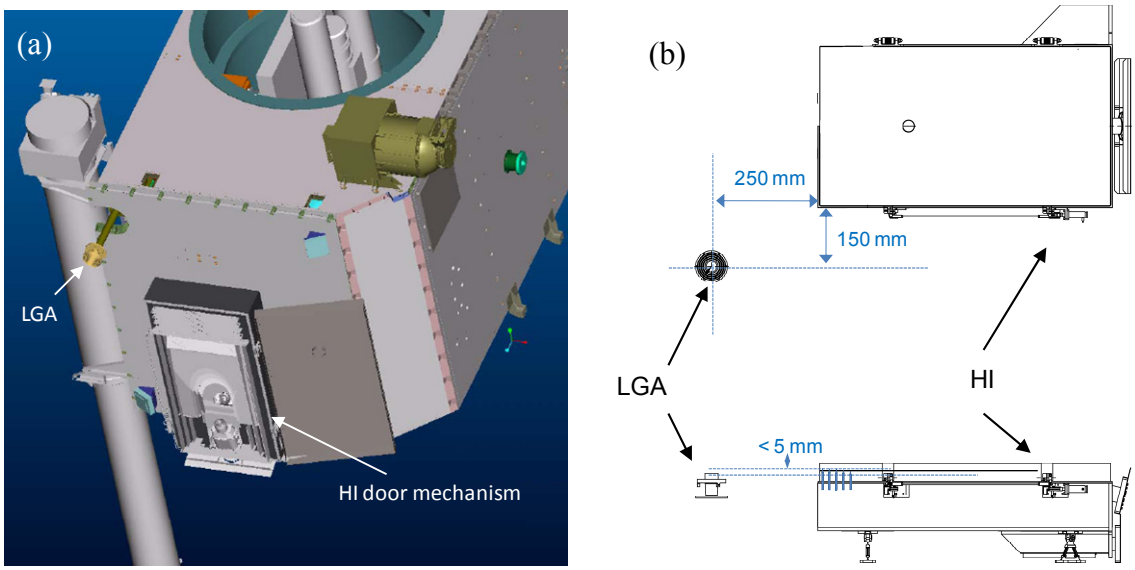

Figure 3-23 : HI door mechanism and LGA (a). The LGA and the door mechanisms are located a few mm below the front baffle edges (b). [Courtesy of Naval Research Laboratory]

As for the SWAVES boom, their brightness can be computed with equation (3-16), assuming the door mechanism and the LGA re-emit over 2 π sr, and have a similar solid angle given by (3-17).

$$B_{LGA} = \frac{\Omega_{LGA}}{2\cdot\pi}\cdot B_0 = \frac{0.017}{2\cdot\pi}\cdot B_0 = 2.7\cdot 10^{-3}\cdot B_0 \qquad \textbf{(3-16)}$$

$$\Omega_{LGA} = \frac{S_{LGA}}{\left(d_{LGA}\right)^2} = \frac{15\text{cm}^2}{(0.3\cdot\text{m})^2} = 0.017 \qquad \textbf{(3-17)}$$

- **Zodiacal light**

  The zodiacal light (F-corona) produces an additional constant background [38].

  The corresponding brightness has been approximated by using the total integrated apparent magnitude of the night sky as seen from Earth ($mv_{zodiacal}$ = -6.5) according to equation (3-22).

$$B_{Zodical} = 2.512^{mv_{Sun}-mv_{Zodical}}\cdot B_0 = 8.3\cdot 10^{-9} B_0 \qquad \textbf{(3-18)}$$

The relative brightness of the straylight contributors is summarised in Table 3-4.

Source	Brightness [B/B$_0$]
Sun	1
LGA and door	3 10^{-3}
SWAVES antenna	2 10^{-5}
Earth	10^{-6} to 10^{-9}
HI-1 flange	10^{-6}
Zodiacal light	10^{-8}
Planets	10^{-8} to 10^{-9}
Stars	8 10^{-11}

Table 3-4 : Straylight source relative brightness B/B$_0$ unit (where B$_0$ is the MSB).

3.3.2. The front baffle

Baffle requirement

The front baffle protects the two HI-1 and HI-2 optical systems from direct solar light. The front baffle requirement R_{baffle} is summarised in Table 3-5 for HI-1 and HI-2. It is obtained with equation (3-19), where B_{source} is the straylight source brightness (= 1 as the source is the Sun) and R_{optic} is the out-of-field lens barrel rejection (from Table 3-3).

$$R_{baffle} = \frac{R_{SL}}{B_{source} \cdot R_{optic}} \qquad \textbf{(3-19)}$$

	Straylight Requirement	Lens barrel rejection	Source brightness	Required rejection at entrance aperture
HI-1	$\leq 3\ 10^{-13}$	$\leq 2.4\ 10^{-5}$	1 (Sun)	$< 10^{-8}$
HI-2	$\leq 10^{-14}$	$\leq 2.7\ 10^{-6}$		$< 10^{-9}$

Table 3-5 : Straylight rejection requirement of the front baffle (in B/B_0, where B_0 is the MSB).

Baffle concept

This baffle is the key component of the instrument, providing the first and major straylight protection.

To achieve a 10^{-9} rejection, a 5 equidistant edges diffractive system has been considered for the front baffle. Its concept is shown in Figure 3-24, adapted from Figure 2-10, with HI-1 and HI-2 camera located in the shadow of the last edge. The instrument allowable dimensions have limited the distance between the edges and the camera entrance apertures.

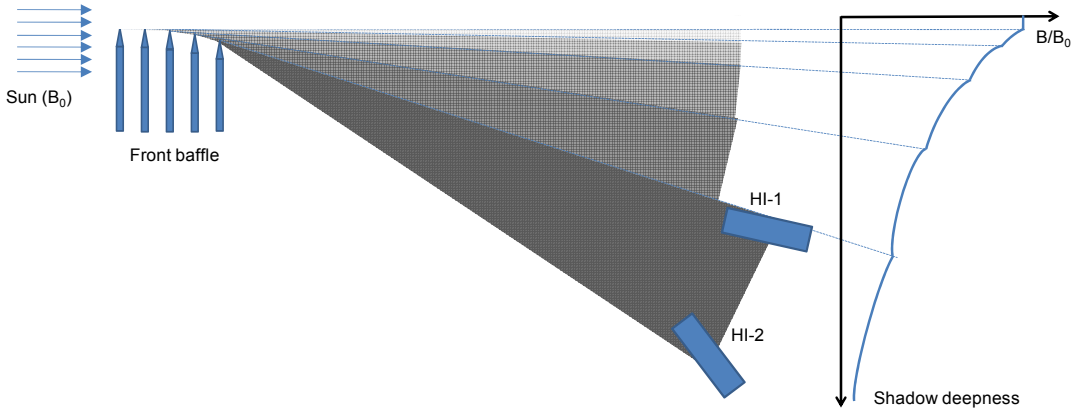

Figure 3-24 : Concept of the diffractive cascade knife-edge system of the STEREO-HI front baffle, showing the typical locations of the entrance apertures of the HI-1 and HI-2 optics in the shadow of the last edge, and the characteristic form of the expected intensity profile versus the angular offset. The drawing is not at scale.

The diffraction intensity profile is calculated using the central wavelength of the instrument (i.e. 700 nm) with relations (2-15). The front baffle edge heights and separation were defined from the diffraction angle θ_d as defined in Figure 3-25 and computed using the relation (3-20) adapted from relation (2-9) with:

- OA is the optical axis of the HI-1 camera measured from the Sun centre (i.e. 13.65 arcdeg)
- Ap is the HI-1 entrance aperture diameter (i.e. 16 mm)
- D is the distance between the 5th edge and the HI-1 entrance aperture (i.e. 436 mm, obtained after optimisation of the inter-edge distance, as described below)
- FOV_{border} is the border of the FOV (i.e. 3.65 arcdeg)
- R_{sun} is the solar radius of 0.267 arcdeg (as seen from 1 AU)[12]

[12] The Sun limb is the upper ray to be occulted and is thus the light source direction. The Sun radius is thus removed from the angle computed w.r.t. to the Sun center.

$$\theta_d = \text{atan}\left[\frac{(D - Ap\cdot\sin(OA))\cdot\tan\left(FOV_{border}\right) - 2\cdot Ap\cdot\cos(OA)}{D + Ap\cdot\sin(OA)}\right] - Rsun = 1.322\text{arcdeg} \quad \textbf{(3-20)}$$

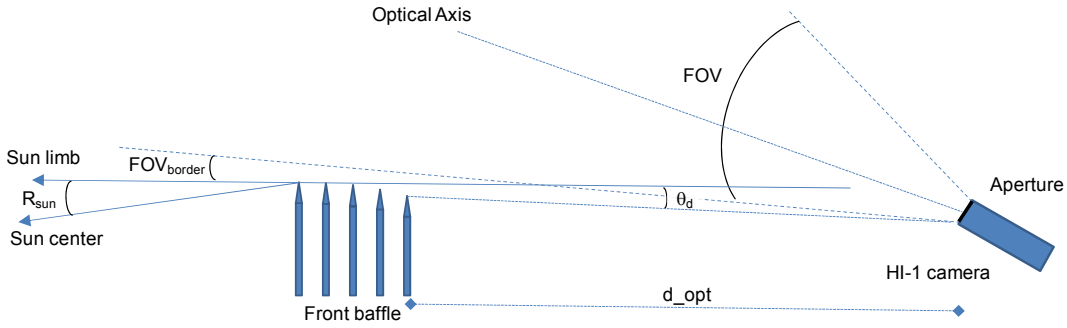

Figure 3-25 : Diffraction angle definition in the STEREO-HI instrument configuration.

As compared with the mock-up used to validate the multi-edge diffraction (Figure 2-33), the first edge is not tilted as direct reflected beam is reflected toward space and there is therefore no need to trap it locally.

The front baffle edges are painted with a black diffuse paint (Chemglaze Z307) to reduce the impact of potential unwanted reflections, and in particular reflection from the HI-1 camera top flange (Figure 3-19).

Baffle performance

Figure 3-26 shows the computed diffraction profile of the front baffle, plotted against distance below the line going from the Sun disk limb to the 1st edge tip (Figure 3-25) for a 700 nm incident wavelength (central to the HI-1 bandpass). The contributions of the successive edges to the overall rejection curve are clearly visible. The B/B_0 rejection at the HI-1 entrance aperture[13] and the H-2 entrance aperture[14] varies respectively from $2\ 10^{-11}$ to $5\ 10^{-12}$ and $5\ 10^{-13}$ to $3\ 10^{-13}$.

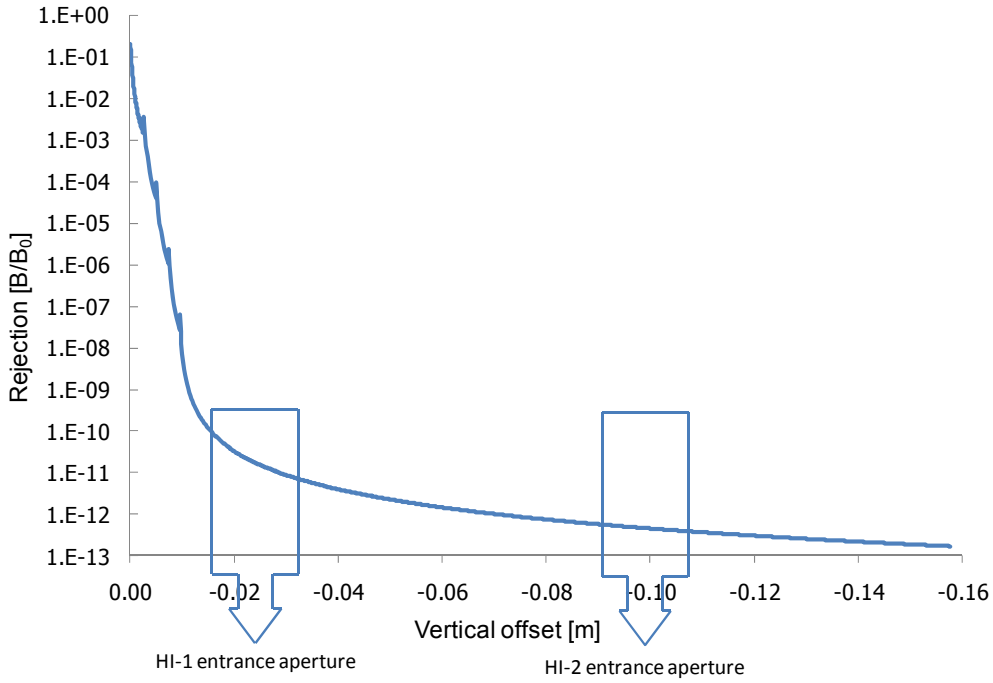

Figure 3-26 : The calculated relative rejection of the STEREO-HI front baffles as a function of distance below an horizontal shadow line going from the Sun disk limb and the 1st front edge tip. The rejection is computed for a 700 nm wavelength. The locations of the entrance apertures of HI-1 and HI-2 cameras w.r.t. the 1st edge are indicated.

[13] Located between 14 and 31 mm in the shadow of the front baffle
[14] Located between 90 and 105 mm in the shadow of the front baffle

Figure 3-28 is equivalent to Figure 3-26 with shadow deepness expressed in angle w.r.t. the sum limb direction around the 5th baffle edge (Figure 3-27).

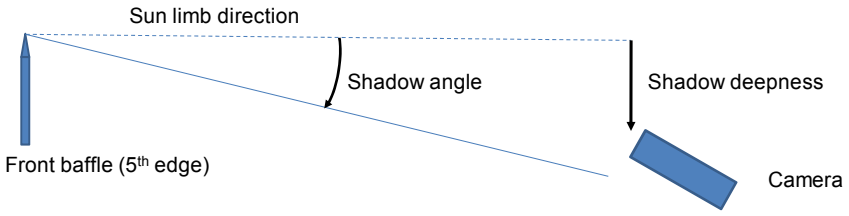

Figure 3-27 : The shadow angle is defined from the front baffle 5th edge and counted from the Sun limb direction.

The HI-1 and HI-2 entrance apertures are located between respectively 1.8 and 3.6 arcdeg, and between 11.6 and 13.5 arcdeg (Figure 3-29). These ranges correspond to the angles from which the front baffle diffracted rays enter the two cameras. By design, these diffracted rays are out of their fields of view, i.e. 0.05 to 1.85 arcdeg for HI-1 and 4.85 to 6.75 arcdeg for HI-2 out of their FOV border (at 3.65 and 18.35 arcdeg respectively).

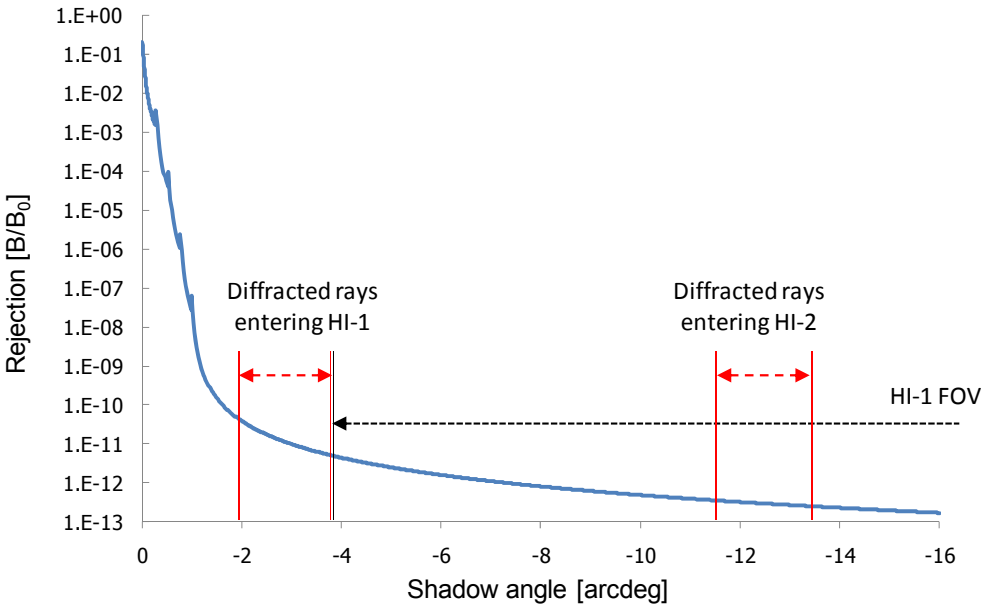

Figure 3-28 : Front baffles relative rejection as a function of shadow angle from the Sun disk limb direction. The angular location of the entrance apertures of HI-1 and HI-2 cameras are indicated, as compared with the HI-1 FOV.

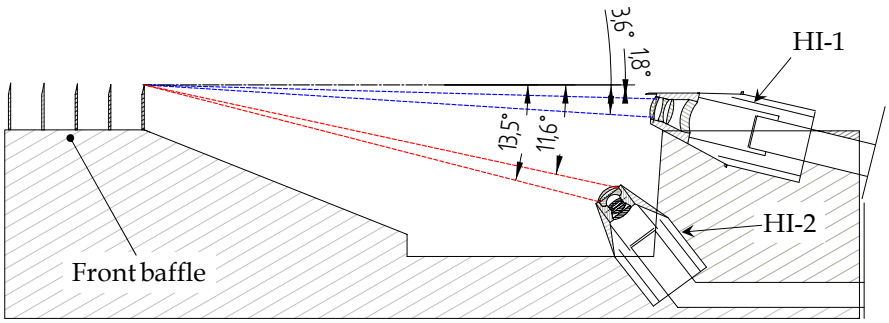

Figure 3-29 : Angles from front baffle last edge to HI-1 and HI-2 respective entrance aperture.

The front baffle rejection is then obtained by integration of the rejection over the angular range of the entrance aperture, as summarised in Table 3-6. It is some orders of magnitude below the required rejection level, providing margin on the straylight at pixel level, which depends on the lens barrel rejection.

	Required baffle rejection	Integrated baffle rejection
HI-1	$< 10^{-8}$	$5.3\ 10^{-11}$
HI-2	$< 10^{-9}$	$2.3\ 10^{-12}$

Table 3-6 : Integrated front baffle rejection as compared with required rejection.

Baffle optimisation

The front baffle performance results from an optimisation of the distance between the edges (d) to minimise the integrated rejection over the HI-1 entrance aperture. The distance (D_{tot}) between the first edge and the optical system entrance aperture (3-21) was kept fixed, as the instrument envelope cannot be increased.

$$D_{tot} = D + 4d \qquad \textbf{(3-21)}$$

The optimum inter-distance of the front baffle is d = 28.5 mm (Figure 3-30) with a corresponding distance D between last edge and entrance pupil of 436 mm, the diffraction angle (3-20) and the edge heights (h) of Table 3-7.

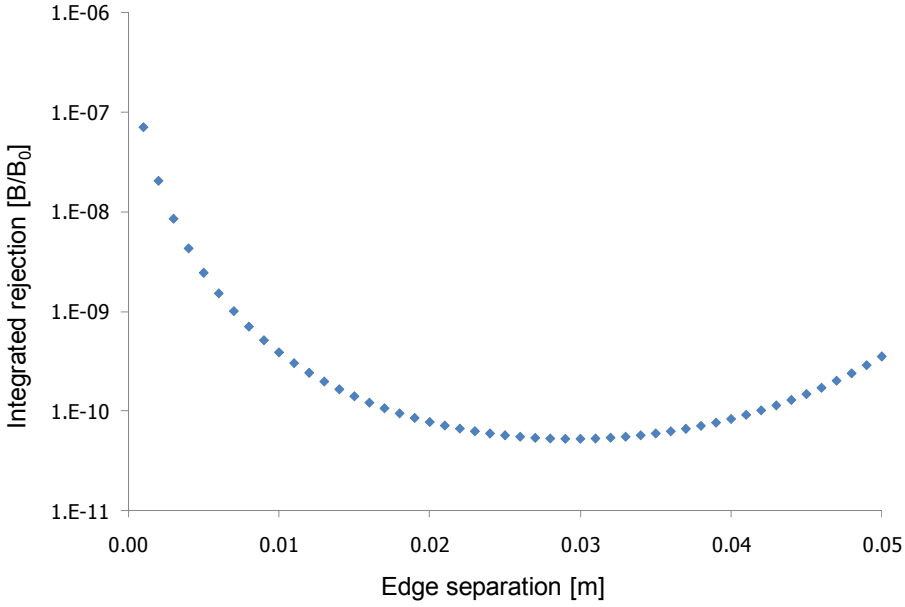

Figure 3-30 : Integrated front baffle rejection over the HI-1 aperture versus the edge separation (for 5 equidistant edges).

The STEREO S/C pointing to the Sun centre, the edge height (H) in Sun centred axis are obtained from the relative height h (in Sun limb axis) using equation (3-22), where R_{Sun} = 16 arcmin and d = 28.5 mm.

$$H = \frac{h + d \cdot \tan(Rsun)}{\cos(Rsun)} \qquad \textbf{(3-22)}$$

The heights H are counted w.r.t. a line passing from the first edge tip toward the Sun centre, as shown on Figure 3-31.

The edge heights (Hv) in Sun centred axis as implemented on the HI instrument (Table 3-7) are obtained from the relative heights H using equation (3-23) where Hv_0 = 0 mm is the first edge reference height.

$$Hv_N = \sum_{i=0}^{N-1} H_i \qquad \textbf{(3-23)}$$

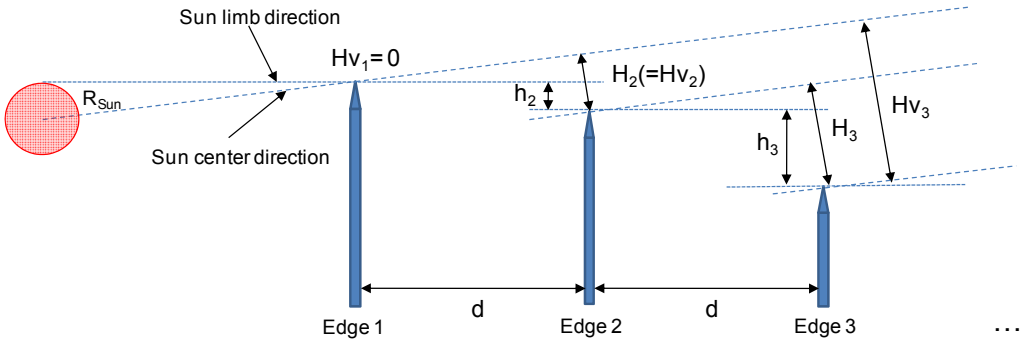

Figure 3-31 : The relative height of the baffle edges expressed w.r.t. the Sun center or limb direction.

Edge #	Relative height (h) in Sun limb axis	Relative height (H) in Sun centre axis	Height (Hv) w.r.t first edge tip in Sun centre axis
1	-	-	0
2	0.132	0.264	0.264
3	0.263	0.396	0.66
4	0.395	0.527	1.187
5	0.526	0.659	1.846

Table 3-7 : STEREO-HI front baffle edge relative and absolute heights (in mm).

Dependence with wavelength

The front baffle performance has been designed and optimised for the central wavelength of the HI-1 and HI-2 bandpass, i.e. at 700 nm. The rejection however varies with wavelength, as shown on Figure 3-32. The rejection varies from 3.4 10^{-11} to 6.3 10^{-11} in the HI-1 spectral range (630 - 730 nm), as compared with a rejection of 5.3 10^{-11} at 700 nm), and from 2.1 10^{-13} to 1.0 10^{-11} in the HI-2 spectral range (400 - 1000 nm), as compared with a rejection of 2.3 10^{-12} at 700 nm. For HI-1, the variation is not large and the central wavelength computation is representative of the rejection in its bandpass. For HI-2 the rejection however varies by a factor 10^3 over the bandpass and the rejection at 700 nm is two orders of magnitude better than the rejection at 1000 nm. The worst-case rejection value over the bandpass shall therefore be considered, and as shown on Table 3-8 it remains below the requirement for that camera.

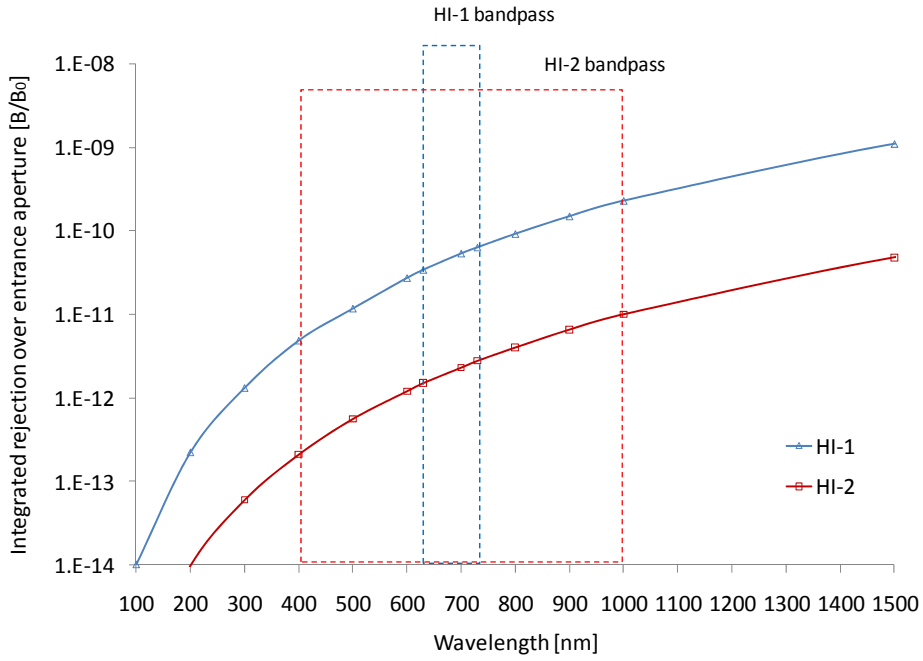

Figure 3-32 : Integrated Front baffle rejection versus incident wavelength, for baffle geometry optimised at 700 nm. The HI-1 and HI-2 bandpass is shown.

	Required baffle rejection	Integrated baffle rejection
HI-1	$< 10^{-8}$	$6.3\ 10^{-11}$
HI-2	$< 10^{-9}$	$1.0\ 10^{-11}$

Table 3-8 : Integrated front baffle rejection computed at respectively 730 nm for HI-1 and 1000 nm for HI-2, as compared with required rejection.

The effective straylight level on the detector front the front baffle is indeed obtained with equation (3-24), where R_{baffle} is the baffle rejection, R_{optic} is the lens barrel rejection (from Table 3-3) and B_{source} is the MSB.

$$SL_{front} = R_{baffle} \cdot R_{optic} \cdot B_{source} \quad \textbf{(3-24)}$$

The comparison of the straylight level on detector (i.e. Sun rejection) with the requirement is given in Table 3-9, with the associated front baffle and lens barrel contributors. The straylight is below the requirements, providing margin for the straylight performance.

	Straylight requirement	Front baffle rejection	Lens barrel rejection	Source brightness	Straylight on detector
HI-1	$\leq 3\ 10^{-13}$	$6.3\ 10^{-11}$	$2.4\ 10^{-5}$	1	$1.5\ 10^{-15}$
HI-2	$\leq 10^{-14}$	$1.0\ 10^{-11}$	$2.7\ 10^{-6}$		$2.7\ 10^{-17}$

Table 3-9 : Straylight level (in B/B_0) from the front baffle on HI-1 and HI-2 detector, as compared with the requirement and with the contributors (in B/B_0, where B_0 is the MSB).

3.3.3. The lateral baffle

Requirement

The lateral baffle protects the two HI-1 and HI-2 optical systems from LGA and HI door mechanism brightness. Their top surface is indeed located only a few mm below the horizontal plane defined by the first edge of the front baffle and the Sun limb as shown on Figure 3-23.

The baffle requirement is summarised in Table 3-10 for HI-1 and HI-2. It is obtained with equation (3-19), where B_{source} is the straylight source brightness (from Table 3-4) and R_{optic} is the out-of-field lens barrel rejection (from Table 3-3).

	Straylight Requirement	Lens barrel rejection	Source brightness	Required rejection at entrance aperture
HI-1	$\leq 3\ 10^{-13}$	$\leq 2.4\ 10^{-5}$	3.10^{-3} (LGA)	$< 4\ 10^{-6}$
HI-2	$\leq 10^{-14}$	$\leq 2.7\ 10^{-6}$		$< 1.2\ 10^{-6}$

Table 3-10 : Straylight rejection requirement of the lateral baffle (in B/B_0 where B_0 is the MSB).

Baffle concept

The lateral baffle is based on the same cascading diffraction principle than the front baffle. However, because of instrument envelope constraints, the lateral baffle is limited to two edges with separation and heights optimised to meet the rejection requirement of Table 3-10.

As shown on Figure 3-33 and Figure 3-34, the lateral baffle is continued on the rear side of the instrument to provide a continuous protection around the instrument cavity from potential unexpected spacecraft payload reflections in the proximity of the instrument.

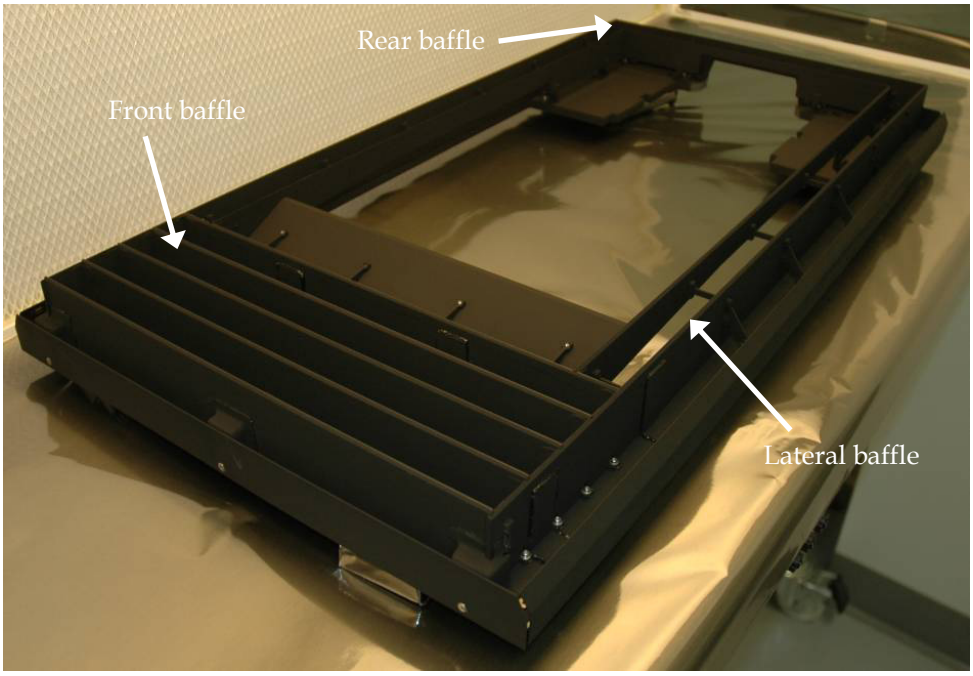

Figure 3-33 : The HI-A front and lateral baffles, before integration on the HI-A structure at the University of Birmingham. The edges are covered with black diffusive paint to reduce the impact of potential unwanted reflections [Courtesy of University of Birmingham].

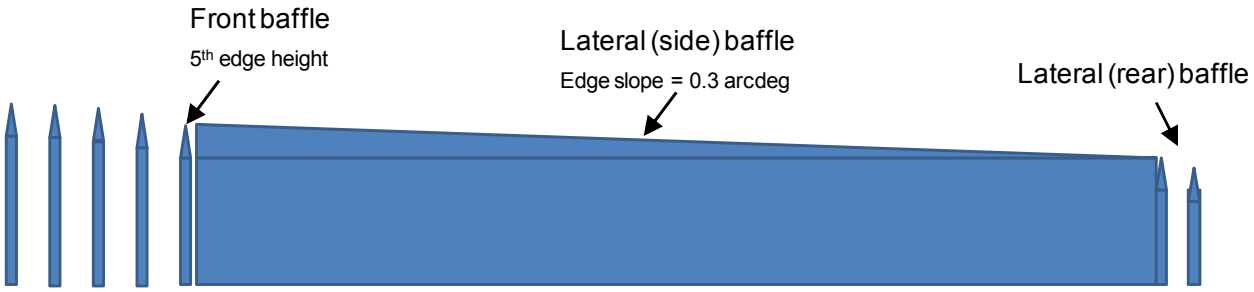

Figure 3-34 : The HI lateral baffle is composed of a two-edge side and two-edge rear parts.

The lateral baffle is located below the 5th edge of the front baffle to ensure it is in its shadow (Figure 3-34). The height of its first (external) edge starts at the 5th front baffle edge and decreases with a 0.3 arcdeg angle toward the backside of the instrument to ensure the rear part of the lateral baffle does not scatter back the Sun (0.267 arcdeg diameter) brightness toward the instrument cavity.

As for the front baffle, the lateral edges are covered with a black diffuse paint (Chemglaze Z307) to reduce the impact of potential unwanted reflections.

Baffle performance

The optimum rejection curve of Figure 3-35 has been obtained for the edge heights of Table 3-11, defined similarly than for the font baffle (Figure 3-31).

Edge #	Relative height (h) in Sun limb axis	Relative height (H) in Sun centre axis	Height (Hv) w.r.t front baffle first edge tip in Sun centre axis	
			Side	Rear
1	0	0	1.846	5.066
2	0.336	0.264	2.182	5.258

Table 3-11 : STEREO-HI lateral baffle edges relative and absolute heights (in mm).

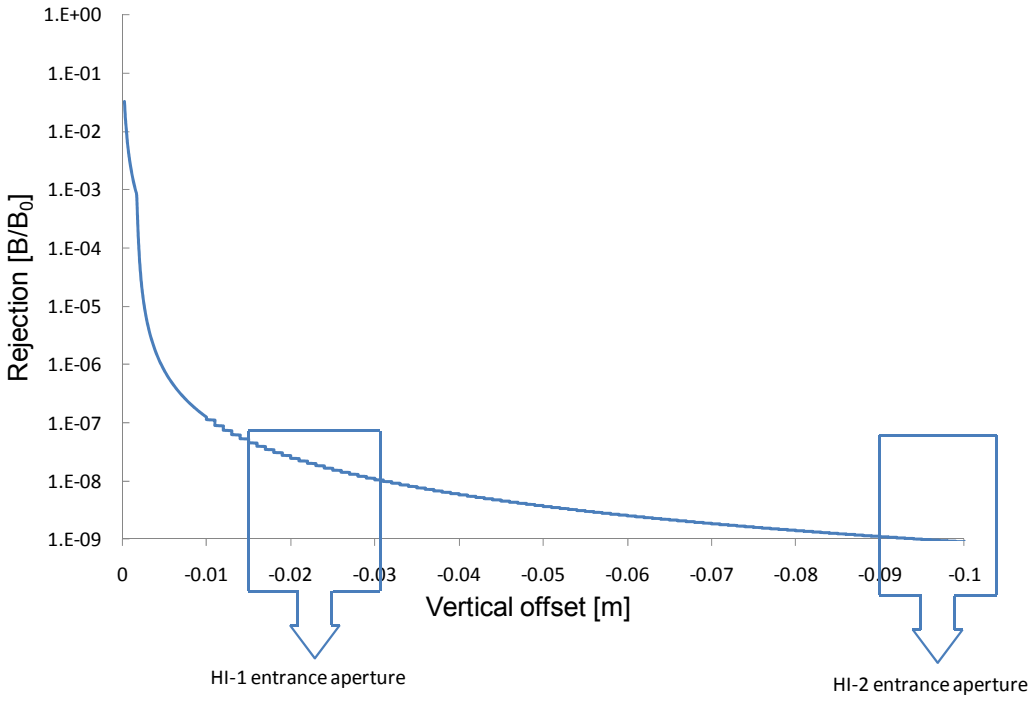

Figure 3-35 : Computed rejection of the lateral baffles as a function of distance below an horizontal shadow line going from the Sun disk limb and the 1st front edge tip.

The lateral baffle rejection is then obtained by integration of the rejection over the angular range of the HI-1 and HI-2 entrance apertures, as summarised in Table 3-12.

	Required baffle rejection	Integrated baffle rejection
HI-1	< 4 10^{-6}	8 10^{-8}
HI-2	< 1.2 10^{-6}	3.6 10^{-9}

Table 3-12 : Integrated lateral baffle rejection as compared with required rejection.

The effective straylight level on the detector front the lateral baffle is obtained with equation (3-24), as for the front baffle. The comparison with the requirement is given in Table 3-13, with the associated baffle and lens barrel contributors. The effective straylight is below the requirements, providing margin for the straylight performance of this baffle.

	Straylight requirement	Lateral baffle rejection	Lens barrel rejection	Source brightness	Straylight on detector
HI-1	≤ 3 10^{-13}	2.9 10^{-7}	2.4 10^{-5}	3 10^{-3}	6 10^{-15}
HI-2	≤ 10^{-14}	3.6 10^{-9}	2.7 10^{-6}		3 10^{-17}

Table 3-13 : Straylight level (in B/B_0) from the lateral baffle on HI-1 and HI-2 detector, as compared with the requirement and with the contributors (also expressed in B/B_0 where B_0 is the MSB).

3.3.4. The internal baffle

Requirement

The internal baffle protects the two HI-1 and HI-2 optical systems from straylight that could be reflected by the instrument cavity. Figure 3-36 shows the potential straylight sources with their relative brightness in a pitch – roll angular map (pitch and roll being defined in Figure 3-37)[15]. This map is derived from Table 3-4 and from upper value of Figure 3-28 for the diffracted Sun source.

[15] Assuming each source is a parallel beam illuminating the HI instrument cavity.

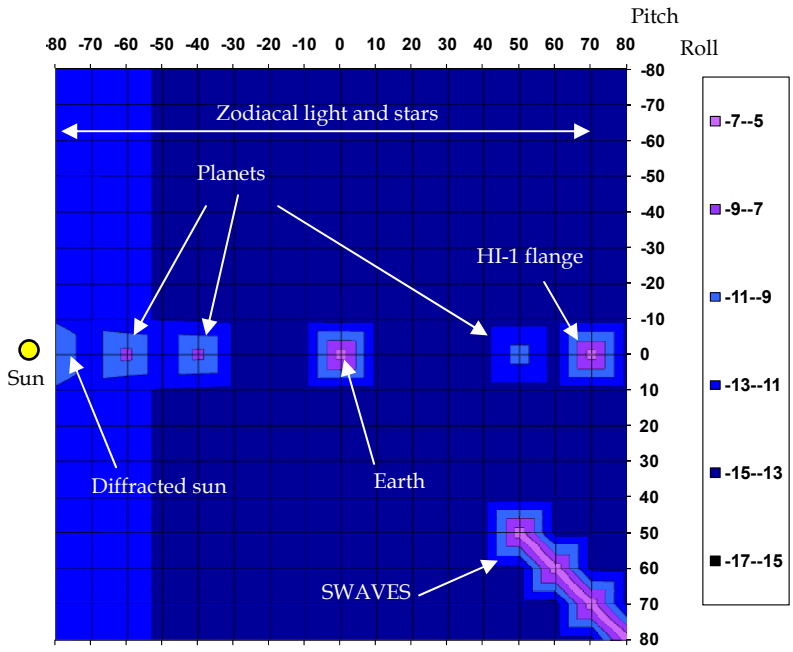

Figure 3-36 : Pitch-roll angular map of straylight sources with their relative B/B_0 brightness (in log scale), where B_0 is the MSB, and approximate angular size. The Sun direction is at a -90 arcdeg pitch angle.

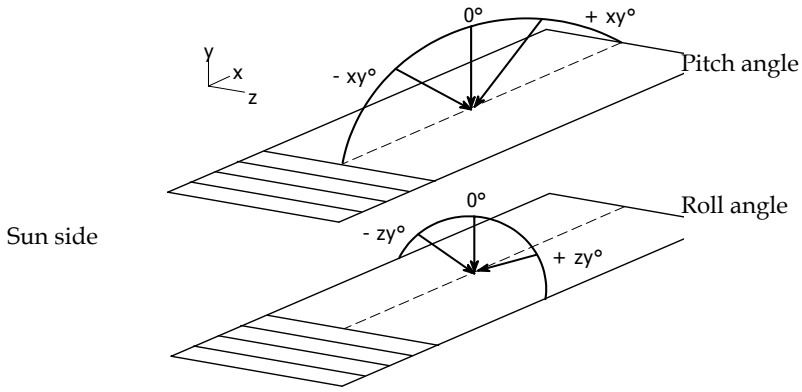

Figure 3-37 : Definition of the pitch and roll angles of the w.r.t. the HI instrument axis.

The internal baffle requirement is summarised in Table 3-14. It is obtained with equation (3-19), where B_{source} is the maximum straylight source brightness from Figure 3-36 (i.e. SWAVES boom) and R_{optic} is the out-of-field lens barrel rejection (from Table 3-3).

	Straylight Requirement	Lens barrel rejection	Maximum source brightness	Required rejection at entrance aperture
HI-1	$\leq 3\ 10^{-13}$	$\leq 2.4\ 10^{-5}$	$2\ 10^{-5}$ (SWAVES)	$< 6\ 10^{-4}$
HI-2	$\leq 10^{-14}$	$\leq 2.7\ 10^{-6}$		$< 1.8\ 10^{-4}$

Table 3-14 : Straylight rejection requirement of the internal baffles (in B/B_0 where B_0 is the MSB).

Baffle concept

On the contrary of the front and lateral baffles, the internal baffle is based on an absorbing multi-vane geometry that takes advantage of the diffusive black paint scattering properties that covers its surface (Chemglaze Z307). The baffle thus attenuates the straylight by absorption and diffusion and not by diffraction.

The baffle has been optimised to take into account the angular size and brightness of the straylight sources (Figure 3-36) and is composed of the following elements.

- **A small vane on top of the HI-1 camera (edge #1)**.

  It provides a protection from direct illumination of the HI-1 entrance aperture by the bright objects facing the instrument, and in particular the Earth. Figure 3-38 shows the HI-1 camera and its small vane. The vane has a 10 arcdeg angle to catch light source of pitch angle from -10 arcdeg.

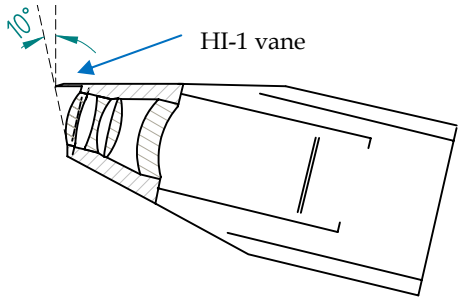

Figure 3-38 : Small vane on top of the HI-1 camera to protect from direct sky and bright object illumination.

- **A set of 5 oval vanes (edges #2-6) and 3 linear vanes in the cavity (edges #7-9)**.

  The five main vanes are located between the front baffle and the cameras, with oval-shaped cut-outs so that their edges are just outside (1 mm, to allow thermal distortion) the HI-2 circular FOV.

  Each vane is oriented towards the small tip vane located on top of the HI-1 camera entrance to trap potential spacecraft straylight sources located on the rear of the instrument (and in particular of the SWAVES antenna). With such configuration, no light can indeed be reflected back to the HI-1 entrance aperture after only one reflection but only after multiple reflections within the internal baffle (Figure 3-39). The number of vanes and their deepness were optimised to reduce the surface lighten by the straylight sources which are directly seen by the optics.

  The oval vanes are complemented by a 3 small linear vanes located under the HI-2 aperture and also oriented towards the HI-1 tip (Figure 3-39).

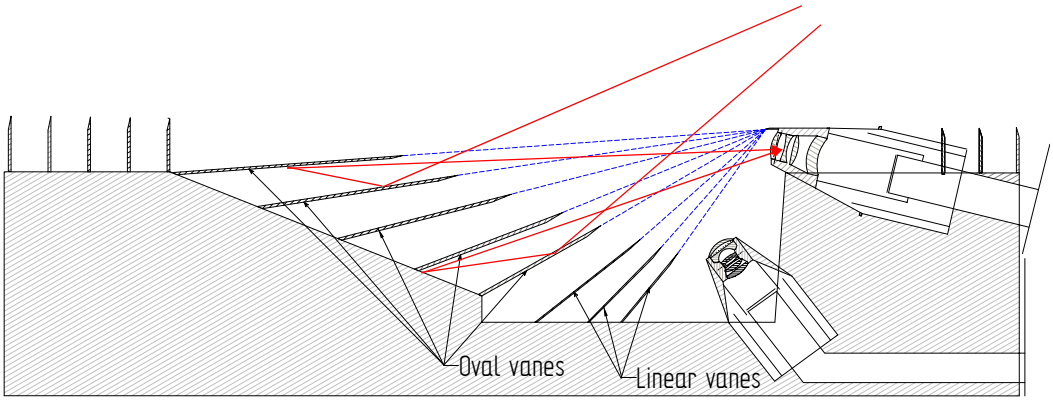

Figure 3-39 : The five oval and three linear vanes of the STEREO-HI internal baffle are oriented towards the edge tip onto of the HI-1 camera to avoid potential straylight source to be reflected back to HI-1 entrance after only one reflection.

These edges also provide an additional protection of the HI-2 entrance from diffracted light by the front baffle as shown on Figure 3-40. It ensures that the front baffle last edge cannot directly illuminate the HI-2 optical system.

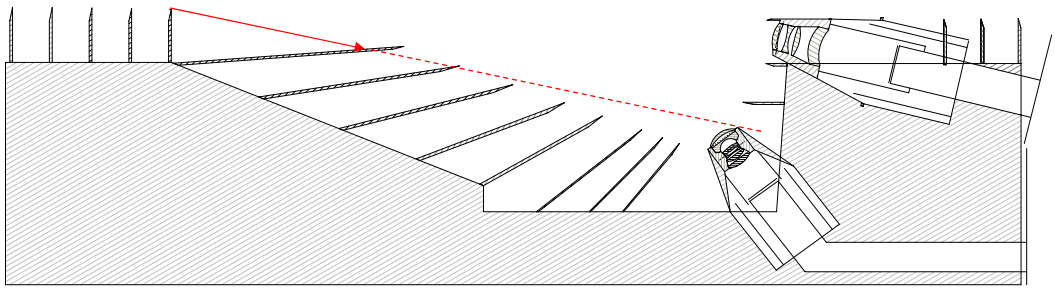

Figure 3-40 : The internal baffle avoids direct view between HI-2 entrance and front baffle edges.

- **A set of 2 small linear vanes between HI-1 and HI-2 (edges #10-11)**

  Their tip positions are optimised to avoid direct reflection from straylight sources towards entrance apertures (Figure 3-41) after reflection on the rear side of the instrument cavity.

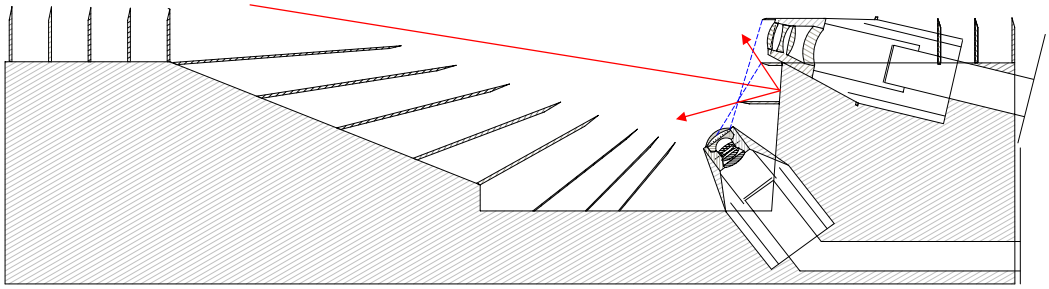

Figure 3-41 : The position of the two small linear vanes located between HI-1 and HI-2 entrances attenuate potential direct reflection towards entrance apertures.

- **A front linear vane (edge #12)**

  It is also located just behind the front baffle to avoid direct back-reflection of light from front baffle last edge toward the entrance of HI-1 camera (Figure 3-42). Its tip is positioned to maximise the shadow on HI-1 without interfering with the HI-2 FOV.

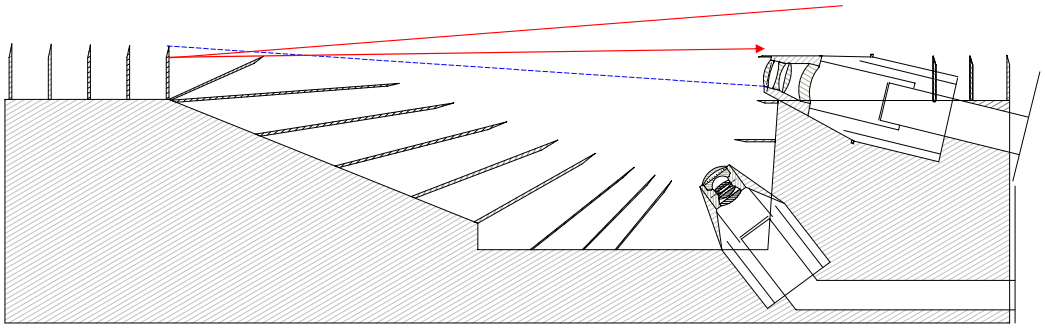

Figure 3-42 : A front linear vane is position on back of the front baffle to limit back-reflection towards HI-1 entrance aperture of the fifth front baffle edge.

Baffle performance

The performance of the internal baffles was computed with the ASAP© ray-tracing software[16], taking into account the measured BRDF of the Chemglaze Z307 black diffuse coating (Figure 2-5) that was used on the internal baffle, as shown in Figure 3-43.

[16] The model was limited to three scattering reflections per incident ray. After three reflections, the effect can be neglected.

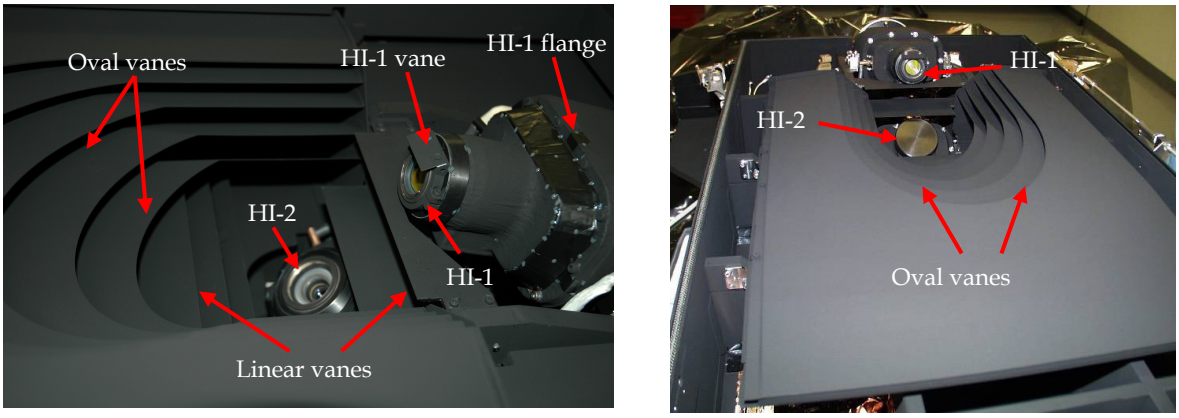

Figure 3-43 : The HI-A internal baffle during integration on the HI-A structure at the University of Birmingham. It is painted with Chemglaze Z307 to reduce the impact of potential unwanted reflections [Courtesy of University of Birmingham].

Figure 3-44 shows a representation of the internal baffle as modelled in ASAP© ray-tracing software.

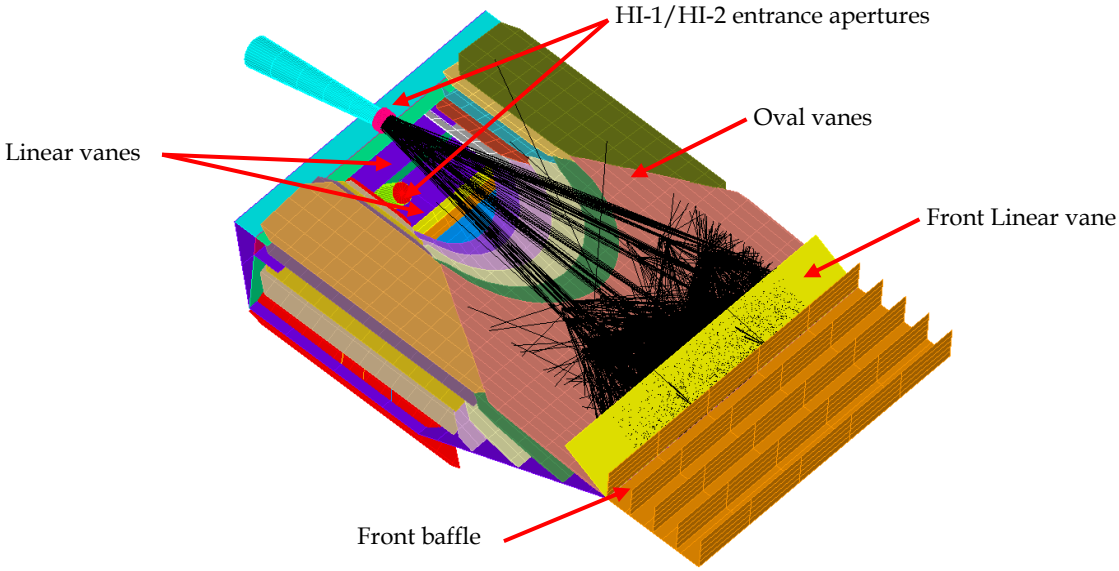

Figure 3-44 : Ray-tracing model of the internal baffle. The two cameras are modeled as entrance apertures and used to determine the baffle rejection. The front baffle is also materialized but only reflection on its last edge (as shown in the particular case of this image) is taken into account (i.e. not the diffraction by direct solar light).

For each incident direction, the internal baffle rejection (R_{baffle}) is computed by ray-tracing as the ratio of the flux at the optic aperture after scattering by the baffle (F_{optic}) over a unitary input flux (F_{input} = 1 W/m²) that illuminates the baffle surface (Figure 3-45).

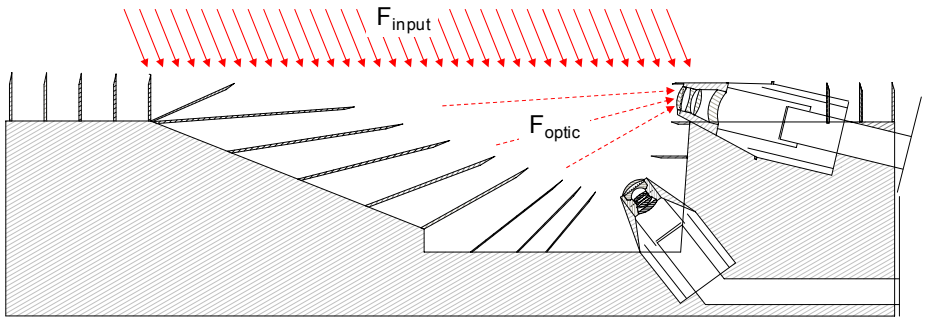

Figure 3-45 : The internal baffle rejection is computed in ray-tracing model for an incoming flux over the baffle surface (here shown for HI-1, but similarly for HI-2).

The internal baffle rejection is thus obtained with equation (3-25), where the ratio F_{optic}/F_{input} is an output of the ray-tracing computation. A geometrical correction factor G of the ray-tracing computation is used to converts the ray-tracing ratio result over a 1 W/m² flux that would directly illuminate the entrance aperture. It is computed with equation (3-26) where S_{baffle} = 0.43 x 0.3 m² is the baffle surface over which the input flux is ray-traced, and pitch/roll are the input direction as defined in Figure 3-37.

$$R(\text{pitch},\text{roll})_{baffle} = \frac{F(\text{pitch},\text{roll})_{optic}}{F_{input}} \cdot G(\text{pitch},\text{roll}) \qquad \textbf{(3-25)}$$

$$G(\text{pitch},\text{roll}) = \frac{1}{S_{baffle} \cdot \cos(\text{pitch}) \cdot \cos(\text{roll})} \qquad \textbf{(3-26)}$$

At each couple of pitch and roll angles of Figure 3-36 corresponds an incident direction of straylight source and a baffle rejection. Figure 3-46 gives the internal baffle efficiency at optic entrance apertures for all these pairs of incident angles. The worst internal baffle rejection from Figure 3-46 at the HI-1 and HI-2 entrance apertures is listed in Table 3-12 as compared with its requirement. The baffle rejection at the HI-1 and HI-2 entrances is below the requirement without some margin for HI-2.

	Required baffle rejection	**Minimum baffle rejection**
HI-1	< 6 10^{-4}	4.8 10^{-4}
HI-2	< 1.8 10^{-4}	1.4 10^{-5}

Table 3-15 : Maximum internal baffle rejection as compared with required rejection.

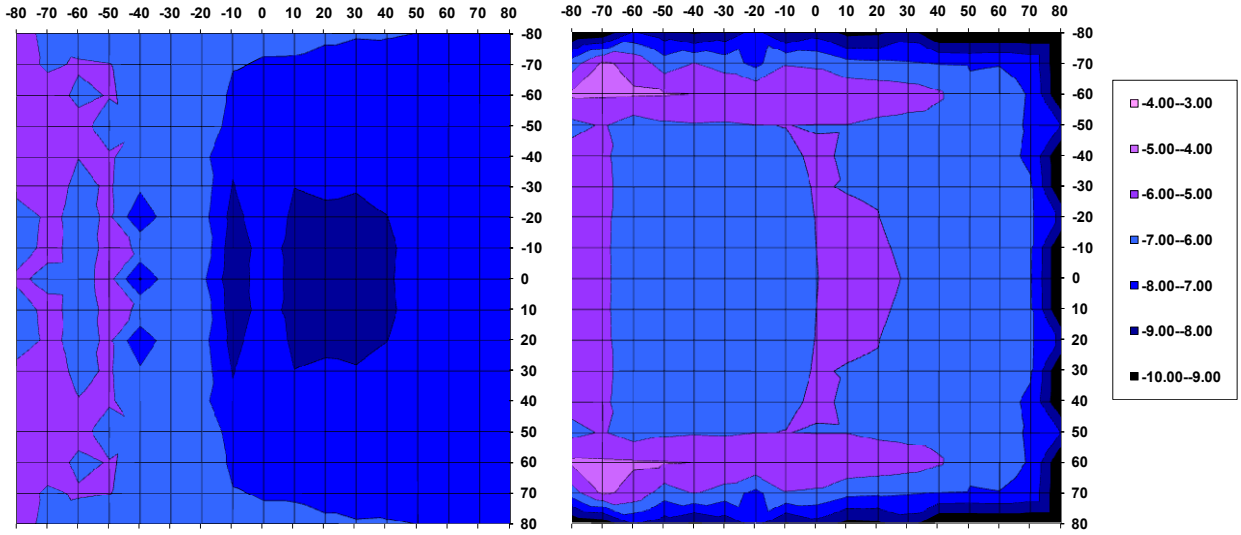

Figure 3-46 : Pitch-roll angular map of internal baffle rejection (in log scale), at the entrance of (left) HI-1 and (right) of HI-2. The sun is on left hand side.

The straylight level on the detector from the internal baffle cannot however be obtained with equation (3-24) using the integrated baffle rejection, because the straylight source brightness depends on the incident angle. The product of the baffle rejection map (Figure 3-46) by the straylight sources map (Figure 3-36), shown on Figure 3-47, is required. The straylight level on the detector is thus obtained with equation (3-27) where SL_{optic} is the straylight at the optic entrances from the internal baffle, obtained by summing the contributions of Figure 3-47 for all incident pitch and roll angles, and R_{optic} is the out-of-field lens barrel rejection (Table 3-3).

$$SL_{baffle} = SL_{optic} \cdot R_{optic} = \left(\sum_{pitch} \sum_{roll} R(\text{pitch},\text{roll})_{baffle} \cdot \text{Source}(\text{pitch},\text{roll}) \right) \cdot R_{optic} \qquad \textbf{(3-27)}$$

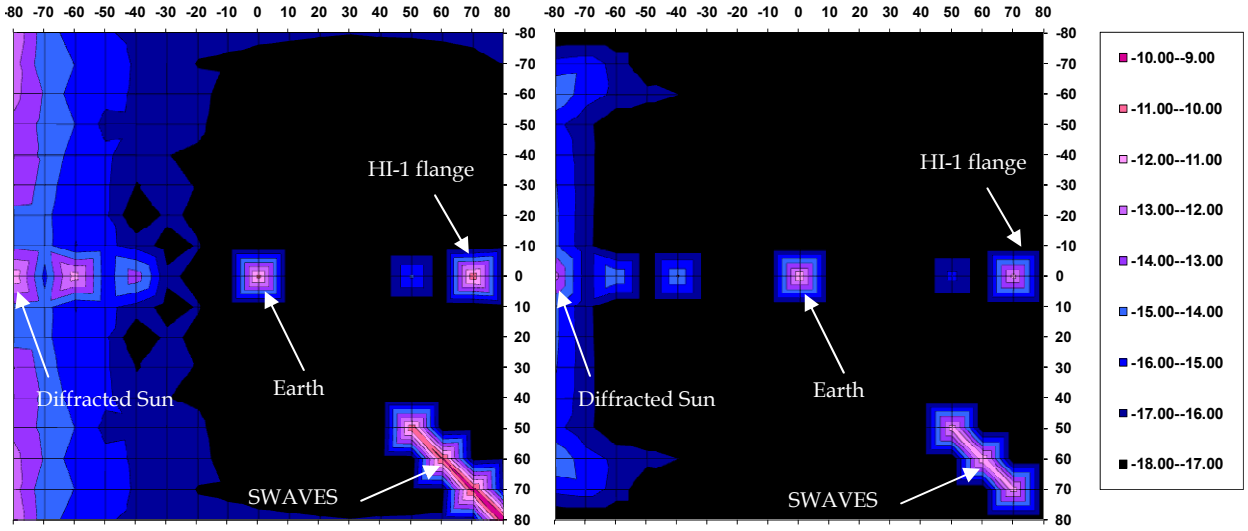

Figure 3-47 : Pitch-roll angular map of the B/B_0 straylight level from internal baffle (in log scale), where B_0 is the MSB, at the entrance of (left) HI-1 and (right) of HI-2 optical systems.

The obtained straylight on the detector (Table 3-16) is below the requirements, providing margin on the straylight at detector level.

	Straylight requirement	**Straylight on detector**
HI-1	$\leq 3\ 10^{-13}$	$6.1\ 10^{-14}$
HI-2	$\leq 10^{-14}$	$7.2\ 10^{-16}$

Table 3-16 : Straylight level (in B/B_0) from the internal baffle on HI-1 and HI-2 detector, as compared with the requirement (in B/B_0 where B_0 is the MSB).

The various straylight contributors can be obtained similarly with equation (3-28), where the summing is done on the couples of angles corresponding to each source.

$$SL_{baffle} = \left(\sum_{pitch(source)} \sum_{roll(source)} R(pitch, roll)_{baffle} \cdot Source(pitch, roll) \right) \cdot R_{optic} \qquad \textbf{(3-28)}$$

The resulting straylight level from the potential sources on the detector is given in Figure 3-48.

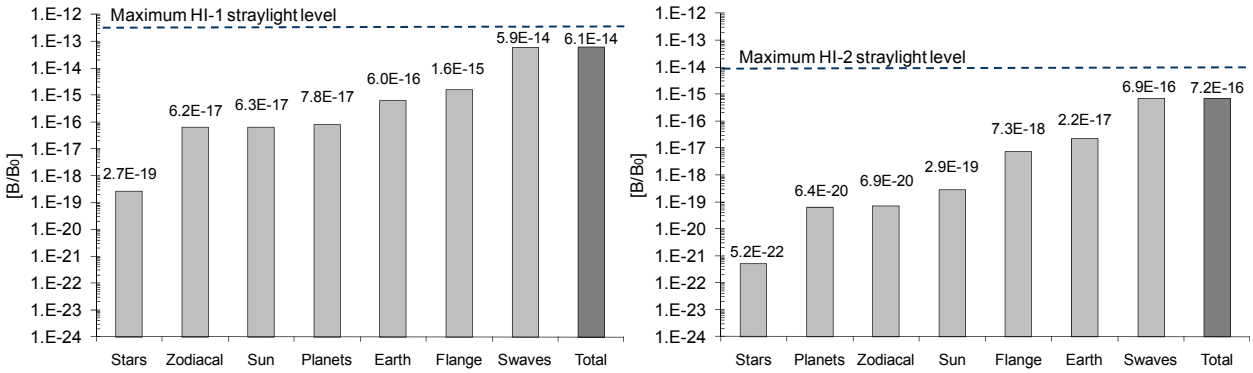

Figure 3-48 : Straylight level from the potential sources on the detector of (left) HI-1 and (right) of HI-2.

3.3.5. Total straylight level

The straylight on the HI-1 and HI-2 detectors after diffraction by the front and lateral baffles, and scattering on the internal baffle for the sources of Table 3-4 is summarised in Table 3-17.

The total straylight is dominated by the internal baffle. On the contrary of diffractive front and lateral baffles, the internal baffle is an absorptive system that relies on its coating properties and on the straylight source orientation, and is consequently limited in efficiency.

	Straylight on detector				
	Requirement	**Front baffle (Sun)**	**Lateral baffle (LGA & door)**	**Internal baffle (Sky & payload)**	**TOTAL**
HI-1	$\leq 3\ 10^{-13}$	$1.5\ 10^{-15}$	$6\ 10^{-15}$	$6.1\ 10^{-14}$	$6.9\ 10^{-14}$
HI-2	$\leq 10^{-14}$	$2.7\ 10^{-17}$	$3\ 10^{-17}$	$7.2\ 10^{-16}$	$7.8\ 10^{-16}$

Table 3-17 : Total straylight level on HI-1 and HI-2 detectors (in B/B_0 where B_0 is the MSB) from the Sun, LGA and door, sky and SWAVES boom, as compared with the requirement at detector level.

3.4. Alignment budget

To guarantee the performance of the baffles, an alignment budget has been built from constraints derived from the baffle design.

3.4.1. Instrument coordinate system and reference cube

The baffle and camera were mounted in the HI instrument and aligned w.r.t. the instrument co-ordinate system, parallel to the STEREO S/C one (Figure 3-49). The HI instrument has a reference cube that materialise these axis. It was used for the alignment of the instrument on the STEREO platform and represents the Sun centre direction.

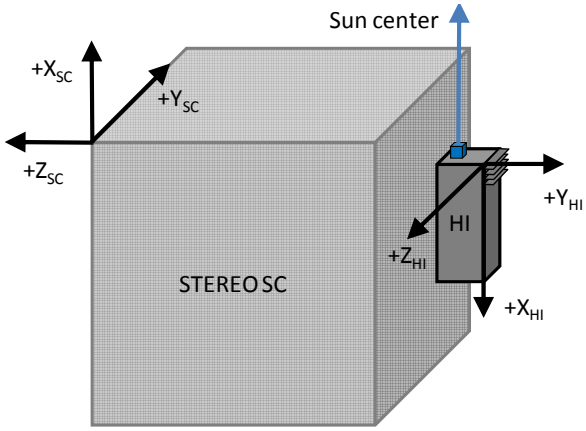

Figure 3-49 : STEREO S/C and HI coordinate systems and HI reference cube. Rotation around the instrument X, Y and Z axes correspond respectively to roll, yaw and pitch angles.

3.4.2. Design constraints

Front baffle

The front baffle rejection profile of Figure 3-28 is very sensitive to the respective edge heights (i.e. along Y_{HI} axis). As shown in Figure 3-50 for the particular case of three edges baffle, if one edge is too high or too low w.r.t. its neighbours one (i.e. in one of the left side configurations of Figure 3-50), it will not participate to the baffle rejection and the front baffle will be much less efficient.

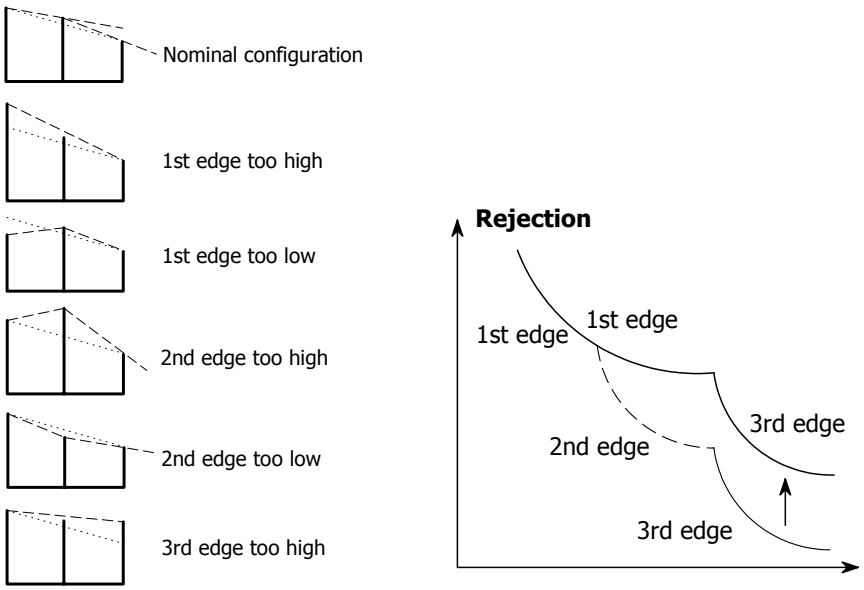

Figure 3-50 : Example of 3 edges configuration. (Left): In the nominal configurations the three edge diffraction efficiency is guaranteed. In the other configurations, the baffle efficiency is reduced. (Right): In case the second edge is too low, the baffle efficiency is reduced to diffraction by the 1st and the 3rd edges.

The height relative difference being of 132 µm (as given in Table 3-7), a -66 µm / +122 µm relative error on consecutive height of the front baffle edges (as shown in Figure 3-51) guarantees that no edge will become inefficient.

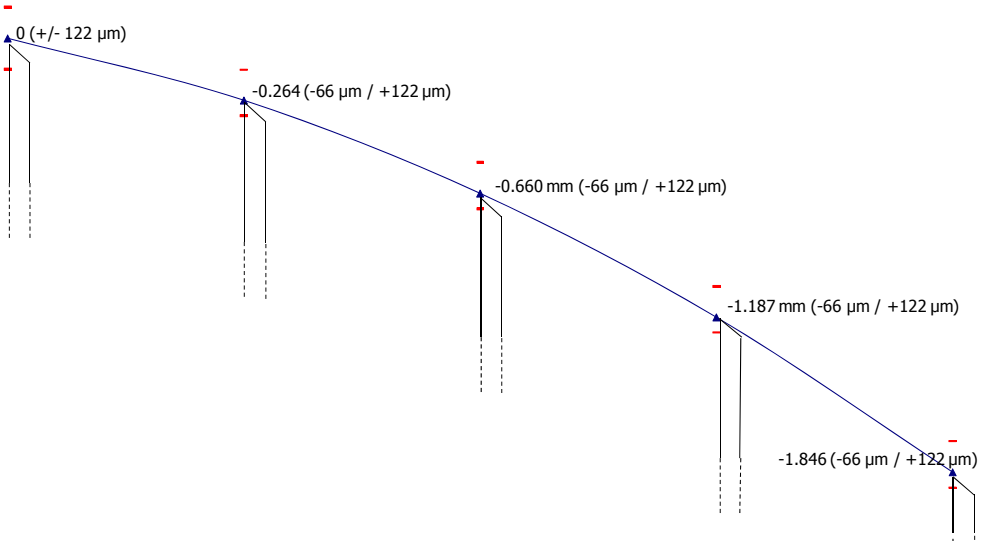

Figure 3-51 : Tolerances on the front baffle edge heights to ensure its overall performance.

This tolerance can be split in two contributors that are summed (RMS sum) as shown in Table 3-18:

Contributions	Value along axis	Contribution on tolerance		
Ty_edge_fwd	50 µm	50.00		
Rz_HI	300 "	41.45		
Total rms		64.95	<	66 µm

Table 3-18 : Front baffle edge contributors to the acceptable front baffle edge height.

- a 50 µm edge position along Y_{HI} axis, that can be decomposed in a positioning and a thermal distortion contributions (Table 3-19).

Positionning	40 µm		40.00	
Thermal expansion	25 µm		25.00	
Total rms			47.17	< 50 µm

Table 3-19 : Contributors to the front baffle edge tip acceptable height variation.

- a 5 arcmin instrument pitch[17], corresponding to a 41 µm edge move

The sensitivity to edge separation along the X_{HI} axis (i.e. 28.5 mm as obtained from Figure 3-30) is much less critical, and a 0.5 mm tolerance was considered.

Lateral baffle

As for the front baffle, the edge heights of the lateral baffle are critical to ensure the baffle performance. The tolerance is however less stringent because the vertical separation is larger. An acceptable tolerance was thus fixed to ± 100 µm.

As for the front baffle, a 0.5 mm tolerance on edge separation along the X_{HI} axis was considered.

[17] For a positive pitch offset (i.e. pointing away from the Sun center), the baffle rejection level is better. For a negative pitch the baffle efficiency is reduced. At an angle of -15.9 arcmin, the first edge of the front baffle becomes inefficient, producing a gap in the integrated rejection over the HI-1 entrance aperture.

Internal baffle

The internal baffle performance mainly depends on the edge orientation. A 20 arcmin tolerance on edge angle was imposed to limit retro-diffusion towards the camera entrances.

To avoid vignetting if the HI-1 and HI-2 fields of view, a 500 µm tolerance on edge height and separation was considered. In the particular case of the front linear edge of the internal baffle (edge 12), a 250 µm tolerance on edge tip position was considered to avoid vignetting of the HI-1 FOV that is very close of it.

HI-1 and HI-2 cameras

To avoid vignetting of HI-1 and HI-2 FOV by respectively last front baffle edge and internal baffle edges, a tolerance of 125 arcsec and 250 arcsec between the border of FOV and reference cube axis was imposed on HI-1 and HI-2 camera angular positioning. To avoid vignetting by lateral edges, a 30 arcmin tolerance was considered.

To ensure than no more than two lines over the 2048 lines of the detector (as shown on Figure 3-52) is affected by a bright edge (in case of potential wrong positioning or height variation), a 201 arcsec tolerance[18] on roll was imposed on HI-1 and HI-2 cameras.

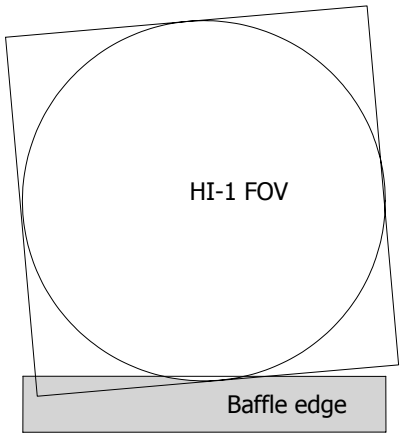

Figure 3-52 : Effect of roll misalignment

3.4.3. Alignment budget

The HI instrument design constraints are summarised in Table 3-20.

System	Constraints	Acceptable error
Front baffle	Avoid loss of one forward edge	Maximum ± 66 µm on edge height difference of two consecutive edges (y direction).
	Keep the optimal inter-edge configuration	± 500 µm on relative edge separations (x direction)
Lateral baffle	Avoid loss of one forward edge and reduce baffle efficiency	± 100 µm on relative edge heights (y direction)
	Keep the optimal inter-edge configuration	± 500 µm on relative edge separations (x & z directions)
Internal baffle	Keep the optimised configuration	± 20 arcmin (θz direction) on edge tilt ± 250-µm on first edge tip (edge #12) ± 500 µm on other vane tips

[18] atan(2/2048) = 201 arcsec

System	Constraints	Acceptable error
HI-1	Avoid vignetting by last front baffle edge	125 arcsec (θz direction) between border of FOV and S/C reference cube
	Avoid vignetting by lateral edges	± 30 arcmin (θy direction) between border of FOV and lateral edge
	Only 1 line of pixels affected by last forward tip illumination (in case of vignetting)	± 201 arcsec of roll (θx direction)
HI-2	Avoid vignetting of HI-2 FOV by internal edges	250 arcsec (θz direction) between border of FOV and the reference cube Sun centre direction
	Avoid vignetting of HI-2 FOV by lateral edges	± 30 arcmin (θy direction) between border of FOV and lateral edge
	Only 1 line of pixels affected by Earth illumination (Earth is moving in the HI-2 FOV).	± 201 arcsec of roll (θx in the HI-2 axes)

Table 3-20 : Tolerances values required to maintain the instrument straylight performance.

Based on these requirements, the overall instrument alignment budget of Figure 3-53 was derived. It is composed of three groups of contributors:

- The acceptable HI reference cube co-alignment error w.r.t. the STEREO axis (i.e. with the Sun centre)
- The acceptable baffles and cameras co-alignment error w.r.t. the HI reference cube, including mechanical and thermo-elastic distortions
- The acceptable camera fields of view orientation error w.r.t. the HI reference cube, i.e. w.r.t. the baffle edges

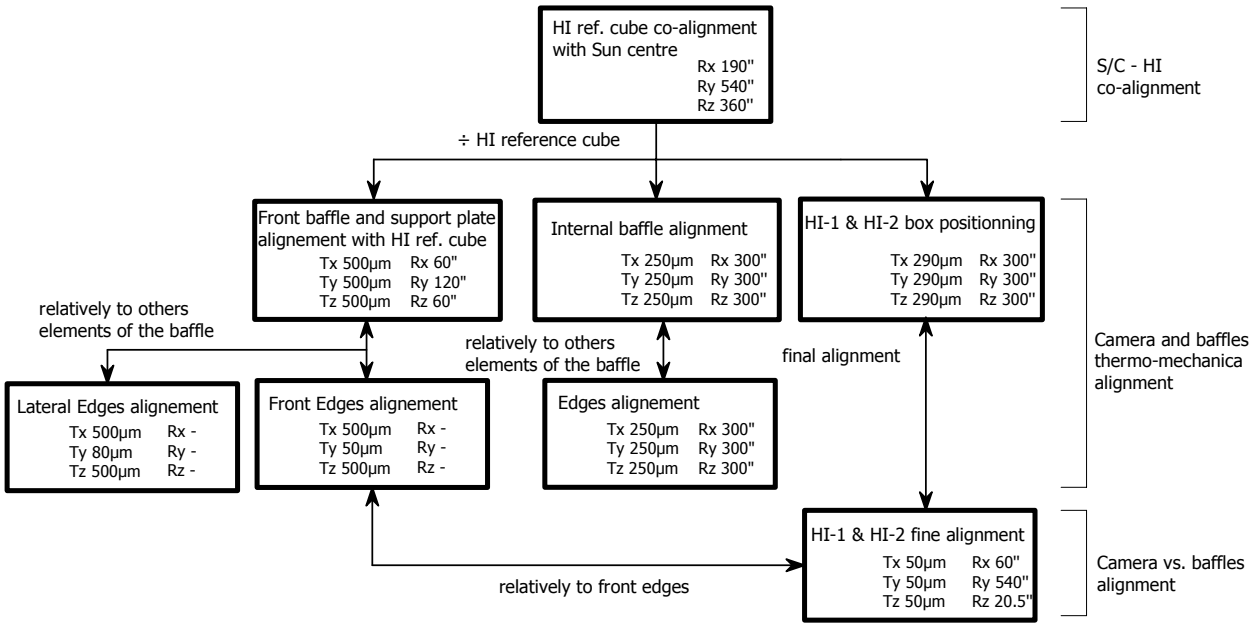

Figure 3-53 : STEREO-HI alignment budget.

3.5. Cleanliness impact

As part of the straylight performance, it is important to ensure the diffractive baffles are clean.

In particular, dust contamination must be limited to avoid diffusion that would produce an additional straylight contribution. In the case of a bright source illuminating the baffle edges, diffusion can indeed dominate the diffraction effect of the edges. Molecular contamination is less critical even if it has a potential impact on the black coating absorptivity.

3.5.1. Baffle cleanliness

The impact of cleanliness on front baffle performance was derived following the scheme of Figure 3-54.

Starting from the front baffle straylight requirement of Table 3-5, a maximum number of diffusing particles is obtained. This value is used to obtain an acceptable surface class cleanliness (according to standard MIL-STD-1246C) which allows to obtain the corresponding particle obscuration, in parts per million (ppm). The instrument having been assembled and tested in a class 100 volume cleanroom (according to standard FED-STD-209), the corresponding fallout rate (in ppm/day) allows to determine the maximum number of days the instrument can remain in this cleanroom. The straylight impact of cleanliness is then obtained by computing the corresponding number of diffusing particles on the baffle surface.

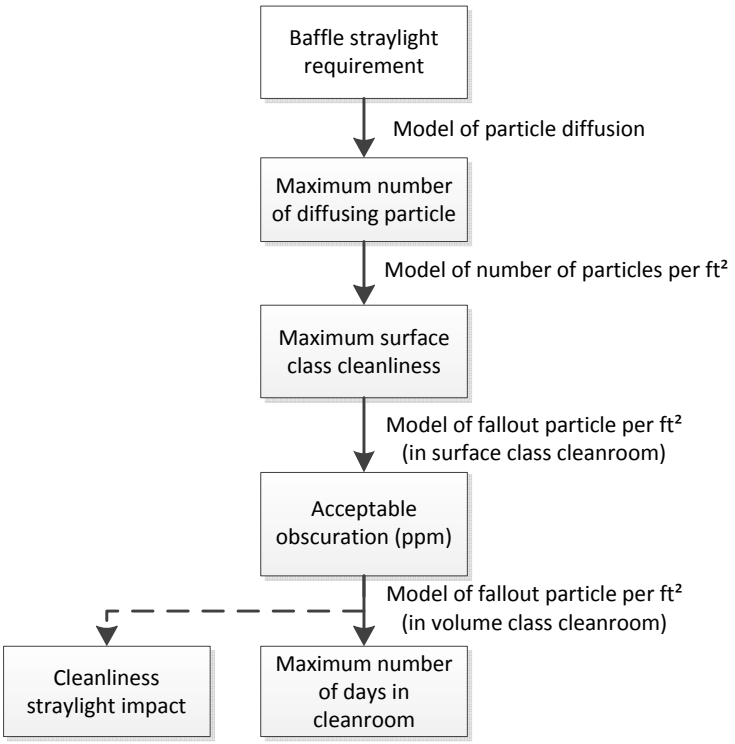

Figure 3-54 : Flow to derive baffle cleanliness impact on straylight.

Maximum number of particles

The maximum number of particles on the instrument edges versus their size is given in Figure 3-55. It is computed with formula (3-29), where $SL_{requirement}$ is the required straylight level at entrance of the HI-1 and HI-2 cameras (Table 3-5), i.e. 10^{-8} and 10^{-9} respectively for HI-1 and HI-2, and $SL(r)_{particle}$ is the straylight contribution due to diffusion by a particle of radius r located on a baffle edge surface.

$$MaxNumber(r) = \frac{SL_{Requirement}}{\sum_{vanes} \left(SL(r)_{particle}\right)} \quad \textbf{(3-29)}$$

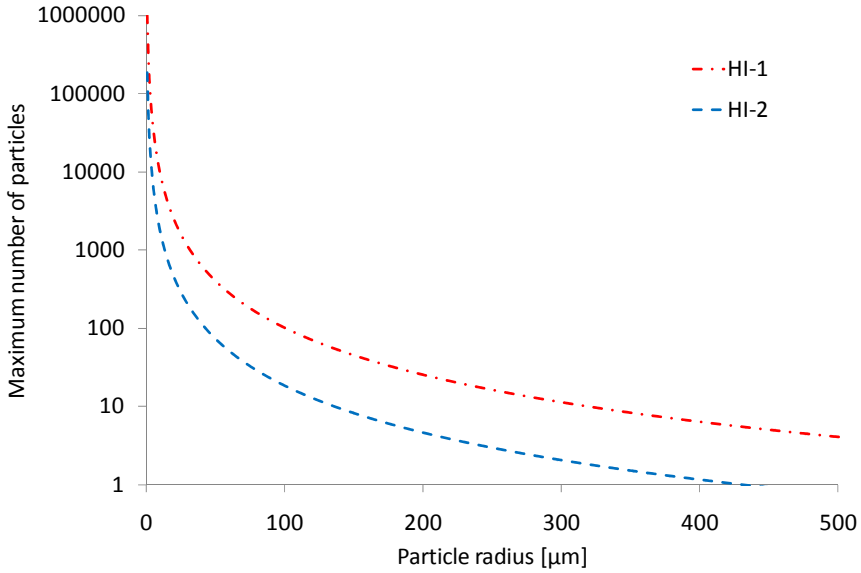

Figure 3-55 : Maximum number of particles (per ft²) versus their radius (in µm) to keep diffusion below the acceptable straylight level.

The particle contribution $SL(r)_{particle}$ is obtained with equation (3-30) where:

- Ω_{edge_apert} is the solid angle of the optical system entrance aperture as seen from each edges
- θ_{edge_apert} is the angle between the normal to the plane of the aperture and the line joining the edge tip to the centre of the aperture
- D_{edge_apert} is the distance between the edges and the optic apertures
- $F_{diffuse}$ is the diffused flux from the edge, assuming that each particle scatter light towards all direction (i.e. in 4π sr)
- F_{source} is the source brightness (in B_0 unit), the worst case being the Earth and SWAVES boom as the Sun brightness is attenuated by the front baffle first edges before being diffused by the other edges
- S_{apert} is the optical system entrance apertures

$$SL(r)_{particle} = \Omega_{edge\_apert} \cdot \frac{F(r)_{diffused}}{S_{aperture}} = \left[\frac{S_{aperture} \cdot \cos\left(\theta_{edge\_apert}\right)}{\left(D_{edge\_apert}\right)^2} \right] \cdot \frac{\left(\frac{\pi \cdot r^2 F_{source}}{4\pi str} \right)}{S_{aperture}} \qquad \textbf{(3-30)}$$

Maximum obscuration

Surface cleanliness is usually defined as a number of fall-out particles per surface unit (ft²) versus the particle radius (r) [58]. The instrument surface class cleanliness can then be derived from (3-31).

The maximum acceptable number of particles SL(r) is integrated over a range of particle size (1 to 500 µm) with the particle distribution $dN(r,Class_S)$ obtained with equation (3-32), where $N(r, Class_S)$ is the number of particle per ft² greater than r (in µm), $Class_S$ is the surface cleanliness class level (as per MIL-STD-1246C standard) with the associated C = 0.926 constant (equivalent to the "slope" of the particle distribution) [58]. The ClassS is per ft², the integral is thus multiplied by the ratio of the baffle surface (3-33) over one ft².

$$Straylight\left(Class_S\right) = \frac{S_{edges}}{ft^2} \cdot \left(\int_{0.5}^{500} SL(r)_{particles} \cdot dN\left(r, Class_S\right) dr \right) \qquad \textbf{(3-31)}$$

$$dN\left(r, Class_S\right) = -\frac{d}{dr} N\left(r, Class_S\right) = -\frac{d}{dr} 10^{C \cdot \left(\log\left(Class_S\right)^2 - \log(2r)^2\right)} \qquad \textbf{(3-32)}$$

$$S_{edges} = S_{Front} + S_{lateral} + S_{Internal} = 0.01 \cdot ft^2 \quad \textbf{(3-33)}$$

The comparison of the required HI-1 and HI-2 straylight level at camera entrances (Table 3-5) with the straylight corresponding to the surface class cleanroom is given in Figure 3-56. From that plot, the maximum acceptable surface cleanliness level can be derived as 330 and 230 for HI-1 and HI-2 respectively.

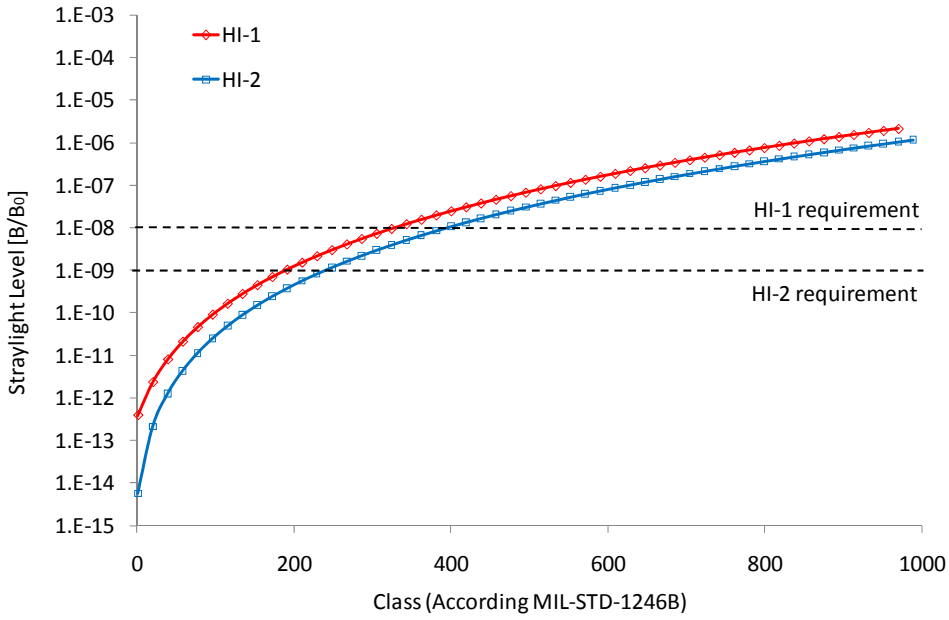

Figure 3-56 : Straylight level in function of the surface class cleanliness, as compared with HI-1 and HI-2 requirements.

From the acceptable surface cleanliness, the maximum number of fallout particles per ft² (expressed in ppm) can be computed, using obscuration formula (3-34), where S(r, α) is the surface obscuration by one particle as a function of the light incident angle α obtained with equation (3-35) [58].

$$\text{Obscuration}\left(\alpha, \text{Class}_S\right) = \frac{1}{ft^2} \cdot \int_0^{\text{Class}_S} S(r,\alpha) \cdot dN\left(r, \text{Class}_S\right) dr \quad \textbf{(3-34)}$$

$$S(r,\alpha) = \frac{2 \cdot \pi \cdot r^2}{\cos(\alpha)} - \frac{2 \cdot r^2}{\cos(\alpha)} \cdot \left(\frac{\pi}{2} - \alpha - \sin(\alpha) \cdot \cos(\alpha)\right) \quad \textbf{(3-35)}$$

The values of 800 ppm for HI-1 and 150 ppm for HI-2 are obtained for an average incident angle of 45 arcdeg. It corresponds to the maximum surface obscuration to remains below the straylight requirement.

Maximum duration in cleanroom

These maximum obscuration values can be compared, as shown in Figure 3-57, with the fallout level obtained with equation (3-36) in an airborne class cleanroom Class_V (according to standard FED-STD-209) where p is a coefficient that depends on the type of cleanroom (p = 578 when in laminar flux) [58]. It allows deriving the maximum duration the instrument can remain in that cleanroom (expressed in days).

$$N_{fallout}\left(\text{time}, p, \text{Class}_V\right) = 10^{\text{root}\left(0.926 \cdot X^2 + \log(X) - f\right)} \quad \textbf{(3-36)}$$

$$f\left(\text{time}, p, \text{Class}_V\right) = \log\left[0.02 \cdot p \cdot \left(\text{Class}_V\right)^{0.773} \cdot \text{time} \cdot \log(5)\right] + 0.926 \log(5)^2 \quad \textbf{(3-37)}$$

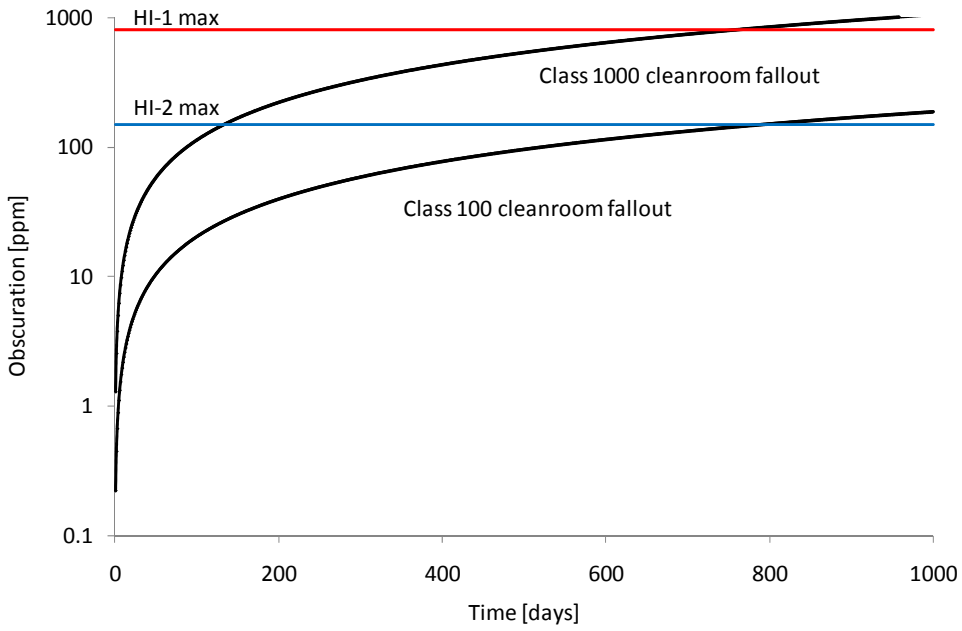

Figure 3-57 : The maximum acceptable surface obscuration to guarantee HI-1 and HI-2 straylight level is compared with fallout level in a class 100 and class 1000 airborne cleanroom to derive the maximum acceptable number of days in cleanroom.

The HI instrument was assembled and tested in class 100 airborne cleanroom under laminar flux, with an average 1.5 ppm per day. A maximum of 100 days in these conditions were thus acceptable for respectively to reach the maximum 150 ppm for HI-2 straylight level.

Straylight level at 100 ppm

The present computation had the purpose to show how critical is the cleanliness aspect in the straylight performance of the diffractive baffle.

Fortunately, the instrument was regularly cleaned and the expected level of obscuration at end of the on-ground activities was below 100 ppm, equivalent to a surface class 240 and the straylight level due to the front baffle contamination is summarised in Table 3-21, where the lens barrel rejection factor of Table 3-3 has been taken into account.

	Straylight on detector	
	Requirement	**Baffle cleanliness**
HI-1	$\leq 3\ 10^{-13}$	$< 6\ 10^{-14}$
HI-2	$\leq 10^{-14}$	$< 3\ 10^{-15}$

Table 3-21 : Straylight level resulting from particles (100 ppm) deposited on the baffles in a class 100 cleanroom (in B/B_0 where B_0 is the MSB), as compared with the requirement at detector level.

3.5.2. Dust particles on first lens

Cleanliness is also critical on the optics. A ray-tracing simulation on the HI-1 camera was used to determine the effect of dust particles on the 1st lens front surface. In this model, the dust particles are considered as light sources (i.e. with point sources that re-emit in every direction the light they receive).

Two study cases were considered for both one particle located in the centre of the first lens and for 16 particles uniformly distributed over the first lens surface.

- without diffusion inside lens barrel (i.e. all the surfaces of the barrel and detector cavity absorb 100% of incoming ray), as shown on Figure 3-58 (a) and Figure 3-59 (a) for one particle, and Figure 3-60 (a) and Figure 3-61 (a) for 16 particles

- with diffusion inside lens barrel (i.e. the lens barrel and detector cavity have reflective coating properties), as shown on Figure 3-58 (b) and Figure 3-59 (b) for one particle, and Figure 3-60 (b) and Figure 3-61 (b) for 16 particles

A dust (or set of dust particles) is therefore not imaged on the detector but results in a uniformly spread background. A relative intensity of 3% of the incident light beam is obtained from the ray-tracing model.

A few percents of background is however non-negligible in case of bright source illuminating the optics.

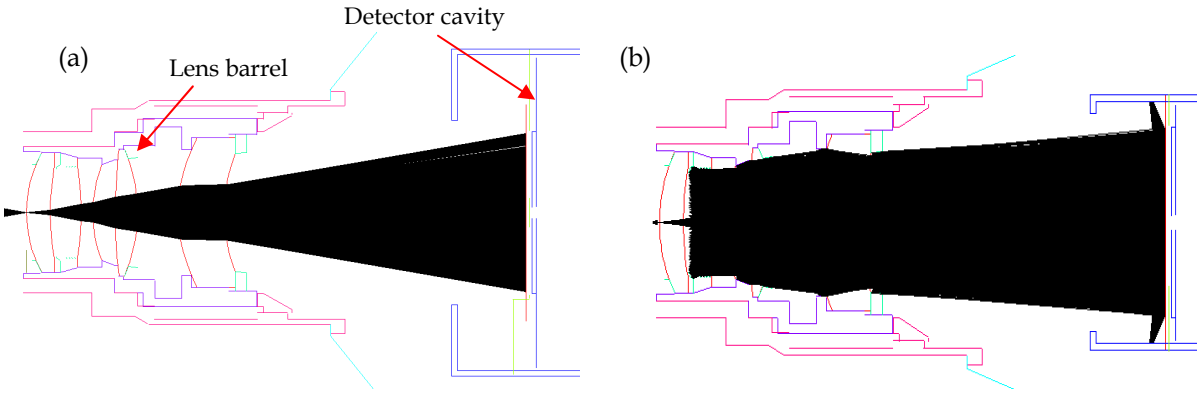

Figure 3-58 : Ray-tracing simulation of the effect of one dust particle located in the centre of 1st lens front surface, without (a) and with (b) diffusion inside the lens barrel

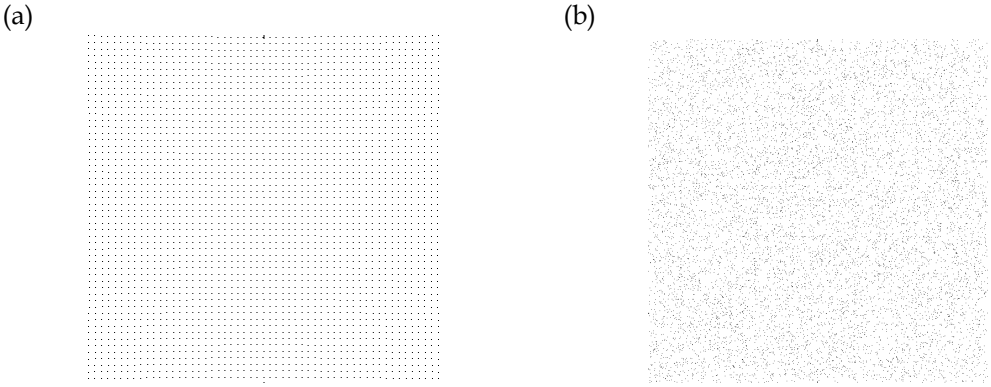

Figure 3-59 : Ray-tracing result of the effect of one dust particle located in the centre of 1st lens front surface: (a) without diffusion inside the lens barrel, (b) with one diffuse reflection. In both cases it results in uniformly spread pattern over the detector with an intensity of 1.3% and 2.8% times the input light.

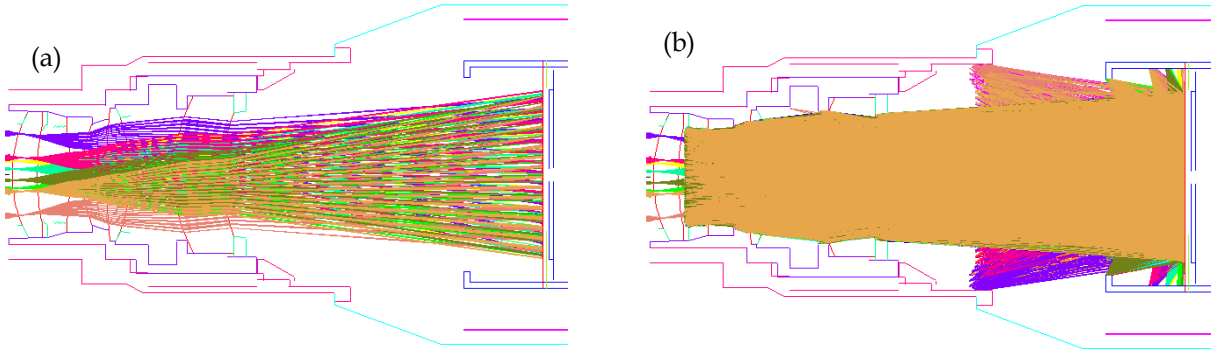

Figure 3-60 : Ray-tracing simulation of the effect of 16 particles uniformly distributed over the 1st lens front surface, without (left) and with (right) diffusion inside the lens barrel.

(a) (b)

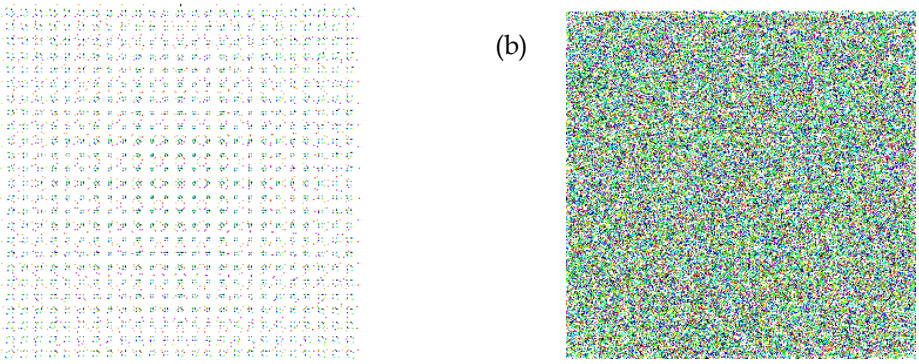

Figure 3-61 : Ray-tracing result of the effect of 16 particles uniformly distributed over the 1st lens front surface: (a) without diffusion inside the lens barrel, (b) with 1 diffuse reflection. In both cases it results in uniformly spread pattern over the detector with an intensity of 1.5% and 2.7% times the input light.

The straylight level $B_{diffusion}$ from particle on optics is computed with equation (3-38), where N_{px} is the number of pixels over which it is diffused, B_{Earth} is the Earth brightness (brightest possible source from Table 3-4 illuminating the optics), B_0 is the MSB, and taking into account the 3% ray-tracing result.

This level is potentially a major straylight contributor, as compared with values of Table 3-17, and a great care on optics cleanliness was therefore requested.

$$B_{diffusion} = \frac{B_{Earth} \cdot 3 \cdot \%}{N_{px}} = \frac{\left(10^{-6} \cdot B_0\right) 3\%}{2048^2} = 7 \cdot 10^{-15} \cdot B_0 \qquad \textbf{(3-38)}$$

It can also be noticed that this value is logically equivalent to the bubble and micro-roughness effect (Table 3-3) when multiplied by the same straylight brightness (i.e. B_{Earth} here).

Assuming the same result applies for both HI-1 and HI-2, the impact of first lens cleanliness is summarised in Table 3-21 together with the front baffle values of Table 3-21, showing that baffle cleanliness is more critical than lens cleanliness.

	Straylight on detector			
	Requirement	**Baffle Cleanliness**	**Lens Cleanliness**	**Total cleanliness**
HI-1	≤ 3 10^{-13}	6 10^{-14}	7.5 10^{-15}	6.75 10^{-14}
HI-2	≤ 10^{-14}	3 10^{-15}	7.5 10^{-15}	1.05 10^{-14}

Table 3-22 : Straylight level resulting from particles deposited on the front baffles and from particles deposited on the first HI-1 and HI-2 lens (in B/B_0 where B_0 is the MSB), as compared with the requirement at detector level.

3.6. Chapter summary

This chapter is focused on the STEREO Heliospheric Imager straylight design. It comprises the front, lateral and internal baffle, but also contribution from the two HI-1 and HI-2 camera lens barrels.

As shown on Table 3-23, where the straylight contributors are summarised, the instrument straylight requirement is met for HI-1 and marginally above requirement for HI-2, assuming the instrument alignment is within the allocated budget of Figure 3-53.

In particular the brightest source, i.e. the direct Sun, is properly attenuated by the front diffractive baffle. The rejection from this baffle is well below the requirements but it is needed to reduce the brightness level on top of HI-1 aperture and the consequent back scattering towards the front baffle last edge.

The internal baffle contribution, i.e. from other straylight sources than the direct sun, dominates the direct Sun straylight. It is however strongly dependent on the effective source brightness of Table 3-4 that were assumed for the computation. The lens barrel contribution is also a major factor in the obtained straylight level. It is based on a ray-tracing model of the camera where assumptions were made on the internal coating properties.

Table 3-23 indicates that the straylight level is dominated by the front baffle cleanliness, even if this contribution is strongly dependent on the effective instrument cleaning. The levels are however very low and at the limit of what can be measured.

	Straylight on detector					
	Requirement	**Front baffle (Sun)**	**Lateral baffle (LGA, door)**	**Internal baffle (sky, payload)**	**Cleanliness (baffle, lens)**	**TOTAL**
HI-1	$\leq 3\ 10^{-13}$	$1.5\ 10^{-15}$	$6\ 10^{-15}$	$6.1\ 10^{-14}$	$6.7\ 10^{-14}$	$1.4\ 10^{-13}$
HI-2	$\leq 10^{-14}$	$2.7\ 10^{-17}$	$3\ 10^{-17}$	$7.2\ 10^{-16}$	$1.1\ 10^{-14}$	$1.1\ 10^{-14}$

Table 3-23 : Total straylight level on HI-1 and HI-2 detectors (in B/B_0) from the Sun, LGA and door, sky and SWAVES boom, as compared with the requirement at detector level.

The straylight contributors can be split into the front baffle contributions (Table 3-24) and the internal contributions (Table 3-25), in order to allow later comparison with on-ground test results. The associated cleanliness contribution is different as the baffle cleanliness level mostly impacts the front baffle rejection.

	Front baffle (Sun)	**Cleanliness (baffle, lens)**	**TOTAL**
HI-1	$1.5\ 10^{-15}$	$6.7\ 10^{-14}$	$6.9\ 10^{-14}$
HI-2	$2.7\ 10^{-17}$	$1.1\ 10^{-14}$	$1.1\ 10^{-14}$

Table 3-24 : Straylight level on HI-1 and HI-2 detectors (in B/B_0) from the front baffle, including the associated cleanliness contribution.

	Internal baffle (sky, payload)	**Cleanliness (lens)**	**TOTAL**
HI-1	$6.1\ 10^{-14}$	$7.5\ 10^{-15}$	$6.8\ 10^{-14}$
HI-2	$7.2\ 10^{-16}$	$7.5\ 10^{-15}$	$8.2\ 10^{-15}$

Table 3-25 : Straylight level on HI-1 and HI-2 detectors (in B/B_0) from the internal baffle, including the associated cleanliness contribution.

Chapter 4. On-ground straylight calibration of the STEREO-HI instruments

4. On-ground straylight calibration of the STEREO-HI instruments

On-ground activities on the STEREO-HI instrument included the performance measurement of the most critical sub-systems (i.e. the front baffle and the lens barrel), but also an overall instrument straylight rejection that demonstrates the instrument reaches its expected performance.

4.1. Front baffle validation

4.1.1. Baffle prototype

As part of the STEREO-HI instrument development, a validation of the real geometry entrance baffle was first performed using a front baffle prototype (Figure 4-1) manufactured by the University of Birmingham. The prototype was composed of five edges mounted on a support allowing co-alignment of the edges with the test setup light source.

To limit back and diffuse reflections by the edges and further reduce the test setup ambient straylight background, the baffle edges and structure were blackened with a low TIS diffusive paint (Chemglaze Z306[19]), as shown on Figure 4-1.

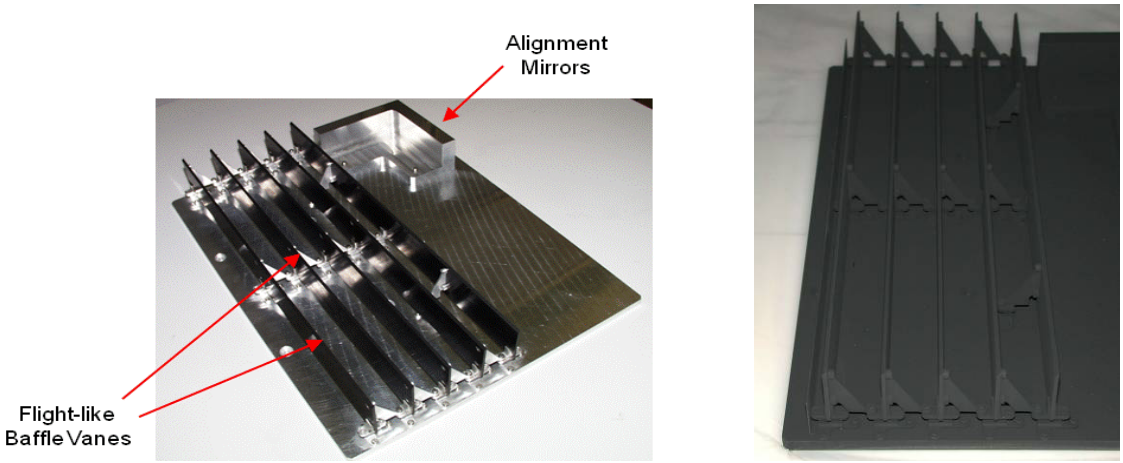

Figure 4-1 **:** Left: Prototype of the STEREO-HI front baffle, used to validate its rejection performance. Right: The baffle system was blackened with diffusive paint (Chemglaze Z306). [Courtesy of University of Birmingham].

The edge tips were manufactured with a 45 degrees angle to the plane of the baffle vane with a 0.1 – 0.2 mm wide edge (Figure 4-2), mainly for manufacturing reasons as it was demonstrated that the tip shape has little impact on diffraction (Figure 2-32).

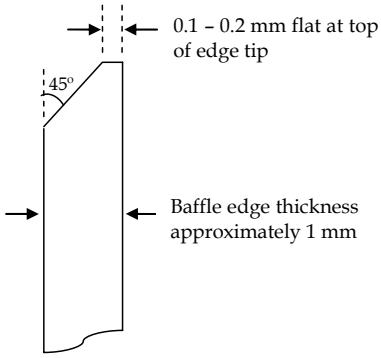

Figure 4-2 **:** Knife edge profile as used for the prototype [20].

[19] On the STEREO flight models, the Chemglaze Z307 was used instead of Z306. Both have equivalent BRDF, Z307 being the electrically conducting version.

The prototype edge heights were however not exactly at the nominal heights of Table 3-7, but at heights of Table 4-1. It corresponds to a baffle edge heights optimised for direct light coming from the Sun centre instead of the sun limb.

Edge #	Nominal heights	Prototype heights
1	0	0
2	0.264	0.218
3	0.66	0.544
4	1.187	0.987
5	1.846	1.565

Table 4-1 : STEREO-HI front baffle nominal and measured prototype edge heights (in mm).

4.1.2. Test setup

The front baffle prototype straylight rejection was measured with the same test equipment (collimator, rotating mechanism, photomultiplier with 1.9 arcdeg field of view, light trap and black shroud) as used to measure the multi-edged diffractive rejection on a mock-up (Figure 2-35 and Figure 2-36).

To reduce the background straylight, which is the main contributor of the error budget (Figure 2-43), the setup was integrated in the largest chamber of the Centre Spatial de Liège test facilities. The chamber is 5 meter diameter and the test setup was located on one end of it to increase the distance with the chamber walls.

As compared with mock-up test, the front panel of the black shroud was removed in order to let direct beam reflections going to the vacuum chamber cavity, taking advantage of its largest dimension. The lateral walls of the chamber were also covered with black Kapton (TIS ~10%) and a Z306 black panel was located in the field of view of the photomultiplier lens system to further reduce the background, as shown on Figure 4-3 and Figure 4-4.

As for the mock-up, the test was successively performed at ambient pressure and under vacuum. A class 100 cleanroom was thus maintained to limit as much as possible diffusion by particles when measurement is done at ambient pressure.

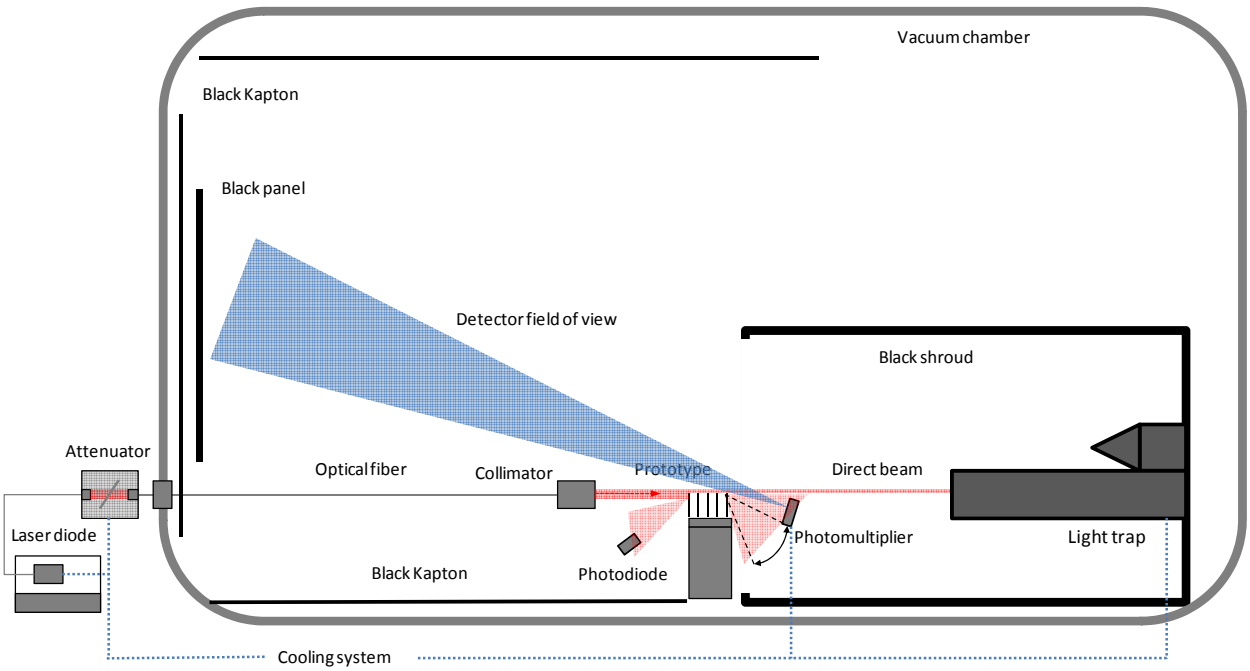

Figure 4-3 : The same test setup as for the mock-up straylight measurement has been used for the STEREO-HI front baffle prototype. It has been included in a larger chamber to reduce environmental background. The drawing is not at scale.

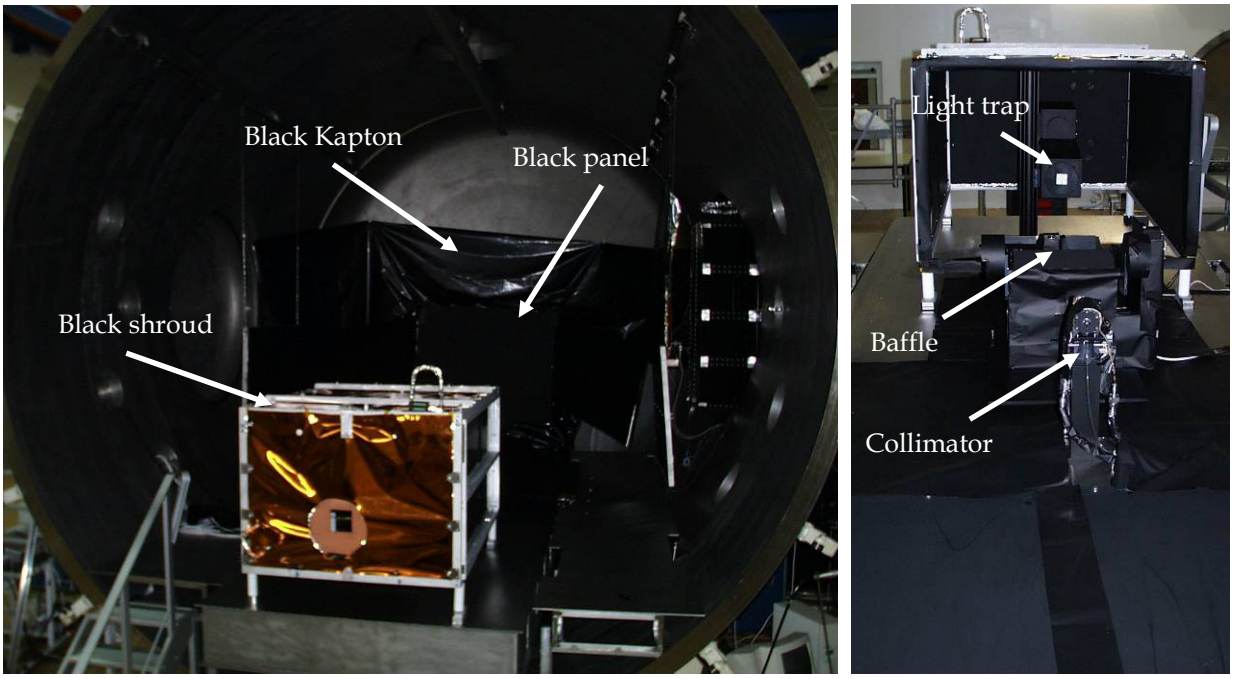

Figure 4-4 : Test setup used for prototype straylight measurement integrated in a 5 meter chamber to reduce environmental background. The rear cover of the chamber is not present in these pictures.

4.1.3. Measured rejection

The relative baffle rejection has been measured over an angular offset range from 0 to 10 arcdeg (Figure 4-5) as compared with the theoretical curve based on edge heights of Table 4-1. The convolved theoretical curve by the detector optical system field of view of 1.9 arcdeg (Figure 2-27) has also been included to allow comparison in the first part of the measured rejection.

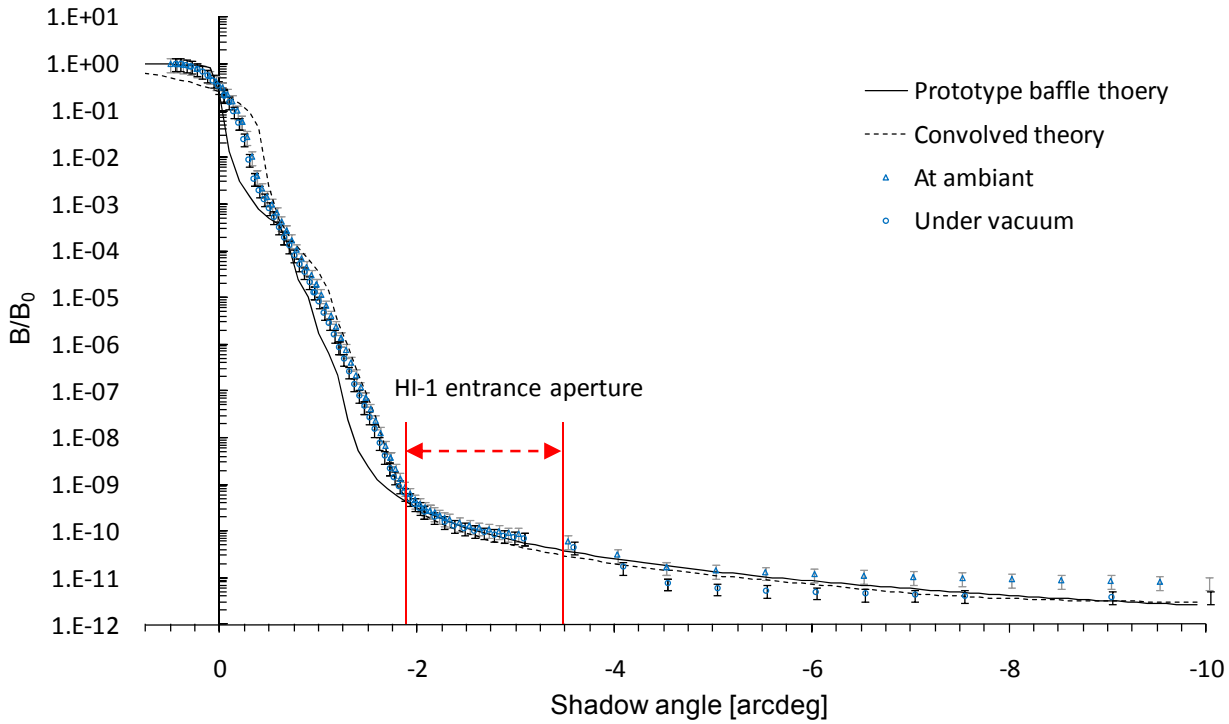

Figure 4-5 **:** Measured straylight relative rejection (B/B_0, where B_0 is the direct beam intensity) of the STEREO-HI front baffle prototype as a function of the shadow angle, together with the theoretical prediction (solid black line) and convolved theory by the detector aperture field of view of 1.9 arcdeg (dashed black line). Measurements at ambient pressure (in class 100 cleanroom) are compared with measurement under vacuum. The angular position of the HI-1 entrance is indicated. The HI-2 entrance aperture is out of the measured angle range.

There is a very good agreement between measurements and theoretical curves computed with edge heights of Table 4-1. At the angles corresponding to the HI-1 entrance apertures (Figure 3-29), the rejection is between 6.5 10^{-10} and 4.6 10^{-11}. For HI-2, located at larger angles, it can be approximated to the lowest measured value, i.e. 3 10^{-12}. As shown in Table 4-2, the measurements are thus very close of the computed values for both HI-1 and HI-2, which demonstrates the front baffle efficiency is as expected.

The improvement resulting from making the measurements under vacuum is very small and only observed for rejection levels below 10^{-11}. With the improved test set-up (i.e. larger chamber) the background light level at low intensities at ambient pressure is indeed now only limited by airborne dust and water vapour particles (unlike in Figure 2-42).

The very small difference between the theoretical and measured curves of the prototype baffle is most probably due to an incorrect alignment of the baffle edges with the direct beam. The aluminium base plate has indeed a polished surface as reference mirror for alignment with the input beam, which resulted in a less accurate alignment with the direct beam than with a real mirror. This effect is equivalent to a change in the relative edge heights that is difficult to evaluate, resulting in vertical shift of the edge diffracting curves.

	Nominal STEREO-HI rejection	**Prototype theoretical rejection**	**Prototype measured rejection**
HI-1	9.1 10^{-11}	6 10^{-10}	6.5 10^{-10}
HI-2	4.1 10^{-12}	2 10^{-12}	< 3 10^{-12}

Table 4-2 : Measured rejection of the front baffle at HI-1 and HI-2 entrance aperture location, at 805 nm, expressed in B/B_0 (where B_0 is the input brightness), as compared with theoretical rejection at 805 nm of the prototype baffle and of the nominal STEREO-HI baffle.

The comparison of the results with the nominal STEREO-HI baffle integrated rejection at the HI-1 and HI-2 entrance aperture at 805 nm is also given in Table 4-2. The difference between the present results and the STEREO-HI front baffle rejection curve of Figure 3-28, in particular for HI-1, is due to the relative edge heights that are not the same than in the nominal STEREO-HI front baffle, showing the high sensitivity of edge relative positioning and alignment with the incident collimated beam.

A 22% error bar has been considered. It is based on the error budget of Figure 4-6, that is very similar to the one derived for mock-up test but with a background offset assumed to be lowered down to 20 % (due to the enlarged chamber).

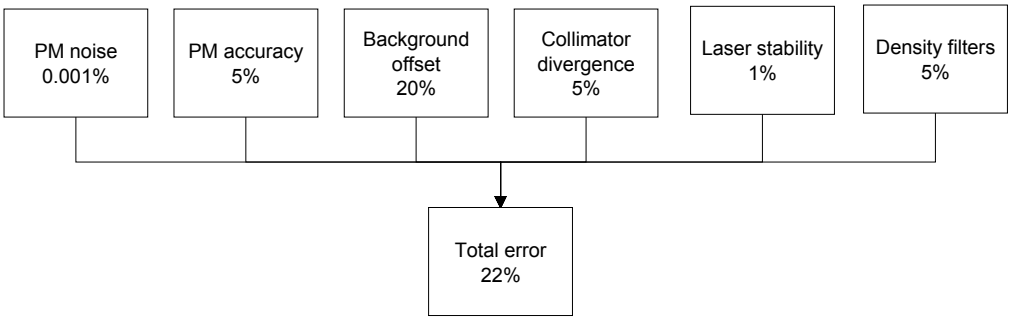

Figure 4-6 : STEREO-HI front baffle prototype measurement error budget.

4.2. Optical system characterization

As part of the overall straylight performance, the optical systems were also characterized.

4.2.1. Lens barrel rejection

The out-of-field lens barrel rejection of HI-1 and HI-2 were measured prior to integration in the camera assemblies. The measurements were performed in class 100 cleanroom with a 633 nm laser source and a 10 mm x 10 mm photodiode (Newport 818-SL) located at the focal plane of the optics (Figure 4-8). The optical systems were mounted on a rotation table to scan from the field of view centre to out-of-field angles.

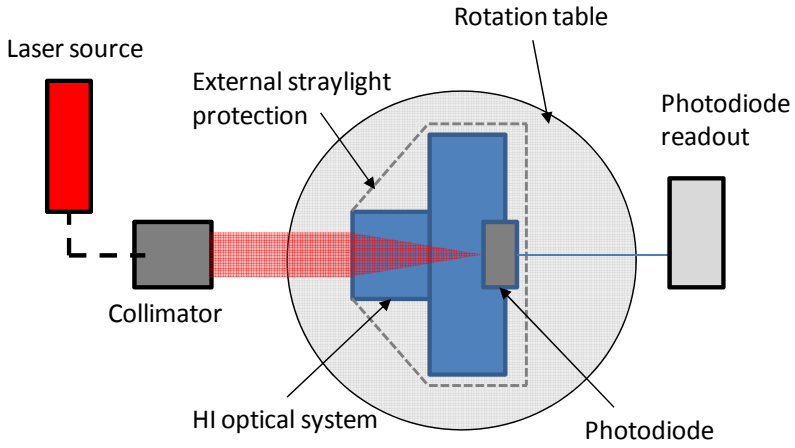

Figure 4-7 : Principle of the test setup used to measure the out-of field rejection of the HI optical systems.

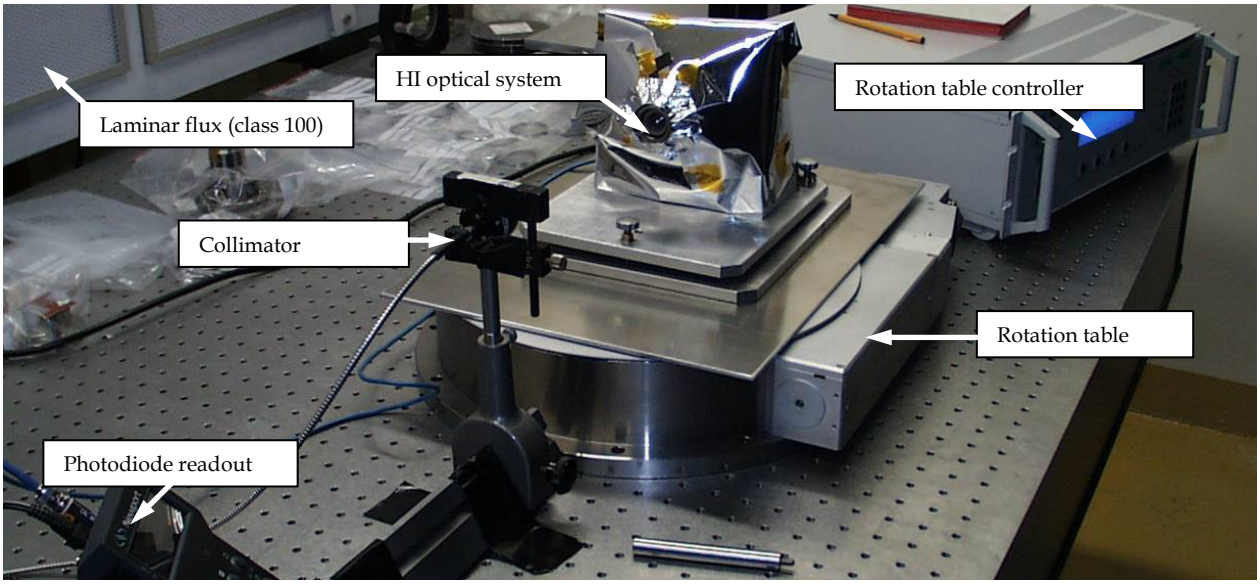

Figure 4-8 **:** Test setup used for out-of field rejection measurement of the HI optical systems.

The HI-1 and HI-2 rejection are shown in Figure 4-9. At the angles corresponding to the edges of the field of view, the straylight contribution levels are ~10^{-2} for both HI-1 and HI-2.

The test detector is however smaller than the STEREO-HI CCD detector. It therefore limits the effective field of view, as shown on Figure 4-9 where the FOV are limited to ±3.5 arcdeg and ±12 arcdeg in HI-1 and HI-2 respectively. The results have thus been extrapolated for the 27.65 mm x 27.65 mm real detector by multiply the angle scale by the factor 27.65/10.00. The resulting real lens barrel rejection is given in Figure 4-10.

The measured rejection however corresponds to an integrated value over a 'single-pixel' detector area. It cannot thus be directly compared with the theoretical values of Figure 3-14 (which represent the maximum rejection per pixel). The comparison of measurement with theoretical rejection in Figure 4-10 is thus obtained by using the computed rejection over the whole detector (which is also an output of the ray-tracing model).

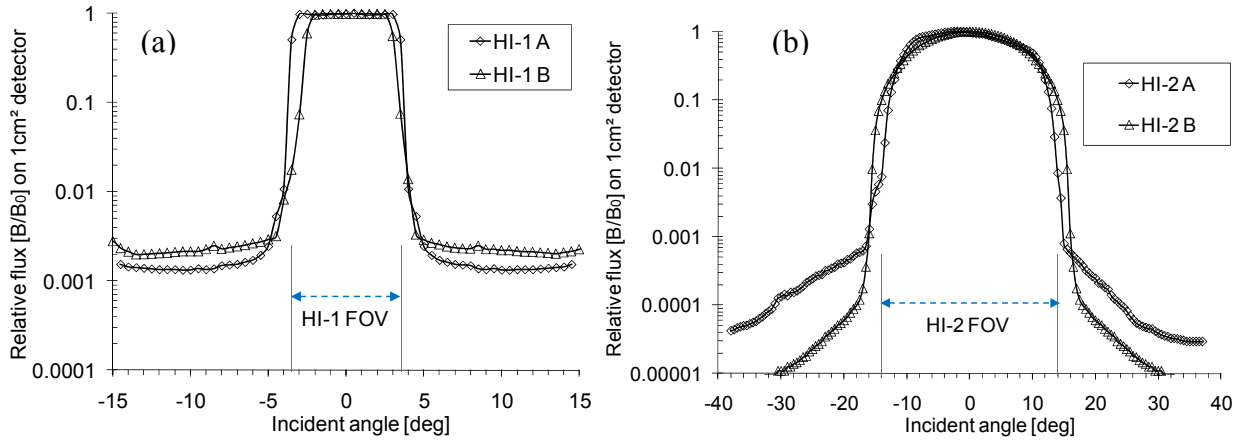

Figure 4-9 **:** Measured out-of-field straylight rejection measured on flight model of the (a) HI-1 and (b) HI-2 lens assemblies, using a 1 cm square detector and a collimated 633 nm laser source.

The integrated rejection value next to the field of view border is ≤ 10^{-2} for HI-1 and between ≤ 10^{-1} for HI-2, i.e. above the predicted values. For large angles, the rejection is ~10^{-3} for HI-1 and < 10^{-2} for HI-2, i.e. below the theoretical curve.

The difference between ray-tracing model and measurement indicates that the ray-tracing model of the lens barrels is too optimistic in the first out FOV degrees. Only a 10^{-2} lens barrel rejection level can therefore be considered for both cameras.

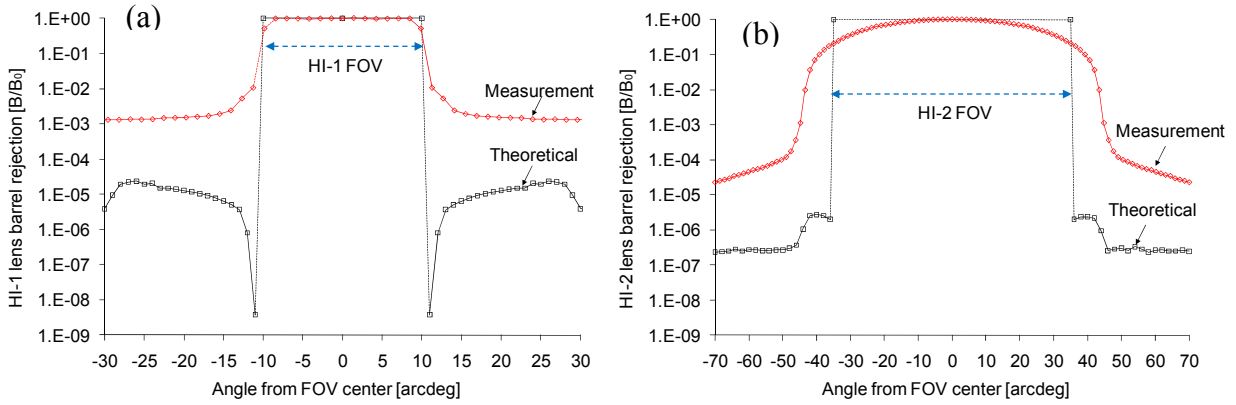

Figure 4-10 **: L**ens barrel rejection (red curves) of HI-1A (a) and HI-2B (b), extrapolated for the 27.6 x 27.6 mm detector from measurements with a 10 x 10 mm detector. The integrated theoretical rejection curves (black curves) are plotted in black.

4.2.2. Optics spectral bandpass

As part of the instrument development, the spectral range of the HI-1 and HI-2 optical system was measured on both flight models (HI-A and HI-B) and on an engineering qualification model (EQM).

A broad-band visible light was injected in a monochromator and its output directed into the HI-1 and HI-2 optical system, as shown on Figure 4-11. The transmission versus the wavelength selected by the monochromator was measured by the same 10 x 10 mm² photodiode than used for lens barrel rejection measurement, the photodiode being located at the optics focus.

As shown in Figure 4-12 [14], the normalised transmission is very similar for the FM and EQM optics.

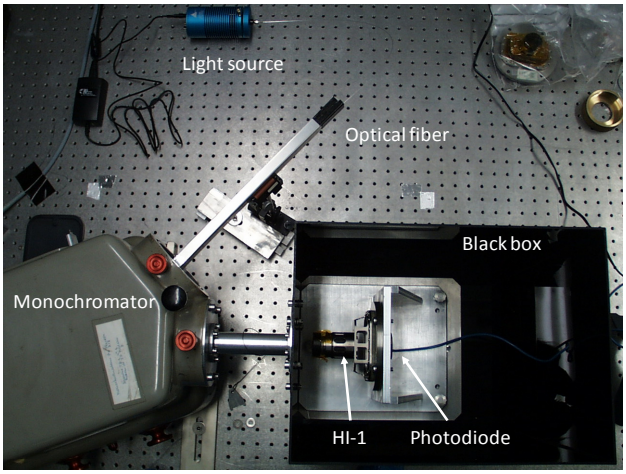

Figure 4-11 : Test setup used in 2005 to measure the spectral transmissions of the HI-1 and HI-2 flight and EQM optical systems.

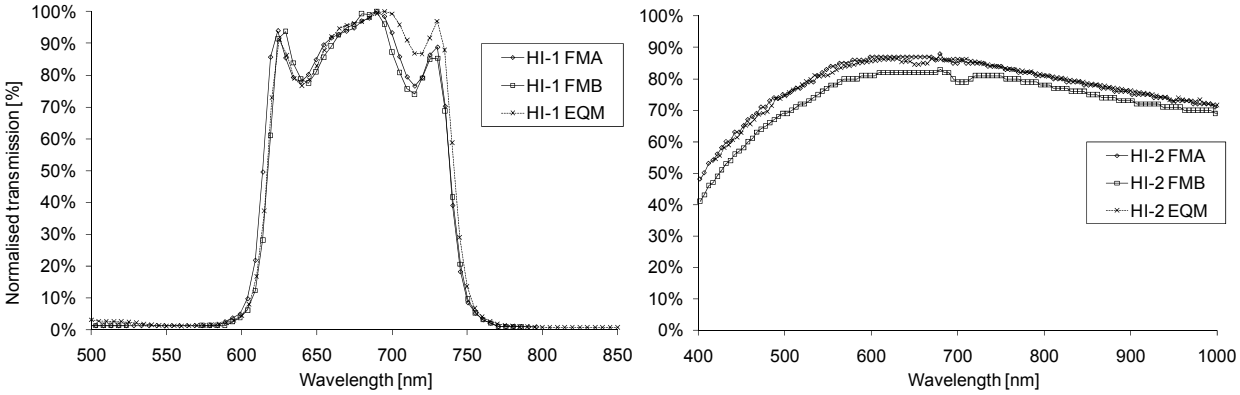

Figure 4-12 : FM-A, FM-B and EQM spectral transmission in 500-850 nm range and 400-1000 nm for HI-1 and HI-2.

4.2.3. Bandpass shift

Following in-flight observations of the Mercury tail in 2008 by the HI-1A camera (Figure 4-13), new transmission measurements were performed on the EQM optics to quantify potential evolution of the HI-1 spectral bandpass. The Mercury tail should indeed only be imaged at a wavelength of 589 nm, corresponding to the sodium gas (NaD), which is at the very edge of the HI-1 bandpass.

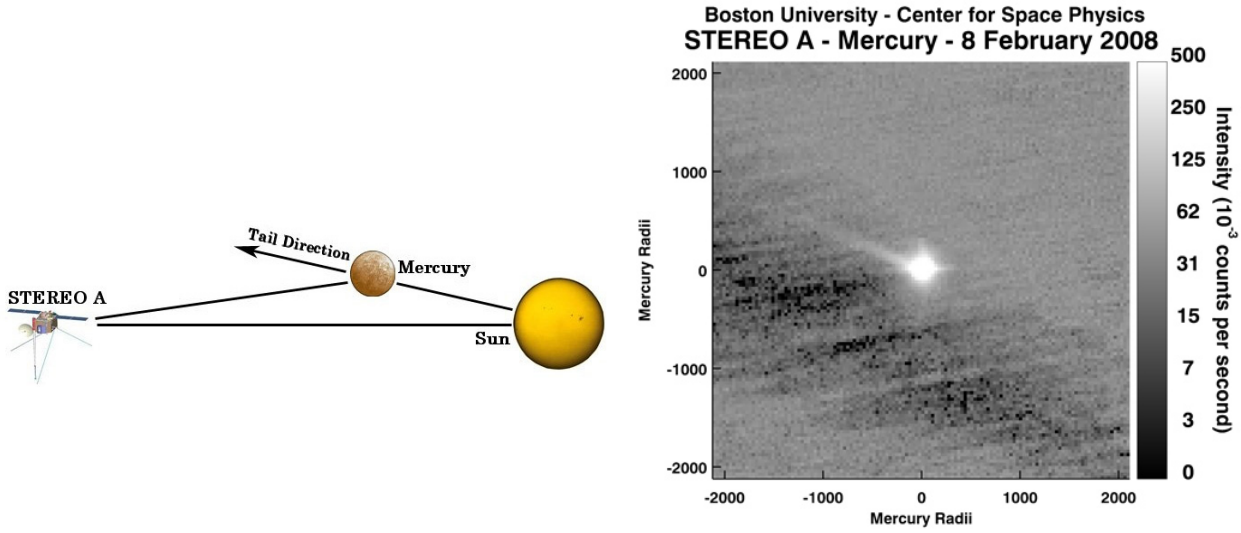

Figure 4-13 : The Mercury tail, produced by the Solar wind (left), has been imaged in HI-1A in 2008 (right) [33].

The test setup used in 2010 is sketched and shown in Figure 4-14. It is composed of an optical fibre that injects broad-band visible light at the focus of the HI-1 optical system and of a lens that collects the output light into a calibrated spectrometer. This setup was designed for vacuum testing, as shown in Figure 4-14 where it is mounted in a thermal shroud within a 1.5 meter vacuum chamber at the Centre Spatial de Liège. The spectral transmission of the HI-1 EQM was therefore measured at room temperature (+20 °C) at ambient pressure and under vacuum, and at -30 °C (in-flight operational temperature).

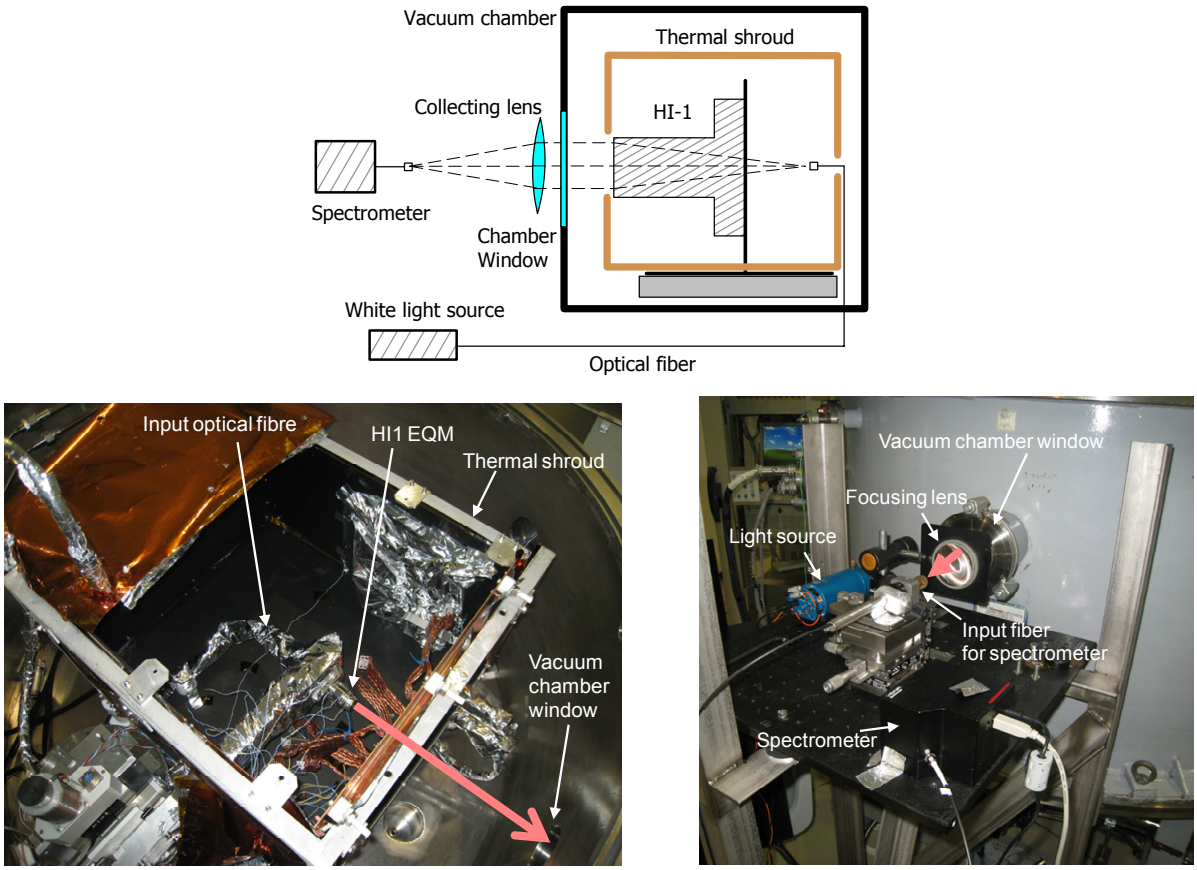

Figure 4-14 : Spectral transmission test setup used in 2010. Bottom left: the optic is in a thermal shroud within the vacuum chamber, white light is injected at its focus. Bottom right: the output light is collected to a spectrometer.

A calibration of the monochromator used in 2005 with the spectrometer used in 2010 was performed to ensure the shift is not due to a wrong calibration of the monochromator used in 2005. As shown on Figure 4-15, a white light is injected to the monochromator and its output is measured by the spectrometer.

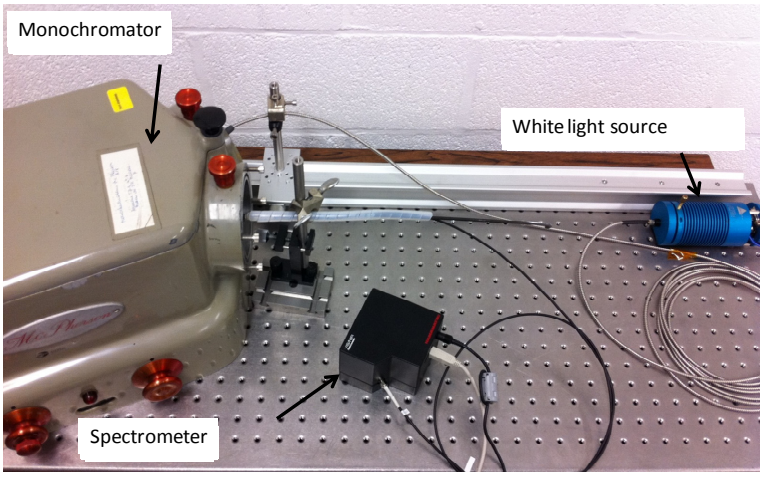

Figure 4-15 : Test setup used to cross-calibrate the monochromator used in 2005 with the spectrometer of 2010.

Figure 4-16 shows the comparison of HI-1 EQM spectral transmission, as measured in 2005 and in 2010 at ambient, with the results obtained under vacuum at +20 °C and -30 °C. A shift of the HI-1 bandpass towards shorter wavelengths by ~ 15–20 nm is effectively observed at ambient.

A second smaller shift ~5 nm is then observed when going under vacuum, and a third minor shift ~ 2 nm is finally observed when cooling down the optic to -30 °C.

- The blue shift of the HI-1 transmission observed at ambient is most probably due to a modification of the ZrO2 coating crystalline structure, which was not stabilized when applied on the optics [57], resulting in a refractive index and a physical thickness change.
- The shift when going under vacuum is due to water outgassing. The bandpass was indeed re-measured a few hours after return to ambient and it fits with the values measured before the vacuum sequence, showing that water in the air is re-absorbed by the coating.

The coating degradation process is relatively fast even if slower at low temperature. The HI-1 FM-A and FM-B in-flight being around -15 °C and -30 °C respectively, the ageing was thus most probably slower than on the EQM (which has been stored in air at +20 °C). After 5 years of flight (under vacuum), both the ageing and the outgassing of the HI-1 FM-A and FM-B filters are however completed and the associated blue shift compared with the 2005 on-ground transmission curves should be similar to the one shown in Figure 4-16.

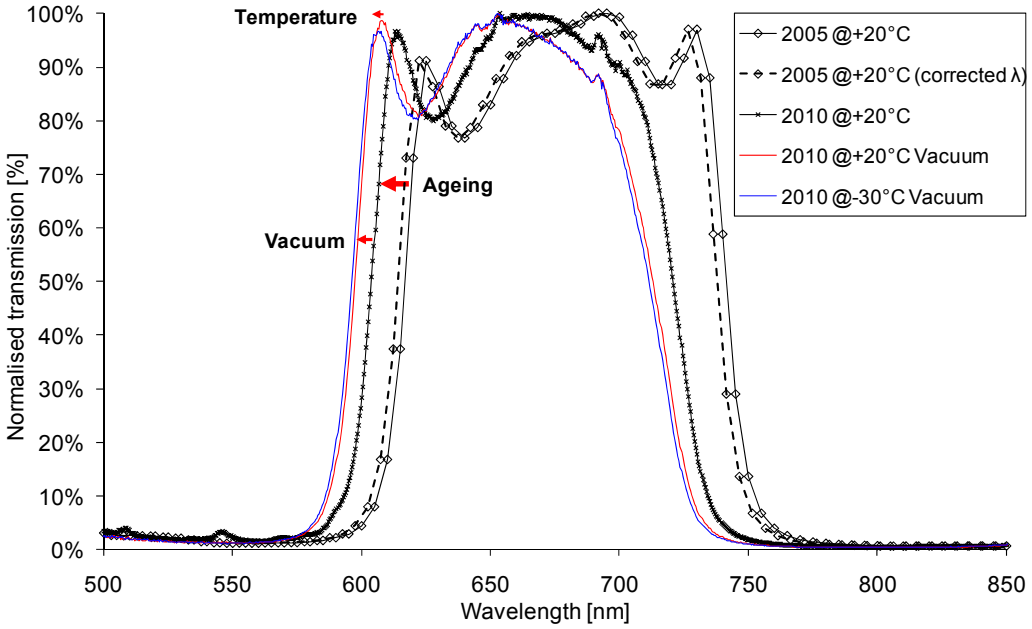

Figure 4-16 : HI-1 EQM spectral transmission in the 500-850 nm measured in 2005 and 2010, at ambient and under vacuum at +20 °C and -30 °C. The 2005 transmission was corrected to take into account a small wavelength difference between the monochromator and the spectrometer ("corrected λ") transmission.

The measured blue shift has fortunately however no impacts on the overall instrument straylight performance as the potential bright straylight sources are broadband light.

4.3. Instrument optical calibration

Before integration on the STEREO spacecrafts, a thermal qualification test and an optical calibration of the two HI flight models were carried out at the Centre Spatial de Liège.

The objective of the thermal qualification was to demonstrate the ability to conduct science operation without a loss/degradation of data or data interference in flight temperature conditions, as well as verifying command/telemetry databases, compiling trending analysis, collecting operating run time, etc. The results of the thermal tests are not further detailed here and more details can be found in [20].

The objective of the optical calibrations was to provide an evaluation at system level of the optical response, in term of optical throughput and Point Spread Function (PSF). Some results are given here as useful for the following straylight measurement, as in particular the photometric conversion factor.

4.3.1. Calibration test setup

The final calibration of the two HI flight models were performed in a vacuum chamber permitting to cool down the CCD detectors in order to limit their noise level.

Figure 4-17 shows the HI-B flight model installed in a 3 meter diameter vacuum chamber at the Centre Spatial de Liège (CSL) before being surrounded with black painted shrouds (Aeroglaze Z306). The two HI-1 and HI-2 detectors are cooled down to -100 °C with a Dewar filled with Liquid Nitrogen, replacing the flight radiators. The HI instrument being close of the EUVI instruments on-board STEREO, its molecular contamination had to be minimized and vacuum sequences were monitored by a Thermally controlled Quartz Crystal Microbalance (TQCM).

The HI instrument was mounted on a remotely-controlled rotary platform allowing rotation about an axis parallel with the front baffle edges (i.e. around the pitch axis of the HI instrument, as defined in Figure 3-37). It allowed scanning the centre-line of the HI-1 and HI-2 fields of view with a fixed collimated light beam.

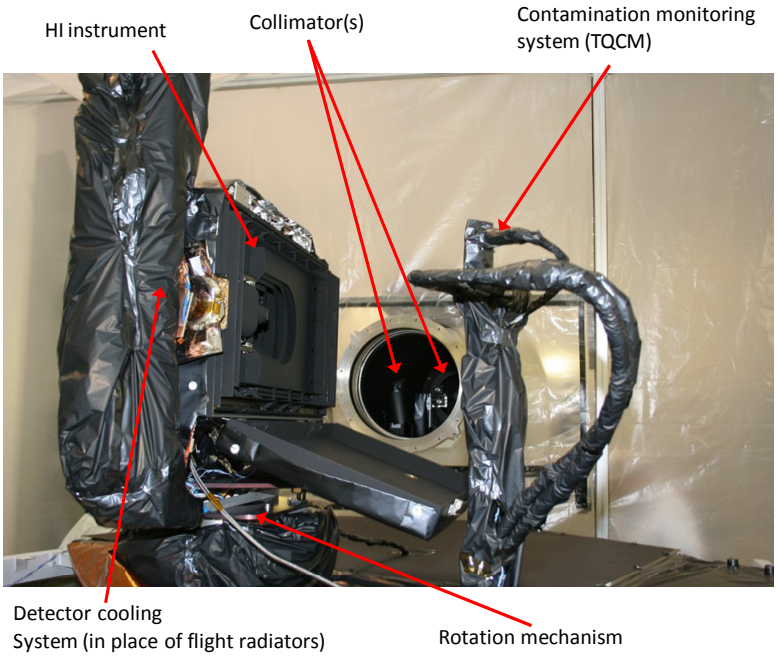

Figure 4-17 **:** The HI-B flight instrument installed in the 3 meter vacuum chamber at CSL for thermal vacuum qualification, optical calibration and end-to-end straylight validation. The chamber cover is here removed, and the instrument is in a class 100 cleanroom.

The optical calibration consisted in a scan of the HI-1 and HI-2 fields of view with a collimated light source to derive plate-scale, focal length, distortion parameter, and point spread function (PSF) of the two cameras as a function of position in their field of view. A response variation across the field of view (i.e. a large-scale flat-field) was also performed [14].

The calibration was performed with an F/10 collimator located in an appendix of the main vacuum chamber (Figure 4-18). It provides a 300 mm diameter collimated beam with a 30 arcsec divergence, much smaller than the Sun divergence (32 arcmin).

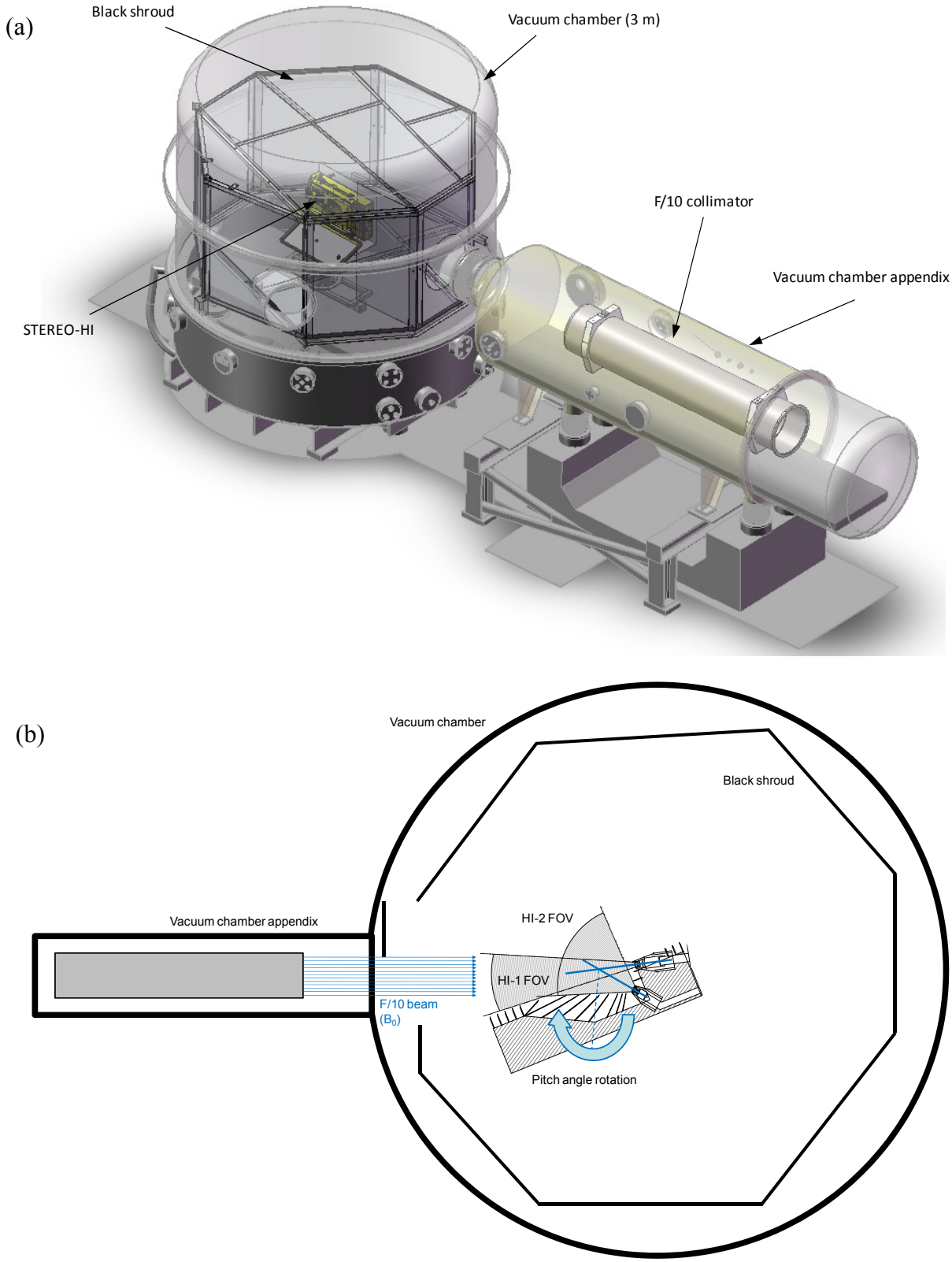

Figure 4-18 **:** (a) 3-D CAD model [Courtesy of CSL] and (b) 2-D sketch of the STEREO-HI flight instruments optical calibration setup, with a 300 mm diameter F/10 collimated beam and a rotation stage allowing rotation about the instrument pitch axis through the intersection of HI-1 and HI-2 optical axis.

The photometric calibration is a key parameter of the instrument performance. A monitoring photodiode was therefore used to calibrate the F/10 collimated beam irradiance versus the wavelength (Figure 4-19). It allowed to derive an accurate preliminary photometric response of the HI-1 and HI-2 cameras.

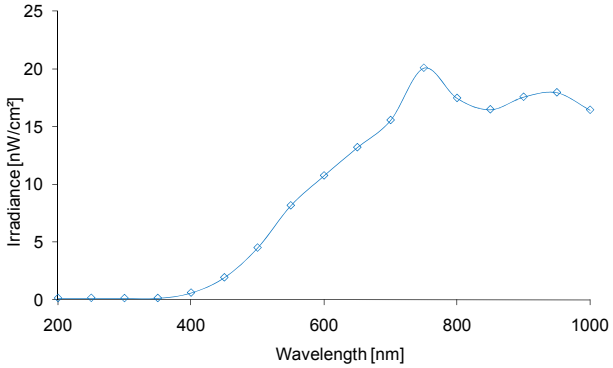

Figure 4-19 **:** F/10 collimated beam irradiance calibration curve, measured in the spectral range of the HI instrument.

4.3.2. Spot size and distortion

The half energy width (HEW) was measured for both cameras of the A and B flight models (Figure 4-20). It provided a quantitative evaluation of the HI-1 and HI-2 spot size along the field of view, even if only measured along one axis (pitch) [14].

The HEW of the HI-1 and HI-2 cameras are respectively between 40-50 µm (i.e. spread over 3-4 pixels) and 40-160 µm (i.e. 3-12 pixels). These measured values are ~ 2 times higher than the instrument design parameters of Table 3-2. It however has a limited impact on the main science objective of CME observation, which is a large and diffuse phenomenon.

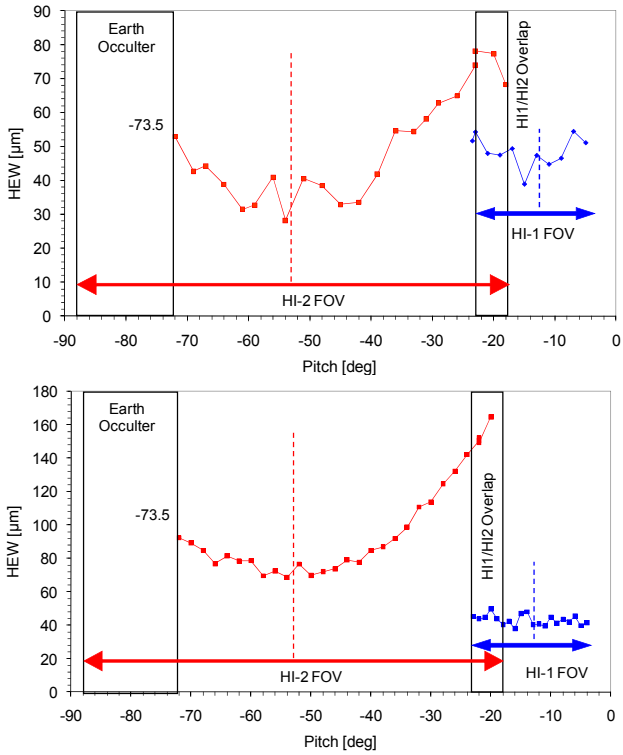

Figure 4-20 **:** Spot of the HI-1 and HI-2 camera for both A and B instrument flight models. The HI-2 field of view is limited on one side by the Earth occulter, and that HI-1 and HI-2 field of view overlaps by 5.54 arcdeg.

The distortion was computed with respect to undistorted optical systems, using formula (4-1), where α is the angular location in field of view and g(α) the distortion function [20]. A best fit with polynomial functions was first performed, but a least-squares fitting of the spot centroids by the Azimuthal/Zenithal Perspective (AZP) projection model of formula (4-2) to obtain a reference for in-flight images with an off-

axis distance onto the detector (4-3), where f is the paraxial focal length and μ the resulting distortion parameter [51].

$$D(\alpha) = \alpha - g(\alpha) \quad \textbf{(4-1)}$$

$$g(\alpha) = \frac{(\mu + 1)\cdot\sin(\alpha)}{\mu + \cos(\alpha)} \quad \textbf{(4-2)}$$

$$r = f\cdot g(\alpha) \quad \textbf{(4-3)}$$

4.3.3. Photometry

The optical throughput and the detector conversion factor in photon/DN @670 nm were obtained with

- the total light flux entering the optical system (computed in the HI-1 and HI-2 FOV along the axis, assuming respectively a 16 mm and 7 mm diameter entrance pupil for HI-1 and HI-2)
- the optics transmission (over the respective HI-1 and HI-2 spectral band-passes of Figure 4-12)

The photometry of HI-A had however large uncertainty because of smearing resulting from shutterless readout. The system was improved for the HI-B final calibration and allowed to derive photometric conversion (4-4) and (4-5) that were considered similar for both A and B instruments.

$$\left(\frac{DN}{s}\right)_{HI1} = 30345\frac{photons}{s} = 9\cdot10^{-5}\frac{nJ}{s} \quad \textbf{(4-4)}$$

$$\left(\frac{DN}{s}\right)_{HI2} = 52626\frac{photons}{s} = 1.6\cdot10^{-5}\frac{nJ}{s} \quad \textbf{(4-5)}$$

4.3.4. Calibration summary

Table 4-3 summarizes the results obtained for each camera of both HI-A and HI-B instruments at +20 °C and detectors at -100 °C, as compared with design values [14][20]. The camera alignments versus instrument reference cubes, compared with design values, are also listed.

	Design	**FM-A**	**FM-B**
HI-1			
Optical axis pitch	13.98 arcdeg	13.97 arcdeg	14 arcdeg
Optical axis yaw	0 arcdeg	0.1544 arcdeg	0.494 arcdeg
Roll	0 arcdeg	0.874 arcdeg	1.021 arcdeg
Focal length	78.456 mm	77.705 mm	77.81 mm
Plate scale	102.4 px / arcdeg	100.471 px / arcdeg	100.613 px / arcdeg
HEW (RMS spot size)	[45.2 μm, 67.6 μm]	[38.8 μm, 54.3 μm]	[37.9 μm , 49.8 μm]
Distortion Fitting parameter	< 0.14 % -	< 0.51 % μ = 0.16675	< 0.11 % μ = 0.10001
Detector conversion	-	(*)	30345 ph/DN @ 670 nm
HI-2			
Optical axis pitch	53.36 arcdeg	53.13 arcdeg	53.31 arcdeg
Optical axis yaw	0 arcdeg	0.02 arcdeg	0.61 arcdeg
Roll	0 arcdeg	0.0174 arcdeg	0.224 arcdeg
Focal length	21.671 mm	21.44 mm	21.64 mm
Plate scale	29.257 px / arcdeg	27.72 px / arcdeg	27.98 px / arcdeg
HEW (RMS spot size)	[105.3 μm, 145 μm]	[31.5 μm, 78.1 μm]	[68.6 μm, 164.8 μm]
Distortion Fitting parameter	< 8.1 % -	< 2.5 % μ = 0.82981	< 2.33 % μ = 0.65062
Detector conversion	-	(*)	52626 ph/DN @ 670 nm

Table 4-3 : Measured HI optical main characteristics (optics at + 20 °C and detectors at -100 °C). No photometric value is available for HI-A (*) because of smearing resulting from shutterless readout.

4.4. End-to-end straylight validation

During the final optical calibration of the HI-A and HI-B flight instruments, an end-to-end straylight validation was performed. It consisted of a characterization of the overall straylight performance of the instrument, and in particular of the front baffle and internal baffle rejection.

4.4.1. Test setup

As compared with the optical calibration, the background straylight in the chamber was lowered as much as possible to reach the straylight rejection capabilities of the instrument

- A black enclosure was created in front of the instrument with a black Kapton layer and a vacuum-compatible black Velvet panel (VelBlack[20], from Energy Science Laboratories Inc) as shown in Figure 4-21. It provided a protection from light reflect by the front baffle, ensuring that at least a small portion of the black shroud is not illuminated by the reflected beam.

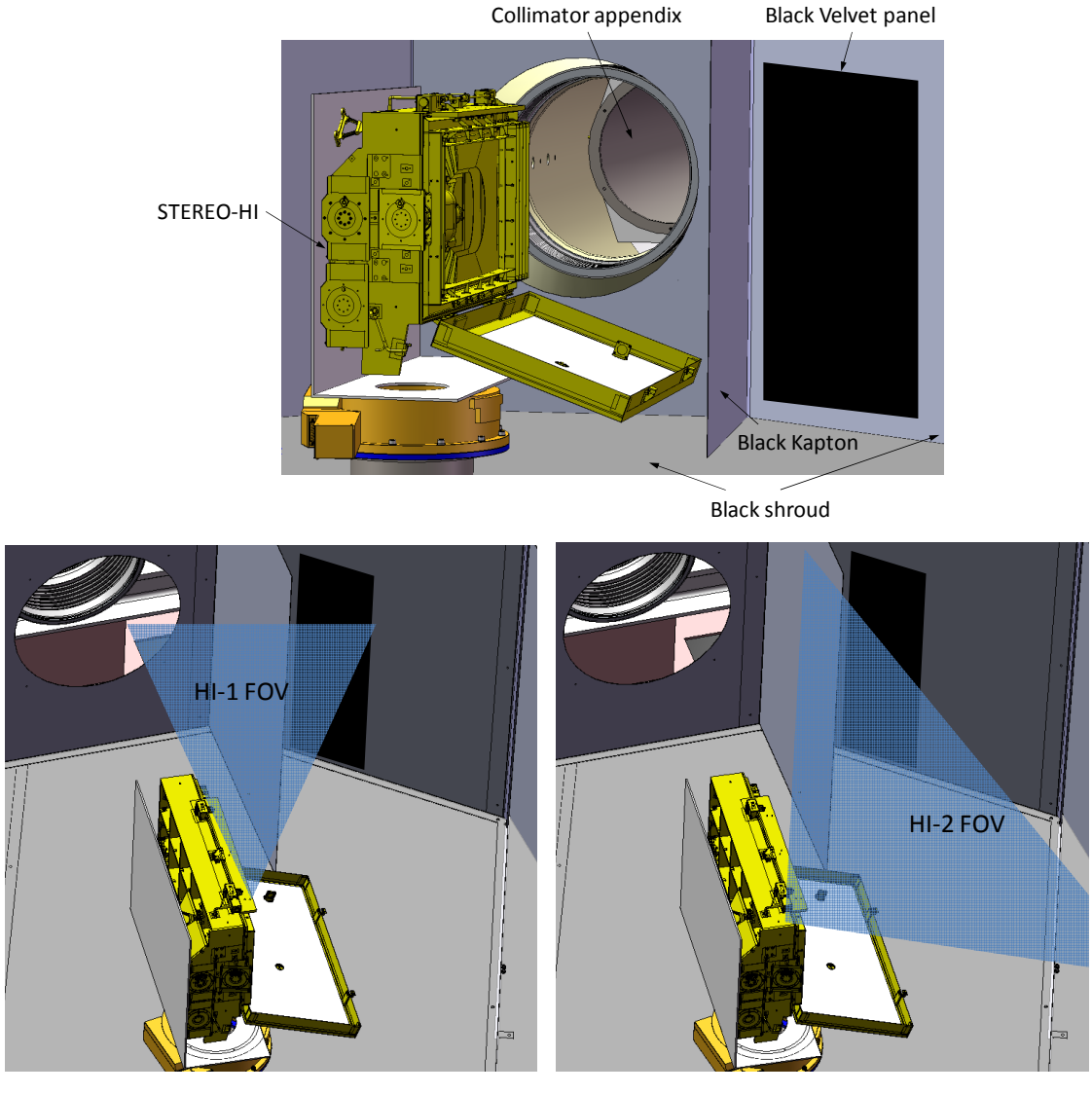

Figure 4-21 : A black cavity was created using VelBlack panel and black Kapton curtain within the HI-1 and HI-2 FOV to provide deep reference black surface.

- Another black Velvet panel was also positioned in the centre of the HI-2 field of view, providing a deep black area facing the instrument, as shown in Figure 4-22.

[20] VelBlack has a TIS ≤ 0.05% at 630 nm, compared with 2–3 % for usual black painted shroud [59].

- A third black Velvet panel was also located behind the instrument to attenuate the part of incident beam which passed over the top of the front baffles (Figure 4-22).

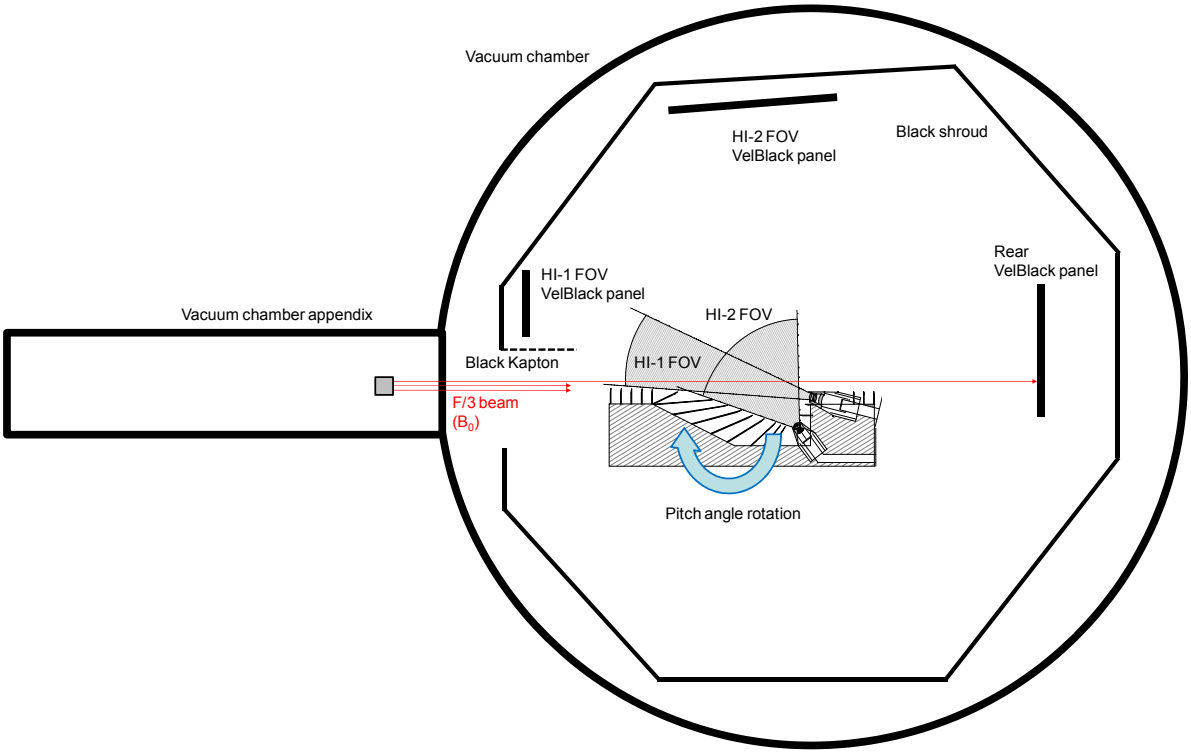

Figure 4-22 **: T**est setup for the STEREO-HI end-to-end straylight validation. VelBlack panels and black Kapton curtains were inserted within the HI-1 and HI-2 FOV to provide deep reference black surface and behind the instrument to catch the direct laser light passing over the instrument.

To measure the front baffle straylight rejection, a 2 W continuous laser diode at 670 nm (within the spectral range of the HI-1 and HI-2 cameras) was used with the F/3 collimator (Figure 2-23) developed for the diffraction measurements on the baffle mock-up and prototype. It provided a collimated output of 83 mW/cm² (Figure 4-23). The collimator divergence of 27.5 arcmin closely matched that of the Sun at 1 AU (i.e. 32 arcmin), and the output intensity was of the same order of magnitude as the total solar flux at 1 AU (i.e. 980 W/m² = 98 mW/cm²).

The internal baffle rejection was measured with the same F/10 collimator used for the photometric calibration (Figure 4-18), with the 2 W laser source. In addition to the monitoring photodiodes used to measure the collimated beams for the photometric calibration, a second similar photodiode allowed to extend the dynamic range of monitoring and cover the higher flux from the F/10 collimator.

The two collimators and the two photodiodes were located in an appendix connected to the main chamber (as shown in Figure 4-22 and Figure 4-24), the photodiodes monitoring the F/10 beam.

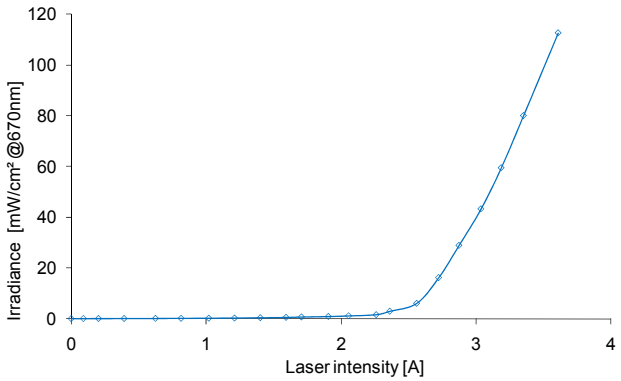

Figure 4-23 **:** F/3 collimated beam irradiance calibration curve measured at 670 nm measured for various laser intensity output. The nominal output of 83 mW/cm² is obtained for 3.35 A.

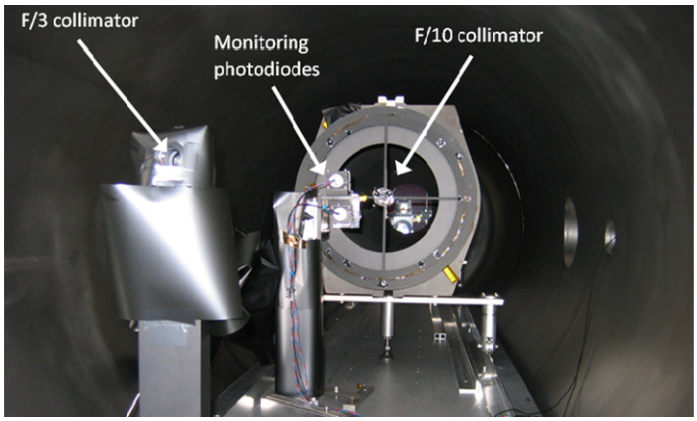

Figure 4-24 **:** The F/3 and F/10 collimators are in an appendix connected to the main vacuum chamber. Two photodiodes were used to monitor the F/10 beam used for optical calibration.

4.4.2. Nominal Sun-pointing – Front baffle

The F/3 beam was set up to be incident and concentrated on the central region of the front baffle top edge, since the diffraction pattern is strongly forward-directed. A larger beam would also have increased the unused flux contributing to the background straylight in the vacuum chamber, without adding significantly to the straylight level at the entrance apertures of the cameras (which are located on the centre-line of the instrument).

Figure 4-25 shows the darkest images captured by the HI-1B and HI-2B cameras during the end-to-end straylight validation with respectively 12 and 60 minutes of exposure duration. The collimated light source is in the nominal Sun direction, *i.e.* 3.65 degrees and 18.35 degrees from the edge of the HI-1 and HI-2 fields of view. In these images, the vacuum chamber appendix is visible with the F/10 collimator, the F/3 collimator simulating Sun is not visible as located out of the FOV, as shown in Figure 4-22. The VelBlack curtains are also part of the image, as shown in Figure 4-21. The instrument door (not fully opened) and internal baffle edges are also imaged in HI-2.

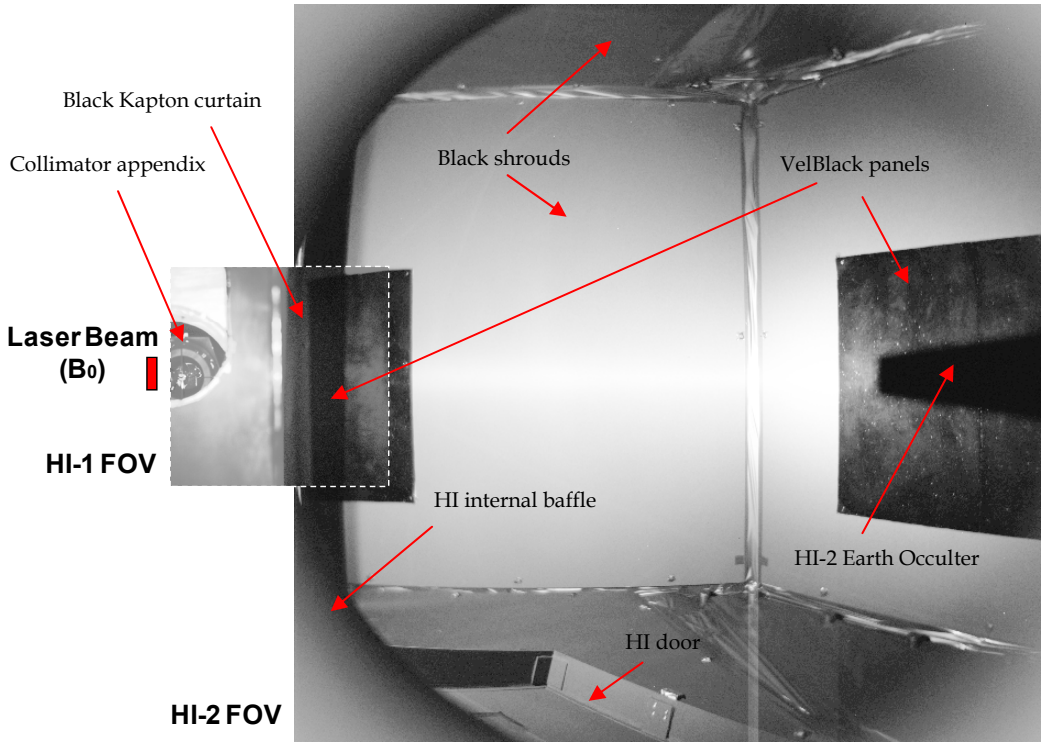

Figure 4-25 **:** Combined HI-1 and HI-2 images (scaled to respective field of view dimensions) captured during end-to-end straylight validation. The direction of the collimated beam is shown (red rectangle) corresponding to the nominal Sun direction. The collimator chamber is imaged by HI-1, with no F/10 beam. The Earth occulter and the door are visible in HI-2. The internal baffle edges are also imaged (defocused) in HI-2.

The measured brightness as a function of the incident beam intensity at some particular points in the HI-1 and HI-2 fields of view is given in Figure 4-26. These values were computed from the knowledge of the incident beam intensity (measured by the monitoring photodiodes) and the photometric responses of the two HI cameras obtained during the optical calibration that was performed before the end-to-end test [14].

The relative rejection (B/B_0) is obtained by dividing the flux (B) on the detector raw image measured in digital number (DN) by the input laser beam flux (B_0) converted in DN.

B_0 is obtained with equation (4-6), where F_{beam} is the beam flux (83 mW/cm², at 670 nm), Ap is the optical system aperture size (Table 3-2), and T_{int} is the integration time (720 s and 3600 s respectively).

$$B_0 = F_{beam} \cdot Ap \cdot T_{int} \qquad \textbf{(4-6)}$$

B_0 is converted in DN units with equations (4-8) and (4-10) obtained from equation (4-7) and (4-4) for HI-1, and (4-9) and (4-5) for HI-2.

$$\left(B_0\right)_{HI1(720s)} = 1.202\times 10^{8}\,nJ = 4\cdot 10^{17}\,ph_{670nm} \qquad \textbf{(4-7)}$$

$$DN_{HI1(720s)} = 7.5\cdot 10^{-14} B_0 \qquad \textbf{(4-8)}$$

$$\left(B_0\right)_{HI2(1800s)} = 1.035\times 10^{9}\,nJ = 3.5\cdot 10^{18}\,ph_{670nm} \qquad \textbf{(4-9)}$$

$$DN_{HI2(1800s)} = 1.5\cdot 10^{-14} B_0 \qquad \textbf{(4-10)}$$

The darkest areas of the images are ~ 1 DN above the detector dark current (DC) offset of 126 DN (measured in the under-scan[21] columns of the detector). Rejection levels of ~ 7.5 10^{-14} B/B_0 and ~ 1.5 10^{-14} B/B_0 for HI-1 and HI-2 respectively were thus derived from these images. These values are at the limit of the detector sensitivity and represent upper limits on instrument straylight levels. The rest of the image was limited by the brightness of the various background features of the vacuum chamber and black enclosure in the fields of view of the cameras.

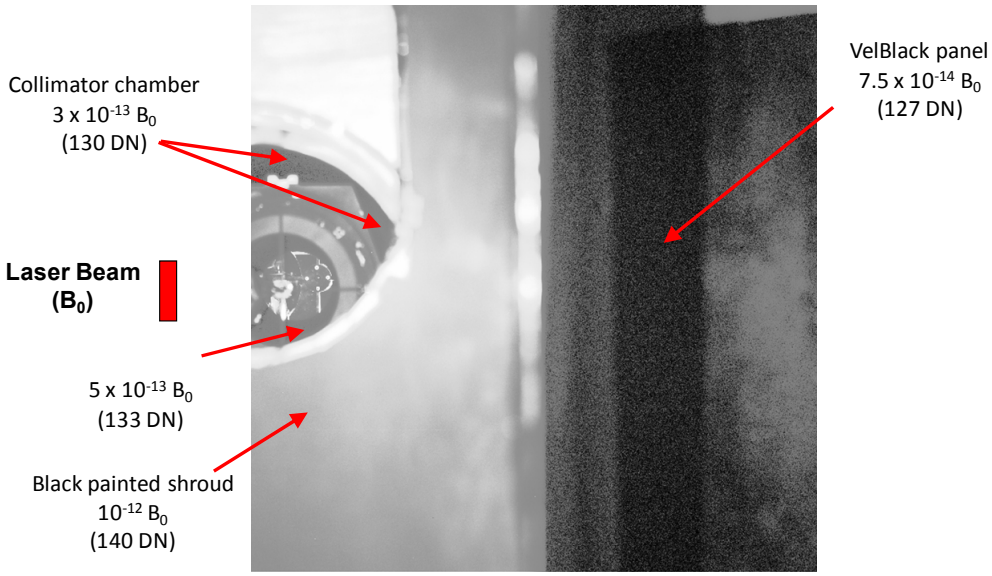

[21] The STEREO SECCHI detectors have 2048 x 2048 imaging pixels. During these tests, the CCD detectors were read out in a 2176 x 2112 pixel format. The first 50 columns were non-imaging "under-scan" columns (DC offset pixels) and the last 78 were "over-scan" columns. The last 64 rows were over-scan rows. The under-scan pixels are used for determining the DC offset, and over-scan pixels to ensure that charge is completely cleared before the next line is transferred into the serial readout register of the CCD [20].

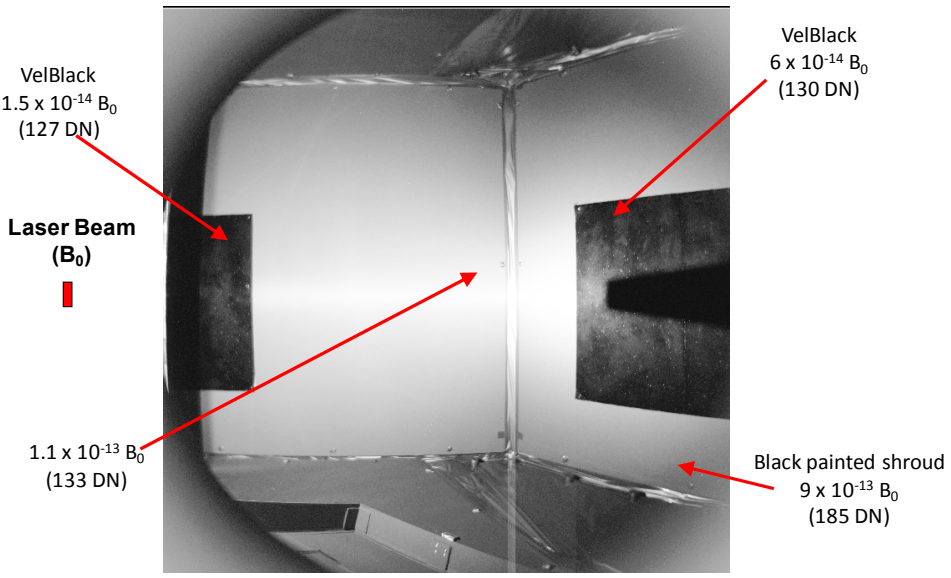

Figure 4-26 : End-to-end straylight evaluation of the (top) HI-1 and (bottom) HI-2 cameras on the HI-B flight instrument. The direction of the collimated beam is shown (red rectangles) corresponding to the nominal Sun direction. The measured level converted in B_0 unit, where B_0 is the light source brightness (and the corresponding DN value) is given at various points in the field of view.

The results are summarised in Table 4-4. They are the same than the computed straylight level of Table 3-24 and very close of the required values. They are however at the limit of what can be measured and their accuracy depends of the knowledge of the DC offset.

In regions where the background scattered light was suppressed sufficiently, *e.g.* by the VelBlack panels, the straylight attenuation of the instrument is at the requirements level. These results thus provide a confirmation of the front baffle straylight performance.

	Straylight requirement	**Computed straylight**	**Measured straylight**
HI-1	≤ 3 10^{-13}	6.9 10^{-14}	7.5 10^{-14}
HI-2	≤ 10^{-14}	1.1 10^{-14}	1.5 10^{-14}

Table 4-4 : HI-1 and HI-2 measured end-to-end straylight, expressed in B/B_0 (where B_0 is the input brightness), as compared with computed straylight level from front baffle and instrument straylight requirement.

4.4.3. Off-pointing – Front baffle

Images were also captured with the same F/3 collimated laser beam at negative pitch off-point angles (i.e. the instrument rotated towards the beam direction, as shown in Figure 4-27) in order to determine the margin on front baffle rejection performance.

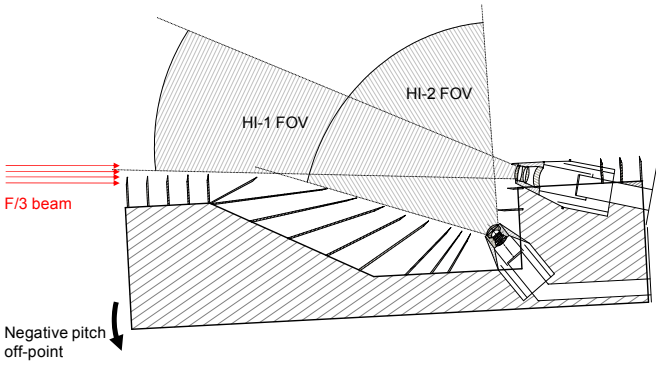

Figure 4-27 **:** To quantify the margin on front baffle rejection, the instrument was rotated towards the beam direction, i.e. with negative pitch angle.

As shown on Figure 4-28, the straylight level logically gradually increases with the off-point. An annulus-like straylight pattern also appears from a pitch angle of -0.33 arcdeg, even if the background straylight remains lower than the required 3 x 10^{-13} B/B_0 down to -0.5 arcdeg off-point. This ring pattern corresponds to the modelled lens barrel out-of-field reflection of Figure 3-15.

For large angles, the straylight from the front baffle increases the background and the intensity of the associated ring pattern rapidly increases. These results however indicate that the rejection from the front baffle presents some margin, and consequently there is a margin of at least 0.33 arcdeg on the instrument pointing towards the Sun.

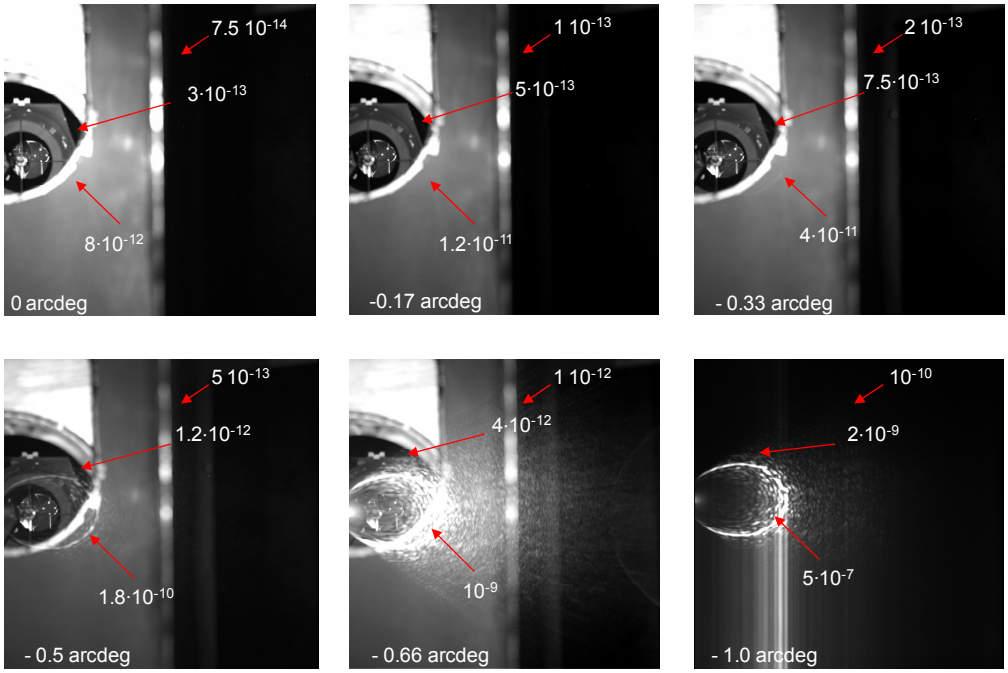

Figure 4-28 **:** HI-1 FM-B images for light sources at 0 to 1.0 arcdeg pitch angles. The measured level (expressed in B/B_0, where B_0 is the direct beam brightness) is given at various locations in the FOV.

4.4.4. Out-of-field and ghost straylight – Internal baffle

To quantify the straylight level from out-of-field straylight source, i.e. from internal baffle, the F/10 collimated beam was used to illuminate as much as possible the internal baffle area. As for previous off-pointing, the instrument was rotated towards the collimated beam, to simulate various incident angles onto the instrument (as shown on Figure 4-29 for some particular angles). It also allowed observing ghosts associated to in-field beam source without damaging the detectors when the beam is focused on it.

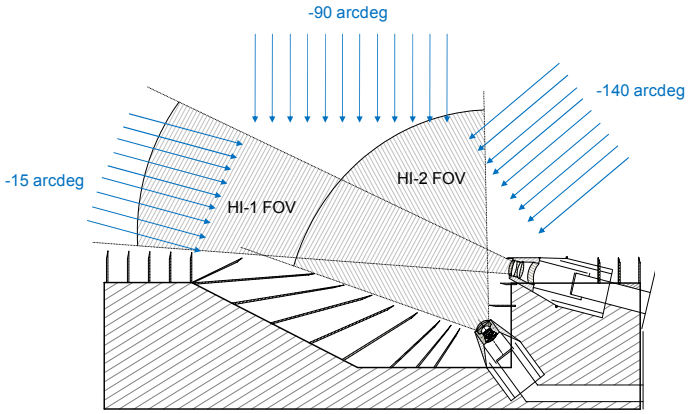

Figure 4-29 **:** Out-of field straylight and ghosts were measured with the F/10 collimated beam. The instrument was rotated towards negative pitch angles in order to illuminate the internal baffle.

For large pitch offsets, when beam is approaching the fields of view, the laser beam intensity and the integration time were reduced to avoid saturation of the image. As shown on Figure 4-30:

- The straylight ring pattern resulting from the out of field beam progressively worsens until being (logically) focused when the beam is in the HI-1 FOV (i.e. between -4 and -24 arcdeg)
- Within the FOV, the camera detectors and ghosts associated with the focused beam were observed and quantified.
- A similar ring pattern then logically appears when the beam is on the other side of the FOV (Figure 4-30).

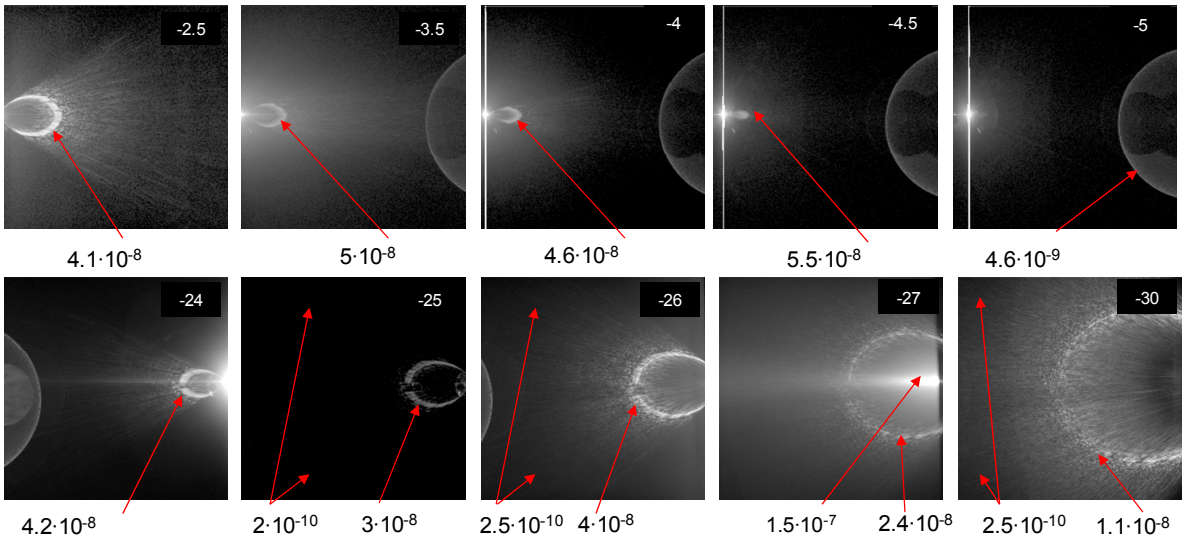

Figure 4-30 **:** HI-1 FM-B images for light sources from -2.5 to -30 arcdeg pitch angles. Images captured between -4 and -24 arcdeg are within the FOV, and consequently the beam is also imaged on the detector. The measured level (in B/B_0 unit, where B_0 is the light source brightness) is given at various locations in the FOV.

As for HI-1, when a bright object is close of the HI-2 field of view border (i.e. below 18 arcdeg or above 88 arcdeg), images contains straylight that come from reflection on the CCD, lens surfaces and on the Earth occulter, but also a diffuse contribution from the internal baffle, as shown on Figure 4-31.

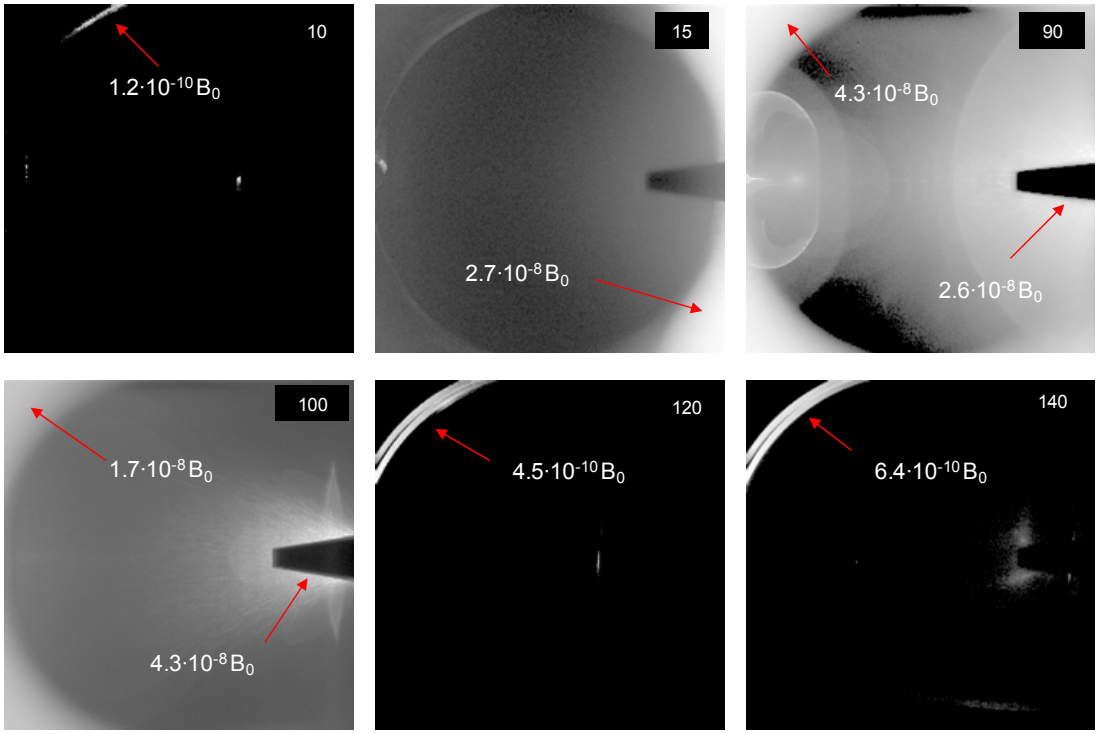

Figure 4-31 **:** Ghost pattern in HI-2 FM-B images with light source out along pitch angle from 10 to 140 arcdeg, measured during the on-ground optical calibration. The measured level (in B_0 unit, where B_0 is the light source brightness) is given at various points in the field of view.

Using the same method than for Figure 4-26, measured brightness in HI-1 and HI-2 as a function of the incident beam intensity was computed at some particular points in the fields of view for the increasing pitch angles. The B_0 value was computed taking into a conversion factor obtained in a similar way than for (4-8) and (4-10) adapted to the beam intensity and integration time (flux of 24 µW @ 652 nm, and integration time between 5 and 180 seconds).

In the FOV, the level of the focused beam corresponds to the B_0 value (i.e. $B/B_0 = 1$), the beam illuminating the whole HI-1 entrance aperture. For out-of-field light, the background straylight level remains respectively below $2.5\ 10^{-10}\ B/B_0$ in HI-1 and $2.6\ 10^{-8}\ B/B_0$ in HI-2, corresponding to the upper level of straylight coming from the internal baffle.

These values are higher than obtained in nominal pointing (Figure 4-26), but the effective straylight at the detector level shall take into account the relative brightness of the out-of-field potential straylight source of Table 3-4 that will effectively illuminate the internal baffle in flight. For HI-1, it is essentially the Earth which is the brightest out-of-field source, with a $10^{-6}\ B/B_0$ relative brightness For HI-2 it is the Earth and the SWAVES boom respectively of $2.10^{-5}\ B/B_0$ and $10^{-6}\ B/B_0$, where B_0 is the Sun brightness.

Table 4-5 summarises the measured out-of-field straylight, i.e. the internal baffle contribution to the instrument straylight level. In HI-1, the straylight is below the requirement. In HI-2, it is at requirement. They are not of the some order of magnitude than the computed rejection Table 3-25 (including first lens cleanliness impact). The difference between measurement and predicted values most probably come from the lens barrel rejection that are different than modelled (as noticed in Figure 4-10).

	Straylight requirement	**Computed straylight**	**Measured straylight**
HI-1	$3\ 10^{-13}$	$6.8\ 10^{-14}$	$2.5\ 10^{-10} \times 10^{-6} = 2.5\ 10^{-16}$
HI-2	10^{-14}	$8.2\ 10^{-15}$	$6.4\ 10^{-10} \times 2.10^{-5} = 1.2\ 10^{-14}$
			$2.6\ 10^{-8} \times 10^{-6} = 2.6\ 10^{-14}$

Table 4-5 : HI-A and HI-2 measured out-of-field straylight, taking into account the two major straylight sources, expressed in B/B_0 (where B_0 is the input brightness), as compared with computed straylight level from internal baffle and instrument straylight requirement.

4.5. Chapter summary

The on-ground calibration of the STEREO-HI instruments included sub-system and system measurements.

At sub-system level, a prototype of the front baffle rejection was tested down to a rejection level of $6\ 10^{-10}$ B/B_0. It validated the front baffle design and provided confirmation of the expected solar disk rejection at HI-1 and HI-2 entrance aperture, even if the edge were not at the flight heights.

The lens barrel assemblies were also tested. In particular the out-of-field lens barrel rejection was measured. The accuracy of the results was however not sufficient to validate the corresponding ray-tracing model and an effective 10^{-2} rejection can only be considered for the theoretical model of both cameras.

The end-to-end straylight verification at instrument level however showed a very good correspondence with the expected instrument straylight level for both the front and the internal baffles, as summarised in Table 4-6.

- The experimental result is better than prediction for HI-1 and slightly higher for HI-2. This is due to the uncertainties on the lens barrel rejections, which was not measured accurately enough to correlate the respective models.
- The straylight level in HI-1 is dominated by the front baffle, as the level coming from the internal baffle is two orders of magnitude lower. In HI-2 it is equally influenced by the front and internal baffle and their sum (i.e. $1.6\ 10^{-14}$ and $2.6\ 10^{-14}$) is slightly above the requirement. The level from the internal baffle however depends on the source brightness, and this value is an upper limit.

	Straylight requirement	**Computed straylight**	**Measured straylight**
HI-1	$3\ 10^{-13}$	$6.9\ 10^{-14}$	$\sim 7.5\ 10^{-14}$
HI-2	10^{-14}	$1.1\ 10^{-14}$	$\sim 4.1\ 10^{-14}$

Table 4-6 : HI-A and HI-2 measured and computed straylight level from front baffle in HI-1 and from front and internal baffle in HI-2, expressed in B/B_0 (where B_0 is the input brightness), as compared instrument straylight requirement.

Chapter 5. In-flight straylight characterization of the STEREO-HI instrument

5. In-flight straylight characterization of the STEREO-HI instrument

Two types of in-flight straylight were characterized: the straylight from the Sun disk, attenuated by the front baffle, and the straylight from the sky and payload, attenuated by the internal baffle.

- The solar straylight was analysed and compared with the on-ground results using images captured when the spacecraft was off-pointing towards the Sun.
- The evolution of the sky and payload straylight with time was quantified on the basis of regular in-flight images.

5.1. In-flight images

5.1.1. Image processing

As for all scientific instruments, dedicated routines have been developed by the scientific community to process the STEREO-HI images and derive scientific results. These routines have been here used for the in-flight straylight analysis, taking care not to remove the straylight contribution of the raw images.

The images used for in-flight straylight characterization are either 2048 x 2048 non-binned or 1024×1024 binned images. They are calibrated using the Solar Soft SECCHI_PREP routine [50] in order to (i) correct for shutterless operations, (ii) take into account a flat-field correction (the SECCHI_PREP version used here applies the flat-field measured during on-ground calibration), (iii) calibrate the instrument pointing [51] and (iv) to weight images according to their exposure time (i.e. convert images from DN to DN/s).

The image processing also ignores images containing bad areas (resulting from telemetry problem), and bad images (such as those contaminated by data from other STEREO instruments). The Not a Number (NaN) values in images were also ignored.

5.1.2. Background removal

The STEREO-HI in-flight images are also enhanced, as described in [20], by subtracting a background image computed using a minimum filter over a set of nominal pointing images. This background principally consists of the slowly varying F-corona with, to a lesser extent, a contribution due to the more rapidly varying K-coronal components (the streamer belt) [38].

An example of such background removal is shown in Figure 5-1 for HI-1 a typical image, revealing the fine structure of the solar corona.

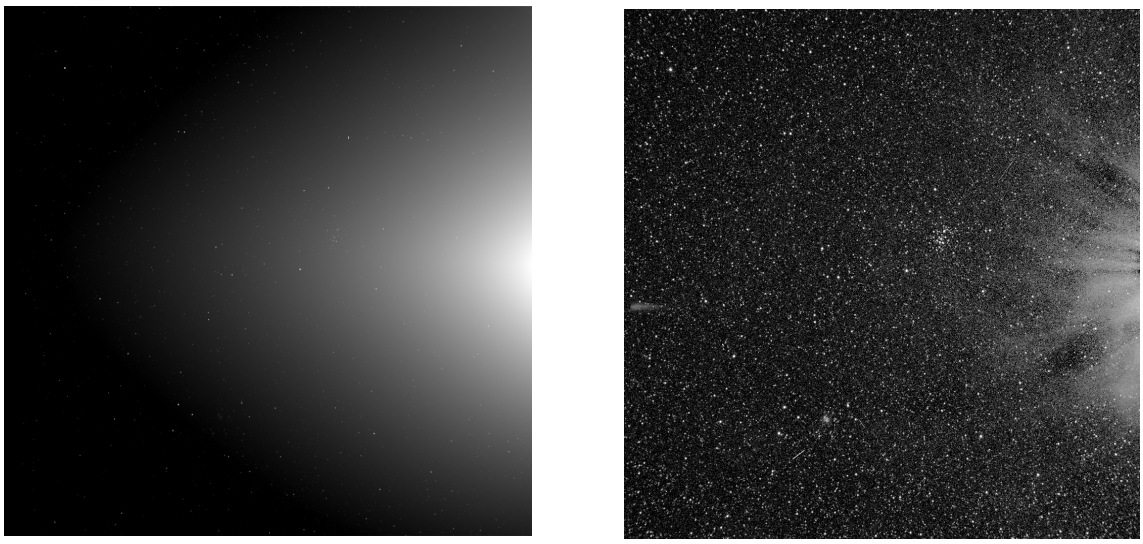

Figure 5-1: Example of a nominal-pointing HI-1A image pre (left) and post (right) zodiacal background removal. The Sun is off the right-hand side of the image.

5.1.3. Conversion factor

To derive quantitative results from the HI flight images, a conversion factor is used to translate from the detector measurement units in $DN.s^{-1}.px^{-1}$ to MSB unit (as defined in equation (3-1)).

Preliminary conversion factors were produced from the on-ground calibration (equation (4-8) and (4-10)), allowing conversion of the data output by the instrument into physical units (DN to nJ or, equivalently, DN to photons at the 670 nm central bandpass wavelength) [14]. These conversion factors were used to compute the straylight level during on-ground straylight validation, but also at the start of the mission in order to confirm the solar rejection performance [16].

More accurate post-launch conversion factors have since been obtained [52][53] and were used to derive the in-flight straylight analysis quantitative results. The difference is however very small and does not affect the comparison between on-ground and in-flight straylight.

	HI-1A	**HI-1B**	**HI-2A**	**HI-2B**
Pre-flight [14]	7.5×10^{-14}		1.5×10^{-14}	
Post-flight [52] [53]	8.89×10^{-14}	8.86×10^{-14}	1.07×10^{-14}	1.14×10^{-14}

Table 5-1: STEREO-HI in-flight conversion factor [$B_0/DN.s^{-1}.px^{-1}$], where B_0 is the MSB.

The conversion factors of Table 5-1 must however be multiplied by 4 when images are processed with SECCHI_PREP, since the intensities are converted to units of $DN.s^{-1}$ per CCD pixel and the conversion factors are based on the total $DN.s^{-1}$ per pixel of the 2 x 2 binned images.

5.2. Solar straylight

The front baffle has been designed to reject the Sun disk brightness. The analysis of in-flight image was thus conducted to determine the effective performance of the front baffle.

5.2.1. Off-pointing images

In-flight solar straylight characterization is based on images captured in a configuration where the STEREO spacecraft was off-pointing as compared to its nominal pointing to the Sun progressively shifting the HI images toward the Sun, similarly to what was simulated during on-ground end-to-end straylight validation (Figure 4-22) where the instrument was rotated towards the collimated beam direction (i.e. negative pitch angle).

For such off-pointed images, the background removal process (as described in § 5.1.1) has been performed using a set of nominal image captured on the day of off-pointing and by shifting the background obtained at nominal pointing horizontally by the number of pixels corresponding to the off-point angle (Figure 5-2). This results in a more accurate background subtraction but has the disadvantage of not providing values in the small region where the shifted background does not overlap with the image.

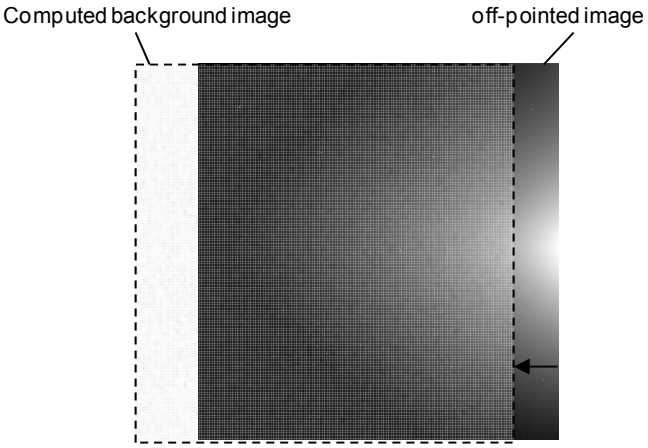

Figure 5-2: Example of background removal for off-pointed images (here HI-1) where the background is shifted horizontally by the number of pixels corresponding to the off-point angle. The Sun is on the right hand side.

No correction for the image distortion has been made when subtracting the shifted background images from the off-pointed images, because distortion is small in the HI-1 cameras (~1% for the edge of the 10 arcdeg circular field of view and ~2% in the image corners [14]). Furthermore, because the off-point angles are small compared to the size of the field of view, the difference in distortion (i.e. the relative plate-scale of the pixels) between pixels in the off-pointed image and those in the shifted background is negligible (<< 1%).

An average over the four consecutive images captured for each off-pointing angle is also performed to reduce the noise in the darkest regions.

5.2.2. Intensity profile

For each pixel within the in-flight images, the angle from the boresight (used as abscises in the rejection curves), i.e. the elongation as defined from the Sun centre, is calculated taking into account the deviation from the gnomonic projection due to the wide-angle nature of the cameras, as described in [51].

The in-flight solar straylight has been characterized on the basis of intensity profile across the detector versus the elongation, obtained either with the image values along the horizontal centre line (Figure 5-3a) or with an horizontal strip obtained by averaging over ±50 pixels (Figure 5-3b) around the central line to reduce statistical fluctuations when endeavouring to assess the instrumental solar straylight.

The intensity profile values were converted from DN/s in B_0 unit using conversion factor of Table 5-1.

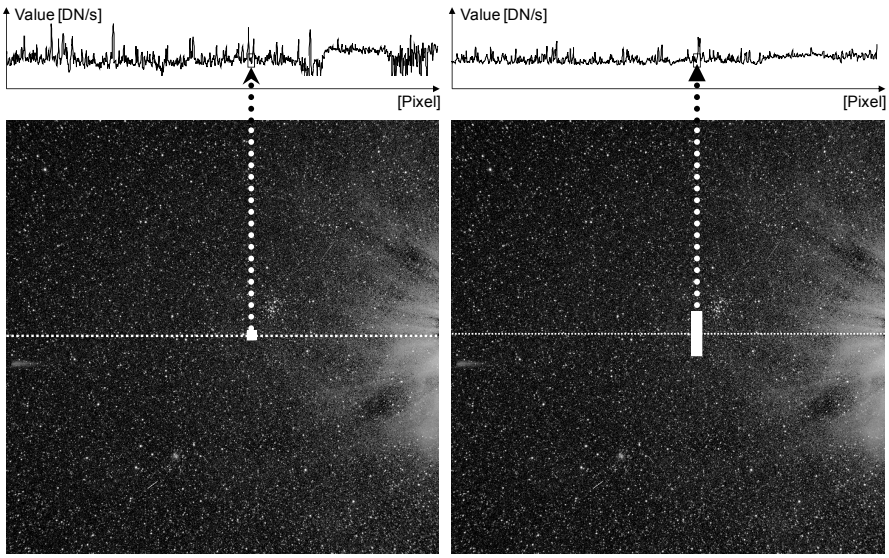

Figure 5-3 : Example of the derivation of an in-flight intensity profile from an HI-1A processed image, for comparison with the theoretical straylight rejection curve using (left) the image horizontal centre line pixel values and (right) image horizontal central strip. The Sun is on the right hand side.

5.2.3. HI-1 cameras

The HI-1 in-flight solar straylight characterization is based on January 2007 and May 2010 (Figure 5-4) pitch off-pointed images.

- The in-flight off-pointed images from January 2007 were taken at instrument pointing angle of -0.25, -0.5, -0.75, -1.00 and -1.50 arcdeg in pitch, progressively shifting the image toward the Sun.
- In May 2010, similar off-pointed images were taken, except that the largest off-point was -1.25 arcdeg instead of -1.5 arcdeg in order to limit the image saturation. Additionally, off-pointed images with positive pitch of +0.5 and +1.0 arcdeg were also taken, shifting the image away from the Sun.

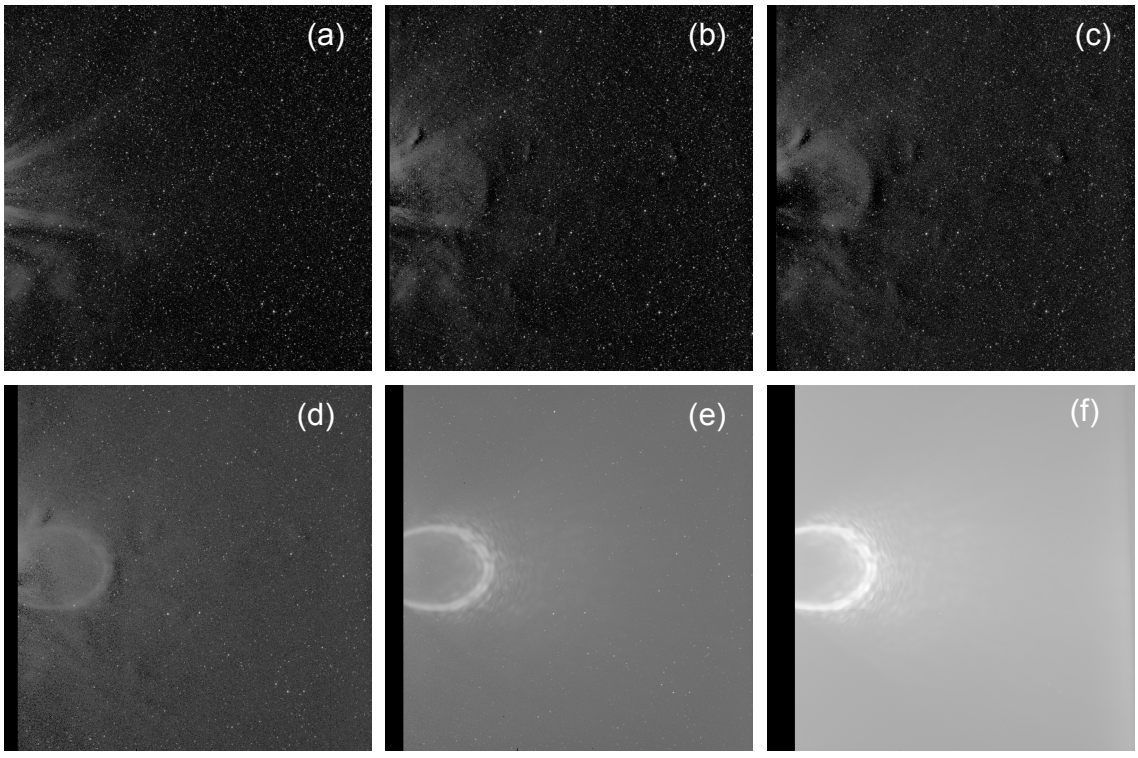

Figure 5-4 : Background subtracted HI-1B in-flight images (May 2010) for increasing pitch off-points (a) 0 arcdeg (b) -0.25 arcdeg (c) -0.5 arcdeg (d) -0.75 arcdeg (e) -1.00 arcdeg (f) -1.25 arcdeg. Negative off-points are towards the Sun which, here for HI-B, is off the left-hand side of the image.

As mentioned in § 3.3.2, the front baffle was designed for an HI-1 boresight offset at 13.65 arcdeg from Sun-centre. To compare with theoretical rejection curve it is therefore necessary to take into account the additional 0.33 arcdeg pitch angle offset that was added during the mounting of the HI instruments onto the STEREO spacecraft (Figure 5-5) [20]. This additional offset provided a margin in the straylight rejection of the front baffle above what was predicted theoretically, resulting in an effective 13.98 arcdeg offset of the HI boresight. The 0 arcdeg off-point is the nominal instrument pointing, but the images taken at a -0.25 arcdeg off-point are therefore the closest to the theoretical diffraction model and were used to compare the measured straylight with theoretical predictions.

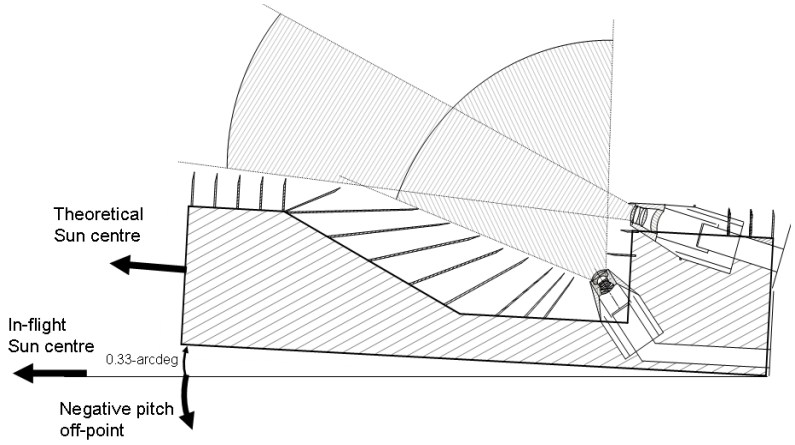

Figure 5-5: HI pitch angle pointing with respect to the Sun-center direction. An additional 0.33 arcdeg has been added to the HI-1 field of view pointing angle from the Sun center as compared to value considered in the front baffle model.

The Figure 5-6 shows the comparison of the theoretical estimate of the straylight with the in-flight computed straylight from -0.25 arcdeg off-point images of 2010, along the central line and the central strip, expressed in units of B_0 and plotted as function of the elongation (defined from the Sun centre). The theoretical prediction is based on the theoretical front baffle rejection curve Figure 3-28 and a 10^{-2} average lens barrel rejection (first out of the FOV measured point of Figure 4-10). The in-flight values were obtained using conversion factor of Table 5-1 (multiplied by a factor 4 as images are processed with SECCHI_PREP).

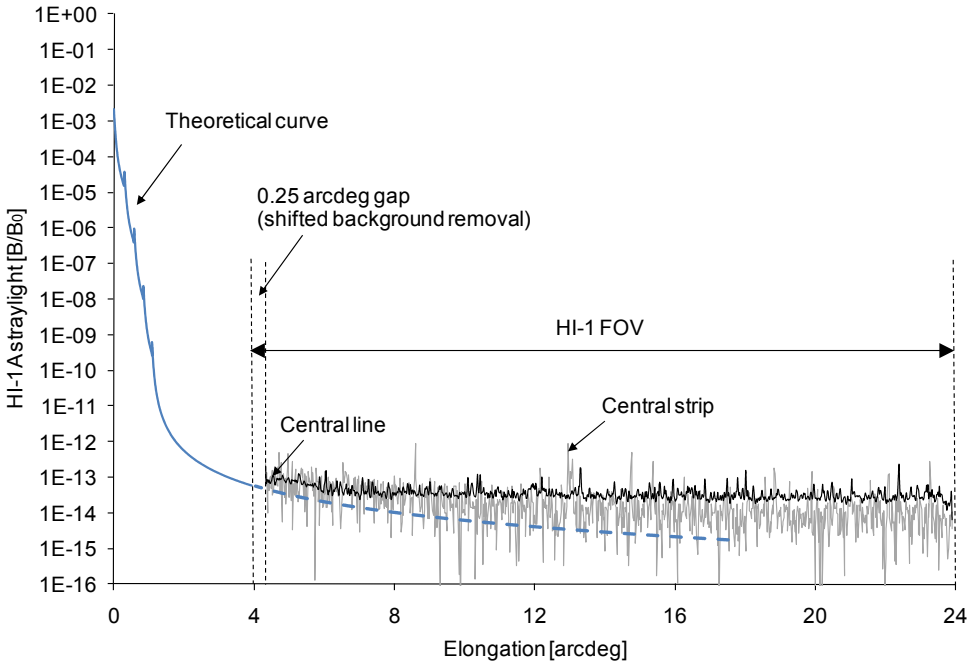

Figure 5-6 : HI-1A straylight level for the -0.25 arcdeg pitch off-point captured in May 2010, quoted in B/B_0 (where B_0 is here the MSB), along both the horizontal centre line and the central strip, plotted as function of elongation. The theoretical straylight curve is show for comparison.

The measured in-flight straylight in the HI-1 field of view, ranging from 4 to 24 arcdeg of elongation, is below 10^{-13} B/B_0. At the FOV border, the measured level is very close of the predicted straylight level. For larger elongation angles, the level is above the theoretical curve because this last one corresponds to an out of field straylight (i.e. not directly imaged on the detector) that is consequently not part of the field of view (dot line in Figure 5-6). It shows the good performance of the instrument baffle system. Figure 5-6 also indicates that the horizontal central strip curve is, as expected, much less noisy but still follows the horizontal central line curve closely, and can therefore be used for comparison with theoretical straylight.

As shown in Figure 5-7 (left), the level in the field of view at +0.5 arcdeg is very similar but slightly below the one obtained with the nominal science images (0 arcdeg off-point). Figure 5-7 (right) also shows that the straylight at 0 arcdeg is not much less than at -0.5 arcdeg off-points towards the Sun. Straylight is thus not completely removed by the background subtraction, and what is measured at this offset is really straylight.

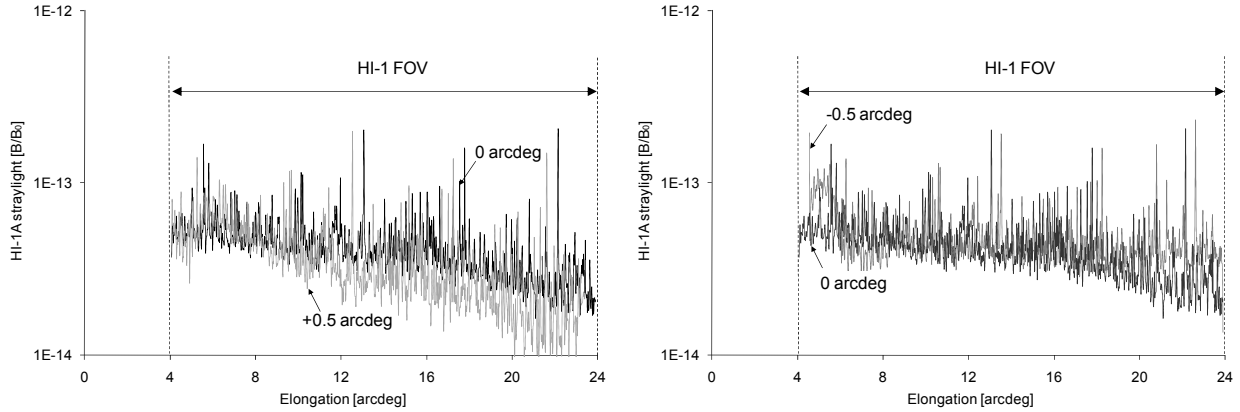

Figure 5-7 : HI-1A straylight level along horizontal central strip (left) for the +0.5 arcdeg pitch off-point as compared with 0 arcdeg, and (right) for the -0.5 arcdeg pitch off-point as compared with 0 arcdeg, from May 2010 and quoted in B/B_0, plotted as function of elongation.

Figure 5-8 shows the comparison of theoretical straylight with in-flight straylight for the HI-1A and HI-1B off-point images from May 2010, calculated along the central strip, expressed in B_0 unit and plotted as a function of the elongation. The straylight level logically increases with increasingly negative off-pointing angle. Figure 5-8 also shows that the straylight along the centre strip is very similar for both HI-1A and HI-1B, as shown in detail in Figure 5-9 (left) for the -0.25 arcdeg off-pointing angle as measured in May 2010.

In Figure 5-8 (right), a small bump is also observed for larger off-pointing angles. It reveals the additional ring-pattern straylight already observed during on-ground measurements (Figure 4-28), which is not due to the sunlight diffracted by the front baffle system but reflections within the HI-1 lens barrel (as visible in Figure 5-4).

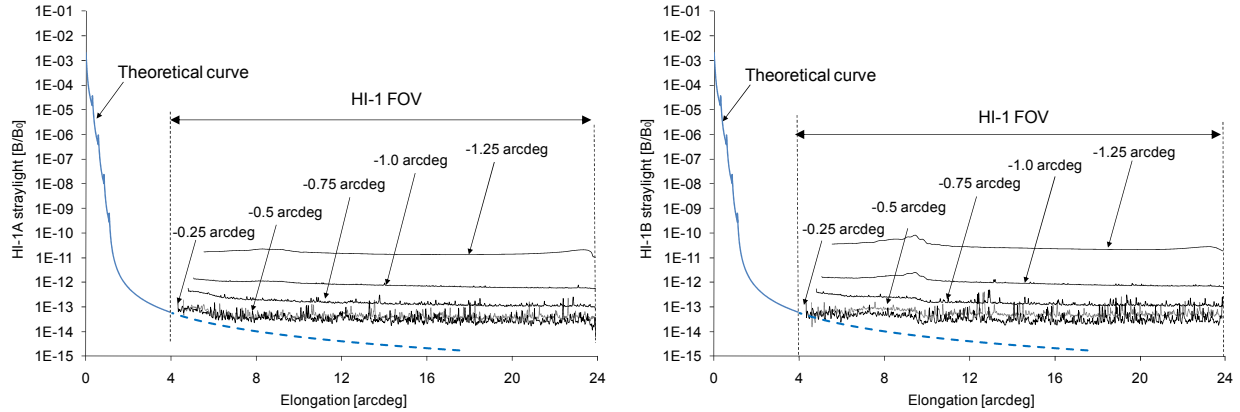

Figure 5-8 : HI-1A (left) and HI-1B (right) straylight level along horizontal central strip, for increasing off-pointing images compared with the theoretical straylight curve, from May 2010 and quoted in B/B_0, as function of elongation.

As shown in Figure 5-9 (right) for the largest off-point angle (-1.25 arcdeg) the ring pattern intensity is slightly higher in HI-1B than in HI-1A, probably because of a difference in the lens barrel internal coatings.

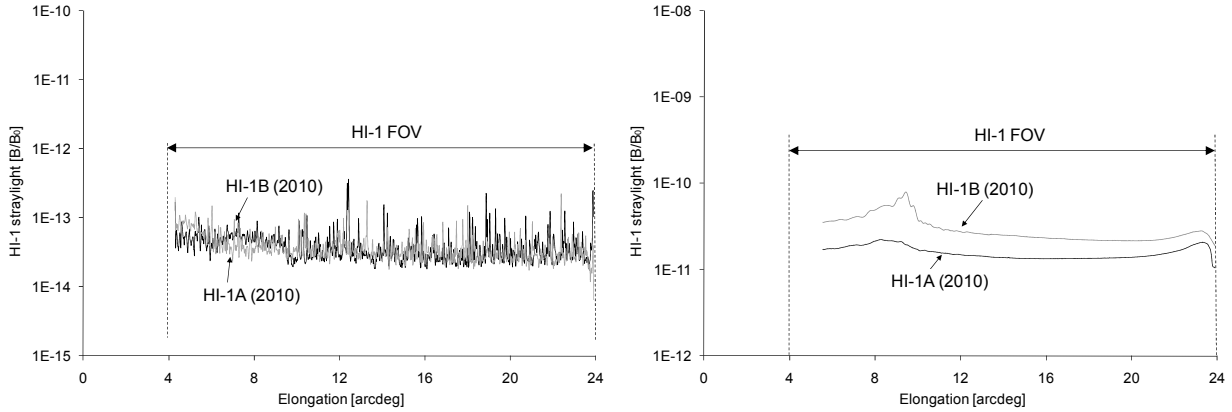

Figure 5-9 : HI-1A and HI-1B straylight along the horizontal centre strip (left) for the -0.25 arcdeg off-pointing (right) for the -1.25 arcdeg off-pointing, from May 2010 and quoted in B/B_0, plotted as function of elongation.

Figure 5-10 provides a comparison between the predicted diffraction curves and the measured straylight level in HI-1B images at the various off-point angles. The theoretical curves are derived from front baffle diffraction model of § 3.3.2 with a diffraction angle increased by the off-point value.

At the smaller off-points the measurements are of a similar magnitude to the predicted diffraction (which assumes a factor of 10^{-2} for the lens barrel rejection), but at the larger off-points the measured curve lies significantly above the prediction, which is consistent with additional reflections within the lens barrel. Because of the additional 0.33 arcdeg pitch offset added for flight (Figure 5-5), the theoretical curves at 0, -0.25, -0.5, -0.75 and -1.0 arcdeg correspond to in-flight images at -0.25, -0.5, -0.75, -1.0 and -1.25 arcdeg.

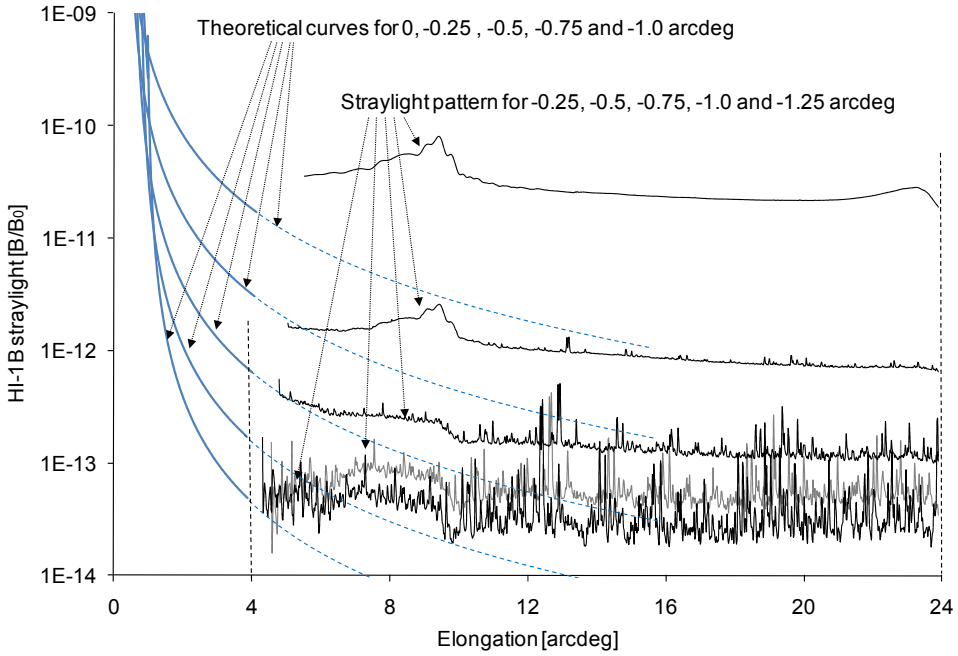

Figure 5-10 : Detail of the HI-1B straylight levels along the horizontal central strip, for increasing off-pointing images, from May 2010, quoted in B/B_0 and plotted as a function of the elongation, revealing additional straylight pattern.

The average over the horizontal centre strip of HI-1A and HI-1B images is shown in Figure 5-11 for increasing off-point of 2010, as compared with lowest values of on-ground images (Figure 4-28). The average of flight image is used (and not the maximum) to avoid spikes in the central line associated to bright stars. The -0.33 arcdeg offset has been added to the on-ground off-pointing angles. The in-flight measured straylight is below the requirement up to -0.75 arcdeg and is very similar to the corresponding on-ground values.

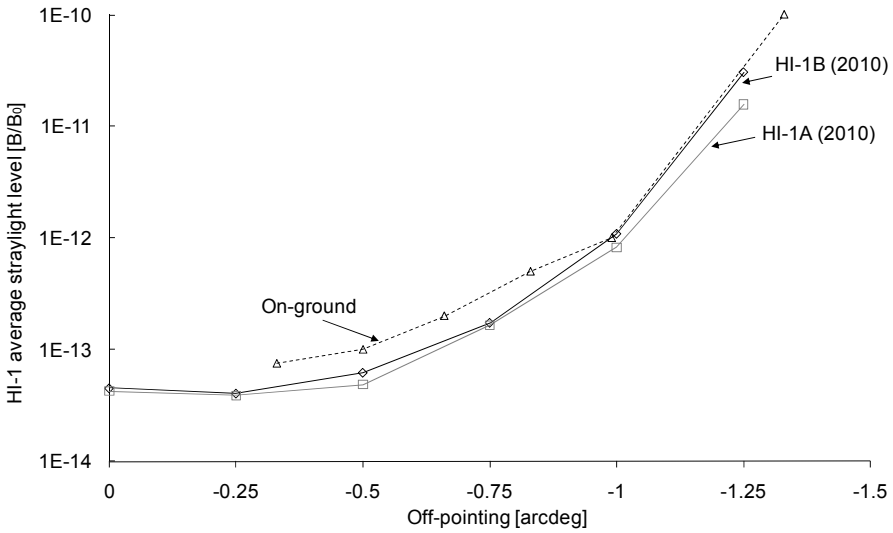

Figure 5-11 : Average straylight level along the horizontal central strip of in-flight HI-1A and HI-1B images (2010), quoted in B/B_0 and plotted as a function of the increasing off-pointing, as compared with corresponding on-ground values (shifted by the -0.33 arcdeg offset).

The average values along the horizontal centre strip for 0 and -0.25 arcdeg off-point is summarised in Table 5-2 for HI-1A and HI-1B, for both 2007 and 2010. Also noted in Table 5-2 is the requirement and on-ground measured value (Figure 4-26) for the per pixel straylight level at the anti-sunward edge of the HI-1 field of view where the signal is the weakest [15]; this is the same for HI-1A and HI-1B.

The straylight levels is thus below the requirement value, showing that the front baffle efficiency is well within the required level in the science images, and is of the same order as the on-ground straylight measurement.

	Requirement	**On-ground straylight**	**0 arcdeg**		**-0.25 arcdeg**	
			2007	**2010**	**2007**	**2010**
HI-1A	$3\ 10^{-13}$	$7.5\ 10^{-14}$	$3.8\ 10^{-14}$	$4.3\ 10^{-14}$	$5.1\ 10^{-14}$	$3.9\ 10^{-14}$
HI-1B			-	$4.5\ 10^{-14}$	-	$4.1\ 10^{-14}$

Table 5-2: HI-1 average level, in B/B_0, at 0 arcdeg and -0.25 arcdeg, compared with straylight requirement and on-ground measured values.

The straylight along the horizontal centre strip as observed by HI-1A also shows only a minor change from 2007 to 2010 for all off-points angles, as shown in Figure 5-12 (left) for -0.25 arcdeg and in Figure 5-12 (right) for -1.0 arcdeg (the largest off-point angle common to 2007 and 2010 series).

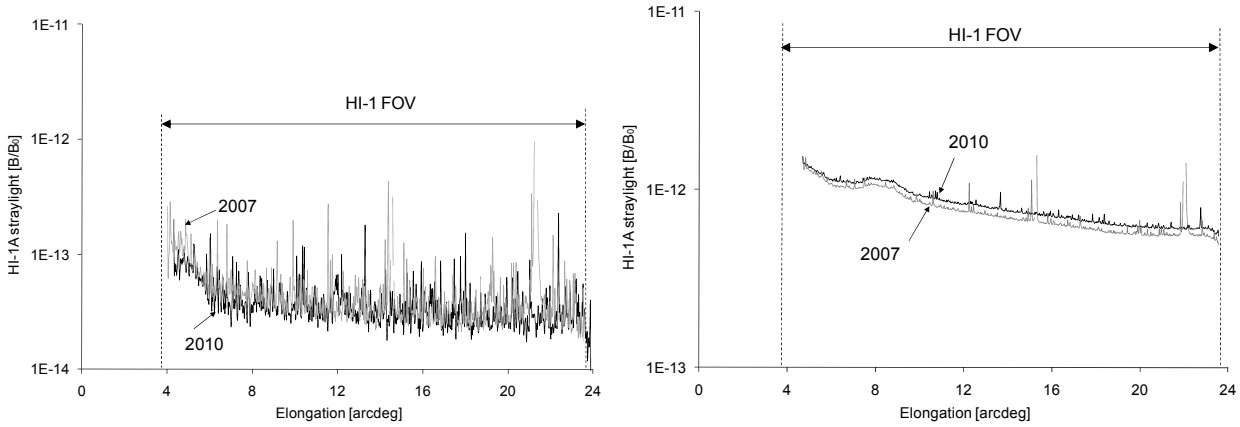

Figure 5-12 : HI-1A straylight along the horizontal centre strip, (left) for -0.25 arcdeg off-point, and (right) -1.0 arcdeg off-pointing angles from January 2007 and May 2010, quoted in units of B_0 and plotted as function of the elongation.

This indicates that the front baffle efficiency, and hence the quality of the multi-edge diffraction, has not been degraded over the three first years of the mission.

The measured level is noisier in 2007 because of many bright stars within the field of view, that are not removed by the background subtraction. Investigation of HI-1B straylight evolution between 2007 and 2010 was also not possible because of the presence of comet Mc-Naught in the off-pointed images taken in January 2007 [22].

Nevertheless, the close similarity between the off-pointed images taken by HI-1A and HI-1B in 2010 (Figure 5-9 a) suggests that straylight evolution for HI-1B is likely to be very similar to that for HI-1A.

5.2.4. HI-2 cameras

As for HI-1, off-pointing images have been used to quantity the solar straylight in H-2. The off-pointing HI-2 images have been processed using the same method that was done for HI-1. Figure 5-13 presents the off-pointed HI-2B background-subtracted images taken in 2010 showing the increase in straylight with the increasing off-point angle, computed using the conversion of the results to B_0 obtained with the in-flight values of Table 5-1 (multiplied by a factor 4 as images are processed with SECCHI_PREP).

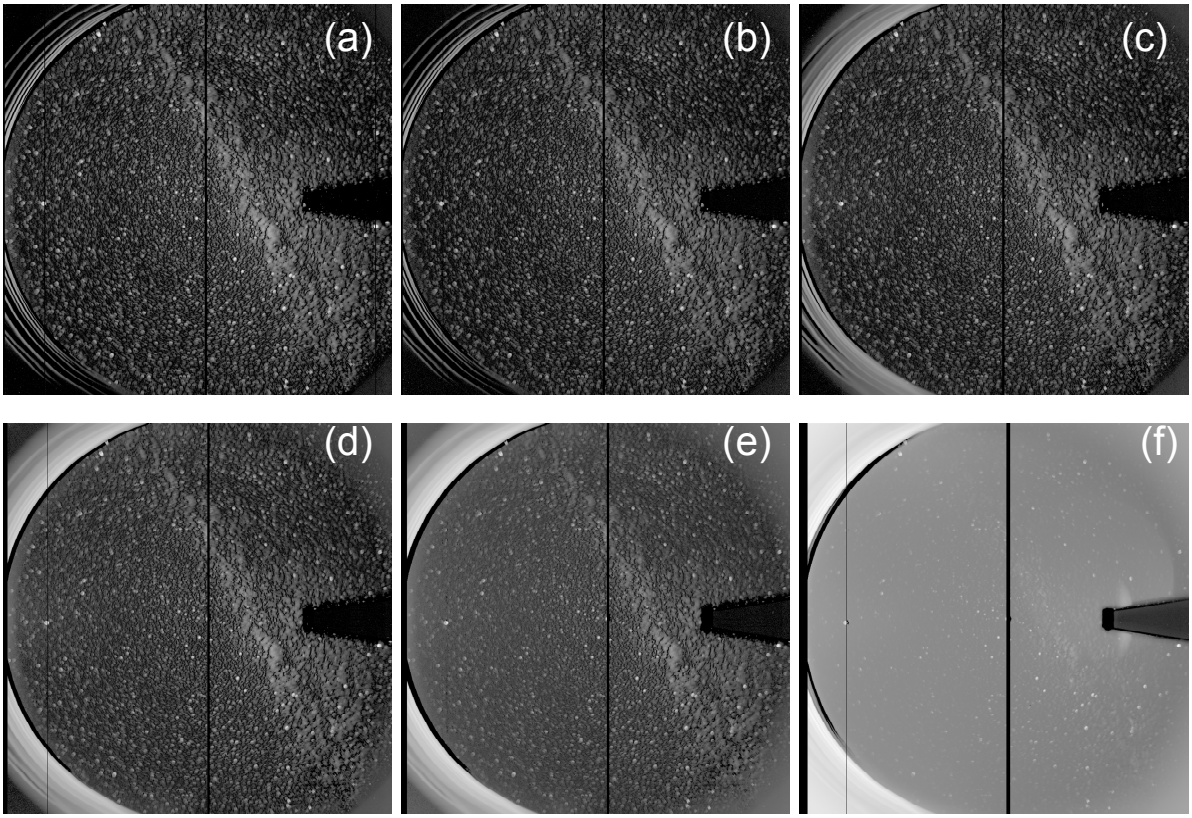

Figure 5-13 : Background-subtracted HI-2B in-flight images from May 2010 for increasing pitch off-points (a) 0 arcdeg (b) -0.25 arcdeg (c) -0.5 arcdeg (d) -0.75 arcdeg (e) -1.00 arcdeg (f) -1.25 arcdeg. Negative off-points are towards the Sun which, here for HI-2B, is off the image's left-hand side.

As compared with HI-1 curves of Figure 5-8, the horizontal central strip curves in HI-2 at the off-pointing angles (Figure 5-14) are dominated by the bright objects within the field of view, in particular in HI-2B where the Milky Way is present.

The intensity along the horizontal central strip in the HI-2A and HI-2B images is $< 2.10^{-14}$ B_0 across the entire field of view for the -0.25 arcdeg off-pointing, except for the region where un-subtracted stars dominates the residual intensity.

The intensity at a fixed elongation (taking into account the off-point) logically increases with increasingly negative off-point. For the largest off-point angle, i.e. -1.25 arcdeg, the image is clearly dominated by solar straylight (Figure 5-13 f).

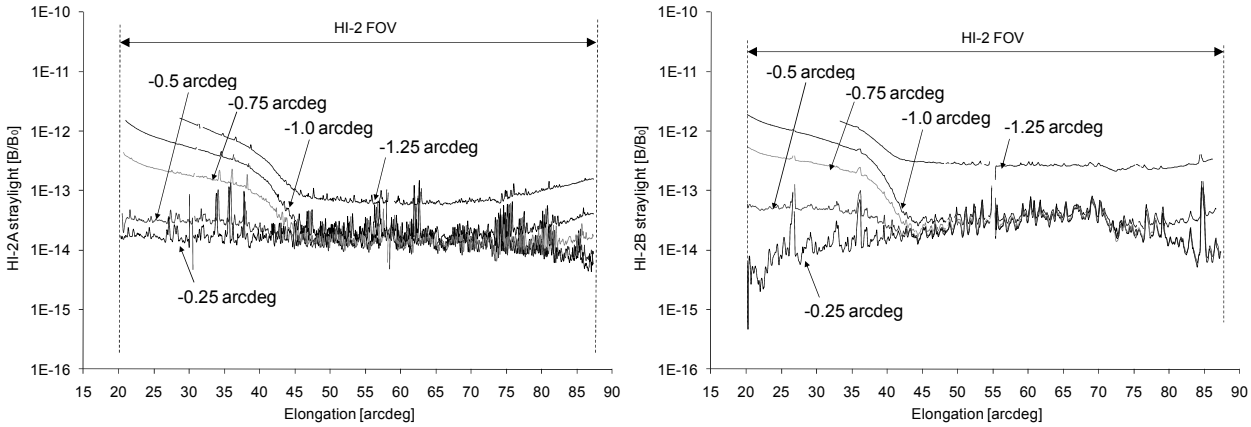

Figure 5-14 : HI-2A (left) and HI-2B (right) straylight level, along the horizontal central strip, for increasing off-pointing images captured in May 2010 and quoted in units of B_0, plotted as function of the elongation.

The average over the horizontal centre strip of HI-2A and HI-2B images is shown in Figure 5-15 for increasing off-point of 2010, as compared with lowest values of on-ground images. The -0.33 arcdeg offset has been added to the on-ground off-pointing angles.

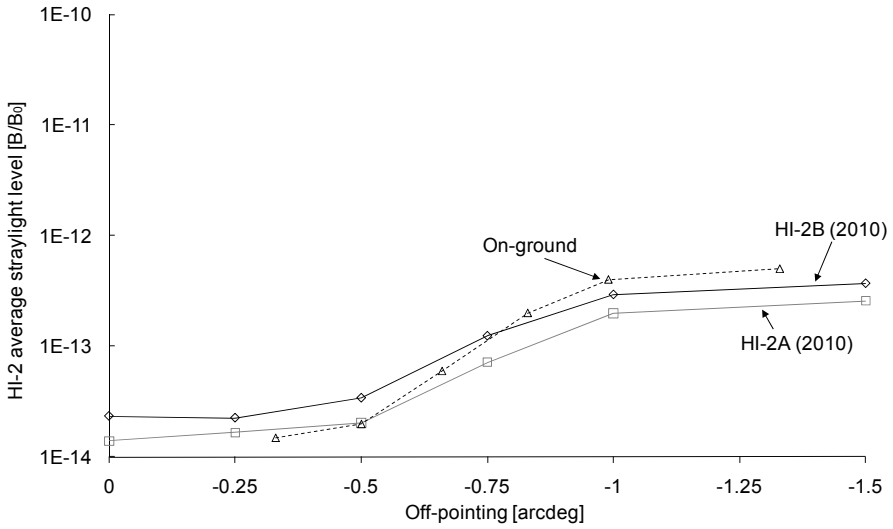

Figure 5-15 : Average straylight level along the horizontal central strip of in-flight HI-1A and HI-1B images (2010), quoted in B/B_0 and plotted as a function of the increasing off-pointing, as compared with corresponding on-ground values (shifted by the -0.33 arcdeg offset).

The average level in HI-2A and HI-2B is summarized in Table 5-3 for 0 and -0.25 arcdeg off-pointing, along with the requirement and on-ground measured values. The overall straylight is at the requirements level in both HI-2A and HI-2B.

	Requirement	**On-ground straylight**	**0 arcdeg**		**-0.25 arcdeg**	
			2007	**2010**	**2007**	**2010**
HI-2A	$1\ 10^{-14}$	$1.5\ 10^{-14}$	$1.7\ 10^{-14}$	$1.4\ 10^{-14}$	$1.9\ 10^{-14}$	$1.7\ 10^{-14}$
HI-2B			-	$1.9\ 10^{-14}$	-	$2.2\ 10^{-14}$

Table 5-3 **:** HI-2 average level, in B/B_0, at 0 arcdeg and -0.25 arcdeg, compared with straylight requirement and on-ground measured values.

As shown on Figure 5-16 (left), the straylight level is also stable since 2007 and is similar in both HI-2A and HI-2B as shown in Figure 5-16 (right).

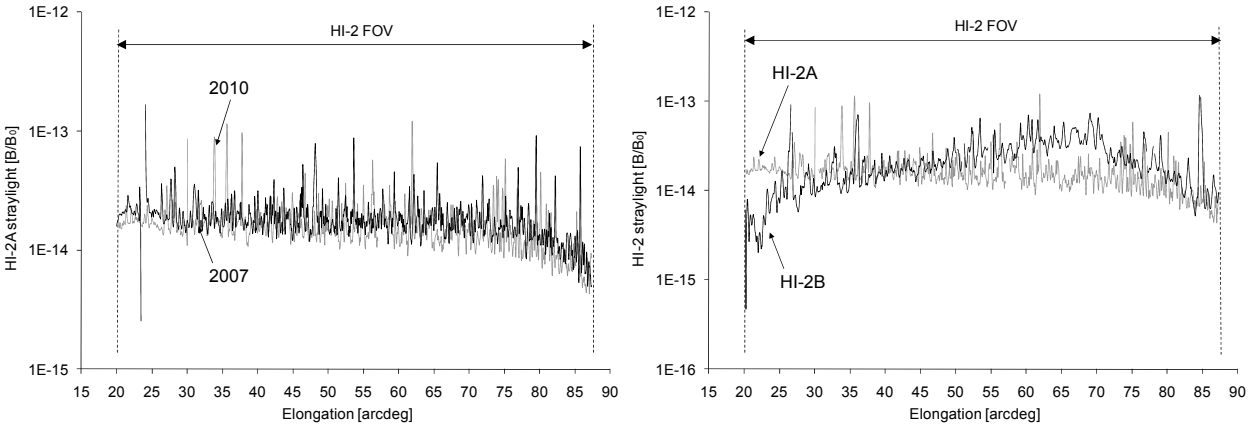

Figure 5-16: Left: Comparison of HI-2A straylight level at -0.25 arcdeg off-point, along the horizontal central strip, from images taken in January 2007 and May 2010. Right: Comparison of HI-2A and HI-2B straylight level at -0.25 arcdeg off-point from images of May 2010. Plots are quoted in B/B_0 as function of the elongation.

5.3. Other straylight sources

The straylight in the HI image results not only from the diffracted direct solar light but also from stellar objects facing the instrument and from bright payload elements located around the instrument cavity, as shown in Figure 3-48. Their light is attenuated by the internal baffle before being reflected to the camera entrance apertures, as shown on Figure 5-17.

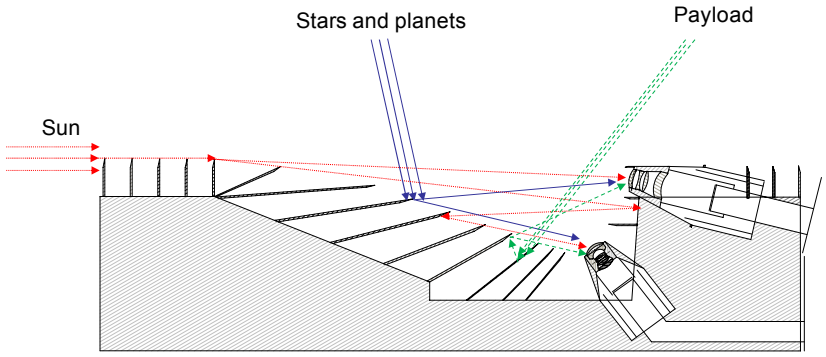

Figure 5-17 : Straylight sources in HI-1 and HI-2 camera: straylight from the Sun (red lines), from bright sources facing the instrument (blue lines) and from payload elements (green lines).

The front baffle performance was analysed with off-pointed images acquired at two periods of the mission. In order to analyse the internal baffle performance and try to determine the contribution of the non-solar straylight sources in the intensity profile plots Figure 5-8 and Figure 5-14, only the nominal pointing images acquired over the mission were available.

The peaks in the central line of the images of Figure 5-4 and Figure 5-13, highlighted in the intensity profile plots Figure 5-8 and Figure 5-14, correspond to bright objects located in the field of view.

Taking advantage of the internal baffle that is part of the HI-2 image, as shown on Figure 5-18, it is possible to follow the evolution of the straylight associated to the internal baffle using the measured intensity of the edges. It is indeed an indicator of the associated straylight diffused over the entire image.

The sunward corners of the HI-2 images (#2 and #4 as defined in Figure 5-14) are indeed completely vignetted by the internal baffle and are imaging regions deep down in the internal baffle cavity. These corners are thus not illuminated by the light sources within the field of view, and a signal in these corners thus stands as straylight (i.e. signal coming from bright sources and illuminated payload elements out of the FOV, mostly from anti-sunward direction, producing a background in the image). The anti-sunward corners of the HI-2 images (#1 and #3 as defined in Figure 5-19) are partially vignetted, being outside the nominal 35 arcdeg FOV. The signal in these corners thus includes light from in-field and a straylight contribution (mostly from sunward direction).

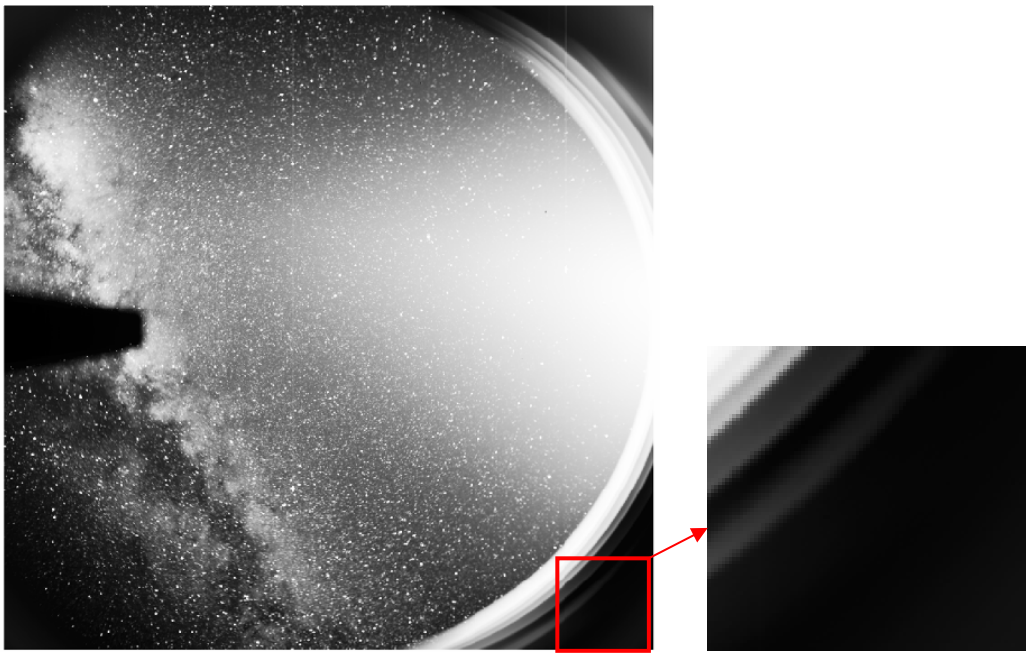

Figure 5-18 : HI-2A in-flight image (background not removed), where non-solar bright sources illuminate the internal baffle. A subset of the image shows the internal baffle edges. The Sun is on the right hand side.

The overall straylight evolution in the HI-2 images has thus been tracked by comparing the average intensity over the four 50 x 50 pixels image corners (Figure 5-19) with the average over the entire field of view, assuming the straylight is uniformly spread over the entire field of view including the corners.

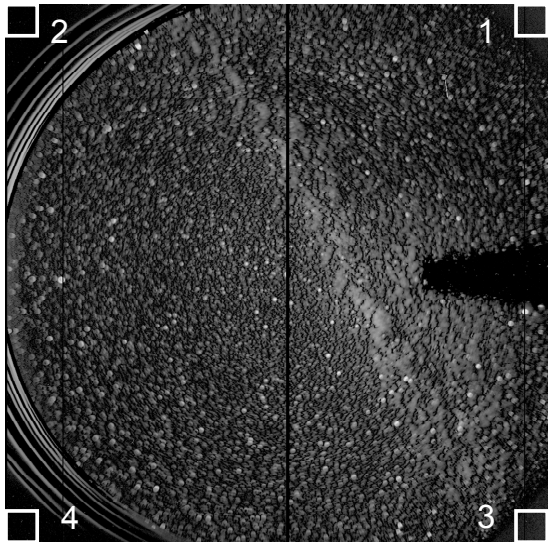

Figure 5-19 : Definition of the image corners in the HI-2 straylight analysis (here shown for HI-2B). Corners 1 and 3 are those on the anti-sunward edge of the field of view (on the right hand side for HI-2A and left hand side for HI-2B), whereas corners 2 and 4 are on the sunward edge.

The straylight evolution in the HI-2A and HI-2B corners has been monitored over the first five years of the mission using non-binned (2048 x 2048) and un-processed images taken in nominal pointing (no off-point).

The HI-2A and HI-2B corner averages is shown in Figure 5-20, quoted in B/B_0 using conversion factor of Table 5-1 (without the multiplicative factor 4 as images are not processed with SECCHI_PREP), as a function of time. The signal level is very similar in the four corners, and consequently the measured level effectively comes from a straylight background and not from in-field objects, otherwise it would differ in corners sunward (2 and 4) and anti-sunward corners (1 and 3) which also contains directly imaged light sources.

(a)

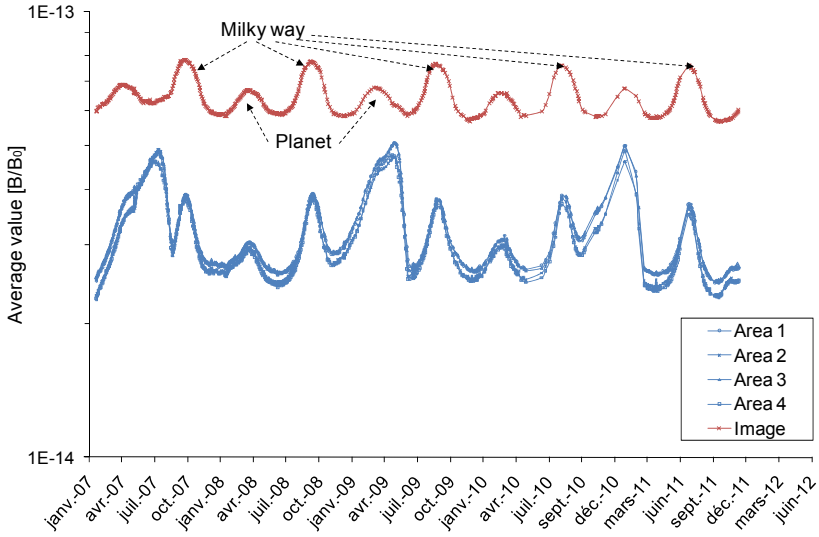

(b)

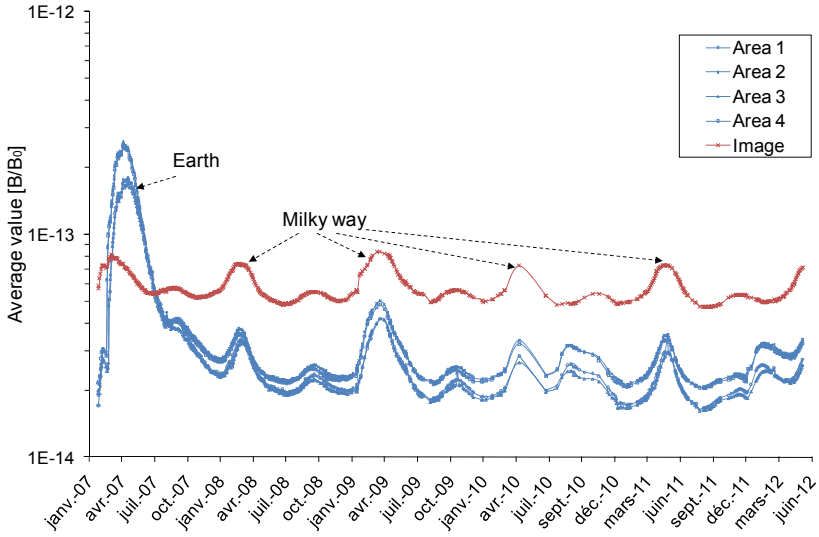

Figure 5-20 : Straylight evolution over time over 5 years in HI-2A (a) and HI-2B (b) corners (blue curves) and entire image (red curve), for nominal pointing image and quoted in B/B_0.

For both HI-2A and HI-2B, the regular transit of the planets and of the Milky Way through the field of view is clearly visible in the image signal of Figure 5-20. The signal in the corners also varies when these bright objects pass through the field of view, but it is much lower than the overall image signal. These corners are thus a good indicator of the straylight from these bright objects.

The straylight sources in the HI-2 field of view can be highlighted using relationship (5-1) of ratio of corner average value over image average value, where date is the time where image was captured and max is the maximum of the ratio over the 5 years of images.

$$SL_{Normalised}(date) = \frac{\frac{Corner_{average}}{Image_{average}}(date)}{\max\left(\frac{Corner_{average}}{Image_{average}}\right)} \qquad \textbf{(5-1)}$$

It results in Figure 5-21 where the evolution of the normalized straylight level over time is shown for both HI-2A and HI-2B with planets, Earth and Milky Way that significantly increase the straylight level when passing in the HI-2 field of view.

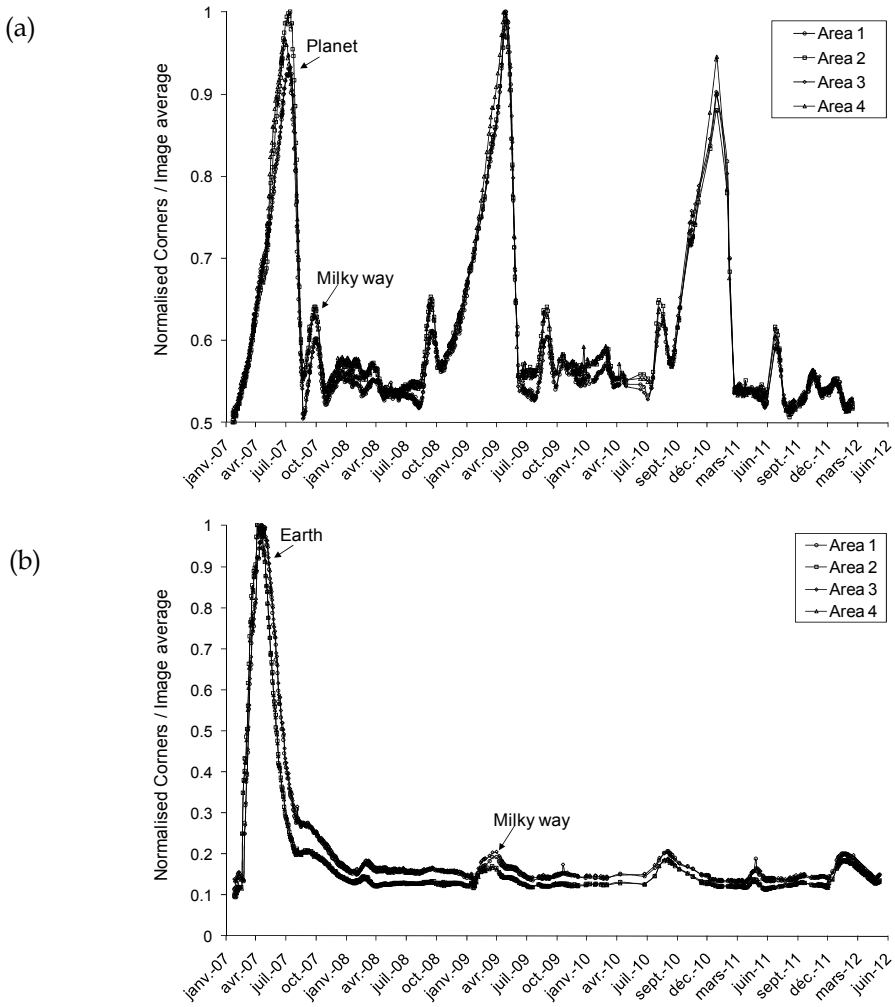

Figure 5-21 : Normalized straylight level evolution over time in HI-2A (a) and HI-2B (b).

Figure 5-22 shows the straylight pattern associated to the Earth that entered the HI-2B field of view, as observed during on-ground calibration shown in Figure 4-31, with associated ghosts that are present even with the Earth occulter.

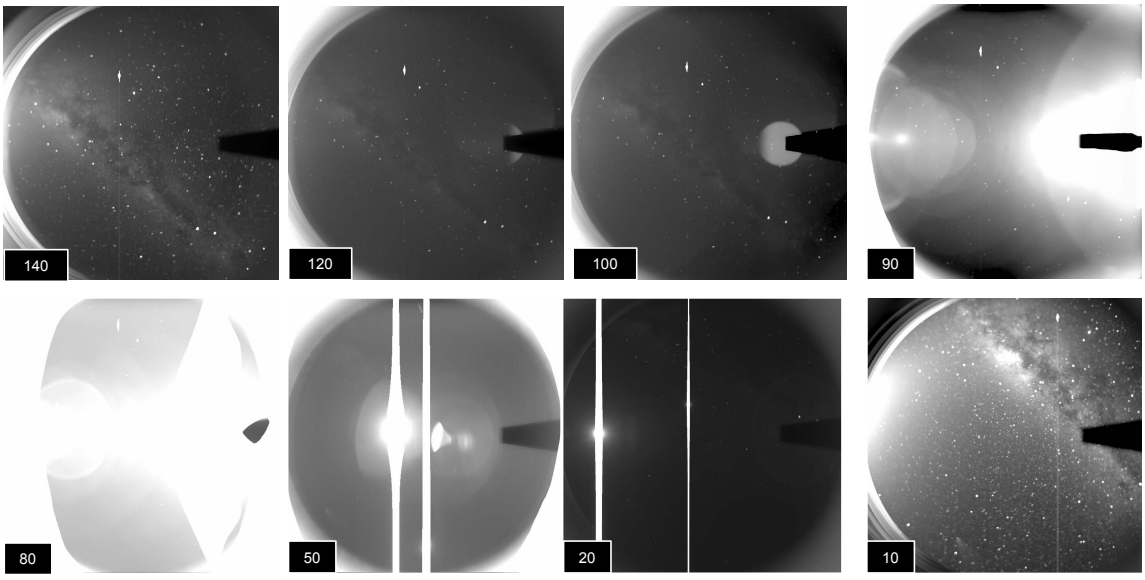

Figure 5-22 : At end of January 2007, the Earth was very close to the STEREO-B spacecraft and passed through the HI-2B FOV during two weeks. The Earth location is given in pitch angle versus Sun pointing direction (Sun-Spacecraft-Earth angle). The Earth is within the HI-2B FOV between 90 and 20 arcdeg images.

The straylight level in the HI-2 image corners (from Figure 5-20) is summarised in Table 5-4 for HI-2A and HI-2B.

- The minimum value is the effective residual straylight level resulting from fixed bright payload and from constant sky background. It is ~2 10^{-14} B/B_0 and confirms the straylight level reported in Table 5-3. It is also very close of the measured on-ground straylight measurements (Table 4-5).
- The maximum value is reached in HI-2A when Milky Way is passing in front of the instrument and in HI-2B when the Earth was facing and very close of the instrument. It fortunately only happens at the very beginning of the mission with limited impact on instrument scientific return.
- The reflection from the SWAVES boom is properly attenuated by the internal baffle, as the minimum straylight level in HI-2 is at the 10^{-14} B/B_0 requirement and the values in the sunward corners (2 and 4) is not significantly higher than in the anti-sunward corners (1 and 3).

	Requirement	**On-ground straylight**	**In-flight minimum**	**In-flight maximum**
HI-2A	10^{-14}	2.6 10^{-14}	2.4 10^{-14}	4.9 10^{-14}
HI-2B			1.8 10^{-14}	2.7 10^{-13}

Table 5-4 **:** Minimum and maximum level over 5 years in HI-2 corner, in B/B_0 unit, compared with straylight requirement and on-ground measured values (Earth direction).

It is however difficult to determine from these results if the straylight in HI-2 is dominated by solar or non-solar sources. We can only conclude that the solar straylight starts to dominate at a -0.5 arcdeg off-pointing (Figure 5-14) and that bright objects raise the straylight level to a maximum value close to what was measured during on-ground tests, providing an indication that solar straylight is not dominating in the nominal pointing images.

5.4. Ghost images

In addition to the residual straylight, which is at the required level for the HI instrument science objectives, a particular type of straylight arises when a bright object (i.e. a planet) approaches the border of the field of view.

A ghost-like pattern has indeed been observed, mostly in HI-1, as shown in Figure 5-23 where the Earth approaches the HI-1B field of view from the anti-sunward direction. The closest is the Earth, the brightest and smallest is the ring pattern.

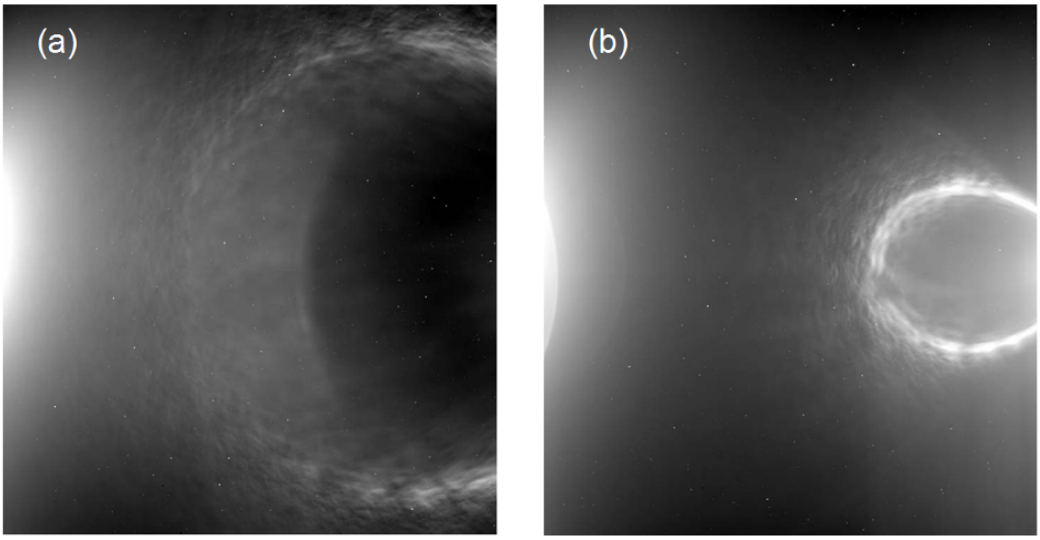

Figure 5-23 : Straylight ring pattern observed in HI-1B flight images (no background subtraction) when the Earth is just off the right-hand (anti-sunward) side of the field of view. At the times that these images were taken, the Earth was at (a) 30 arcdeg and (b) 26 arcdeg of elongation.

It has also been observed when a bright planet was in the field of view, close to a corner or a border, as shown in Figure 5-24. This effect arises wherever the bright source is located around the field of view, as the lens barrel is symmetric, but is most pronounced when the bright source is close to a corner of the detector.

When the object is very bright, as the Sun, the associated straylight dominates the image, as shown in Figure 5-4 (e) and (f). A detail of the straylight ring pattern obtained at -1.0 arcdeg during on-ground calibration and at -1.5 arcdeg off-pointing is shown on Figure 5-25.

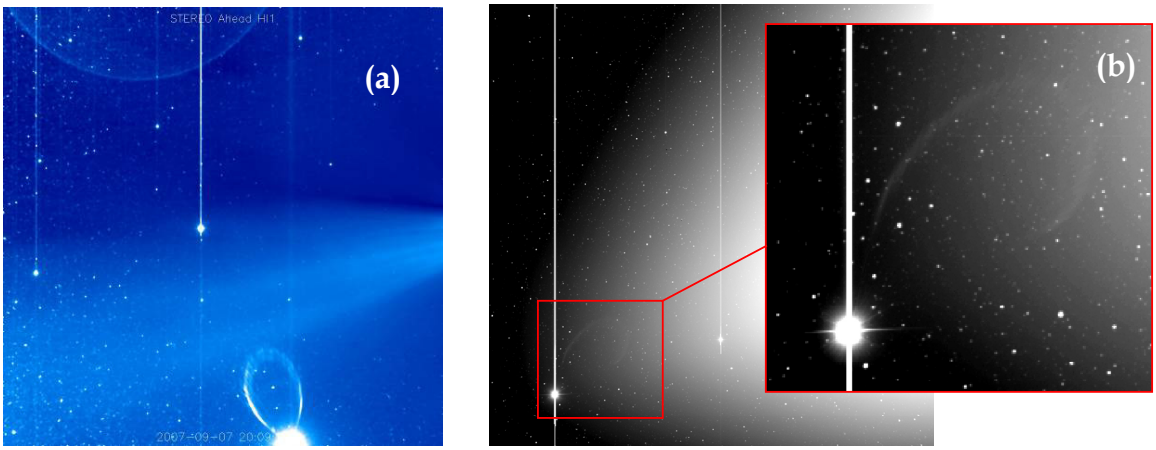

Figure 5-24 : Straylight ring pattern in HI-1A flight image (no background subtraction) produced by a bright planet (a) next to the field of view and (b) within the field of view close to one corner (the Sun being on right hand side).

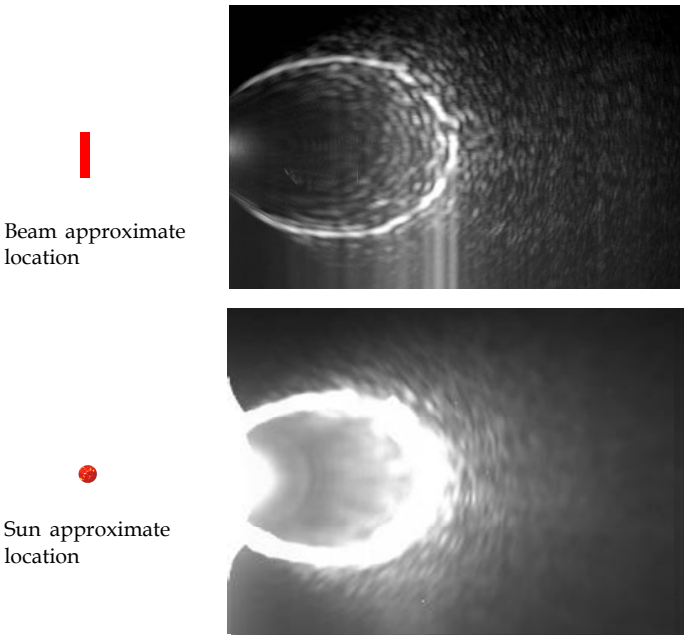

Figure 5-25: Detail of the HI-1 straylight pattern (top) obtained at -1.0 arcdeg pitch off-pointing during on-ground calibration, and (bottom) obtained at -1.5 arcdeg pitch off-pointing of HI-1A in 2007 (with Sun approximate location and size).

This ring-pattern has already been noticed in the ray-tracing mode of the camera lens barrel (Figure 3-15, Figure 3-16, and Figure 3-17). It is produced by a reflection on the last two retainers of the lens barrel. The farther outside the field of view this light source is, the larger and less bright the ring. This pattern has also observed during on-ground calibration (Figure 4-28 and Figure 4-30) and in the off-pointing in-flight images (Figure 5-4) where the Sun produced the ring pattern when very close to the edge of the camera field of view.

Using the conversion factor given in Table 5-1, the ring pattern level has been quantified. The maximum intensity of the ring patterns (for background-subtracted images) formed by the Sun for an off-point of 1.5 arcdeg, by the Earth when located 2.35 arcdeg out of the field of view, and by Venus at the field of view border are given in Table 5-5. It gives an order of magnitude of the straylight level, which is over the requirement, even is localised in the image. The level of Venus when in the HI-1 FOV border is logically similar to the Earth when it was in the HI-2 field of view at the beginning of mission (Table 5-4).

Fortunately such phenomenon only happens a few times over the mission and did not restrict the scientific use of the instrument.

Sun (with a 1.5 arcdeg off-point)	**Earth (at 2.35 arcdeg out of field of view)**	**Venus (on field of view border)**
$1.5\ 10^{-12}$	$9.9\ 10^{-13}$	$2.7\ 10^{-13}$

Table 5-5 : Level (in B/B_0) of the HI-1 ring pattern observed for three particular bright objects located out of near the field of view.

5.5. Detector ageing

Since launch, images of LED located in the vicinity of the detector (Figure 3-10) are regularly acquired in the four HI-1 and HI-2 A/B cameras. These sequences have been used to derive detector stability over the five first years of the mission.

The average over the detector area has been computed and normalised using relationship (5-2), where t is the time where LED image were captured and max is the maximum over the 5 years of the LED image average.

$$LED_{Normalised}(date) = \frac{Image_{average}(date)}{\max\left(Image_{average}\right)} \qquad \textbf{(5-2)}$$

From the normalised average of the LED images (Figure 5-26), no significant detector ageing can be derived. The response variation to the LED light remains within 1% in HI-1 and 3% in HI-2. The straylight evolution shown in Figure 5-12 and Figure 5-16 is therefore not entached by a systematic error from detector ageing.

The LED images were however captured without shutter, i.e. while the rest of the scene is present in the image. Even if the scene is much fainter than LED signal, it has an impact on the results as mostly visible on HI-2A where the normalised average changes when of the bright planets and stars pass through the fields of view (Figure 5-21) and contribute to the detector response.

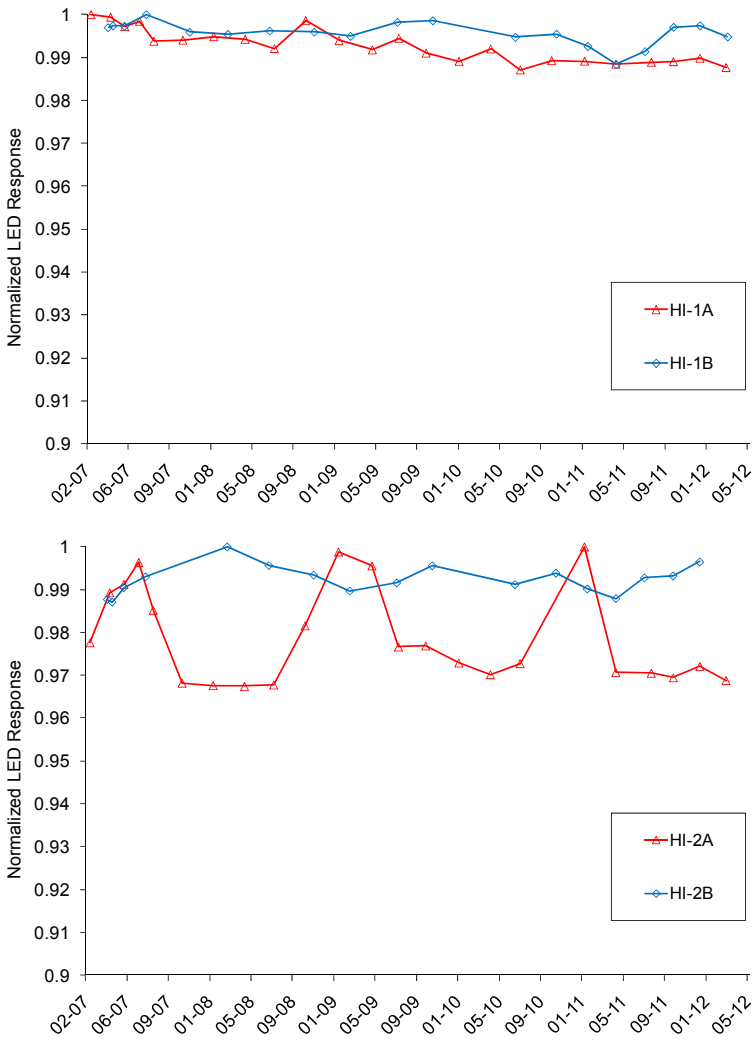

Figure 5-26 : Normalised average of LED calibration image sequences (top: HI-1, bottom: HI-2), showing the evolution of the detector response over time.

5.6. Chapter summary

The analysis of in-flight images has confirmed that the straylight level of the STEREO-HI instrument is below the requirement in both HI-1 and HI-2.

The first two columns of Table 5-6 shows the comparison of measured in-flight straylight level with on-ground and computed values for solar and sky/payload sources.

- The in-flight solar straylight value is very close of theoretical values and on-ground measurements. The difference with theoretical values (that shall be compared with in-flight values at -0.25 arcdeg off-point even if very similar to nominal pointing) comes from the particle diffusion effect that is lower than expected. The difference with on-ground measurements comes from the background subtraction that removes a fraction of the straylight.
- The sky and payload straylight was measured in HI-2, taking advantage of field of view vignetting by the internal baffle. The minimum of corner corresponds to the nominal residual straylight, resulting from constant sky and fixed bright payload located around the instrument (as the SWAVES boom) that is properly attenuated. It is logically similar to levels measured in the 0.25 arcdeg (and 0 arcdeg) off-pointed images.

  The in-flight straylight level in HI-2 however increases by one order of magnitude (maximum straylight value) when a bright source (like the Earth) is facing the instrument. The corresponding value also shows a very good correspondence with the measured on-ground straylight value from internal baffle (Table 4-5).

  In HI-1, the in-flight straylight contribution from the internal baffle cannot however be distinguished from the solar straylight.

Table 5-6 also shows the effective overall in-flight straylight as compared with on-ground and computed values. For the theoretical and on-ground ones, it is the sum of solar and sky/payload straylight level, as they were modeled and tested independently of each other.

- The on-ground level is of the same order as the theoretical values, slightly below in HI-1 and above in HI-2. It is due to the internal baffle contribution that was over-estimated for HI-1 and under-estimated in HI-2. The values are however very close and the slight differences are negligible as compared with the already very low straylight level achieved.
- The in-flight level is of the same order and very close of the on-ground values. The very small difference (factor ~2) comes from background straylight in the chamber (beam reflection but also diffusion by particles on the test setup) that is not present in flight.

		Solar straylight (front baffle)	**Sky and payload straylight (internal baffle)**	**Overall straylight**	**Requirement**
HI-1	Theory	$6.9\ 10^{-14}$	$6.8\ 10^{-14}$	$1.4\ 10^{-13}$	$3\ 10^{-13}$
	On-ground	$7.5\ 10^{-14}$	$2.5\ 10^{-16}$	$7.5\ 10^{-14}$	
	In-flight	$3.8 – 5.1\ 10^{-14}$	-	$\sim 4\ 10^{-14}$	
HI-2	Theory	$1.1\ 10^{-14}$	$8.2\ 10^{-15}$	$1.9\ 10^{-14}$	10^{-14}
	On-ground	$1.5\ 10^{-14}$	$2.6\ 10^{-14}$	$4.1\ 10^{-14}$	
	In-flight	$1.4 - 2.2\ 10^{-14}$	$1.8 - 2.4\ 10^{-14}$ (min corner)	$\sim 2\ 10^{-14}$ (nominal)	

Table 5-6 **:** Comparison of in-flight straylight level (in B/B_0 unit) with on-ground flight measurement and computation results (including cleanliness contribution), and with instrument straylight requirement.

Chapter 6. Conclusions

6. Conclusions

A multi-edge diffractive baffle can provide very high straylight protection from the Sun disk brightness necessary for solar wide-field imager, allowing sensitive observation of the heliosphere and associated solar events. The STEREO-HI instrument was the first generation of a solar wide-field imager based on such a diffractive baffle. Taking heritage of the STEREO-HI front baffle concept, similar instruments are under developments and other applications are potentially promising.

6.1. Summary

6.1.1. Major results

The present work has first demonstrated the adequacy of the cascading model of Fresnel diffraction for a multi-edge linear baffle with an un-precedent rejection of 2.10^{-12} obtained for 5 equidistant edges.

For that purpose, a dedicated test setup was designed and developed to measure the rejection of a baffle mock-up under vacuum. It was shown that such measurement requires to minimise the setup environmental straylight that can perturb the measurement, and in particular that cleanliness has an impact on very faint straylight measurements because of air diffusion that generates additional noise in the measurement.

The multi-edge diffraction performance was confirmed in the frame of the STEREO Heliospheric Imager instrument by on-ground evaluation of its diffractive front baffle rejection. Straylight levels of $7.5\ 10^{-14}$ and $1.5\ 10^{-14}$ B/B_0 on the two camera detectors were measured during the on-ground testing of the instrument flight models, proving that the instrument straylight requirement is achieved.

It was also shown that the front diffractive baffle of a wide-field imager must be complemented by a well designed instrument cavity to trap additional parasitic straylight from surrounding bright objects and from the sky. An efficient camera lens barrel reflection is also necessary to achieve the required straylight at pixel level. This is especially valid when bright objects are very close to the edge of the field of view, as it is the case for the STEREO-HI where the front baffle latest edge is very close to the HI camera field of view. The present work thus includes the overall STEREO-HI straylight design and test, i.e. its internal and lateral baffles and its optical system lens barrel rejection.

The importance of edge cleanliness has also been highlighted as part of this overall straylight performance. The particular cleanliness must be very tight to ensure that the straylight performance is not degraded by diffusion on the edges. The effect of dust on optical system also results in a diffuse background on the detector, even if of second order.

The overall in-flight straylight performance of the STEREO-HI instrument at detector level of both cameras is of the same order than the on-ground measured values, with some margins for HI-1, as shown in Table 6-1. The in-flight straylight level is ~$4\ 10^{-14}$ and $2\ 10^{-14}$ B/B_0 respectively in the HI-1 and HI-2 cameras, unchanged after some years of in-flight operation. This would not have been possible without the front diffractive baffle, protecting from the very large Sun disk brightness.

		Straylight level	**Straylight requirement**
HI-1	Theory	$1.4\ 10^{-13}$	$3\ 10^{-13}$
	On-ground	$7.5\ 10^{-14}$	
	In-flight	~$4\ 10^{-14}$	
HI-2	Theory	$1.9\ 10^{-14}$	10^{-14}
	On-ground	$4.1\ 10^{-14}$	
	In-flight	~$2\ 10^{-14}$	

Table 6-1 **:** STEREO-HI overall straylight level (in B/B_0 unit) compared with straylight requirement.

6.1.2. Lessons learned

In addition to the major results of this work, the following specific points can be highlighted:

- The best efficiency for a multi-edge diffractive baffle is obtained when the edges are arranged in an arc such that the angle between the light source direction (i.e. the Sun limb in case of the STEREO-HI instrument) and the line connecting the last edge to the optical system entrance is equally divided between each edge, i.e. for equidistant edges. This geometry ensures that the diffraction of the N^{th} edge starts at the maximum diffraction slope of the $N\text{-}1^{th}$ edge. The optical system protected by the multi-edge baffle shall be located in the shadow of the last edge where the diffraction from the N edges is combined. The baffle geometry (heights and distances between edges) thus depends on the camera field of view border w.r.t. the light source direction, and on the available distance between edges and camera. The larger the distance between the diffractive baffle and the camera entrance aperture and the more edges are considered, the best will be the baffle efficiency (i.e. the shadow at the camera entrance aperture), but also the larger will be the optimum distance between the edges.
- As part of the overall straylight performance, the lens barrel rejection must be carefully measured to validate ray-tracing model and avoid over or under estimation of its contribution. The use of detector array, with enough sensitivity, is preferred to avoid measuring an integrated value than cannot be easily combined with the baffle rejection curves.
- A careful on-ground calibration of the instrument response, i.e. conversion from ph to DN/s is mandatory to properly evaluate straylight level. A correct calibration of the test setup parts, and in particular of the detectors and light sources, is also very important to avoid wrong interpretation of the results.
- A spectral shift of the HI-1 optical system transmission (Figure 4-16) has also been observed. It is due to ageing of the non-stabilised coating combined with vacuum and temperature effects on the coating properties. For the science objectives of the HI instrument (i.e. CME observations), and for straylight performance, it has only a fairly minor effect since the relative change in the response to the broad solar spectrum is small. Further tests should however be conducted on (non-stabilized) coating samples to confirm ageing. For future similar instruments it is also recommended to stabilise the lens coatings and to measure their transmission under vacuum at their expected operational temperature.
- The contribution of the sky background in the field of view can be reduced by image summing (as described in [20] for the STEREO-HI instrument). The sky brightness, in particular the stars, however adds significant noise to the images and a reliable measurement of a star's brightness is needed to discriminate them from the observed scene. An accurate measurement of the PSF over the entire field of view should therefore be performed during the on-ground calibration.

6.1.3. Personal involvement

The diffractive baffle design takes heritage of an existing concept that was tested in laboratory. The present work aimed to go further by providing a simple computation method, and performing the measurement of a 5-edges diffractive baffle with a rejection down to 10^{-12}.

The concept was applied to the STEREO-HI instrument with the design of its baffles and lens barrels, in iteration with the University of Birmingham which was responsible for their mechanical implementation and with the Naval Research Laboratory which was leading the scientific requirements.

All the on-ground straylight tests (from diffractive baffle mock-up to STEREO-HI flight models) were performed in the facilities of the Centre Spatial de Liège. In the frame of this work, the test setup and the associated tools were developed (i.e. light trap, detector system) to allow such very faint measurement but also to increase the dynamic of the measurement (attenuator with density filters).

Finally, the in-flight characterization of the STEREO-HI instrument was performed with the support of the Rutherford Appleton Laboratory team that is in charge of the in-flight operations.

In the frame of this work, started 5 years before launch and extended 5 years after launch, many papers were also published and are listed in the bibliography of the present manuscript.

6.2. Scientific results of the STEREO-HI instruments

6.2.1. CME imaging

After launch at the end of 2006, the HI instrument of both STEREO spacecrafts provided the first fine observations of CME far away from the Sun, as shown on the typical HI images of Figure 6-1 captured in January 2007 by the HI-1A camera. The STEREO-HI instrument allows since launch to observe CME propagation, as shown on Figure 6-2 sequence captured over a two days period in January 2007.

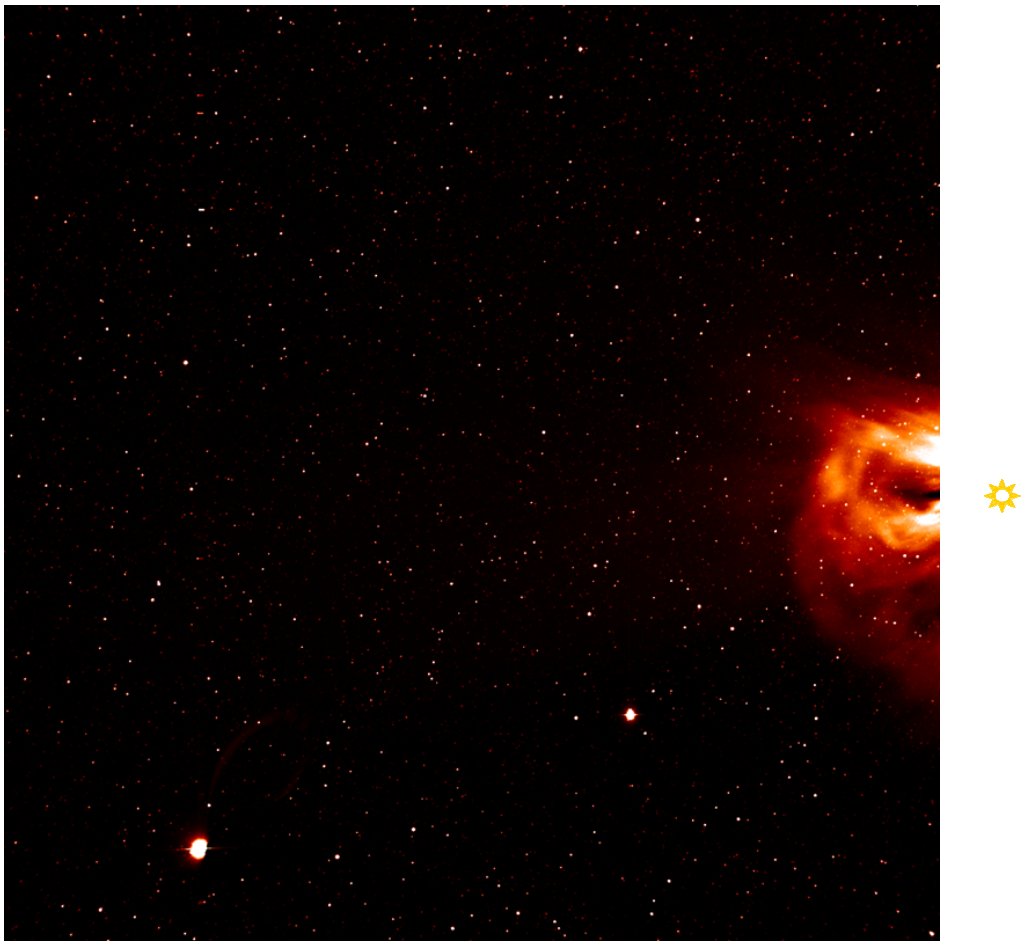

Figure 6-1: A CME is captured by the STEREO-HI instrument (HI-1A camera, background removed) in January 2007. The Sun approximate location and apparent dimension is on the right hand side. The image is colored with red tone, which corresponds to the instrument wavelength bandpass. The image is 20 x 20 arcdeg wide, and the Sun is located at 3.98 arcdeg on the right out of the image (HI-1 camera, background removed). [Courtesy of Rutherford Appleton Laboratory].

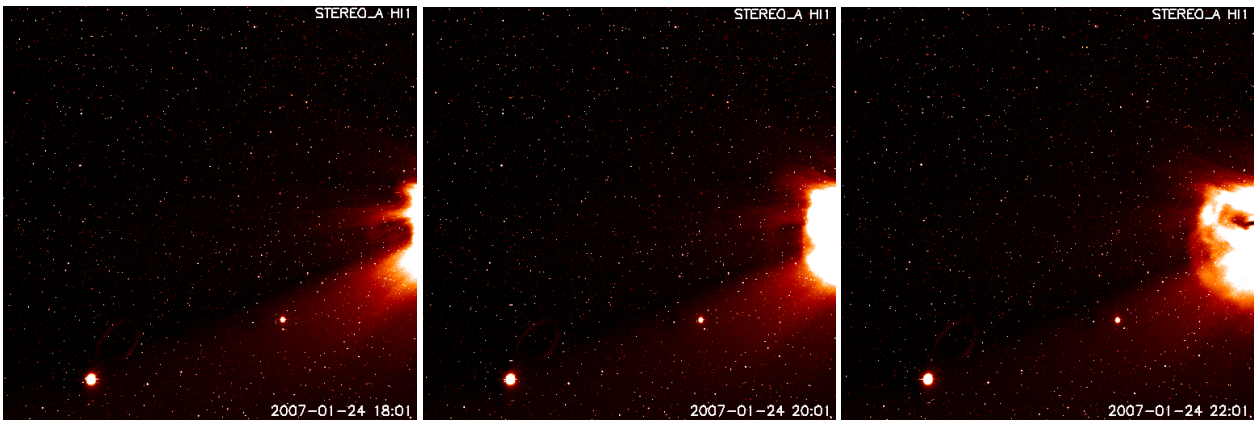

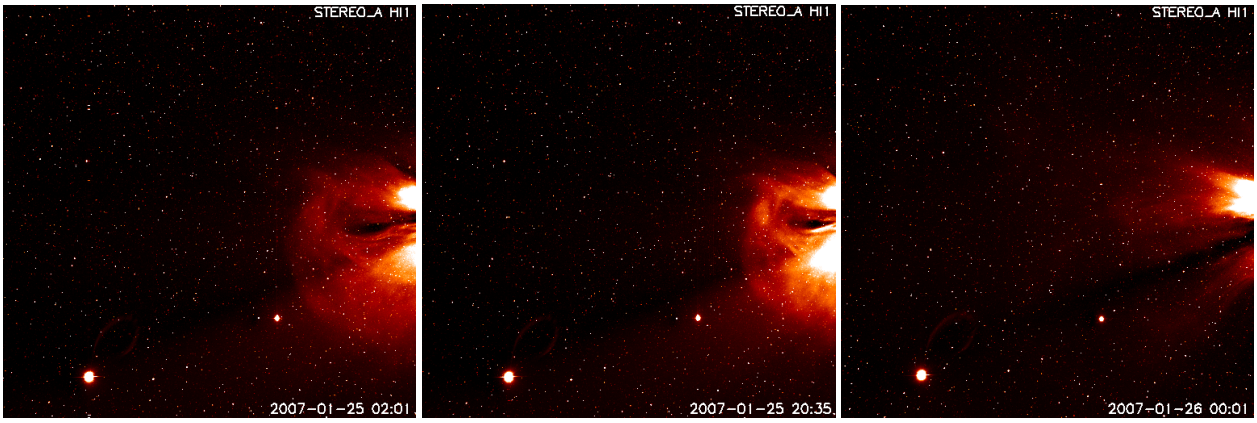

Figure 6-2: One of the first CME sequence observed by the STEREO-HI camera over a two days period in January 2007. [Courtesy of Rutherford Appleton Laboratory].

When the HI-1 and HI-2 images are combined, the CME propagation can be tracked in both fields of view, as in Figure 6-3.

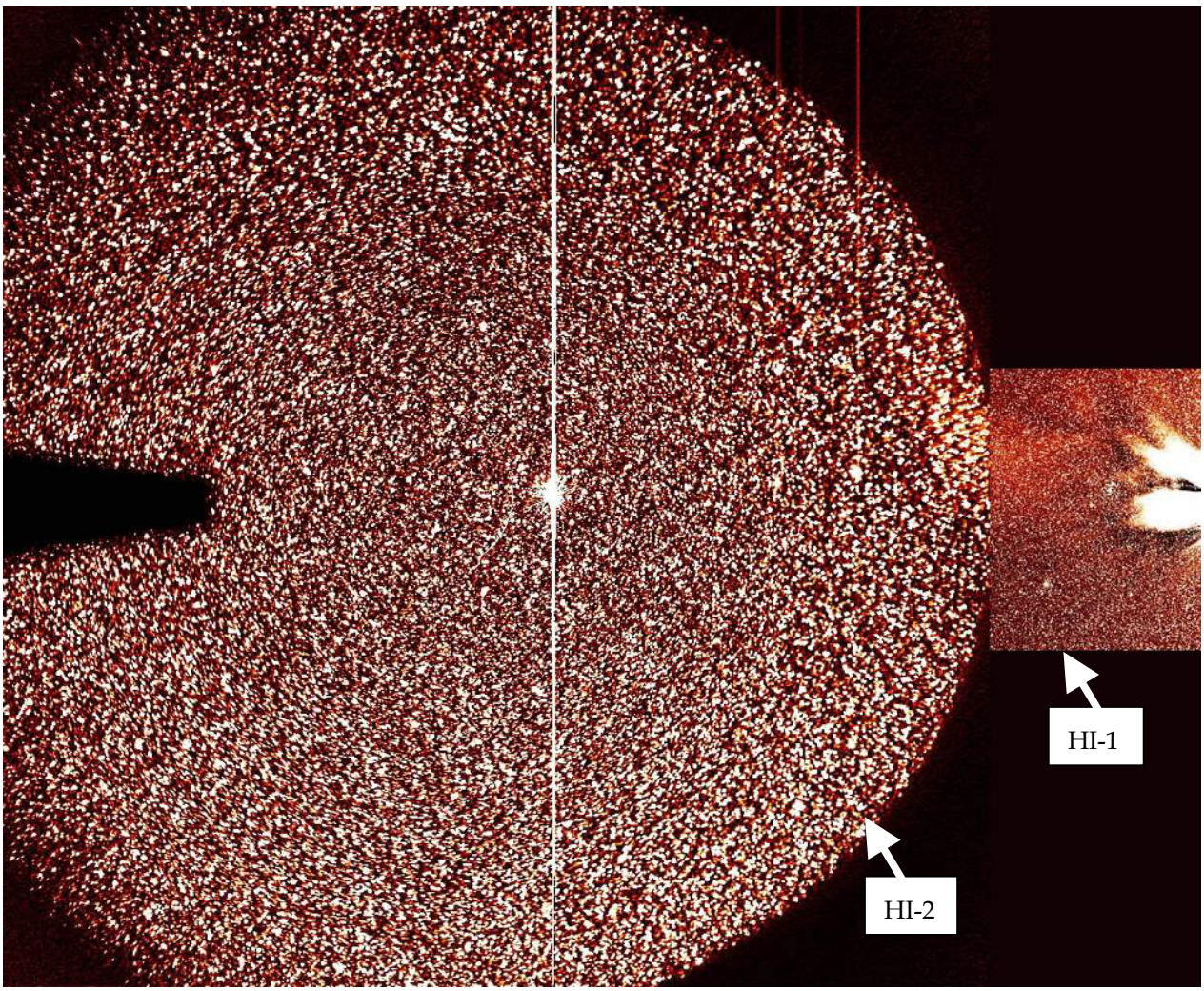

Figure 6-3: CME can be observed in HI-1 and in HI-2 cameras (images captured in July 2007). The images are colored with red tone for visual effect. The Sun is on the right hand side (not shown). [Courtesy of Rutherford Appleton Laboratory].

Figure 6-4 shows an image resulting from the combination of the four STEREO-HI cameras, providing a very wide field of view centred on the ecliptic and with a very high sensitivity.

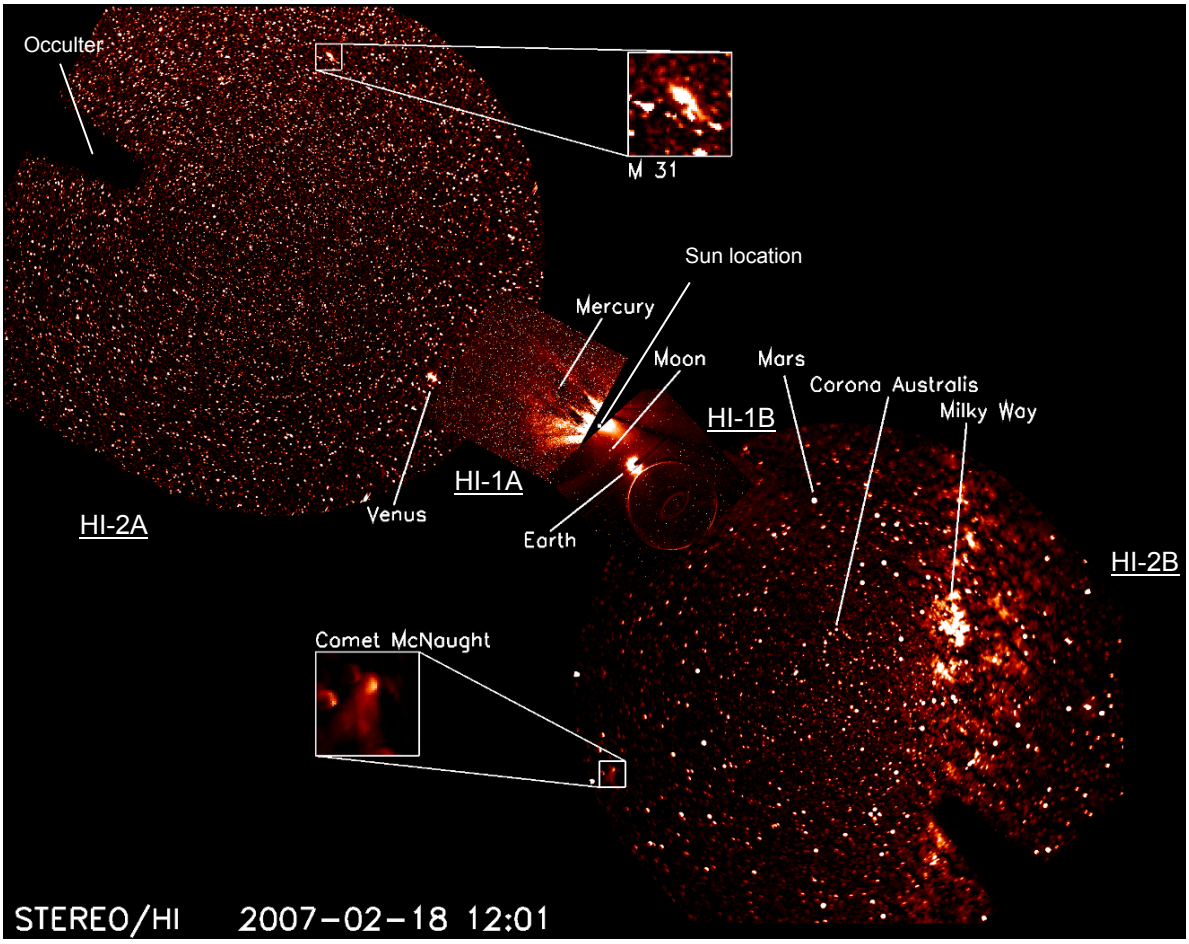

Figure 6-4: Combination of the four cameras (HI-1A and HI-2A on left, HI-1B and HI-2B on right). Images were captured in February 2007, when Earth was within the HI-1B field of view (before progressively moving out of the fields of view). The Sun is located in the center (not visible) and some particular stellar objects and planets are identified [Courtesy of Naval Research Laboratory].

6.2.2. CME velocity and direction

The combination of HI-1 and HI-2 images (as shown for example on Figure 6-5 where elongation from the Sun centre is shown) is also used to derive CME velocities and directions along very large elongation.

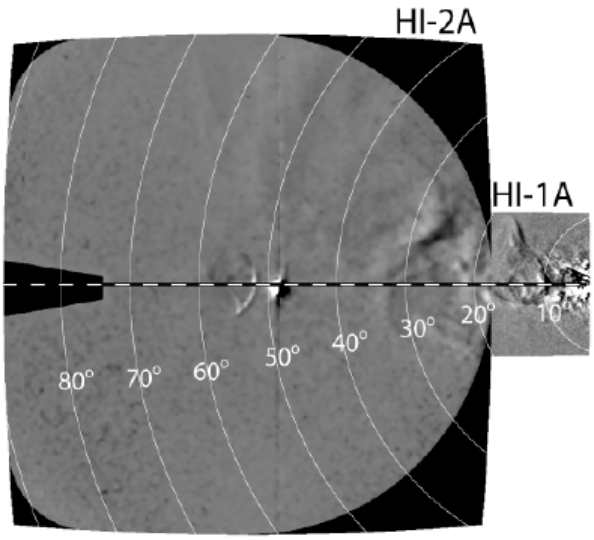

Figure 6-5: Combined HI-1 and HI-2 images, where the curved lines show contours of constant elongation [28][29].

The plot of the integrated value for each elongation in the HI-1 and HI-2 images (i.e. along elongation lines of images similar to Figure 6-5) over time provides an "elongation-time map", also called "JPlot" map (Figure 6-6). In this map, the CME flowing in the solar wind away from the Sun (i.e. with increasing elongation) is shown as diagonal lines. The slope of these diagonal lines provides their velocity [28][29].

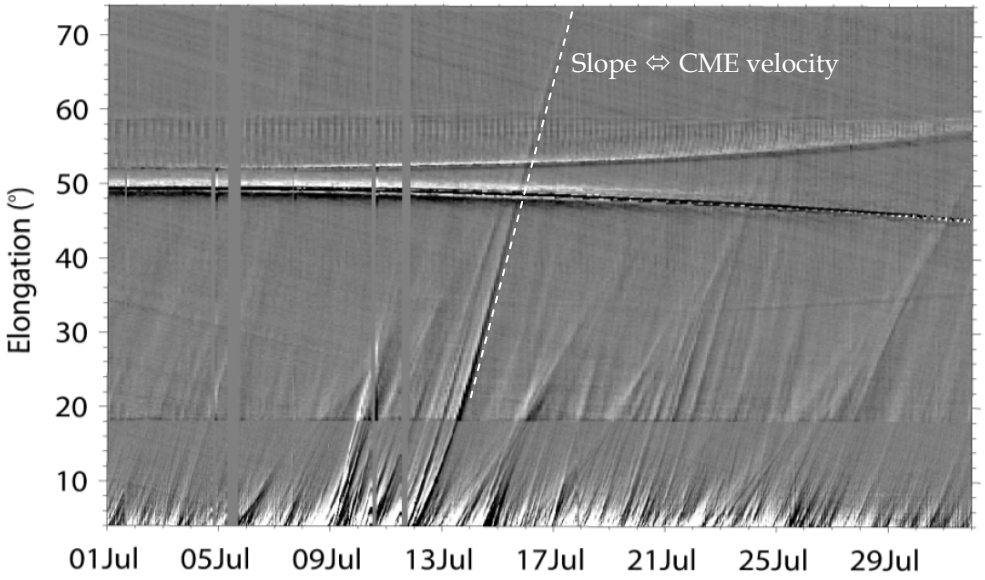

Figure 6-6: Elongation-time plot (here, covering the period of July 2007). Gaps are due to missing image, filled in grey [28][29].

6.2.3. Stellar objects

The very high sensitivity of the STEREO-HI instrument allows to track CME but also to image stellar objects down to magnitude 12 (apparent limiting magnitude being almost 14) [20]. In particular a number of new binary stars have been discovered [66] and excellent data have been obtained on known variable stars as shown for example in Figure 6-7.

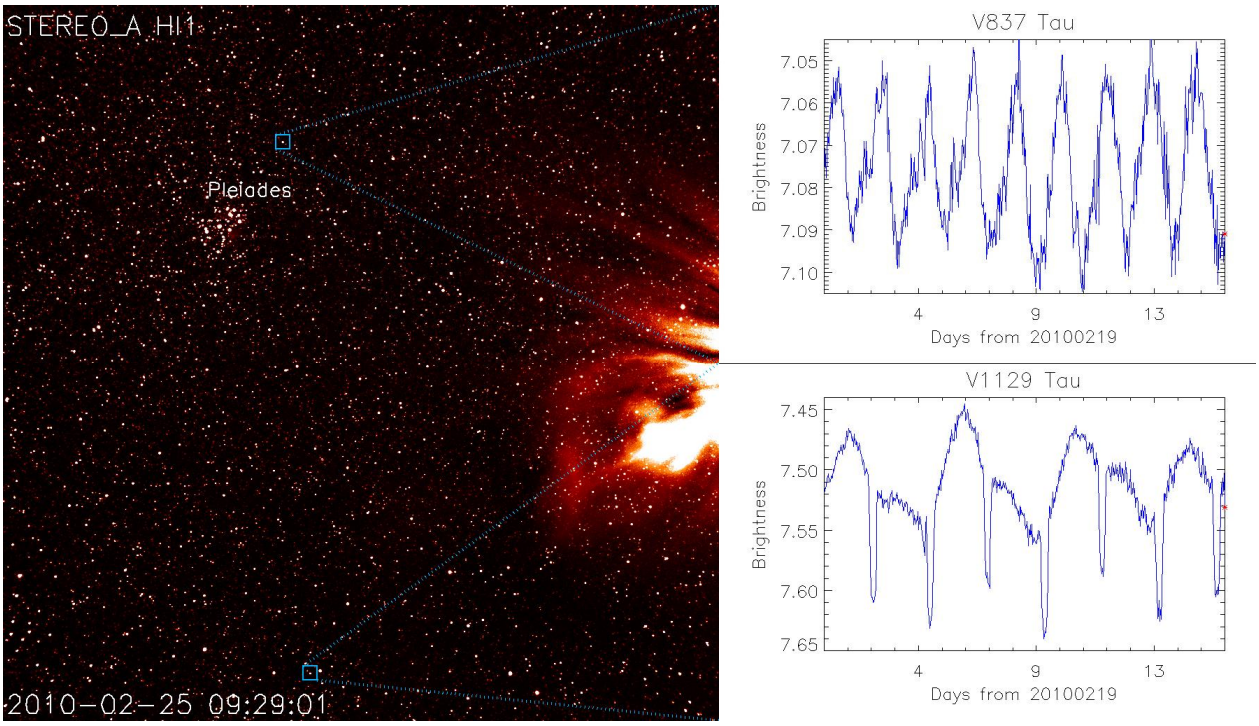

Figure 6-7: HI-1A image of March 7, 2010 (left) with two variable stars highlighted in the image. The varying brightness of the two stars, V837 Tau and V1129 Tau are shown (right top and bottom, respectively). [Courtesy of NASA/STEREO/D. Bewsher].

Comets have also been observed with high resolution and sensitivity. The closest one was comet C/2006 P1 (Mc Naught comet) of magnitude 5.5, for which high-resolution images of dust tail in the HI-A field of view (Figure 6-8) gave the possibility to perform an analysis of its composition [22]. Another comet is the comet Encke, with the first observation of a cometary tail perturbed by a coronal mass ejection (Figure 6-9) [25][34].

Figure 6-8: Mac Naught comet in the HI-1A field of view on 11 January 2007 [Courtesy of Rutherford Appleton Laboratory].

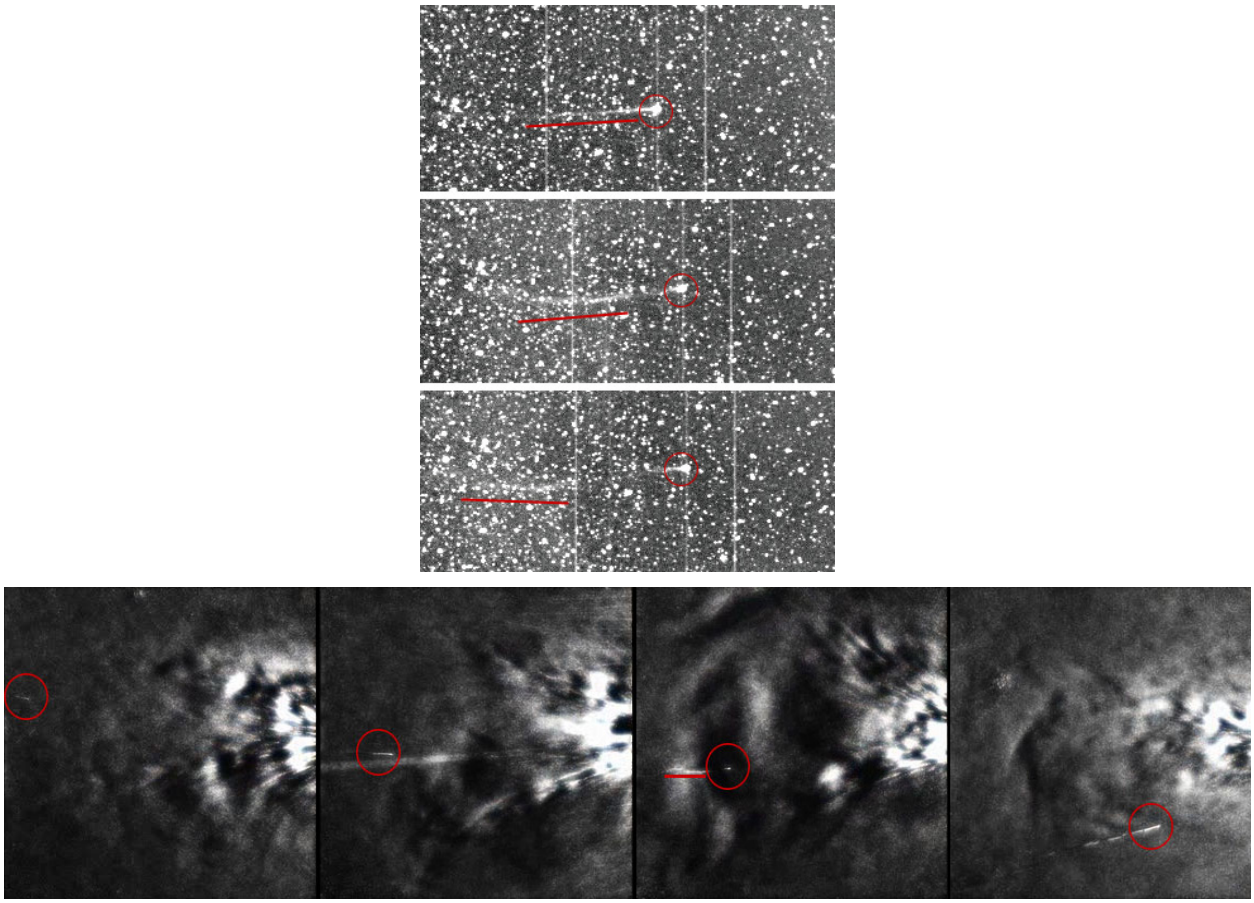

Figure 6-9: Encke comet in the HI-1B field of view on 20 May 2007 [71].

6.3. Perspectives

6.3.1. The SOLOHI and WISPR instruments

The next generation of wide-field solar imagers are under development for the ESA Solar Orbiter (SO) and NASA Solar Probe Plus (SPP) missions, under the lead of the NRL [49].

- The **SOL**ar **O**rbiter **H**eliospheric **I**mager (SOLOHI)
- The **W**ide Angle **I**mager on-board **S**olar **PR**obe Plus (WISPR)

These two imagers (Figure 6-10) are based on the same type of diffractive straylight protection, taking heritage of the STEREO-HI instrument, but with only one camera (instead of two in the STEREO-HI instrument).

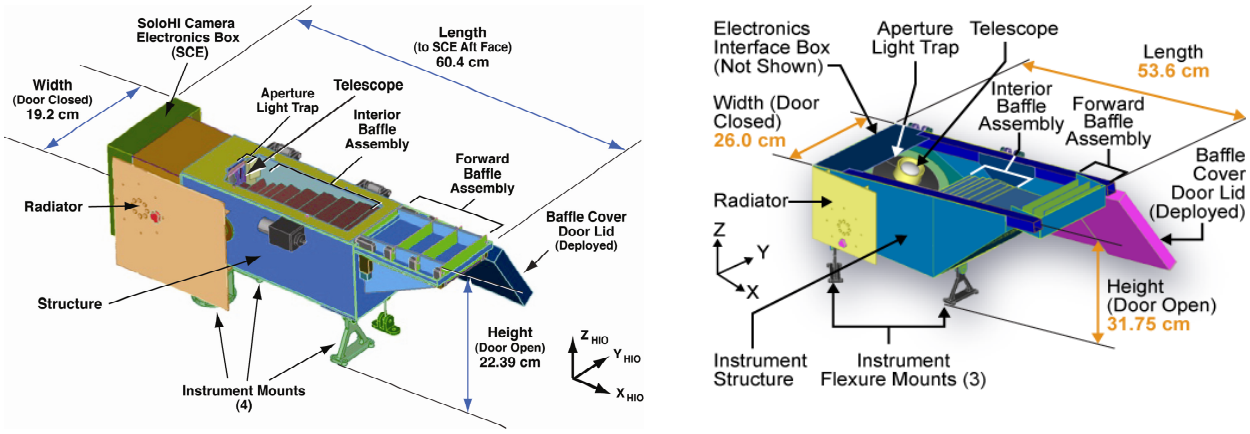

Figure 6-10 : Overview of the SOLOHI (left) and WISPR (right) instruments [Courtesy of Naval Research Laboratory].

The present work provided the basis for the front diffractive baffle to be used on these two wide-field imagers. Due to spacecraft constraints, the first edge is however located on the spacecraft front panel at 0.6 m ahead of the four other edges, as shown on Figure 6-11.

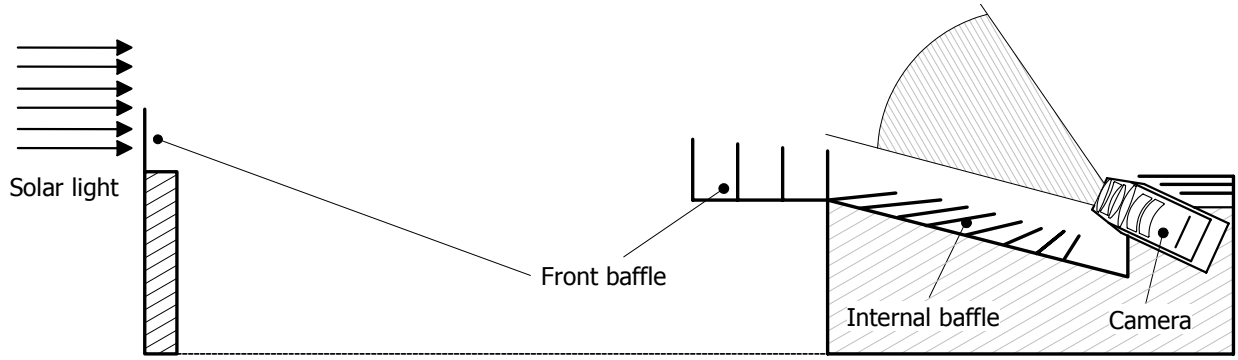

Figure 6-11 : Front baffle geometry of the SOLOHI and WISPR instruments. The first edge is located away of the other edges on top of the spacecraft front panel facing the Sun.

The spacecraft front panel is indeed a heat shield providing barrier against the high solar flux encountered at perihelion where the distance to the Sun are only 0.28 AU for Solar Orbiter and 9.5 solar radii for Solar Probe Plus. As a consequence the first edge height w.r.t. the rest of these two instruments is also subject to thermo-elastic variations that have to be taken into account in the straylight rejection model. In addition, the Sun diameter varies from perihelion to aphelion and the front baffle has to be optimised for the worst case. Figure 6-12 shows the theoretical relative rejection curve computed using equations (2-13), the edges not being equidistant.

The internal baffle has also been optimised for specific platform reflexions that could potentially degrade the instrument performance. For example, on Solar Orbiter, a solar panel and a boom antenna will reflect the solar light requiring proper attenuation at the corresponding angles. As on STEREO-HI, the lens barrel will also be optimised to trap out of field straylight.

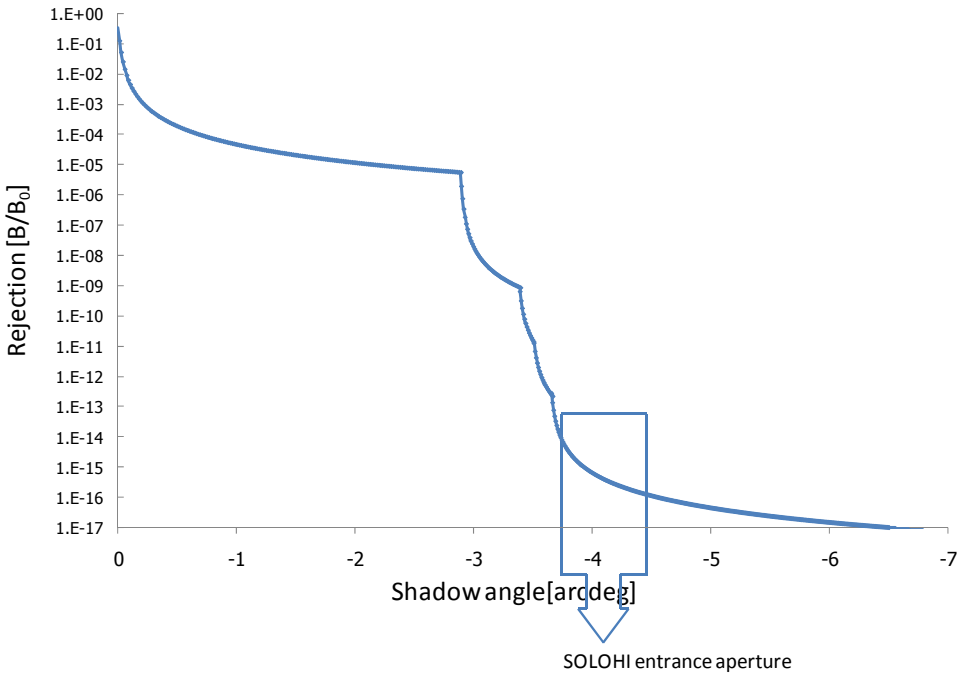

Figure 6-12 : SOLO HI front baffle theoretical rejection curve (at 0.28 AU Sun in nominal pointing).

An end-to-end straylight validation of these two instruments is under preparation at the Centre Spatial de Liège. These tests will use some of the tools and methods that were developed in the frame of the STEREO-HI instrument. The tests will however be more focused on the internal baffles. The front baffle diffraction theory has indeed already been proved on STEREO-HI and the second major potential straylight source is the spacecraft solar panel located on the back of the instruments.

The test setup has thus been improved to allow the illumination of the internal baffle along the two directions, as shown on Figure 6-13 where two stages support the instrument mock-up, allowing pitch and yaw rotation.

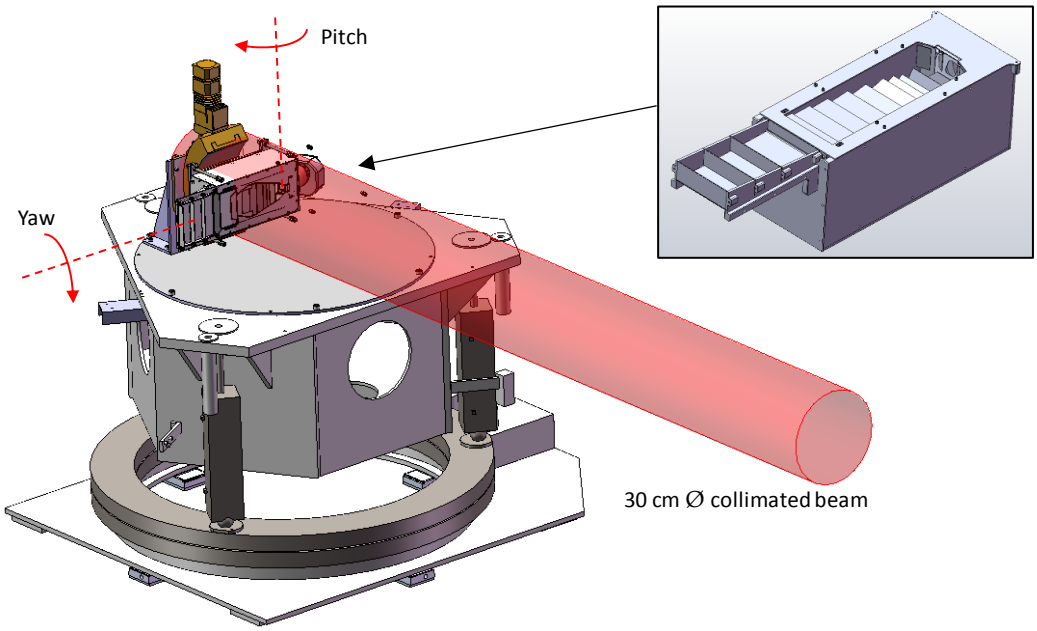

Figure 6-13 : The SOLOHI mock-up is mounted on two rotation stages and is illuminated with a 30 cm diameter collimated beam to validate internal baffle rejection.

The SOLOHI mock-up will be tested in the same vacuum chamber as for the end-to-end straylight test of the STEREO-HI and within the same black shroud. The collimator will however be improved with a baffling to reduce its potential contribution to the measured straylight. A panel covered with VelBlack

will also surround the mock-up to limit reflection of the incident collimated beam within the shroud cavity (Figure 6-14).

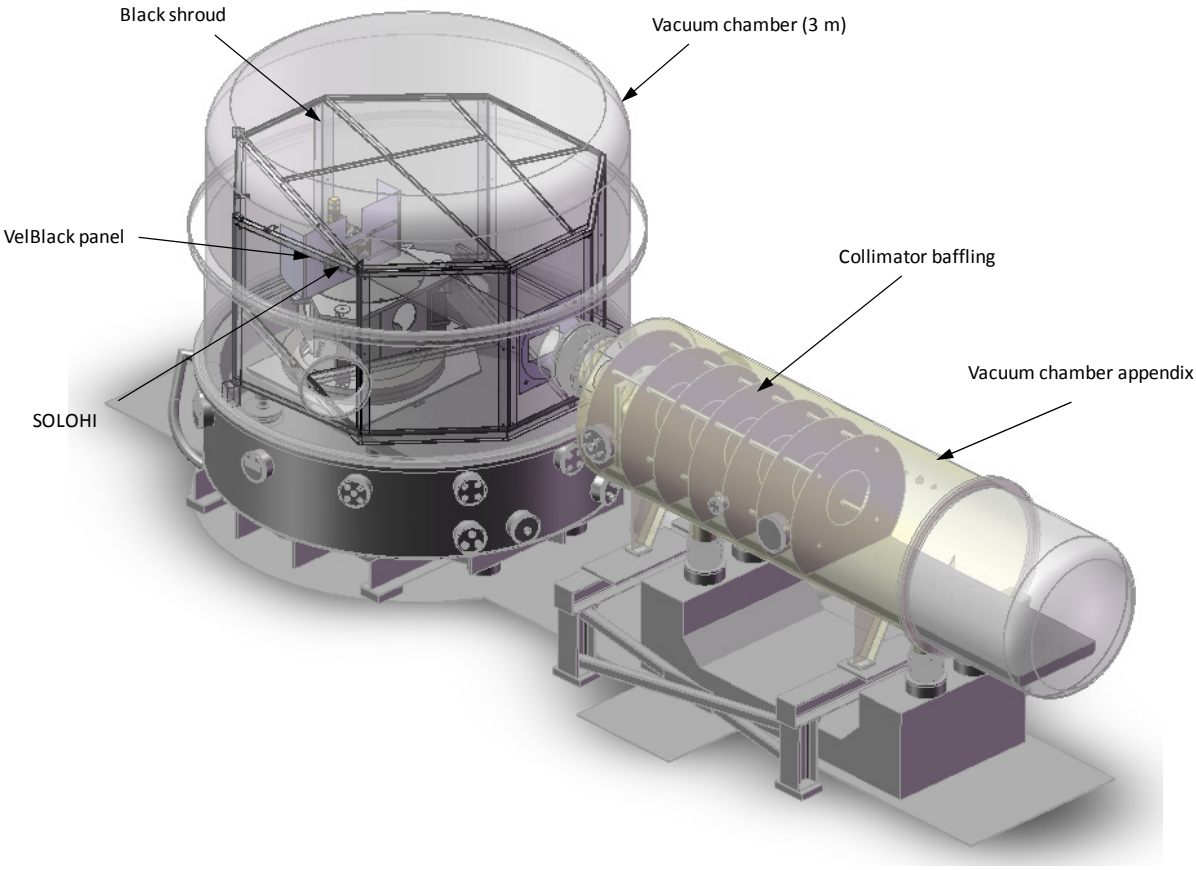

Figure 6-14 : The SOLOHI mock-up will be tested in the 3 m vacuum chamber of the Centre Spatial de Liège as for the STEREO-HI end-to-end straylight test [Courtesy of CSL].

6.3.2. Circular diffractive baffle

In addition to heliospheric imagers similar to the STEREO one, the multi-edge diffractive computation method can be extended to other types of baffle, as for example a circular diffractive baffle to be used as internal occulter of traditional coronographs, or as external occulter of other type of wide-field imagers, as sketched in Figure 6-15.

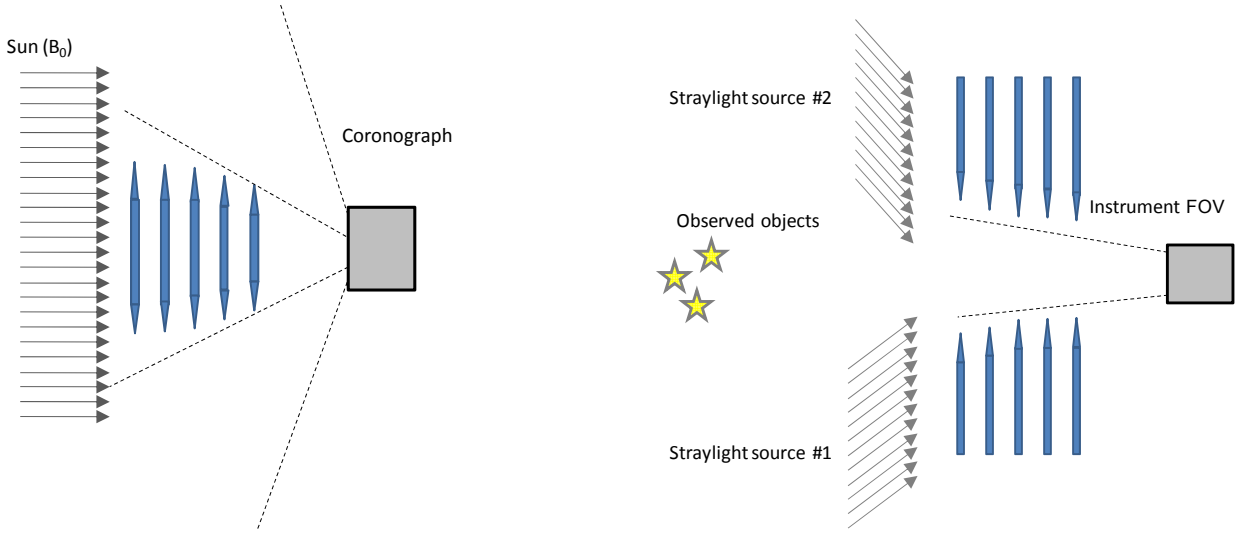

Figure 6-15 : Potential application of a multi-edge diffractive baffle for a coronograph (left) and a wide-field imager needed to be protected from more than one light source (right).

6.3.3. Continuous baffle

Another potential efficient diffractive baffle can be obtained by replacing the edges with a curved surface, as shown on Figure 6-16. This surface shall be equivalent to infinity of very small spaced edges, i.e. its shape must be optimised w.r.t. the diffraction angle θ_d.

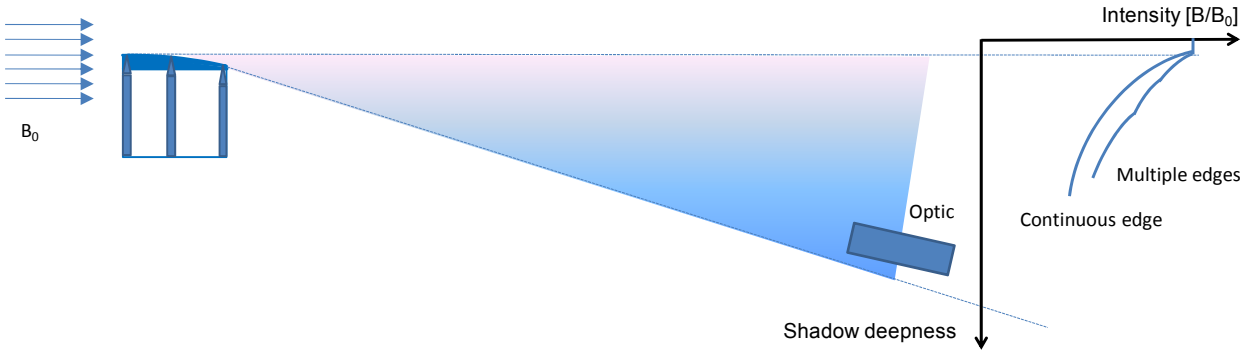

Figure 6-16 : A continuous diffractive baffle should provide better rejection than N edges for equivalent instrument geometry.

The rejection of such continuous baffle cannot however directly derived from the Fresnel based method because it assumes that the diffractive edges act independently, which is not valid for a continuous surface [7].

Another method needs to be developed to determine the rejection of this type of baffle. Preliminary studies were conducted allowing to quantify the performance of such a baffle [8][9] which is a potential future generation of diffractive straylight rejection system for wide field imagers.

Bibliography

Bibliography

The present bibliography is organised per topic of interest. In each topic, the references are sorted by increasing publication date.

Diffraction and Straylight

[1] *Physico-Mathesis de Lumine, coloribus, et iride*. Francesco Maria Grimaldi.

[2] *Principles of Optics*, M. Born and E. Wolf, Pergamon Press, New York, 1980, 7th edition (1999).

[3] *Stray light suppression in a reflecting white light coronagraph*, M. Romoli, H. Weiser, L.D. Gardner and J.L. Kohl, Applied Optics (1993), **32**:3559-3569.

[4] *Stray Light Suppression in Optical Space Experiments*, C Leinert, D Klüppelberg, Appl. Opt. (1974), 13(3):556-64.

[5] *Wide-angle stray-light reduction for a spaceborne optical hemispherical imager,* Buffington, A. Jackson, B.V. and Korendyke, C.M., Applied Optics (1996), **35**: 6669-6673.

[6] *Very-wide-angle optical systems suitable for spaceborne photometric measurements*, A. Buffington, Applied Optics (1998), **37**:4284-4293.

[7] *Improved design for stray-light reduction with a hemispherical imager*, A. Buffington, Applied Optics (2000), **39**: 2683-2686.

[8] *Evaluation of Diffraction by a Rounded Surface*, D.M. Rabin, American Astronomical Society, Solar Physics Division Meeting (2011).

[9] *Quantitative Evaluation of Continuous Diffractive Baffles for Heliospheric Imagers*, D.M. Rabin, American Geophysical Union, Fall Meeting (2011).

STEREO-HI instrument

[10] *The NASA Solar Terrestrial Relations Observatory (STEREO) Mission Heliospheric Imager*, D. G. Socker, R.A. Howard, C. M. Korendyke, G. M. Simnett, D. F. Webb. Proc. SPIE (2000), Vol. **4139**, 284.

[11] *Straylight Tests for the Heliospheric Imager of STEREO*, J.-M. Defise, J.-P. Halain, E. Mazy, P. Rochus. ESA 4th International Symposium on Environmental Testing for Space Programmes (2001).

[12] *Design of the Heliospheric Imager for the STEREO mission*, J.M. Defise, J.Ph. Halain, E. Mazy, P. Rochus, R. A. Howard, J. D. Moses, D. G. Socker, G. M. Simnett, D. F. Webb. Proc SPIE (2001) **4498**.

[13] *Design and tests for the Heliospheric Imager of the STEREO mission,* J.M. Defise, J.Ph. Halain, E. Mazy, P. Rochus, R. A. Howard, J. D. Moses, D. G. Socker, R. Harrison, G. M. Simnett. Proc SPIE (2002) **4853**.

[14] *Design and Performances of the Heliospheric Imager for the STEREO Mission*, E. Mazy, J.Ph. Halain, J.M. Defise, P. Ronchain, R. A. Howard, J. D. Moses, C. Eyles, R. Harrison. Proc SPIE (2005) **5962.**

[15] *In-orbit verification, calibration and performance of the Heliospheric Imager on the STEREO mission*, C.J. Eyles, C.J. Davis, R.A. Harrison, N.R. Waltham, J.-P. Halain, E. Mazy, J.-M. Defise, R.A. Howard, D.J. Moses, J. Newmark, S. Plunkett. Proc. SPIE (2007) **6689.**

[16] *STEREO – Heliospheric Imager Design, pre-flight and in flight response comparison*, J.Ph. Halain, E. Mazy, J.M. Defise, A. Mazzoli, P. Rochus, J.D. Moses, J.S. Newmark, C. Korendyke, R. Howard, S. Plunkett, C. Eyles, R. Harrison, C. Davis. Proc SPIE (2007) **6689.**

[17] *The STEREO Mission [solar space satellites]*, C. Russell, Springer, 2008.

[18] *The STEREO Mission: An Introduction*, Kaiser, M. L., Kucera, T. A., Davila, J. M., St. Cyr, O. C., Guhathakurta, M., Christian, E. ,Space Science Reviews (2008), **136**,5-16.

[19] *Sun Earth Connection Coronal and Heliospheric Investigation (SECCHI)*, R.A. Howard, J.D. Moses, A. Vourlidas, J.S. Newmark, D.G. Socker, S.P. Plunkett, C.M. Korendyke, J.W. Cook, A. Hurley, J.M. Davila, W.T. Thompson, O.C. St Cyr, E. Mentzell, K. Mehalick, J.R. Lemen, J.P. Wuelser, D.W. Duncan, T.D. Tarbell, C.J.Wolfson, A. Moore, R.A. Harrison, N.R. Waltham, J. Lang, C.J. Davis, C.J. Eyles, H. Mapson-Menard, G.M. Simnett, J.P. Halain, J.M. Defise, E. Mazy, P. Rochus, R. Mercier, M.F. Ravet, F. Delmotte, F. Auchere, J.P. Delaboudiniere, V. Bothmer, W. Deutsch, D. Wang, N. Rich, S. Cooper, V. Stephens, G. Maahs, R. Baugh, D. McMullin, T. Carter. Space Sci Rev (2008), **136**: 67–115.

[20] *The Heliospheric Imagers On-Board the STEREO mission*, C.J. Eyles, R.A. Harrison, C.J. Davis, N.R. Waltham, B.M. Shaughnessy, H.C.A. Mapson-Menard, D. Bewsher, S.R. Crothers, J.A. Davies, G.M. Simnett, R.A. Howard, J.D. Moses, J.S. Newmark, D.G. Socker, J.Ph. Halain, J.M. Defise, E. Mazy, P. Rochus. Solar Physics (2009), **254**:387-445.

[21] *Straylight-Rejection Performance of the STEREO HI Instruments*, J.-P. Halain, C. J. Eyles, A. Mazzoli, D. Bewsher, J. A. Davies, E. Mazy, P. Rochus, J.M. Defise, C. J. Davis, R. A. Harrison, S. R. Crothers, D.S. Brown, C. Korendyke, J. D. Moses, D. G. Socker, R. A. Howard, J. S. Newmark. Solar Physics (2011), **271**:197:218.

STEREO science

[22] *Discovery of the atomic iron tail of comet McNaught using the Heliospheric Imager on STEREO*, M. Fulle, F. Leblanc, R.A. Harrison, C.J. Davis, C.J. Eyles, J.-P. Halain, R.A. Howard, D. Bockelee-Morvan, G. Cremonese and T. Scarmato. Ap. J. Lett. (2007), **661**, L93.

[23] *Searching for solar clouds in interplanetary space*, R.A. Harrison, C.J. Davis, C.J. Eyles, J.-P. Halain and R. Howard. COSPAR Information Bulletin (2007), **168**: 25-31.

[24] *First Imaging of Coronal Mass Ejections in the Heliosphere Viewed from Outside the Sun-Earth Line*, R. A. Harrison, C.J. Davis, C.J. Eyles, D. Bewsher, S. Crothers, J.A. Davies, R.A. Howard, D.J. Moses, D.G. Socker, J.-P. Halain, J.-M. Defise, E. Mazy, P. Rochus, D.F. Webb, G.M. Simnett. Solar Physics (2007), **247**: 171-193.

[25] *First direct observation of the interaction between a comet and a coronal mass ejection leading to a complete plasma tail disconnection*, A. Vourlidas, C.J. Davis, C.J. Eyles, S.R. Crothers, R.A. Harrison, R.A. Howard, J. D. Moses, and D. G. Socker, The Astrophysical Journal, 668 (2007): L79–L82.

[26] *SECCHI observations of the Sun's garden-hose density spiral*, N. R. Sheeley Jr., A. D. Herbst, C. A. Palatchi, Y.-M. Wang, R. A. Howard, J. D. Moses, A. Vourlidas, J. S. Newmark, D. G. Socker, S. P. Plunkett, C. M. Korendyke, L. F. Burlaga, J. M. Davila, W. T. Thompson, O. C. St Cyr, R. A. Harrison, C. J. Davis, C. J. Eyles, J. P. Halain, D. Wang, N. B. Rich, K. Battams, E. Esfandiari, and G. Stenborg. Astrophys. J. (2008), **674**:109–112.

[27] *Heliospheric Images of the solar wind at Earth*, N. R. Sheeley, Jr., A. D. Herbst, C. A. Palatchi, Y.-M. Wang, R. A. Howard, J. D. Moses, A. Vourlidas, J. S. Newmark, D. G. Socker, S. P. Plunkett, and C. M. Korendyke, L. F. Burlaga, J. M. Davila, W. T. Thompson, and O. C. St Cyr, R. A. Harrison and C. J. Davis, J. P. Halain, D. Wang, N. B. Rich, K. Battams, and E. Esfandiari, and G. Stenborg. Astrophys. J. (2008), **675**:853-862.

[28] *Deriving solar transient characteristics from single spacecraft STEREO/HI elongation variations: a theoretical assessment of the technique.* A. O. Williams, J. A. Davies, S. E. Milan, A. P. Rouillard, C. J. Davis, C. H. Perry, and R. A. Harrison, Ann. Geophys. (2009), **27**, 4359–4368.

[29] *Two Years of the STEREO Heliospheric Imagers*, R. A. Harrison, J. A. Davies, A. P. Rouillard, C. J. Davis, C. J. Eyles, D. Bewsher, S. R. Crothers, R. A. Howard, N. R. Sheeley, A. Vourlidas, D. F. Webb, D. S. Brown, G. D. Dorrian, Solar Phys (2009) **256**: 219–237.

[30] *Study of CME Propagation in the Inner Heliosphere: SOHO LASCO, SMEI and STEREO HI Observations of the January 2007 Events*, D.F. Webb, T.A. Howard, C.D. Fry, T.A. Kuchar, D. Odstrcil, B.V. Jackson, M.M. Bisi, R.A. Harrison, J.S. Morrill, R.A. Howard, J.C. Johnston, Solar Phys (2009) **256**: 239–267.

[31] *The Impact of Geometry on Observations of CME Brightness and Propagation*, J.S. Morrill, R.A. Howard, A. Vourlidas, D.F. Webb, V. Kunkel Solar Phys (2009) **259**: 179–197.

[32] *A Heliospheric Imager for Deep Space: Lessons Learned from Helios*, SMEI, and STEREO, B.V. Jackson, A. Buffington, P.P. Hick, M.M. Bisi, J.M. Clover. Solar Phys (2010) **265**: 257–275.

[33] Mercury's Comet-like Appearance Spotted by Satellites Looking at the Sun, Boston University Center for Space Physics (http://sirius.bu.edu/News), 22 Sept 2010.

[34] *Solar wind speed inferred from cometary plasma tails using observations from STEREO HI-1*. J.M. Clover, B.V. Jackson, A. Buffington, P.P. Hick and M.M. Bisi, The Astrophysical Journal 713 (2010) 394.

Solar observation

[35] Minnaert, M. 1930, Z. Astrophys., 1, 209.

[36] *La couronne solair étudiée en dehors des éclipses*, B. Lyot. 1930, C.R. Acad. Sci. Paris 191, 834.

[37] *The Solar Corona*, Tousey, R. Space Research XIII, edited by M.J. Rycroft and S.K. Runcorn, p 713, Akademie-Verlag, Berlin, 1973.

[38] *The F-corona and the circum-solar dust evidences and properties*, S. Koutchmy and P.L. Lamy, "Properties and Interactions of the Interplanetary Dust," IAU Colloq. (1985), pp. 63-74.

[39] The HELIOS spacecraft zodiacal light photometers used for comet observations and views of the comet west bow shock, B. V. Jackson and R. M. Benensohn. Earth, Moon, and Planets (1990) **48**, Number 2, 139-163.

[40] *The Large angle spectroscopic coronagraph (LASCO),* G.E. Brueckner, R.A. Howard, M.J. Koomen, C.M. Korendyke, D.J. Michels, J.D. Moses, D.G. Socker, K.P. Dere, P.L. Lamy, A. Llebaria, M.V. Bout, R. Schwenn, G.M. Simnett, D.K. Bedford, C.J. Eyles, Solar Physics (1995), **162**: 357-402.

[41] *EIT: Extreme-Ultraviolet Imaging Telescope for the SOHO mission*, J.-P. Delaboudinière, G. E. Artzner, j. Brunaud, A. H. Gabriel, J. F. Hochedez, F. Millier, X. Y. Song, B. Au, K. P. Dere, R. A. Howard, R. Kreplin, D. J. Michels, J. D. Moses, J. M. Defise, C. Jamar , P. Rochus, J. P. Chauvineau, J. P. Marioge, R. C. Catura, J. R. Lemen, L. Shing, R. A. Ster, J. B. Gurman, W. M. Neupert, A. Maucherat, F. Clette, P. Cugnon and E. L. Van Dessel. Solar Phys (1995). **162**, 291.

[42] *Movies and Images of the Solar Corona from the LASCO coronagraph on SOHO*, K. Dere, R. Howard, P. Reiser, N. Rich, D. Socker, A. Vourlidas, D. Wang (http://lasco-www.nrl.navy.mil/solcd/spcd.html).

[43] *LASCO observations of the coronal rotation*, D.J. Lewis, G.M. Simnett, G.E. Brueckner, R.A. Howard, P.L. Lamy and R. Schwenn, Solar Physics (1999), Volume **184**, Number 2, 297-315.

[44] *Mapping the inner zodiacal light with clementine*, J. M. Hahn. Lunar and Planetary Science XXXII (2001).

[45] *The Solar Mass Ejection Imager Optics and Baffles Design and Construction*, B.V. Jackson, A. Buffington, P. Hick. Technical Report AFRL-VS-TR-2001-1515.

[46] *The Solar Mass Ejection Imager (SMEI)*, C.J. Eyles, G.M. Simnett, M.P. Cooke, B.V. Jackson, A. Buffington, P.P. Hick, N.R. Waltham, J.M. King, P.A. Anderson and P.E. Holladay. Solar Phys (2003) **217**: 319–347.

[47] *The Proper Treatment of Coronal Mass Ejection Brightness: A New Methodology and Implications for Observations*, A. Vourlidas and R. A. Howard. The Astrophysical Journal (2006), **642**:1216-1221.

[48] *Solar Mass Ejection Imager (SMEI) observations of coronal mass ejections (CMEs) in the heliosphere*, D. F. Webb, D. R. Mizuno, A. Buffington, M. P. Cooke, C. J. Eyles, C. D. Fry, L. C. Gentile, P. P. Hick, P. E. Holladay, T. A. Howard, J. G. Hewitt, B. V. Jackson, J. C. Johnston, T. A. Kuchar, J. B. Mozer, S. Price, R. R. Radick, G. M. Simnett, and S. J. Tappin. Journal of Geophysical Research (2006), Vol. **111**, A12101.

[49] *Observations of the White Light Corona from Solar Orbiter and Solar Probe Plus*, R. Howard, A. Thernisien, A. Vourlidas et al., AGU 2011.

Image processing

[50] *SolarSoft: Overview, Installation, Configuration and Tutorials, http://www.lmsal.com/solarsoft/*, S.L. Freeland, B.N. Handy, Solar Phys (1998). 182, 497.

[51] *Calibrating the Pointing and Optical Parameters of the STEREO Heliospheric Imagers*, D.S. Brown, D. Bewsher, C.J. Eyles, Solar Phys (2009) **254**: 185–225

[52] *Determination of the Photometric Calibration and Large-Scale Flatfield of the STEREO Heliospheric Imagers: I. HI-1*, D. Bewsher, D.S. Brown, C.J. Eyles, B.J. Kellett, G.J. White, B. Swinyard. Solar Phys (2010) **264**: 433–460.

[53] *Long-Term Evolution of the Photometric Calibration of the STEREO Heliospheric Imagers: I. HI-1*, D. Bewsher, D.S. Brown, C.J. Eyles. Solar Phys (2012) **276**:491–499.

Miscaleneous

[54] Allen's Astronomical Quantities, 4th Edition.

[55] ASAP Technical Guide. WAVE OPTICS IN ASAP. January 23, 2008.

[56] ASAP Technical Guide. SCATTERING IN ASAP. May 29, 2012.

[57] *Effect of the dopant content on the physical properties of Y2O3–ZrO2 and CaO–ZrO2 thin films produced by evaporation and sputtering techniques*, M. Boulouz, L. Martin, A. Boulouz., A. Boyer. Materials Science and Engineering B (1999), **67**, 122–131.

[58] Guidelines for contamination control of space optical systems. CLEAN Report, UG-CSL-CLE-00001_1.0

[59] Optical Characterization of Black Appliques. Snail, Keith A.; Brown, Dennis P.; Costantino, Joseph P.; Shemano, Wendy C.; Schmidt, Carl W.; Lynn, William F.; Seaman, Christopher L.; Knowles, Timothy R., Proc. SPIE Vol. 2864, p. 465-474, Optical System Contamination V, and Stray Light and System Optimization, A. Peter M. Glassford; Robert P. Breault; Stephen M. Pompea.

Internet links

[60] European Space Weather portal, www.spaceweather.eu

[61] International Space weather: http://ilwsonline.org/, http://www.spaceweather.com/, http://www.swpc.noaa.gov/

[62] SOHO-LASCO http://lasco-www.nrl.navy.mil

[63] SOHO-EIT http://umbra.nascom.nasa.gov/eit/

[64] STEREO-HI http://www.stereo.rl.ac.uk/

[65] SOHO http://sohowww.nascom.nasa.gov/

[66] STEREO http://stereo.gsfc.nasa.gov/

[67] ASAP http://www.breault.com/software/asap.php

[68] FRED http://www.photonengr.com/software

[69] ZMAX http://www.radiantzemax.com

[70] SIMBAD Astronomical Database http://simbad.u-strasbg.fr/simbad

[71] Encke Comet http://www.nasa.gov/mission_pages/stereo/news/encke.html

Appendix

Appendix

The STEREO-HI front baffle computation sheet

1. Constants

1.1 Units

$arcdeg := \frac{\pi}{180}\cdot rad$ $arcsec := \frac{arcdeg}{3600}$ $Ang := 10^{-10}\cdot m$ $nm := 10^{-9}\cdot m$ $\mu m := 10^{-6} m$

1.2 Optical data

Angular radius of Sun: $Rsun := 960\cdot arcsec$

2. Input parameters

2.1 FOV and aperture

HI1 FOV along Y: $FOV := 20\cdot arcdeg$

$FOV\_border := 3.65\cdot arcdeg$

Lens 1 physical radius: $L1R := \frac{17.2}{2}\cdot mm$ $L1R = 8.6mm$

Aperture stop radius: $L1Rstop := 8\cdot mm$

Optical axis angle: $OA := FOV\_border + \frac{FOV}{2}$ $OA = 13.65arcdeg$

2.4 Diffraction data

Evaluation wavelength: $\lambda d := 7000\cdot Ang$

Number of edges $Nd := 5$

Edge separation: $dd := 28.5\cdot mm$

First edge to center of HI-1 entrance pupil: $D0 := 550mm$

Entrance pupil position in HI-1 barrel: $d\_pup := 4.5\cdot mm$

3. Diffraction computation

3.1 Diffraction angle

Off-pointing angle $\alpha := 0deg$

FOV border vs. Sun limb. $FOV\_limb := FOV\_border - Rsun$ $FOV\_limb = 3.383arcdeg$

Diffraction angle: angle of the line intersecting the front baffle last edge and the upper side of the HI-1 aperture stop, measured w.r.t. the limb direction. This is the brightest shaddow line entering the aperture stop.

$$WL(z) := z + L1Rstop\cdot\sin(OA)$$

$$HL(z) := (z - L1Rstop\cdot\sin(OA))\cdot\tan(FOV\_border) - 2\cdot L1Rstop\cdot\cos(OA)$$

$$\theta d(z) := \operatorname{atan}\left(\frac{HL(z)}{WL(z)}\right) - Rsun + \alpha$$

In our case, the distance d is defined by the first vane location, the number of vanes and the distance inter-vane:

$d\_opt := D0 - (Nd - 1)\cdot dd$ $\quad d\_opt = 436mm$

$\theta d(d\_opt) = 1.322deg$

3.2 Edge heights

The height of edge relatively to the top of the first edge is defined by Hv:

$$H := \left| \begin{array}{l} inter_{Nd} \leftarrow (d\_opt + L1Rstop\cdot\sin(OA))\cdot\tan(\theta d(d\_opt) + Rsun) \\ \theta i \leftarrow \theta d(d\_opt) \\ \text{for } n \in Nd - 1..1 \\ \quad \left| \begin{array}{l} \theta i \leftarrow \theta i - \dfrac{\theta d(d\_opt)}{Nd} \\ inter_n \leftarrow inter_{n+1} + dd\cdot\tan(\theta i + Rsun) \end{array} \right. \\ inter \end{array} \right.$$

$Hv := H_1 - H$ $\quad Hv = \begin{pmatrix} 0 \\ 0.264 \\ 0.66 \\ 1.187 \\ 1.846 \end{pmatrix} mm$

The location of the 5 edges relatively to first one is:

$n := 1..Nd - 1$ $\quad P_{n+1} := n\cdot dd$ $\quad P = \begin{pmatrix} 0 \\ 28.5 \\ 57 \\ 85.5 \\ 114 \end{pmatrix} mm$

3.3 HI-1 entrance aperture location

The height between the first vane edge and the top edge of HI-1 first lens is

$Htop := HL(d\_opt) + Hv_5$ $\quad Htop = 13.99mm$

$D0\_top := D0 + L1Rstop\cdot\sin(OA)$ $\quad D0\_top = 551.888mm$

The height between the first vane edge and the bottom edge of HI-1 first lens is

$Hbot := Htop + 2\cdot L1Rstop\cdot\cos(OA)$ $\quad Hbot = 29.538mm$

$D0\_bot := D0 - L1Rstop\cdot\sin(OA)$ $\quad D0\_bot = 548.112mm$

The top and bottom of aperture to consider for front baffle diffraction are

$H\_top := Htop + d\_pup\cdot\tan\left(\dfrac{FOV}{2}\right)$ $\quad H\_top = 14.784mm$

$H\_bot := H\_top + 2\cdot L1R\cdot\cos(OA)$ $\quad H\_bot = 31.498mm$

3.4 One edge Fresnel computation

$\lambda := \lambda d$

$z := D0$

The diffraction is estimated according the Fresnel diffraction by a straight edge (B&W).

$$CC(\omega) := \int_0^{\omega} \cos\left(\frac{\pi}{2}\cdot x^2\right) dx \qquad SS(\omega) := \int_0^{\omega} \sin\left(\frac{\pi}{2}\cdot x^2\right) dx$$

$$C(\omega) := if(\omega > 29, 0.5, if(\omega < -29, -0.5, CC(\omega)))$$

$$S(\omega) := if(\omega > 29, 0.5, if(\omega < -29, -0.5, SS(\omega)))$$

$$B(\omega) := \frac{1}{2}\cdot\left[\left(\frac{1}{2} + C(\omega)\right)^2 + \left(\frac{1}{2} + S(\omega)\right)^2\right] \qquad f(\omega) := \frac{1}{2\cdot\pi^2}\cdot\omega^{-2}$$

$$B(\omega) := if(\omega > 29, 1, if(\omega < -29, f(\omega), B(\omega)))$$

For one vane we can use wx for ω, and corresponding xw:

$$wx(\xi, \zeta, \delta) := \sqrt{\frac{2}{\lambda}\cdot\frac{1}{\zeta}}\cdot\xi\cdot\cos(\delta)$$

$$xw(\omega, \zeta, \delta) := \frac{-\omega}{\sqrt{\frac{2}{\lambda}\cdot\frac{1}{\zeta}}\cdot\cos(\delta)}$$

3.5 Five edges computation

The diffraction angle is divided between the 5 edges

$$\theta d := \frac{\theta d(d\_opt)}{Nd} \qquad \theta d = 0.264\,arcdeg$$

The w and x variables with vane are redefined:

$$wd(\xi, \zeta, \sigma, \gamma) := \sqrt{\frac{2}{\lambda}\cdot\left(\frac{1}{\zeta} + \frac{1}{\sigma}\right)}\cdot\xi\cdot\cos(\gamma)$$

$$xd(\omega, \zeta, \sigma, \gamma) := \frac{-\omega}{\sqrt{\frac{2}{\lambda}\cdot\left(\frac{1}{\zeta} + \frac{1}{\sigma}\right)}\cdot\cos(\gamma)}$$

The angle between two consecutive vanes being θ and the height difference h are defined by :

$$j := 1, 2 .. Nd - 1$$

$$\theta_j := j\cdot\theta d \qquad \theta = \begin{pmatrix} 0.264 \\ 0.529 \\ 0.793 \\ 1.058 \end{pmatrix} arcdeg$$

$$h_j := dd\cdot\tan(\theta_j) \qquad h = \begin{pmatrix} 0.132 \\ 0.263 \\ 0.395 \\ 0.526 \end{pmatrix} mm$$

And the angles γ are defined by: $k := 2 .. Nd - 1$

$$\gamma_1 := 0 \qquad \gamma_k := \operatorname{atan}\left[\frac{\left(\tan(\theta_k) + \tan(\theta_{k-1})\right)}{2}\right]$$

$$\gamma_{Nd} := \operatorname{atan}\left[\frac{\left(d\_opt\cdot\tan(Nd\cdot\theta d) + dd\cdot\tan(\theta_{Nd-1})\right)}{dd + d\_opt}\right] \qquad \gamma = \begin{pmatrix} 0 \\ 0.397 \\ 0.661 \\ 0.925 \\ 1.306 \end{pmatrix} arcdeg$$

NB: in the axes pointing to center of the Sun, we have:

$$Hv\_relatif := \frac{h + dd\cdot\tan(Rsun)}{\cos(Rsun)} \qquad Hv\_relatif = \begin{pmatrix} 0.264 \\ 0.396 \\ 0.527 \\ 0.659 \end{pmatrix} mm$$

The x-part (and corresponding ω) at entrance aperture position affected by the edges are :

$$xz_1 := z\cdot\tan(\theta_1)$$

$$xz_k := \sum_{l=1}^{k-1} h_l + [\, z - (k-1)\cdot dd \,]\cdot\tan(\theta_k)$$

$$xz_{Nd} := H\_bot$$

$$xz = \begin{pmatrix} 2.538 \\ 4.945 \\ 7.22 \\ 9.364 \\ 31.498 \end{pmatrix} mm$$

$$w_1 := wx(-xz_1, z, \gamma_1)$$

$$w_k := wx\left[-xz_k, z - (k-1)\cdot dd, \gamma_k\right]$$

$$w_{Nd} := wx\left[-xz_{Nd}, z - (Nd-1)\cdot dd, \gamma_{Nd}\right]$$

$$w = \begin{pmatrix} -5.785 \\ -11.573 \\ -17.38 \\ -23.22 \\ -80.61 \end{pmatrix}$$

The rejection of each edge on top of respective following vane is same for all edges:

$$B\_h_1 := B\left(wx(-h_1, dd, \gamma_1)\right)$$

$$B\_h_2 := B\left[wd\left[-(h_2 - h_1), dd, dd, \gamma_1\right]\right]$$

$$B\_h = \begin{pmatrix} 0.026 \\ 0.014 \end{pmatrix}$$

So, global rejection can be computed as product of each vanes rejection.

$$B1(\omega) := B(\omega)$$

$$B2(\omega) := B\_h_1\cdot B(\omega)$$

$$B3(\omega) := B\_h_1\cdot B\_h_2\cdot B(\omega)$$

$$B4(\omega) := B\_h_1\cdot (B\_h_2)^2\cdot B(\omega)$$

$$B5(\omega) := B\_h_1\cdot (B\_h_2)^3\cdot B(\omega)$$

To plot resulting rejections, the following w (i.e. w) variables ranges are used

$$\omega 1 := (w_1), (w_1) + 0.1..0$$

$$\omega 2 := (w_2 - w_1), (w_2 - w_1) + 0.5..-0.5$$

$$\omega 3 := (w_3 - w_2), (w_3 - w_2) + 0.5..0$$

$$\omega 4 := (w_4 - w_3), (w_4 - w_3) + 0.5..0$$

$$\omega 5 := (w_5 - w_4), (w_5 - w_4) + 0.5..0$$

The influence of each vane is computed in the H-1 entrance aperture plane at following vertical postions

$$x1(\omega 1) := xw(\omega 1, z, \gamma_1)$$

$$x2(\omega 2) := xw(\omega 2, z - dd, \gamma_2) + xz_1$$

$$x3(\omega 3) := xw(\omega 3, z - 2\cdot dd, \gamma_3) + xz_2$$

$$x4(\omega 4) := xw(\omega 4, z - 3\cdot dd, \gamma_4) + xz_3$$

$$x5(\omega 5) := xw(\omega 5, z - 4\cdot dd, \gamma_5) + xz_4$$

The rejection values at some particular points are given:

$x1(0) = 0\,\text{mm}$ $\quad x1(w_1) = 2.538\,\text{mm}$ $\quad B1(0) = 0.25$ $\quad B1(w_1) = 1.513\times 10^{-3}$

$x2(0) = 2.538\,\text{mm}$ $\quad x2(w_2 - w_1) = 5.011\,\text{mm}$ $\quad B2(0) = 6.594\times 10^{-3}$ $\quad B2(w_2 - w_1) = 3.986\times 10^{-5}$

$x3(0) = 4.945\,\text{mm}$ $\quad x3(w_3 - w_2) = 7.357\,\text{mm}$ $\quad B3(0) = 9.305\times 10^{-5}$ $\quad B3(w_3 - w_2) = 5.591\times 10^{-7}$

$x4(0) = 7.22\,\text{mm}$ $\quad x4(w_4 - w_3) = 9.575\,\text{mm}$ $\quad B5(0) = 1.853\times 10^{-8}$ $\quad B4(w_4 - w_3) = 7.797\times 10^{-9}$

$x5(0) = 9.364\,\text{mm}$ $\quad x5(w_5 - w_4) = 31.789\,\text{mm}$ $\quad B5(0) = 1.853\times 10^{-8}$ $\quad B5(w_5 - w_4) = 1.14\times 10^{-12}$

The integrated intensity over the HI-1 aperture is

$wtop := wx(-H\_top, z - 4\cdot dd, \gamma_5)$ $\quad wtop = -37.835$

$wbot := wx(-H\_bot, z - 4\cdot dd, \gamma_5)$ $\quad wbot = -80.61$

$Bint := \int_{wbot}^{wtop} B5(s)\,ds$ $\quad Bint = 5.267\times 10^{-11}$

The integrated intensity over the HI-2 aperture is

$H\_top := 0.09\,\text{m}$ $\quad H\_bot := 0.105\,\text{m}$

$wtop := wx(-H\_top, z - 4\cdot dd, \gamma_5)$ $\quad wtop = -230.331$

$wbot := wx(-H\_bot, z - 4\cdot dd, \gamma_5)$ $\quad wbot = -268.72$

$Bint := \int_{wbot}^{wtop} B5(s)\,ds$ $\quad Bint = 2.329\times 10^{-12}$

Following picture presents multiple rejections for external baffles (5 vanes), x range at distance z (0.550m) Each vane influence starts where previous vane influence finishes.